VOLUME NINE

ADVANCES IN PLANAR LIPID BILAYERS AND LIPOSOMES

EDITORIAL BOARD

VOLUME NINE

ADVANCES IN PLANAR LIPID BILAYERS AND LIPOSOMES

Editor

PROFESSOR DR. A. LEITMANNOVA LIU
Department of Physiology, Michigan State University, East Lansing, Michigan, USA
and
Centre for Interface Sciences, Microelectronics Department, Faculty of Electrical Engineering & Information Technology, Slovak Technical University, Bratislava, Slovak Republic

Founding Editor

PROFESSOR DR. H.T. TIEN
Department of Physiology, Michigan State University, East Lansing, Michigan, USA

ELSEVIER

Amsterdam • Boston • Heidelberg • London • New York • Oxford
Paris • San Diego • San Francisco • Singapore • Sydney • Tokyo
Academic Press is an imprint of Elsevier

Academic Press is an imprint of Elsevier
Linacre House, Jordan Hill, Oxford OX2 8DP, UK
32 Jamestown Road, London NW1 7BY, UK
30 Corporate Drive, Suite 400, Burlington, MA 01803, USA
525 B Street, Suite 1900, San Diego, California 92101-4495, USA

First edition 2009

Copyright © 2009 Elsevier Inc. All rights reserved

No part of this publication may be reproduced or transmitted in any form or by any means, electronic or mechanical, including photocopy, recording, or any information storage and retrieval system, without permission in writing from the publisher

Permissions may be sought directly from Elsevier's Science & Technology Rights Department in Oxford, UK: phone (+44) 1865 843830, fax: (+44) 1865 853333; E-mail: permissions@elsevier.com. You may also complete your request online via the Elsevier homepage (http://elsevier.com), by selecting "Support & Contact" then "Copyright and Permission" and then "Obtaining Permissions"

Notice
No responsibility is assumed by the publisher for any injury and/or damage to persons or property as a matter of products liability, negligence or otherwise, or from any use or operation of any methods, products, instructions or ideas contained in the material herein. Because of rapid advances in the medical sciences, in particular, independent verification of diagnoses and drug dosages should be made

Library of Congress Cataloging-in-Publication Data
A catalog record for this book is available from the Library of Congress

British Library Cataloguing-in-Publication Data
A catalogue record for this book is available from the British Library

ISBN: 978-0-12-374822-5
ISSN: 1554-4516

For information on all Academic Press publications
visit our website at www.elsevierdirect.com

Printed and bound in USA

08 09 10 11 12 10 9 8 7 6 5 4 3 2 1

Working together to grow
libraries in developing countries

www.elsevier.com | www.bookaid.org | www.sabre.org

ELSEVIER BOOK AID International Sabre Foundation

CONTENTS

3. Physicochemical and Pharmacokinetic Characterization of Ultradeformable Vesicles using Calcein as Hydrophilic Fluorescent Marker **65**

Ana Paula Corrêa Oliveira Bahia, Larissa Barbosa Rabelo, Warley Cristiano Souza, Lucas Antonio Miranda Ferreira, and Frédéric Frézard

CONTRIBUTORS

Hrushikesh Agashe

Department of Pharmaceutical Sciences, College of Pharmacy, University of Oklahoma Health Science Center, Oklahoma City, OK 73117, USA

Valery F. Antonov

Department of Medical and Biological Physics, Moscow Sechenov Medical Academy, 119992 ul.Trubetskaja, 8 Moscow, Russia

Vibhudutta Awasthi

Department of Pharmaceutical Sciences, College of Pharmacy, University of Oklahoma Health Science Center, Oklahoma City, OK 73117, USA

Ana Paula Corrêa Oliveira Bahia

Departamento de Fisiologia e Biofísica, ICB, Universidade Federal de Minas Gerais, Av. Antônio Carlos 6627, Pampulha, 31270-901 Belo Horizonte, MG, Brazil

Klemen Bohinc

Faculty of Health Studies, University of Ljubljana, Slovenia

Laboratory of Physics, Faculty of Electrical Engineering, University of Ljubljana, Slovenia

Matej Daniel

Laboratory of Biomechanics, Faculty of Mechanical Engineering, Czech Technical University in Prague, Czech Republic

Gregor Dolinar

Laboratory of Mathematics, Faculty of Electrical Engineering, University of Ljubljana, Slovenia

Lucas Antonio Miranda Ferreira

Faculdade de Farmácia, Universidade Federal de Minas Gerais, Av. Antônio Carlos 6627, Pampulha, 31270-901 Belo Horizonte, MG, Brazil

Frédéric Frézard

Departamento de Fisiologia e Biofísica, ICB, Universidade Federal de Minas Gerais, Av. Antônio Carlos 6627, Pampulha, 31270-901 Belo Horizonte, MG, Brazil

Aleš Iglič
Faculty of Health Studies, University of Ljubljana, Slovenia

Laboratory of Biophysics, Faculty of Electrical Engineering, University of Ljubljana, Slovenia

Veronika Kralj-Iglič
Laboratory of Clinical Biophysics, Faculty of Medicine, University of Ljubljana, Slovenia

Mojca Kržan
Department of Pharmacology and Experimental Toxicology, Faculty of Medicine, University of Ljubljana, Korytkova 2, Si-1000 Ljubljana, Slovenia

P.B. Sunil Kumar
Department of Physics, Indian Institute of Technology Madras, Chennai, India

Werner Kunz
Institute of Physical and Theoretical Chemistry, University of Regensburg, D-93040 Regensburg, Germany

Derek Laver
School of Biomedical Sciences, University of Newcastle, Callaghan, NSW 2308, Australia

Metoda Lipnik-Štangelj
Department of Pharmacology and Experimental Toxicology, Faculty of Medicine, University of Ljubljana, Korytkova 2, Si-1000 Ljubljana, Slovenia

Kenichi Morigaki
Research Institute for Cell Engineering, National Institute of Advanced Industrial Science and Technology (AIST), Ikeda 563-8577, Japan

Vladimir P. Norik
Department of Medical and Biological Physics, Moscow Sechenov Medical Academy, 119992 ul.Trubetskaja, 8 Moscow, Russia

Katja Perdan
Department of Pharmacology and Experimental Toxicology, Faculty of Medicine, University of Ljubljana, Korytkova 2, Si-1000 Ljubljana, Slovenia

Šárka Perutková
Laboratory of Biophysics, Faculty of Electrical Engineering, University of Ljubljana, Slovenia

Larissa Barbosa Rabelo
Departamento de Fisiologia e Biofísica, ICB, Universidade Federal de Minas Gerais, Av. Antônio Carlos 6627, Pampulha, 31270-901 Belo Horizonte, MG, Brazil

Michael Rappolt
Institute of Biophysics and Nanosystems Research, Austrian Academy of Sciences c/o Sincrotrone Trieste, Italy

Elena Yu. Smirnova
Department of Medical and Biological Physics, Moscow Sechenov Medical Academy, 119992 ul.Trubetskaja, 8 Moscow, Russia

Warley Cristiano Souza
Departamento de Fisiologia e Biofísica, ICB, Universidade Federal de Minas Gerais, Av. Antônio Carlos 6627, Pampulha, 31270-901 Belo Horizonte, MG, Brazil

Didier Touraud
Institute of Physical and Theoretical Chemistry, University of Regensburg, D-93040 Regensburg, Germany

Nina Vlachy
Institute of Physical and Theoretical Chemistry, University of Regensburg, D-93040 Regensburg, Germany

Masahito Yamazaki
Department of Physics, Faculty of Science, Shizuoka University, Shizuoka 422-8529, Japan

Integrated Bioscience Section, Graduate School of Science and Technology, Shizuoka University, 836 Oya, Suruga-ku, Shizuoka 422-8529, Japan

Jasna Zelko
Laboratory of Clinical Biophysics, Faculty of Medicine, University of Ljubljana, Slovenia

PREFACE

Volume 9 continues in our effort to cover the recent research results on both planar lipid bilayers (also referred to as BLMs) and spherical vesicles from many scientific groups working worldwide in this exciting field. In this volume we continue in the established tradition, namely to include not only the chapters with research results of well-established scientists but also chapters from younger generation of scientists who follow this interdisciplinary field of research worldwide. Nowadays there are already many new venues to be followed in this interdisciplinary field of research and we are convinced that they will continue to multiply even more in many years to come. During his lifetime, late Prof. H. Ti Tien wanted to see these new ideas of interface sciences to be implemented in the everyday life and he was one of the pioneers who started to develop some useful practical applications such as new molecular electronic devices, biosensors, etc.

As is described in seven already published volumes as well as in the present volume of this *Advances* series, the research based on planar lipid bilayers and spherical liposomes has developed into an important, interdisciplinary-oriented scientific field. Today, after nearly five decades of continuous research, this well-established discipline has a great impact in certain areas of membrane biophysics, cell biology, and also biotechnology and medicine. The lipid bilayer, existing in all cell membranes, is most unique in that it not only serves merely as a physical barrier among cells but also functions as a two-dimensional matrix for all sorts of reactions. Also, the lipid bilayer, after suitable modification, acts as a conduit for ion transport, as a framework for antigen–antibody binding, as a bipolar electrode for redox reactions, and as a reactor for energy conversion (e.g., light to electric to chemical energy). Furthermore, a modified lipid bilayer performs as a transducer for signal transduction (i.e., sensing) and numerous other functions as well. All these myriad activities require the ultra thin lipid bilayer of 5 nm thickness.

As of today, black lipid membranes (BLMs or planar lipid bilayers) have been used in a number of applications ranging from fundamental membrane biophysics including photosynthesis, practical AIDS research, and "microchips" study. In reactions involving light, BLMs have provided insights to the conversion of solar energy via water photolysis, and to photobiology comprising apoptosis and photodynamic therapy. Supported bilayer lipid membranes (s-BLMs) are being used in biosensor development. In addition, this volume reviews the studies of others in collaboration with our laboratory and also recent research of others on the use of BLMs as models of certain biomembranes.

We would like to stress some important biophysical aspects of this *Advances* series. Biophysics is composed of many subfields including cell biology, genetics, and physiology. Training in biophysics effectively prepares younger generation of researchers to acquire many necessary skills for careers in a research world that increasingly values interdisciplinary and integrative outlook, which we stress in this *Advances* series. There are many research areas in biophysics such as electrophysiology, bioenergetics, supramolecular assemblies, and membranes. In this book we will focus our attention mainly on the physiological, physical, and biochemical aspects of membranes using experimental planar lipid bilayers and spherical liposomes/vesicles.

Volume 9 of *Advances* series on planar lipid bilayers and liposomes continues to include several invited chapters on a wide range of topics, covering interesting results not only from valuable theoretical research but also from many experimental studies and, last but not least, the published results also refer to new practical applications in many areas of interface sciences dealing exclusively with both planar lipid bilayers and liposomes. The contributed chapters are separate entities to themselves, but they have one common feature. They are based on planar lipid bilayers or spherical liposomes and their practical applications. We are thankful to all contributors for their willingness to honor the memory of late Prof. H. Ti Tien through their contribution of very interesting and inspiring chapters, which are very much appreciated by the whole scientific community.

Only the first stage of editorial work of Volume 1 of the *Advances* series was still based on a joint effort of late Prof. H. T. Tien and me. I wish to use this occasion to express my deep gratitude to everybody who contributed a chapter to one of our already published volumes of this *Advances* series. I highly value the support and help of Dr. Kostas Marinakis, Publisher of Chemistry and Chemical Engineering Department in Elsevier and all his coworkers, especially Dr. Deirdre Clark in Elsevier Office in Amsterdam, The Netherlands, and also his coworkers from the newly established Elsevier Office in Chennai, India, in different stages of preparation of this book series. I am particularly thankful to all of them for their big help in preparation of this book series, which had a very challenging start shortly after the unexpected death of Prof. H. Ti Tien, the founding editor in the year 2004. We will try our best to keep these *Advances* series alive in both fields covering the planar lipid bilayers and spherical liposomes. In this way we all members of the research community in this interdisciplinary field continue to pay our respect to the scientific achievements of Prof. H. Ti Tien.

Angelica Leitmannova Liu

CHAPTER ONE

CURRENT PERSPECTIVES IN LIPOSOME-ENCAPSULATED HEMOGLOBIN AS OXYGEN CARRIER

Hrushikesh Agashe *and* Vibhudutta Awasthi*

Contents

Abstract

Liposome-encapsulated hemoglobin (LEH) is a formulation of hemoglobin-based oxygen carriers where hemoglobin is encapsulated within the lipid bilayers. It is believed that the encapsulated form of hemoglobin is the preferred means of delivering oxygen *in vivo*, because of the favorable toxicity profile, and efficient delivery of oxygen to the hypoxic tissue. This chapter describes the recent

---

* Corresponding author. Tel.: +1 405 271 6593; Fax: +1 405 271 7505;
E-mail address: vawasthi@ouhsc.edu

Department of Pharmaceutical Sciences, College of Pharmacy, University of Oklahoma Health Science Center, Oklahoma City, OK 73117, USA

Advances in Planar Lipid Bilayers and Liposomes, Volume 9
ISSN 1554-4516, DOI: 10.1016/S1554-4516(09)09001-2

advances made in the field of LEH. Specifically, various factors that determine the selection of constituent materials of LEH are discussed. A brief description of the current method of manufacturing LEH has also been described.

1. INTRODUCTION

Every year, nearly 14 million units of packed red blood cells (RBCs) are transfused in the United States alone [1]. Blood transfusion forms an essential component of medical treatment in several different complications ranging from acute hemorrhage to major accidents. Though, transfusion procedures have become relatively safe, issues like requirement of blood-typing and cross-matching, short storage-life, and inadequate supply of safe blood still remain unresolved [2]. Responding to the need of a self-stable oxygen carrier in special situations such as war and natural disasters, researchers around the world are vigorously investigating the development of an artificial oxygen carrier [3]. As discussed in this chapter, the growth and quality of published literature suggests that we are close to vital breakthroughs in this field.

Ideal oxygen-carrying resuscitative fluid should emulate as many functions of fresh whole blood as possible. For example, it should have the capacity to carry and deliver oxygen as RBCs as well as provide plasma-like oncotic activity to maintain circulatory-filling pressure. Like RBCs, it should persist in the intravascular space for a prolonged time period with full functionality, but without any toxicity or immunogenicity. This oxygen-carrying resuscitative fluid may also contain therapeutic agents to address other pathophysiological manifestations during hemorrhagic shock and resuscitation, such as complement activation and reperfusion injury. In addition, the optimal substitute is desired to have properties beyond those of RBCs self-stability at room temperature, ease of use and moderate cost. Even with all these positive characteristics, it is also preferable that the oxygen carrier remains simple in regards to its formulation constitution, and amenable to large scale production.

Oxygen carriage is attributed to be a major function of RBCs, because of the presence of hemoglobin. Quite naturally, the earliest attempts revolved around the administration of unmodified hemoglobin. Hemoglobin is a tetramer containing two pairs of globular peptides (α and β subunits) noncovalently bound to each other. Each subunit contains one heterocyclic ring called porphyrin ring that contains one iron atom (Fe^{2+}). This iron atom in hemoglobin is the binding site of oxygen [3]. However, the use of unmodified hemoglobin is associated with biological toxicity characterized by renal failure and severe vasoconstriction [4, 5]. In addition, in the absence of advanced technology, the initial preparations were often contaminated with remnant RBC stroma that resulted in severe toxicity [6]. The preparation demonstrated short intravascular persistence because of hemoglobin's tendency to break down into its constituent chains and elimination via renal system. To overcome some of these problems, researchers modified the hemoglobin molecule. These second-generation preparations were typified by intravascular nitric oxide (NO) scavenging, and high affinity of hemoglobin for oxygen [7]. These hemoglobin-based oxygen carriers (HBOCs) are categorized as acellular HBOCs. They are nothing but hemoglobin preparations where hemoglobin molecules have been polymerized, cross-linked, polymer-conjugated or otherwise chemically modified to alter one or more of the biological and/or physicochemical properties [3, 8]. Acellular HBOCs are not compartmentalized in any cell-like structure and the hemoglobin comes in direct contact with the biological milieu resulting in a spectrum of undesired physiological effects. A few of such hemoglobin products are in various stages of clinical development and are being pursued in commerce [3].

Cellular HBOCs, on the other hand, rely on encapsulating hemoglobin in some form of vesicular structure. Although not clearly understood, there must be some reason for vertebrate hemoglobin to naturally evolve in a spatially isolated existence inside the RBCs. We know that free hemoglobin acts as a proinflammatory protein that may be detrimental if administered for resuscitation in traumatic brain injury [9]. At the same time, autooxidation of hemoglobin produces harmful reactive oxygen species [10] and, therefore, hemoglobin has been called an oxidative neurotoxin. It may contribute to brain cell injury after brain trauma and hemorrhagic shock [11]. Products that encapsulate hemoglobin are less likely to cause these proinflammatory effects. Encapsulated hemoglobin is devoid of vasoconstrictive effect that is commonly seen with molecularly modified free hemoglobin [12, 13].

The notion of hemoglobin encapsulation within artificial membranes was first investigated by Chang in 1964 [14]. Since then, nanocapsular and liposome-encapsulated hemoglobin (LEH) products have been developed, and currently are in preclinical phase. Compared to free hemoglobin products, encapsulated hemoglobin has several attractive properties: (1) a longer circulation time, (2) reduced vasoactivity, (3) potential to coencapsulate allosteric modifiers and hemoglobin stabilizers, (4) RBC-like oxygen diffusivity, and (5) metabolic clearance by the reticuloendothelial system (RES) in a fashion similar to that of RBCs. In a recent study, acellular preparations (cross-linked, pyridoxylated polyoxyethylene-conjugated, hydroxyethyl starch-conjugated, and polymerized hemoglobin preparations) were compared with hemoglobin encapsulated within the polyethylene glycol-bearing liposomes of 224 ± 76 nm diameter [15]. Based on the permeation studies, the authors concluded that all the products tested have the ability to reach and deliver oxygen even to the areas of thrombosis or infarction where flow of RBCs would not be sufficient. Few acellular hemoglobin products were found responsible for RBC aggregation, which *in vivo* might lead to impaired blood flow. At the same time, hemoglobin liposomes are excluded from the endothelial permeation resulting in the absence of NO-scavenging and vasoconstriction. In addition, the encapsulated hemoglobin had an advantage of the longest circulation time among the products tested [15].

Encapsulation of hemoglobin inside lipid bilayers or liposomes came naturally to various research groups [16–22]. During its initial development phase, LEH met with the same challenges that were common to all liposome research at that time [23]. During this period the most important test was to circumvent the rapid removal of LEH from circulation by the RES. Another problem was the need to develop a large-scale production technology without altering the oxygen-carrying properties of the encapsulated hemoglobin. Major breakthroughs in LEH research came when a high-shear method was used to encapsulate hemoglobin inside the lipid bilayers [24, 25], and polyethylene glycol-lipid in the lipid bilayer was found to overcome RES uptake [26]. Today, the methods of hemoglobin encapsulation are much improved, and allow encapsulation of large amounts of hemoglobin in a stable and functional form. Products that encapsulate highly concentrated and purified hemoglobin within phospholipid membranes are variably called hemoglobin vesicles, neo-red cells or LEH. In this chapter we will discuss the technical aspects of LEH preparation followed by its biological behavior in animal models.

2. LIPID COMPOSITION OF LEH

The synthetic phospholipids and cholesterol remain the backbone of LEH preparations. Proper selection of phospholipids is very important because it not only affects the processing of LEH, but also determines the encapsulation efficiency and oxidative stability of the formulation. The presence of an iron atom in hemoglobin makes it a player in oxidative reactions resulting in phospholipid peroxidation, especially of unsaturated phospholipids. Use of saturated phospholipids (hydrogenated phosphatidylcholine) and synthetic saturated lipids (diacylphosphatidylcholine) reduces the problem of peroxidation. At the same time, unsaturated phospholipids may also oxidize hemoglobin into methemoglobin. There is a good correlation between lipid peroxidation and hemoglobin oxidation, indicating a mutually detrimental effect. [27, 28]. In fact, upon prolonged incubation of the unsaturated lipids and hemoglobin, complete hemoglobin denaturation and dissociation of heme from globin may occur. It is, therefore, clear that saturated lipids are a preferred choice despite being relatively expensive.

Currently, distearoyl phosphatidylcholine (DSPC, $T_m = 55\,°C$) and dipalmitoyl phosphatidylcholine (DPPC, $T_m = 41\,°C$) remain the most widely used phospholipids in LEH compositions. Transition temperatures of these lipids influence the processing conditions during manufacturing and *in vivo* stability after administration. DSPC-LEH is more stable *in vivo*, but demands a processing methodology involving higher shear compared to DPPC-LEH.

Encapsulating a large amount of hemoglobin with least possible phospholipids is another issue in formulation optimization. The encapsulation efficiency is generally expressed in terms of hemoglobin-to-lipid ratio. A high value of this ratio implies better hemoglobin encapsulation. Reports suggested that the presence of anionic lipids like dipalmitoylphosphatidylglycerol (DPPG) and dimyristoylphosphatidylglycerol (DMPG) in lipid composition results in an enhanced protein encapsulation inside the liposomes [29, 30]. It is suggested that anionic lipids interact with oppositely charged domains of proteins to cause this enhancement. However, anionic lipids have their own disadvantages. They have increased tendency to interact with *in vivo* factors, such as complement proteins and other opsonizing factors resulting in rapid clearance from circulation by the RES. Their presence in liposomes has also been associated with toxic effects like vasoconstriction, pulmonary hypertension, dyspnea, etc. [31]. Needless to say, a fine balance has to be accomplished between the necessity of maximizing hemoglobin encapsulation in the least amount of lipid using anionic lipids, and the importance of keeping charge-associated toxicity in control. Recently, a synthetic anionic lipid, 1,5-dipalmitoyl-L-glutamate-*N*-succinic acid, has been synthesized and shown to have improved tolerance profile [32]. The absence of phosphate group in this novel lipid has been attributed for the improved toxicity profile. Interestingly, our group has reported that the inclusion of anionic lipid in the LEH composition had significant effect on LEH retention in blood, yet the encapsulation efficiency of hemoglobin was not significantly different among the preparations [33]. We are also experimenting with a synthetic, inexpensive anionic lipid (unpublished and proprietary), and have found enhanced encapsulation of hemoglobin in the LEH. Among other synthetic anionic lipids, our experience with cholesterol hemisuccinate has been poor.

Cholesterol is another important ingredient that is commonly used in all LEH compositions. Addition of cholesterol increases the rigidity of bilayer that otherwise show considerable fluidity *in vivo*. It is also thought to reduce oxidation of hemoglobin. Since cholesterol has a tendency to transfer between cell membranes and artificial lipid vesicles, cholesterol-less liposomes consisting of pure phospholipid serve as net recipients of cholesterol from interacting cells. This is important because the stability of LEH is affected by ionic strength of the surrounding and enclosed aqueous environment. Cholesterol, to a certain limit, also reduces the tendency of vesicles to fuse together and eventually collapse. Thus, it is believed that cholesterol contributes to the mechanical strength of LEH [34]. Other than inclusion of cholesterol, few groups have attempted polymerization of phospholipids, or coating liposomes with polymers, in order to impart mechanical strength to liposomes [35]. Recently, Palmer and coworkers reported the use of actin matrix in the aqueous core of LEH for improved mechanical stability of the preparation [36].

In an attempt to enhance the stability of LEH in biological environment, lipids that polymerize upon UV-irradiation have also been tested for encapsulation of hemoglobin [37]. The potential of hemoglobin oxidation by UV light is minimized by using carbonyl hemoglobin as a precursor. Polymerization of lipid is thought to impart more stable physical structure, and maintains the particle size of LEH even after repeated freeze–thaw cycles [38]. Novel nonphospholipid LEH using polyoxyethylene-2-cetyl ether and cholesterol (3:1 M ratio) has also been reported, but it has not been studied further [39].

3. PEG MODIFICATION OF LEH SURFACE

An ideal LEH preparation should circulate in blood for a long period of time. At the same time, it should not elicit any complement response. Liposomes made up only of phosphatidylcholine, and cholesterol are rapidly cleared from circulation by the RES. Decoration of the LEH surface with biocompatible, hydrophilic polymers like poly(ethylene glycol) or PEG has been the most common strategy adopted to circumvent the RES uptake. It has been realized that avoiding the RES uptake of LEH is a prerequisite for prolonged LEH efficacy. Ganglioside GM1 which is also used for increasing the circulation time of liposomes proved of little value in case of LEH [40]. PEG has been used for the modification of circulation time of many different delivery systems [41]. PEG-conjugated lipids of various molecular weights are currently commercially available. Conventional PEGylation process of using PEG-lipids in the initial composition of LEH resulted in sub-par use of expensive PEG-lipids, besides lowering the hemoglobin encapsulation. Therefore, postinsertion of PEG lipid into the LEH bilayer is a more popular method of PEGylation of LEH surface rather than incorporating the PEG-phospholipid during thin film formation [33, 42]. In postinsertion technique preformed, LEH is incubated with PEG-lipid solution where its concentration is below the critical micelle concentration. At this concentration, the PEG-phospholipid molecules exist in monomeric form which favors its incorporation into the LEH. The lipid portion inserts into the bilayer, leaving the hydrophilic PEG portion extended outwards [32, 33]. The degree of incorporation is a function of PEG chain length, fatty acid chain length, concentration of lipids, and incubation temperature [43, 44].

Although PEGylation appears to improve the circulation persistence, it must be realized that it only delays the unavoidable clearance of LEH via the RES. The PEGylated stealth systems can get opsonized, activate complements and are prone to macrophage-mediated phagocytosis [45]. Based on the phagocytosis studies with fluorescently-labeled PEG-LEH, it has been demonstrated that it may be a receptor driven process involving CD14, CD36, and CD51/61 receptors [46]. Another important factor to consider about PEG-LEH is its inability to circumvent clearance mechanisms in the body upon repeated administrations. Accelerated blood clearance phenomenon for PEGylated liposomes after repeated administrations has been documented recently [47, 48].

As the entire rationale behind the development of PEG-LEH is to administer large volumes as a substitute of RBCs, it is important that PEG-LEH has the properties matching those of blood. At the same time, it is expected that the administration does not alter the characteristics of recipient's blood. It has been shown that both PEG-LEH and LEH without PEG do not interact with RBCs, but LEH without PEG has a tendency to aggregate by itself [49]. The investigators also demonstrated no effect of PEG-LEH preparation on the viscosity of blood. On the contrary, non-PEGylated LEH preparation increased the viscosity of blood. [49]. Recently, our group has shown the relative tendency of PEGylated and non-PEGylated LEH formulations to activate platelets in blood circulation [50]. The results strongly suggest the role of anionic charge in LEH-mediated platelet reactivity, which is significantly subdued by the incorporation of PEG-lipid in the LEH bilayer. PEGylation not only influences biological properties of the LEH preparations but also positively affects some of its physicochemical properties. For instance, PEGylation improves self-stability of LEH by retarding aggregation and settling of the particulate material. PEG-LEH remains stable even in liquid state at ambient temperature for 1 year. Non-PEG-LEH, on the other hand, was found prone to aggregation [51].

4. HEMOGLOBIN SOURCE

As with any other HBOC, the choice of hemoglobin for the LEH is limited to that from human or bovine origin. Currently, stroma-free human hemoglobin from outdated RBCs is the source of hemoglobin for most LEH research around the world. However, during early stages of development, purified bovine hemoglobin has been investigated for preparing LEH [52–55]. Relative abundance, economy and higher stability are few advantages of bovine hemoglobin over human hemoglobin. The deoxygenated and carbonylated bovine hemoglobin preparations have denaturation transition temperatures at 83 and 87 °C, respectively, which are higher than those of human hemoglobin. Therefore, bovine hemoglobin may be subjected to pasteurization [56]. It is also relatively easy to regulate oxygen affinity of bovine hemoglobin, because of its responsiveness to chloride ion (human hemoglobin responds to DPG). Although immunological response to multiple infusions of bovine hemoglobin-based LEH is still a concern, bovine hemoglobin appears to be a convenient and abundant choice for LEH preparation. It has been shown that antibody response does not affect oxygen binding properties of bovine hemoglobin in dogs [57]. Converting from human to bovine source of hemoglobin could also have significant advantages in terms of the economics of LEH production.

At higher temperatures, native human hemoglobin is prone to denaturation and oxidation, which makes cold processing of LEH (4–8 °C) a mandatory requirement. A more common practice is to use carbonylated form of hemoglobin (CO-hemoglobin) instead of oxyhemoglobin. CO-hemoglobin is a more stable form, and it resists oxidative denaturation even at temperatures as high as 60 °C for several hours. Carbonylation is generally carried out by saturating hemoglobin solution with pure carbon monoxide. Once the final processing of LEH is accomplished, hemoglobin is reclaimed as oxyhemoglobin by oxygenation under bright light [58].

At this point, it is worth acknowledging recombinant hemoglobin as a potential source of hemoglobin for LEH [59]. Although attractive, but it has to go a long way before becoming a viable alternative. In an innovative approach, Kobayashi et al. transformed the protoheme moiety of the hemoglobin molecule into an amphiphilic compound. The amphiphilicity imparted to the protoheme enables it to interact with lipid bilayer of LEH for efficient encapsulation. It also protects heme from oxidative degradation [60].

5. PARTICLE SIZE

As stated earlier that an ideal LEH preparation should be able to carry as large amount of hemoglobin as possible. At the same time it should be able to circulate in blood for a long period of time. In the absence of PEGylation, both these properties depend to a considerable extent on the size of LEH. Empirically, we know that a smaller size of LEH allows only a limited encapsulation of hemoglobin. On the other hand, an increase in size invites rapid clearance from circulation by the RES. Hence an empirical selection of an appropriate LEH size must be performed. In general, circulation kinetics is largely determined by the size of liposome, although other factors like charge and lipid composition, etc., also play important role. LEH is considered as foreign particulate material by the body defense mechanism, and is rapidly removed from the circulation.

The RES uptake of LEH seems to be a size-dependent phenomenon. Liposomes having size >200 nm are more prone to complement activation, opsonization and protein binding, and are cleared rapidly by the RES [61]. In order to avoid the RES uptake, it is customary to maintain a smaller sized liposome preparation. AmBisome^{TM}, for example, has a size range of 45–80 nm [62]. A smaller liposome size, however, does not guaranty its longer circulation. It has been reported that liposomes in the size range of approximately 80 nm accumulate in hepatocytes. These smaller liposomes have an ability to cross the hepatic fenestration (100 nm in size), and interact with hepatocytes. Even relatively larger (400 nm) phosphatidylserine-containing liposomes have been shown to cross endothelial fenestration and localize in hepatocytes by a blood cell-mediated forced extrusion mechanism of deformation and squeezing of large liposomes through endothelial fenestration [63, 64].

Understanding the process of clearance of liposomes becomes even more complicated as the role of electrical charge carried by the liposomes comes into play. Negatively charged lipids are commonly incorporated in LEH composition as they allow higher hemoglobin encapsulation and resist aggregation. The same negative charge is also responsible for enhanced activation of complement system, and LEH clearance from circulation [61]. PEGylation of LEH surface is a widely adopted technique for managing the issue of circulation kinetics; however, PEGylation has its own limitations. There seems to be a size threshold beyond which the positive effect of PEGylation dwindles in regards to the enhancing circulation persistence. In the case of LEH, this threshold appears to be about 275 nm when PEG5000-lipid is postinserted into the lipid bilayer [65]. PEGylation also alters the apparent hydrodynamic diameter of the LEH preparations as was observed by postinserting DSPE-PEG in DPPC/cholesterol/DPPG hemoglobin vesicles [49]. Contradicting this observation is a reported decrease in size of liposomes with increasing PEG-lipid content [66]. While the lipid composition of liposomes may have something to do with this divergent observation, but the latter group argued that with increasing PEG-DSPE concentration, the lateral tension between PEG chains increase, and to reduce this tension, the curvature of the liposome surface increases resulting in decrease in their size. They also observed a shift from lamellar to miceller configuration with increasing PEG-lipid concentration [66]. It is possible that the method (conventional versus postinsertion) of PEGylation has something to do with these divergent observations.

6. HEMOGLOBIN AND OXYGEN AFFINITY

Oxygen affinity of hemoglobin is defined as a partial pressure of oxygen to cause 50% saturation of hemoglobin or p50. Its normal value is about 27 Torr; it is an important factor in regular feeding of the biological machinery with oxygen. Each hemoglobin molecule can bind four molecules of oxygen. The sigmoidal nature of oxygen association–dissociation curve serves well for hemoglobin to load oxygen from 21% oxygenated, alveolar, moist air in lung (100 mm Hg) and unload oxygen in hypoxic tissues (5–20 mm Hg). The unique shape of the curve is governed by the cooperativity demonstrated by hemoglobin subunits. Deoxyhemoglobin has a constrained configuration (tense-state), which upon oxygen binding becomes relaxed. The relaxed configuration of hemoglobin makes it easy for other subunits to bind oxygen.

Oxygen affinity of hemoglobin in the human RBCs is regulated by the presence of an allosteric modifier called 2,3-diphosphoglycerate (DPG). DPG has a strong negative charge, and binds to the central cavity of deoxyhemoglobin molecule. It cross-links the amino acids of β-subunits, and stabilizes the tense-state [67]. When hemoglobin is isolated from RBCS, DPG is lost during processing, resulting in very high affinity of hemoglobin for oxygen. Reconstitution of hemoglobin preparations with allosteric modifiers is a convenient way of recovering the natural p50 of hemoglobin. One of the most commonly used allosteric factors is pyridoxal-5′-phosphate (PLP) which when coencapsulated with hemoglobin significantly alters p50. The main binding site of PLP is the N-terminal of the α- and β-chains and β-82 lysine within the β-cleft. The change in p50 of LEH is related to the PLP concentration [68]. Similar to PLP, inositol hexaphosphate (IHP) has also been used to regulate p50 value [69].

Based on the assumption that it is physiological to match the p50 of artificial oxygen carriers with that of natural blood, LEH formulations have invariably been manufactured with an allosteric modifier. With the object of restoring oxygen-carrying capacity of blood, very little attention was paid to the actual exchanges taking place at microvascular level, and the role oxygen affinity of hemoglobin plays therein. The emphasis was mainly on the development of blood substitutes with p50 similar to or higher than normal blood to facilitate oxygen delivery [70]. However, it has been recently realized that the efficacy of LEH would be dependent on more complex and interdependent factors than mere capacity to deliver oxygen. In fact, it was found that LEH preparation with high p50 would release most of bound oxygen in the arterioles, before they reach microvasculature, where actual oxygen exchange to the hypoxic tissues takes place. Hyperoxygenation of arteriolar wall triggers autoregulatory vasoconstriction, leading to reduced blood flow, which is contrary to the objective of resuscitation in the first place. On the other hand, LEH preparations with low p50 value (high oxygen affinity) have the capacity to unload oxygen only at anoxic or hypoxic tissues, thus attaining targeted oxygen delivery [71]. Using a hamster window model, it has been reported that an LEH preparation with p50 adjusted to 8 Torr released oxygen more slowly as compared to the preparation with a p50 value of 28, suggesting that LEH with low p50 could be a significant source of oxygen under ischemic conditions [72]. At the same time it has been found that under extreme hemodilution partial pressure of oxygen attained is significantly higher for LEH with lower p50 (8 Torr) compared to the high p50 LEH (29 Torr). This effect was attributed to the improvements at the microvascular level characterized by the increased arteriolar blood flow and arterial pressure with low p50 LEH [73]. The importance of improved microvascular physiology in resuscitation is highlighted by the observation that mean arterial pressure, heart rate, and partial pressure of oxygen were restored independently of hemoglobin content after resuscitation with LEH preparations carrying 3.8 or 7.6 g/dl of hemoglobin [56].

7. VISCOSITY OF LEH PREPARATION

The rheology of blood plays a critical role in the regulation of cardiovascular physiology. The normal blood viscosity is a composite of RBC concentration (hematocrit) and plasma viscosity. LEH is particulate in nature, and demonstrates non-Newtonian flow behavior [74]. It has a lower viscosity as compared to the equivalent concentration of free hemoglobin solution. It is recommended that the viscosity of an HBOC/blood mixture should be at least 2 cP in order to ensure normal microvascular function [75]. The viscosity of LEH dispersion can be easily adjusted to a desired value by adding viscosity building material to the dispersion phase. As such, human serum albumin (HSA), recombinant HSA, hydroxyethyl starch, dextran, etc., have been investigated to impart blood-like viscosity to the LEH preparations [76]. The viscosity of LEH/albumin suspension is similar to that of human blood when albumin concentration is about 5% [77].

Recent findings in the field of blood substitutes have challenged the conventional thought that low-viscosity LEH will improve blood flow, and hence the physiological consequence of resuscitation. It is now believed that in hypovolemia, restoration of volume and microvascular function is of immediate priority, and restoration of oxygen delivery capacity only comes next. It has been determined that after hemorrhagic shock, survival depends on functional capillary density (FCD or density of capillaries with RBCs transit), and is independent of the tissue oxygenation. The FCD can be restored by maintaining capillary hydraulic pressure to normal level. Use of a high-affinity (low p50) oxygen carrier in combination with restoration of FCD delivers adequate oxygen at a much lower dose of hemoglobin, improving efficacy and economy of the preparation. In light of these observations, it is now believed that a blood substitute should not only have the ability to deliver oxygen, but should also act as a high-viscosity plasma expander [71]. This is contrary to the earlier belief that the low-viscosity plasma expander would be more useful in negotiating the peripheral resistance and improving cardiac output.

At 50% decrease in hematocrit, even nonoxygen-carrying plasma expander having viscosity similar to plasma can provide effective resuscitation. Plasma expander compensates for the reduced hematocrit by increasing the cardiac output. Beyond the so-called transfusion trigger, blood transfusion or increasing plasma density becomes essential to restore the normal FCD value. At 11% hematocrit, maintenance of plasma viscosity to 2 cP using high-viscosity dextran (500 kDa) successfully maintained the FCD value to normal [78]. It has been postulated that the reduced viscosity decreases the shear stress as well as the release of vasodilating factors resulting in vasoconstriction, and decreased perfusion and O_2 delivery to the tissue. On the contrary, high-viscosity plasma expanders have exactly opposite effect leading to increased blood flow and oxygenation of tissue. At a certain level of hemodilution, enhancing viscosity improves microcirculation by directly influencing the vascular diameter via endothelial wall shear stress [79]. However, too viscous of an LEH/plasma expander suspension may result in aggregation and capillary blockage, and may also increase the diffusion barrier for the flux of oxygen from LEH to the tissues.

8. Oncotic Pressure and Isotonocity

Blood is a complex system with a variety of circulating proteins that not only enhance the viscosity of blood but also exert oncotic pressure in the vasculature. Oncotic pressure acts in opposition to the hydrostatic pressure and balances the fluid distribution between blood and interstitial fluid compartments. Normal plasma has colloidal oncotic pressure of about 28 mm Hg [80, 81]. Unencapsulated hemoglobin solutions exert oncotic pressure by virtue of their high hemoglobin concentration, and any modification of hemoglobin has a significant impact on its oncotic property [82]. On the other hand, encapsulated hemoglobin has very little effect on both the overall osmolarity and the oncotic activity of LEH. Therefore, LEH by itself has a poor oncotic pressure. An adequate oncotic activity in LEH is necessary to correct and maintain the vascular volume deficit. To this effect, the LEH preparations are made oncotically active by adding albumin, pentastarch, or other such substance to the dispersion medium. LEH preparation with 5% extravesicular albumin has a colloidal oncotic pressure close to that of plasma.

Like the oncotic pressure, the osmotic pressure is also a colligative property, and depends on the number of species in solution. The osmotic properties of LEH depend upon the constitution of the dispersion medium, which usually contains salts and oncotic agents. Intuitively, a resuscitative fluid containing LEH should be isotonic with plasma since it will be administered in large quantities. However, the existing theory is confronted by the abundant evidence in support of the utility hypertonic saline as a resuscitative fluid [83–85]. The widespread beneficial effects of hypertonic saline have made this fluid an attractive choice, especially when combined with hyperoncotic colloid [85, 86]. Not surprisingly, a combination of LEH and hypertonic saline was found to be associated with improved blood pressure, reduced acidosis, and increased survival in a rat model of 70% hypovolemic shock [87]. It will be worthwhile to further investigate the resuscitative properties of improved LEH formulations available today in combination with a hypertonic dispersion phase. The effect of hyperosmotic external medium on the long-term physicochemical stability of LEH also needs further investigation.

9. HEMOGLOBIN AUTO-OXIDATION AND METHEMOGLOBIN FORMATION

Useful encapsulation of hemoglobin within the lipid bilayer depends on the mutual, but compatible interaction between the two. Hemoglobin interacts with the phospholipid bilayer by both electrostatic and hydrophobic forces [88]. Hemoglobin has a tendency to undergo auto-oxidation. Oxidation of hemoglobin increases the rate of heme loss resulting in its denaturation and precipitation. Pure oxyhemoglobin is prone to auto-oxidation even at refrigerated temperature. Deoxyhemoglobin retards auto-oxidation, and is known to be more stable against thermal and chemical denaturation [89]. However, preparing oxygen-free hemoglobin is technically difficult, because partially saturated hemoglobin is more susceptible to auto-oxidation than the fully oxygenated hemoglobin [90]. Molecular oxygen binds to ferrous atom of deoxyhemoglobin and can acquire one of the unpaired electrons of the outer shell of ferrous to produce methemoglobin and superoxide free radical (Eq. (1)). Auto-oxidation also is a regular phenomenon inside the RBCs; however, native hemoglobin is kept in functional form by a highly specialized enzymatic system present inside the RBCs. Cellular methemoglobin reductase, superoxide dismutase, catalase, glutathione peroxidase, and glutathione reductase help control the oxidative end products [91]. The activities of these enzymes depend on a constant supply of reduced nicotinamide dinucleotides.

$$\mathrm{HbFe}^{2+} + \mathrm{O}_2 \Rightarrow \mathrm{HbFe}^{2+} - \mathrm{O}_2 \Leftrightarrow \mathrm{HbFe}^{3+} - \mathrm{O}_2^{-} \Rightarrow \mathrm{HbFe}^{3+} + \mathrm{O}_2^{-}. \tag{1}$$

Purified hemoglobin is not expected to have an RBC-like protection, because most of the enzymes and cofactors are lost during the isolation process. Early attempts of using enzyme systems for *in vitro* reduction of methemoglobin were based on reductases [41, 92]. While maintaining free hemoglobin unoxidized is still an unconquered challenge, in LEH it is possible to coencapsulate components of the enzyme system with hemoglobin. LEH containing 0.1 mM β-NAD, 100 mM D-glucose, 2 mM adenine, 2 mM inosine, 1 mM $MgCl_2$, 1 mM KCl, 9 mM KH_2PO_4, and 11 mM Na_2HPO_4 has been reported to reduce methemoglobin formation from 1% to 0.4% per hour at 37 °C [93]. The use of reductants (thiols, ascorbate, methylene blue, etc.) and enzymes (catalase and superoxide dismutase) has also been investigated [94]. The effectiveness of the reducing agents depends upon their redox potential relative to that of the ferrous–ferric system. Thus, homocysteine and glutathione are more efficient than the easily oxidizable cysteine. In fact, cysteine demonstrates prooxidative behavior because of its rapid auto-oxidation and generation of free radicals [95]. Coencapsulation of catalase (5.6×10^4 U/ml) within the LEH reduces peroxide-dependent methemoglobin formation [93]. Coencapsulation of catalase and superoxide dismutase together with homocysteine (5–10 mM) in LEH improves the reduction process as compared to the use of homocysteine alone [95]. Our own experience with the use of the reducing systems to maintain hemoglobin in functional form has been mixed. It is important to remember that any additional component added to the LEH formulation will potentially impact encapsulation efficiency of hemoglobin.

The reducing systems described above work well *in vitro*, but have a tendency to fail *in vivo* [94]. *In vivo*, hemoglobin is saturated and desaturated continuously depending upon the pO_2 that ranges from 100 mm Hg in the arterial blood to about 20 mm Hg in the tissue capillaries. Considering that deoxyhemoglobin is prone to rapid oxidation, and is produced at tissue pO_2, its repeated encounters with oxygen in lung may be the reason for the failure [94]. It is possible to reduce hemoglobin oxidation by adding reductants, such as methylene blue and ascorbate in the external phase of LEH, but the external reductants are irreversibly and rapidly consumed [94]. From a manufacturing viewpoint, a photochemical method of reducing methemoglobin in the presence of flavin electron acceptor [96] to the reduction of methemoglobin in LEH has been investigated [97]. Visible light irradiation (435 nm) of LEH containing flavin mononucleotide and ethylenediaminetetraacetic acid (EDTA) rapidly reduces methemoglobin. But there are practical limitations to this method for achieving methemoglobin reduction. First, the EDTA-based reaction produces unwanted side products, and second, the reaction requires significant dilution of LEH suspension to allow visible light to penetrate and execute the reduction process.

In regards to the question of lipid oxidation in liposomes, there are several well-presented reports in the literature. Suffice is to say that the inclusion of α-tocopherol appears to retard lipid peroxidation by free radicals [98–101].

10. CURRENT MANUFACTURING TECHNOLOGY

It is not surprising to note that encapsulation of hemoglobin has been attempted by most of the traditional methods of liposome manufacturing including freeze–thaw, sonication [102], reverse-phase evaporation [103], dehydration–rehydration [104], and detergent dialysis [105]. Conservation of oxygen-carrying property of hemoglobin and accomplishing optimal particle size are the chief factors governing the method of LEH preparation. In addition, the ability to scale-up production of LEH in large volumes is also an important determinant. The two techniques that have fulfilled these requirements, at least partially, are extrusion through membrane filters of uniform pore size, and high-shear homogenization.

In the conventional extrusion method, the lipid–hemoglobin mixture is sequentially passed through filters of decreasing pore size [32]. Although polycarbonate filters provide uniform-sized pores, they have a tendency to rapidly clog when a highly concentrated lipid–hemoglobin suspension is extruded. Cellulose ester membranes are relatively easier to work with, but they do not provide a sharp cut-off in pore size. To improve the rate of extrusion and encapsulation efficiency, and to impart reduced lamallarity to the LEH, anionic lipids are added to the formulation. For practical purposes, extrusion temperature needs to be maintained close to the T_m of the lipid, but not so high as to damage and denature hemoglobin. This condition limits the choice of saturated phosphatidylcholine to those with low melting temperature. Although hemoglobin can be stabilized by carbonylation, the successful laboratory method of converting CO-hemoglobin back to oxy-hemoglobin is limited in scale-up. To ease the process of extrusion, and to prevent the filter from clogging, a proliposome approach is often recommended. In this approach, about 250 nm precursor liposomes are prepared by repeated extrusion, freeze-drying, and rehydration [32]. This additional step produces a proliposome powder with a stabilized and controlled size which upon reconstitution with hemoglobin solution attains a particle size close to that of the precursor liposomes. Such a method is reported to yield highly uniform LEH, with large encapsulation efficiency and is exemplified by a reproducibly high-quality LEH [106]. Appropriate selection of encapsulation conditions, such as pH, ionic strength, temperature, and the content of anionic lipid results in a maximization of hemoglobin encapsulation [107]. The extruder-produced LEH has been characterized in detail [108], and has been a method of choice for several groups in Japan promoting LEH to clinical phase [109]. Modern liposome extruders have the capacity to produce large amounts of LEH, in both continuous as well as batch operations.

Another useful method to produce LEH is based on homogenization of lipid phase with hemoglobin solution in high-shear conditions. It all started with the use of microfluidizer (Microfluidics Corp., Newton, MA), and has catalyzed in the promotion of several other homogenizers. Simplicity and scalability are the major advantages of this technique. The capacities of the homogenizers vary from few milliliters to several liters. The actual process of microfluidization and parameter setup have not changed too much since it was first used for LEH production [17, 105]. The microfluidizer forces the lipid–hemoglobin mixture at high pressure through an interaction chamber where two high-velocity streams of liquid collide against each other resulting in particle size reduction. The pressure may be applied by a pneumatically driven pump. The final particle size of LEH depends upon the channel size of the chamber, the number of times the suspension is passed through the chamber, lipid composition, the processing temperature and pressure [110]. Processing the material several times through the interaction chamber ensures uniformity in particle size; however, homogenous and compact size distribution is difficult to obtain. It has been reported that the addition of 5–10 mg/ml albumin offers a limited control over postmicrofluidization size distribution [42]. In one of the current LEH manufacturing technique, M110T model microfluidizer is used to pass the mixture 15 times through an interaction chamber (200–400 μm) under 20–40 psi [42]. It is possible to produce 175–250 nm LEH under these conditions with optimization of the lipid formulation [111]. Even with optimal processing methods, the hemoglobin encapsulation efficiency is usually no more than 5–25%. To improve the utilization of hemoglobin, recycling of unencapsulated hemoglobin has been successfully investigated [42]. More advanced homogenizers that combine the high shear process of microfluidizers and the size control of extruders have recently become available from Avestin Inc. (Ottawa, Canada). These combination machines offer a significant advancement in LEH manufacturing, and are a machine of choice in our current laboratory research (Fig. 1).

11. TOXICOLOGICAL ISSUES

The major advantage of LEH over acellular HBOCs is that the encapsulation of hemoglobin imparts vasoinactivity to the oxygen carrier. Acellular HBOC are small in size, and can diffuse easily through the endothelial wall. These products are thought to scavenge natural

Front View Back View Finished LEH

Emulsiflex C3 Homogenizer from Avestin (Ontario, Canada) installed in a laminar hood

Figure 1 **Photographs of current manufacturing setup inside a laminar hood. The laminar hood was modified to accommodate the homogenizer driven by an electric motor. Also shown is a batch of finished LEH product consisting of DPPC, cholesterol, DSPE-PEG$_{5000}$, anionic lipid, and vitamin E. The p50 of the LEH was modulated to 35 by coencapsulating pyridoxal-5′-phosphate (PLP:Hb molar ratio = 2.5:1).**

vasodilator, nitric oxide resulting in vasoconstriction and hypertensive response. Overoxygenation of vessel wall by free hemoglobin in circulation could be an additional factor contributing to the vasoconstriction. In case of acellular hemoglobin carriers, the oxygen delivery to vessel wall is an additive process where diffusion of free oxygen and facilitated diffusion of oxygen bound to hemoglobin are the two components involved. Net result is overoxygenation of the vessel wall triggering the autoregulatory constriction response. Facilitated diffusion process is absent in case of the LEH because of its larger size. The LEH, due to its larger size (~250 nm), is also unable to pass through the endothelial membrane, and scavenge nitric oxide. As a result LEH preparations are devoid of hypertensive response [70].

Encapsulation of hemoglobin subdues the toxicity observed with free hemoglobin, but the liposome itself has a typical toxicity profile. The lipid composition of LEH has a significant impact on LEH toxicity. LEH made up of hydrogenated soy lecithin induces several transient untoward biological responses, such as hypertension, tachycardia, thrombocytopenia, hemoconcentration, and elevation of thromboxane B2. The fact that platelet-activating factor (PAF) antagonist BN 50739 prevents these hemodynamic changes, indicates that PAF is partially responsible for these effects of LEH [112]. Use of synthetic DSPC in place of soy lecithin significantly improves this toxicity profile [112]. Liposomes also have a tendency to interact with complement proteins and cause pulmonary hypertension and other hypersensitivity reactions in patients [113–115]. A marked reduction in circulating thrombocytes has also been observed in animals [13, 42]. Incorporation of anionic phospholipid in the LEH composition aggravates thrombocytopenic reaction. These effects have been grouped within complement activation-related pseudoallergy or CARPA [42, 113]. LEH-mediated complement activation is dependent on the particle size, size distribution, endotoxin contamination, charge, and surface coating. It may be partially prevented by PEGylation, uniform size distribution, and by reducing the content of anionic lipids.

Administration of large doses of LEH may also result in the RES toxicity. It has been shown that LEH causes only a transient change in plasma enzyme profiles in rats without any irreversible damage to the RES [116, 117]. A similar observation was made earlier when LEH was administered in mice (25% top-load); liver and spleen abnormalities were transient and disappear within 1–2 weeks with no significant alteration of blood chemistry [118]. The animals receiving LEH (20 ml/Kg body weight, phospholipid 4 g/dl) show splenomegaly for several days after infusion, but the total body weight tends to remain normal [116]. The phagocytic index initially drops before reversibly increasing for several days beyond the basal level [116].

In an attempt to investigate the effect of LEH on host immune response to infection, Sherwood et al. injected phosphatidylinositol or PEG-PE-containing LEH in mice challenged with *Listeria monocytogenes* [119]. LEH enhanced mortality and reduced *in vitro* phagocytic activity of rat alveolar macrophages [119]. In regards to the potential of generating antibody response, LEH with homologous hemoglobin injected subcutaneously in rats with or without Freund's adjuvant were found to be nonantigenic. Heterologous hemoglobin showed an insignificant increase in antibody titers with Freund's adjuvant [120]. How these results affect the possible use of bovine hemoglobin in LEH preparations is not yet clear.

12. *IN VIVO* BIODISPOSITION

Opsonization of the vesicles by immunoproteins is the most likely path of LEH clearance; however, an opsonin-independent pathway of LEH clearance has been reported where monocytic uptake of LEH is blocked by anti-CD14, anti-CD36, and anti-CD51/61 antibodies [46]. Like conventional liposomes, the extent of RES uptake depends on several factors including size, lipid composition, dose, surface modification, and the animal species. The development of stable labeling of liposomes with the gamma ray-emitting radionuclide, technetium-99m (Tc-99m), opened the possibility of utilizing nuclear imaging to noninvasively follow LEH biodisposition [121]. This method has been extensively used to evaluate LEH biodistribution in small animals. When Tc-99m-LEH (DPPC, cholesterol DPEA, PEG-DSPE, 5:5:1:0.033 M ratio) was administered (top-load, 14 ml/Kg), RES organs accounted for about 27% and 14% in rats and rabbits, respectively, after 48 h; circulating LEH was 33.3% in rats and 51% in rabbits [122]. It is important to note that the RES is also the normal route for elimination of senescent RBCs. The accumulated LEH disappears from liver and spleen within a week of infusion [116]. In a slightly different formulation of LEH (DSPC:cholesterol:vitamin E, 51.4:46.4:2.2), administration of a small dose (2 ml) of LEH in rabbits yielded 14% circulating LEH, and enormous accumulation in liver (52.1%) after 24 h. PEGylation of the same formulation improved the circulating LEH to 40% and reduced the liver uptake to 19.1% of administered dose at 24 h [33]. In contrast to the liver uptake, PEGylation increased the spleen uptake by 8.5-fold. With 10% of anionic lipid (DMPG), the liver uptake of LEH dropped from 35% (non-PEGylated) to 11.5% (PEGylated). A larger dose (25% of circulating blood) of the same LEH in a rodent models of 25% hypovolemia demonstrated 18% and 31% of circulating LEH even after 48 h in rats and rabbits, respectively [42]. Liver uptake (rats, 10.3% and rabbits, 5.4%) and spleen accumulation (rats, 2.4% and rabbits, 0.8%) showed a corresponding drop. Using nuclear imaging, it has been possible to visualize the temporal accumulation of LEH in liver and spleen [26, 123, 124]. The relative contribution of these organs to the LEH metabolism is a function of liposome size, composition, and the presence of surface PEG-coating. These recent studies demonstrate a significant improvement in the handling of LEH in animal models, mostly attributed to the advances in formulation and manufacturing technology.

It is desired that the intravascular persistence of LEH in humans should be at least 5–7 days, which is the time the body needs to regenerate lost RBCs [125, 126]. While circulation half-life of LEH is governed by its RES-based elimination from circulation, functional capacity of circulating LEH is determined by the rate of hemoglobin-to-methemoglobin conversion. Once administered, methemoglobin is generated at a rate of about 1–2% per hour [127]. While it is not possible to prevent this process, it is possible to retard hemoglobin oxidation by coencapsulating catalase and cofactors [94]. Circulation $T_{1/2}$ of LEH is also affected by the amount administered [128]. A large dose of LEH exhausts the endocytotic or the plasma-opsonizing capacity, and tends to increase the circulating liposomes in blood [29]. On the basis of circulation kinetics in 25% hypovolemic exchange models, the half-life of Tc-99m-LEH in blood was found to be 30 and 39.8 h in rats and rabbits, respectively. Although it is difficult to accurately estimate circulation half-time of LEH in humans, on the basis of animal experiments, it has been roughly estimated that a circulation half-life of 12–20 h in rats translates into 40–60 h in humans [129]. Based on this relationship, half-life of 30 h of current formulation of LEH in rats would yield over 90 h of circulation half-life in humans.

13. PHYSIOLOGICAL AND SURVIVAL STUDIES IN ANIMAL MODELS OF HEMORRHAGIC SHOCK

The ultimate objective of LEH resuscitation is to globally improve the physiology of shock, and enhance survival situations of in acute blood loss. Cardiovascular parameters, such as mean arterial pressure, cardiac output, heart rate, blood gas, and mixed venous oxygen tension are usually measured as surrogate markers to evaluate the physiological responses to LEH infusion in animal models of shock. The most comprehensive assessment of LEH efficacy has been performed by Tuschida and colleagues. Unlike albumin solution, LEH (10 g/dL in 5% albumin) maintained mean arterial blood pressure, heart rate, aortic blood flow, and peripheral resistance near basal levels when up to 90% of circulating blood in rats was exchanged with LEH [130]. The LEH also preserved oxygen delivery and consumption similar to the homologous RBCs for at least 30 min after the completion of the exchange; however, renal cortical oxygen tension and skeletal muscle oxygenation were significantly below the level seen in animals transfused with RBCs [130]. Lower tissue oxygenation with LEH may be due to the loss of shear-induced vasodilation or the complement-mediated vasoconstriction [49]. Exchange transfusion (90%) with PEGylated LEH shows higher blood flow in abdominal aorta than that with LEH without PEG [49]. It is possible that nonaggregating behavior of PEG-LEH improves its rheological properties in small capillaries. PEG-LEH was also shown to supply oxygen better than the LEH without PEG [49]. At the microvascular level, LEH was found to improve subcutaneous blood flow and tissue oxygenation in a conscious hamster model of 50% shock [56]. In regards to the efficacy of LEH to improve survival, rats with 50% hypovolemic shock receiving LEH suspended in recombinant albumin showed 100% 6-h survival as compared to only 75% 6-h survival of rats infused with albumin alone [76]. Although important, not many long-term survival studies are reported in the literature. Our group has recently reported a novel noninvasive technique to quantify cerebral metabolic rate of oxygen in a rat model of hemorrhagic shock using positron emission tomography and inhalation of O-15 labeled oxygen gas. It was found that the LEH resuscitation improved oxygen metabolism in brain tissue [131].

14. SUMMARY

Spatial separation of hemoglobin inside the lipid bilayers confers many desirable properties to the LEH. Yet, like other HBOCs, it is not a complete resuscitation fluid for hypovolemic shock. In severe hemorrhage, providing enhanced oxygen-carrying capacity by the resuscitation fluid is not enough. At the same time, other associated pathophysiology related to hemorrhage calls for additional components, such as oncotic and haemostatic agents. Based on these facts, the artificially assembled hemoglobin preparations are rightly described as oxygen therapeutics rather than as complete blood substitutes. A complex LEH formulation which is stable over a wide range of temperatures, contains inhibitors of complement activation, reperfusion injury, oncotic substance, and has long circulation and functional half-life with minimal toxicity will be ideal and come close to replacing whole blood for resuscitation. At the same time, many of the important milestones have been achieved, and LEH continues to show promise as part of an advanced armamentarium of oxygen therapeutics.

ACKNOWLEDGMENTS

The authors acknowledge the grant support from the National Institutes of Health (R21 EB005187-02).

REFERENCES

[1] J.L. Stollings, L.J. Oyen, Oxygen therapeutics: Oxygen delivery without blood, Pharmacotherapy 26 (2006) 1453–1464.

[2] J.P. Allain, Transfusion risks of yesterday and of today, Transfus. Clin. Biol. 10 (2003) 1–5.

[3] M.S. Inayat, A.C. Bernard, V.S. Gallicchio, B.A. Garvy, H.L. Elford, O.R. Oakley, Oxygen carriers: A selected review, Transfus. Apher. Sci. 34 (2006) 25–32.

[4] S.A. Gould, G.S. Moss, Clinical development of human polymerized hemoglobin as a blood substitute, World J. Surg. 20 (1996) 1200–1207.

[5] V. Awasthi, Pharmaceutical aspects of hemoglobin-based oxygen carriers, Curr. Drug Deliv. 2 (2005) 133–142.

[6] M. Feola, J. Simoni, P.C. Canizaro, Quality control of hemoglobin solutions. I. The purity of hemoglobin before modification, Artif. Organs 15 (1991) 243–248.

[7] T.J. Reid, Hb-based oxygen carriers: Are we there yet? Transfusion 43 (2003) 280–287.

[8] H.W. Kim, A.G. Greenburg, Artificial oxygen carriers as red blood cell substitutes: A selected review and current status, Artif. Organs 28 (2004) 813–828.

[9] J.B. Gibson, R.A. Maxwell, J.B. Schweitzer, T.C. Fabian, K.G. Proctor, Resuscitation from severe hemorrhagic shock after traumatic brain injury using saline, shed blood, or a blood substitute, Shock 17 (2002) 234–244.

[10] T. Kawano, H. Hosoya, Oxidative burst by acellular haemoglobin and neurotransmitters, Med. Hypotheses 59 (2002) 11–15.

[11] R.F. Regan, B. Rogers, Delayed treatment of hemoglobin neurotoxicity, J. Neurotrauma 20 (2003) 111–120.

[12] K. Nakai, N. Matsuda, M. Amano, T. Ohta, S. Tokuyama, K. Akama, Y. Kawakami, E. Tsuchida, S. Sekiguchi, Acellular and cellular hemoglobin solutions as vasoconstrictive factor, Artif. Cells Blood Substit. Immobil. Biotechnol. 22 (1994) 559–564.

[13] W.T. Phillips, R. Klipper, D. Fresne, A.S. Rudolph, M. Javors, B. Goins, Platelet reactivity with liposome-encapsulated hemoglobin in the rat, Exp. Hematol. 25 (1997) 1347–1356.

[14] T.M. Chang, Semipermeable microcapsules, Science 146 (1964) 524–525.

[15] H. Sakai, H. Hara, M. Yuasa, A.G. Tsai, S. Takeoka, E. Tsuchida, M. Intaglietta, Molecular dimensions of Hb-based O(2) carriers determine constriction of resistance arteries and hypertension, Am. J. Physiol. Heart Circ. Physiol. 279 (2000) H908–H915.

[16] L. Djordjevich, I.F. Miller, Synthetic erythrocytes from lipid encapsulated hemoglobin, Exp. Hematol. 8 (1980) 584–592.

[17] M.C. Farmer, S.A. Johnson, R.L. Beissinger, J.L. Gossage, A.B. Lynn, K.A. Carter, Liposome-encapsulated hemoglobin: A synthetic red cell, Adv. Exp. Med. Biol. 238 (1988) 161–170.

[18] B.P. Gaber, P. Yager, J.P. Sheridan, E.L. Chang, Encapsulation of hemoglobin in phospholipid vesicles, FEBS Lett. 153 (1983) 285–288.

[19] R. Rabinovici, A.S. Rudolph, F.S. Ligler, E.F. Smith, 3rd, G. Feuerstein, Biological responses to exchange transfusion with liposome-encapsulated hemoglobin, Circ. Shock 37 (1992) 124–133.

[20] A.S. Rudolph, The freeze dried preservation of liposome encapsulated hemoglobin: A potential blood substitute, Cryobiology 25 (1988) 277–284.

[21] A.S. Rudolph, Encapsulated hemoglobin: Current issues and future goals, Artif. Cells Blood Substit. Immobil. Biotechnol. 22 (1994) 347–360.

[22] E. Tsuchida, Perspestives of blood substitutes, in: E. Tsuchida (Ed.), Blood Substitutes—Present and Future Perspectives, Elsevier Science S.A., Tokyo, 1998, pp. 1–14.

[23] A.D. Bangham, Liposomes: Realizing their promise, Hosp. Pract. (Off. Ed.) 27 (1992) 51–56, 61–52.

[24] R.L. Beissinger, M.C. Farmer, J.L. Gossage, Liposome-encapsulated hemoglobin as a red cell surrogate. Preparation scale-up, ASAIO Trans. 32 (1986) 58–63.

[25] M.C. Farmer, B.P. Gaber, Liposome-encapsulated hemoglobin as an artificial oxygen-carrying system, Methods Enzymol. 149 (1987) 184–200.

[26] W.T. Phillips, R.W. Klipper, V.D. Awasthi, A.S. Rudolph, R. Cliff, V. Kwasiborski, B.A. Goins, Polyethylene glycol-modified liposome-encapsulated hemoglobin: A long circulating red cell substitute, J. Pharmacol. Exp. Ther. 288 (1999) 665–670.

[27] Y. Huang, W. Chung, I. Wu, Effect of saturated/unsaturated phosphatidylcholine ratio on the stability of liposome-encapsulated hemoglobin, Int. J. Pharm. 172 (1998) 161–167.

[28] J. Szebeni, C.C. Winterbourn, R.W. Carrell, Oxidative interactions between haemoglobin and membrane lipid. A liposome model, Biochem. J. 220 (1984) 685–692.

[29] D.C. Drummond, O. Meyer, K. Hong, D.B. Kirpotin, D. Papahadjopoulos, Optimizing liposomes for delivery of chemotherapeutic agents to solid tumors, Pharmacol. Rev. 51 (1999) 691–743.

[30] P. Walde, S. Ichikawa, Enzymes inside lipid vesicles: Preparation, reactivity and applications, Biomol. Eng. 18 (2001) 143–177.

[31] H. Kiwada, H. Matsuo, H. Harashima, Identification of proteins mediating clearance of liposomes using a liver perfusion system, Adv. Drug Deliv. Rev. 32 (1998) 61–79.

[32] K. Sou, Y. Naito, T. Endo, S. Takeoka, E. Tsuchida, Effective encapsulation of proteins into size-controlled phospholipid vesicles using freeze-thawing and extrusion, Biotechnol. Prog. 19 (2003) 1547–1552.

[33] V.D. Awasthi, D. Garcia, R. Klipper, B.A. Goins, W.T. Phillips, Neutral and anionic liposome-encapsulated hemoglobin: Effect of postinserted poly(ethylene glycol)-distearoylphosphatidylethanolamine on distribution and circulation kinetics, J. Pharmacol. Exp. Ther. 309 (2004) 241–248.

[34] D.R. Arifin, A.F. Palmer, Determination of size distribution and encapsulation efficiency of liposome-encapsulated hemoglobin blood substitutes using asymmetric flow field-flow fractionation coupled with multi-angle static light scattering, Biotechnol. Prog. 19 (2003) 1798–1811.

[35] K. Akama, W.L. Gong, L. Wang, S. Tokuyama, E. Tsuchida, Stable preservation of hemoglobin vesicles as a blood substitute, Polym. Adv. Technol. 10 (1999) 293–298.

[36] S. Li, J. Nickels, A.F. Palmer, Liposome-encapsulated actin-hemoglobin (LEAcHb) artificial blood substitutes, Biomaterials 26 (2005) 3759–3769.

[37] J.A. Hayward, D.M. Levine, L. Neufeld, S.R. Simon, D.S. Johnston, D. Chapman, Polymerized liposomes as stable oxygen-carriers, FEBS Lett. 187 (1985) 261–266.

[38] T. Satoh, K. Kobayashi, S. Sekiguchi, E. Tsuchida, Characteristics of artificial red cells. Hemoglobin encapsulated in poly-lipid vesicles, ASAIO J. 38 (1992) M580–M584.

[39] K.D. Vandegriff, D.F. Wallach, R.M. Winslow, Encapsulation of hemoglobin in nonphospholipid vesicles, Artif. Cells Blood Substit. Immobil. Biotechnol. 22 (1994) 849–854.

[40] B. Goins, F.S. Ligler, A.S. Rudolph, Inclusion of ganglioside GM1 into liposome encapsulated hemoglobin does not extend circulation persistence at clinically relevant doses, Artif. Cells Blood Substit. Immobil. Biotechnol. 22 (1994) 9–25.

[41] M. Hamidi, A. Azadi, P. Rafiei, Pharmacokinetic consequences of pegylation, Drug Deliv. 13 (2006) 399–409.

[42] V.D. Awasthi, D. Garcia, R. Klipper, W.T. Phillips, B.A. Goins, Kinetics of liposome-encapsulated hemoglobin after 25% hypovolemic exchange transfusion, Int. J. Pharm. 283 (2004) 53–62.

[43] A.R. Nicholas, M.J. Scott, N.I. Kennedy, M.N. Jones, Effect of grafted polyethylene glycol (PEG) on the size, encapsulation efficiency and permeability of vesicles, Biochim. Biophys. Acta 1463 (2000) 167–178.

[44] P.S. Uster, T.M. Allen, B.E. Daniel, C.J. Mendez, M.S. Newman, G.Z. Zhu, Insertion of poly(ethylene glycol) derivatized phospholipid into pre-formed liposomes results in prolonged *in vivo* circulation time, FEBS Lett. 386 (1996) 243–246.

[45] S.M. Moghimi, J. Szebeni, Stealth liposomes and long circulating nanoparticles: Critical issues in pharmacokinetics, opsonization and protein-binding properties, Prog. Lipid Res. 42 (2003) 463–478.

[46] N. Shibuya-Fujiwara, F. Hirayama, Y. Ogata, H. Ikeda, K. Ikebuchi, Phagocytosis *in vitro* of polyethylene glycol-modified liposome-encapsulated hemoglobin by human peripheral blood monocytes plus macrophages through scavenger receptors, Life Sci. 70 (2001) 291–300.

[47] T. Ishida, K. Atobe, X. Wang, H. Kiwada, Accelerated blood clearance of PEGylated liposomes upon repeated injections: Effect of doxorubicin-encapsulation and high-dose first injection, J. Control. Release 115 (2006) 251–258.

[48] T. Ishida, T. Ichikawa, M. Ichihara, Y. Sadzuka, H. Kiwada, Effect of the physicochemical properties of initially injected liposomes on the clearance of subsequently injected PEGylated liposomes in mice, J. Control. Release 95 (2004) 403–412.

[49] H. Sakai, S. Takeoka, S.I. Park, T. Kose, H. Nishide, Y. Izumi, A. Yoshizu, K. Kobayashi, E. Tsuchida, Surface modification of hemoglobin vesicles with poly (ethylene glycol) and effects on aggregation, viscosity, and blood flow during 90% exchange transfusion in anesthetized rats, Bioconjug. Chem. 8 (1997) 23–30.

[50] V. Awasthi, B. Goins, W.T. Phillips, Insertion of poly(ethylne glycol)-lipid reduces the liposome-encapuslated hemoglobin induced thrombocytopenic reaction, Am. J. Pharmacol. Toxicol. 2 (2007) 98–105.

[51] H. Sakai, K.I. Tomiyama, K. Sou, S. Takeoka, E. Tsuchida, Poly(ethylene glycol)-conjugation and deoxygenation enable long-term preservation of hemoglobin-vesicles as oxygen carriers in a liquid state, Bioconjug. Chem. 11 (2000) 425–432.

[52] C. Fronticelli, T. Sato, C. Orth, E. Bucci, Bovine hemoglobin as a potential source of hemoglobin-based oxygen carriers: Crosslinking with bis(2,3-dibromosalycyl)fumarate, Biochim. Biophys. Acta 874 (1986) 76–81.

[53] F.S. Ligler, L.P. Stratton, A.S. Rudolph, Liposome encapsulated hemoglobin: Stabilization, encapsulation, and storage, Prog. Clin. Biol. Res. 319 (1989) 435–450; discussion 451–435.

[54] M. Mobed, T. Nishiya, T.M. Chang, Purification and characterization of liposomes encapsulating hemoglobin as potential blood substitutes, Biomater. Artif. Cells Immobil. Biotechnol. 20 (1992) 53–70.

[55] A.S. Rudolph, R.W. Klipper, B. Goins, W.T. Phillips, *In vivo* biodistribution of a radiolabeled blood substitute: 99mTc-labeled liposome-encapsulated hemoglobin in an anesthetized rabbit, Proc. Natl. Acad. Sci. USA 88 (1991) 10976–10980.

[56] H. Sakai, S. Takeoka, R. Wettstein, A.G. Tsai, M. Intaglietta, E. Tsuchida, Systemic and microvascular responses to hemorrhagic shock and resuscitation with Hb vesicles, Am. J. Physiol. Heart Circ. Physiol. 283 (2002) H1191–H1199.

[57] R.G. Hamilton, N. Kelly, M.S. Gawryl, V.T. Rentko, Absence of immunopathology associated with repeated IV administration of bovine Hb-based oxygen carrier in dogs, Transfusion 41 (2001) 219–225.

[58] H. Sakai, K. Hamada, S. Takeoka, H. Nishide, E. Tsuchida, Physical properties of hemoglobin vesicles as red cell substitutes, Biotechnol. Prog. 12 (1996) 119–125.

[59] J. Creteur, W. Sibbald, J.L. Vincent, Hemoglobin solutions—Not just red blood cell substitutes, Crit. Care Med. 28 (2000) 3025–3034.

[60] K. Kobayashi, E. Tsuchida, H. Nishide, Totally synthetic hemes: Their characteristics and oxygen carrying capacity in dogs, in: E. Tsuchida (Ed.), Artificial Red Cells: Materials, Performances and Clinical Study as Blood Substitutes, John Wiley & Sons Ltd., Chichester, UK, 1995, pp. 93–116.

[61] T. Ishida, H. Harashima, H. Kiwada, Liposome clearance, Biosci. Rep. 22 (2002) 197–224.

[62] T. Lian, R.J. Ho, Trends and developments in liposome drug delivery systems, J. Pharm. Sci. 90 (2001) 667–680.

[63] T. Daemen, M. Velinova, J. Regts, M. de Jager, R. Kalicharan, J. Donga, J.J. van der Want, G.L. Scherphof, Different intrahepatic distribution of phosphatidylglycerol and phosphatidylserine liposomes in the rat, Hepatology 26 (1997) 416–423.

[64] G.L. Scherphof, J.A. Kamps, The role of hepatocytes in the clearance of liposomes from the blood circulation, Prog. Lipid Res. 40 (2001) 149–166.

[65] V.D. Awasthi, D. Garcia, B.A. Goins, W.T. Phillips, Circulation and biodistribution profiles of long-circulating PEG-liposomes of various sizes in rabbits, Int. J. Pharm. 253 (2003) 121–132.

[66] S. Sriwongsitanont, M. Ueno, Physicochemical properties of PEG-grafted liposomes, Chem. Pharm. Bull. (Tokyo) 50 (2002) 1238–1244.

[67] A. Gaudard, E. Varlet-Marie, F. Bressolle, M. Audran, Drugs for increasing oxygen and their potential use in doping: A review, Sports Med. 33 (2003) 187–212.

[68] L. Wang, K. Morizawa, S. Tokuyama, T. Satoh, E. Tsuchida, Modulation of oxygen-carrying capacity of artificial red cells (ARC), Polymers Adv. Technol. 4 (1992) 8–11.

[69] T. Oda, Y. Nakajima, T. Kimura, Y. Ogata, Y. Fujise, Hemodilution with liposome-encapsulated low-oxygen-affinity hemoglobin facilitates rapid recovery from ischemic acidosis after cerebral ischemia in rats, J. Artif. Organs 7 (2004) 101–106.

[70] H. Sakai, Y. Suzuki, M. Kinoshita, S. Takeoka, N. Maeda, E. Tsuchida, O_2 release from Hb vesicles evaluated using an artificial, narrow O_2-permeable tube: Comparison with RBCs and acellular Hbs, Am. J. Physiol. Heart Circ. Physiol. 285 (2003) H2543–H2551.

[71] M. Intaglietta, P. Cabrales, A.G. Tsai, Microvascular perspective of oxygen-carrying and -noncarrying blood substitutes, Annu. Rev. Biomed. Eng. 8 (2006) 289–321.

[72] H. Sakai, P. Cabrales, A.G. Tsai, E. Tsuchida, M. Intaglietta, Oxygen release from low and normal P50 Hb vesicles in transiently occluded arterioles of the hamster window model, Am. J. Physiol. Heart Circ. Physiol. 288 (2005) H2897–H2903.

[73] P. Cabrales, H. Sakai, A.G. Tsai, S. Takeoka, E. Tsuchida, M. Intaglietta, Oxygen transport by low and normal oxygen affinity hemoglobin vesicles in extreme hemodilution, Am. J. Physiol. Heart Circ. Physiol. 288 (2005) H1885–H1892.

[74] H. Sakai, M. Yuasa, H. Onuma, S. Takeoka, E. Tsuchida, Synthesis and physicochemical characterization of a series of hemoglobin-based oxygen carriers: Objective comparison between cellular and acellular types, Bioconjug. Chem. 11 (2000) 56–64.

[75] M. Intaglietta, Microcirculatory basis for the design of artificial blood, Microcirculation 6 (1999) 247–258.

[76] H. Sakai, Y. Masada, H. Horinouchi, M. Yamamoto, E. Ikeda, S. Takeoka, K. Kobayashi, E. Tsuchida, Hemoglobin-vesicles suspended in recombinant human serum albumin for resuscitation from hemorrhagic shock in anesthetized rats, Crit. Care Med. 32 (2004) 539–545.

[77] T.W. Chung, J.F. Wang, Viscosity measurements for LEH suspended in different plasma expanders, Artif. Cells Blood Substit. Immobil. Biotechnol. 25 (1997) 393–406.

[78] A.G. Tsai, B. Friesenecker, M. McCarthy, H. Sakai, M. Intaglietta, Plasma viscosity regulates capillary perfusion during extreme hemodilution in hamster skinfold model, Am. J. Physiol. 275 (1998) H2170–2180.

[79] J.P. Muizelaar, E.P. Wei, H.A. Kontos, D.P. Becker, Cerebral blood flow is regulated by changes in blood pressure and in blood viscosity alike, Stroke 17 (1986) 44–48.

[80] M.H. Weil, R.J. Henning, V.K. Puri, Colloid oncotic pressure: Clinical significance, Crit. Care Med. 7 (1979) 113–116.

[81] K.D. Vandegriff, M. McCarthy, R.J. Rohlfs, R.M. Winslow, Colloid osmotic properties of modified hemoglobins: Chemically cross-linked versus polyethylene glycol surface-conjugated, Biophys. Chem. 69 (1997) 23–30.

[82] G.C. Kramer, Hypertonic resuscitation: Physiologic mechanisms and recommendations for trauma care, J. Trauma 54 (2003) S89–99.

[83] M.C. Mazzoni, P. Borgstrom, K.E. Arfors, M. Intaglietta, Dynamic fluid redistribution in hyperosmotic resuscitation of hypovolemic hemorrhage, Am. J. Physiol. 255 (1988) H629–637.

[84] J.L. Pascual, K.A. Khwaja, P. Chaudhury, N.V. Christou, Hypertonic saline and the microcirculation, J. Trauma 54 (2003) S133–140.

[85] F.A. Moore, B.A. McKinley, E.E. Moore, The next generation in shock resuscitation, Lancet 363 (2004) 1988–1996.

[86] G.C. Kramer, Hypertonic resuscitation: Physiologic mechanisms and recommendations for trauma care, J. Trauma 54 (2003) S89–S99.

[87] R. Rabinovici, A.S. Rudolph, J. Vernick, G. Feuerstein, A new salutary resuscitative fluid: Liposome encapsulated hemoglobin/hypertonic saline solution, J. Trauma 35 (1993) 121–126discussion 126–127.

[88] J. Szebeni, H. Hauser, C.D. Eskelson, R.R. Watson, K.H. Winterhalter, Interaction of hemoglobin derivatives with liposomes. Membrane cholesterol protects against the changes of hemoglobin, Biochemistry 27 (1988) 6425–6434.

[89] E.E. Di Iorio, Preparation of derivatives of ferrous and ferric hemoglobin, Methods Enzymol. 76 (1981) 57–72.

[90] D.A. Akintonwa, Theoretical mechanistic basis of oxidants of methaemoglobin formation, Med. Hypotheses 54 (2000) 312–320.

[91] T. Asakura, M. Tamura, M. Shin, Enzymatic reduction of spin-labeled ferrihemoglobin, J. Biol. Chem. 247 (1972) 3693–3694.

[92] A. Rossi-Fanelli, E. Antonini, B. Mondovi, Enzymic reduction of ferrimyoglobin, Arch. Biochem. Biophys. 68 (1957) 341–354.

[93] S. Takeoka, T. Ohgushi, H. Sakai, T. Kose, H. Nishide, E. Tsuchida, Construction of artificial methemoglobin reduction systems in Hb vesicles, Artif. Cells Blood Substit. Immobil. Biotechnol. 25 (1997) 31–41.

[94] Y. Teramura, H. Kanazawa, H. Sakai, S. Takeoka, E. Tsuchida, Prolonged oxygen-carrying ability of hemoglobin vesicles by coencapsulation of catalase *in vivo*, Bioconjug. Chem. 14 (2003) 1171–1176.

[95] J. Everse, Photochemical reduction of methemoglobin and methemoglobin derivatives, Methods Enzymol. 231 (1994) 524–536.

[96] H. Sakai, Y. Masada, H. Onuma, S. Takeoka, E. Tsuchida, Reduction of methemoglobin via electron transfer from photoreduced flavin: Restoration of O_2-binding of concentrated hemoglobin solution coencapsulated in phospholipid vesicles, Bioconjug. Chem. 15 (2004) 1037–1045.

[97] G. Gregoriadis, Fate of liposomes *in vivo* and its control: A historical perspective, in: D.D. Lasic, F. Martin (Eds.), Stealth Liposomes, CRC Press, Boca Raton, FL, 1995, pp. 7–12.

[98] S.N. Chatterjee, S. Agarwal, Liposomes as membrane model for study of lipid peroxidation, Free Radic. Biol. Med. 4 (1988) 51–72.

[99] M. Grit, D.J. Crommelin, Chemical stability of liposomes: Implications for their physical stability, Chem. Phys. Lipids 64 (1993) 3–18.

[100] P.B. McCay, Vitamin E: Interactions with free radicals and ascorbate, Annu. Rev. Nutr. 5 (1985) 323–340.

[101] P.B. McCay, P.M. Pfeifer, W.H. Stipe, Vitamin E protection of membrane lipids during electron transport functions, Ann. N Y Acad. Sci. 203 (1972) 62–73.

[102] C.A. Hunt, R.R. Burnette, R.D. MacGregor, A.E. Strubbe, D.T. Lau, N. Taylor, H. Kiwada, Synthesis and evaluation of a prototypal artificial red cell, Science 230 (1985) 1165–1168.

[103] R.L. Shew, D.W. Deamer, A novel method for encapsulation of macromolecules in liposomes, Biochim. Biophys. Acta 816 (1985) 1–8.

[104] B. Jopski, V. Pirkl, H.W. Jaroni, R. Schubert, K.H. Schmidt, Preparation of hemoglobin-containing liposomes using octyl glucoside and octyltetraoxyethylene, Biochim. Biophys. Acta 978 (1989) 79–84.

[105] A. Vidal-Naquet, J.L. Gossage, T.P. Sullivan, J.W. Haynes, B.H. Gilruth, R.L. Beissinger, L.R. Sehgal, A.L. Rosen, Liposome-encapsulated hemoglobin as an artificial red blood cell: Characterization and scale-up, Biomater. Artif. Cells Artif. Organs 17 (1989) 531–552.

[106] V.P. Torchilin, M.I. Papisov, Why do polyethylene glycol-coated liposomes circulate so long? J. Liposome Res. 4 (1994) 725–739.

[107] P.R. Cullis, A. Chonn, S.C. Semple, Interactions of liposomes and lipid-based carrier systems with blood proteins: Relation to clearance behaviour *in vivo*, Adv. Drug Deliv. Rev. 32 (1998) 3–17.

[108] S. Takeoka, T. Ohgushi, K. Terase, T. Ohmori, E. Tsuchida, Layer-controlled hemoglobin vesicles by interaction of hemoglobin with a phospholipid assembly, Langmuir 12 (1996) 1755–1759.

[109] M. Takaori, Approach to clinical trial considering medical ethics and efficacy for HbV, liposome encapsulated hemoglobin vesicle, Artif. Cells Blood Substit. Immobil. Biotechnol. 33 (2005) 65–73.

[110] R. Barnadas-Rodriguez, M. Sabes, Factors involved in the production of liposomes with a high-pressure homogenizer, Int. J. Pharm. 213 (2001) 175–186.

[111] P. Labrude, B. Chaillot, C. Vigneron, Influence of physical conditions on the oxidation of hemoglobin during freeze-drying, Cryobiology 21 (1984) 33–38.

[112] R. Rabinovici, A.S. Rudolph, T.L. Yue, G. Feuerstein, Biological responses to liposome-encapsulated hemoglobin (LEH) are improved by a PAF antagonist, Circ. Shock 31 (1990) 431–445.

[113] J. Szebeni, L. Baranyi, S. Savay, M. Bodo, D.S. Morse, M. Basta, G.L. Stahl, R. Bunger, C.R. Alving, Liposome-induced pulmonary hypertension: Properties and mechanism of a complement-mediated pseudoallergic reaction, Am. J. Physiol. Heart Circ. Physiol. 279 (2000) H1319–1328.

[114] A. Chanan-Khan, J. Szebeni, S. Savay, L. Liebes, N.M. Rafique, C.R. Alving, F.M. Muggia, Complement activation following first exposure to pegylated liposomal doxorubicin (Doxil): Possible role in hypersensitivity reactions, Ann. Oncol. 14 (2003) 1430–1437.

[115] M.J. Parnham, H. Wetzig, Toxicity screening of liposomes, Chem. Phys. Lipids 64 (1993) 263–274.

[116] H. Sakai, H. Horinouchi, K. Tomiyama, E. Ikeda, S. Takeoka, K. Kobayashi, E. Tsuchida, Hemoglobin-vesicles as oxygen carriers: Influence on phagocytic activity and histopathological changes in reticuloendothelial system, Am. J. Pathol. 159 (2001) 1079–1088.

[117] H. Sakai, H. Horinouchi, Y. Masada, S. Takeoka, E. Ikeda, M. Takaori, K. Kobayashi, E. Tsuchida, Metabolism of hemoglobin-vesicles (artificial oxygen carriers) and their influence on organ functions in a rat model, Biomaterials 25 (2004) 4317–4325.

[118] R.O. Cliff, F. Ligler, B. Goins, P.M. Hoffmann, H. Spielberg, A.S. Rudolph, Liposome encapsulated hemoglobin: Long-term storage stability and *in vivo* characterization, Biomater. Artif. Cells Immobil. Biotechnol. 20 (1992) 619–626.

[119] R.L. Sherwood, D.L. McCormick, S. Zheng, R.L. Beissinger, Influence of steric stabilization of liposome-encapsulated hemoglobin on *Listeria monocytogenes* host defense, Artif. Cells Blood Substit. Immobil. Biotechnol. 23 (1995) 665–679.

[120] T.M. Chang, C. Lister, Nishiya, R. Varma, Immunological effects of hemoglobin, encapsulated hemoglobin, polyhemoglobin and conjugated hemoglobin using different immunization schedules, Biomater, Artif. Cells Immobil. Biotechnol. 20 (1992) 611–618.

[121] W.T. Phillips, A.S. Rudolph, B. Goins, J.H. Timmons, R. Klipper, R. Blumhardt, A simple method for producing a technetium-99m-labeled liposome which is stable *in vivo*, Int. J. Rad. Appl. Instrum. B 19 (1992) 539–547.

[122] K. Sou, R. Klipper, B. Goins, E. Tsuchida, W.T. Phillips, Circulation kinetics and organ distribution of Hb-vesicles developed as a red blood cell substitute, J. Pharmacol. Exp. Ther. 312 (2005) 702–709.

[123] B. Goins, R. Klipper, J. Sanders, R.O. Cliff, A.S. Rudolph, W.T. Phillips, Physiological responses, organ distribution, and circulation kinetics in anesthetized rats after hypovolemic exchange transfusion with technetium-99m-labeled liposome-encapsulated hemoglobin, Shock 4 (1995) 121–130.

[124] B.A. Goins, W.T. Phillips, The use of scintigraphic imaging as a tool in the development of liposome formulations, Prog. Lipid Res. 40 (2001) 95–123.

[125] G.S. Hughes, S.F. Francome, E.J. Antal, W.J. Adams, P.K. Locker, E.P. Yancey, E.E. Jacobs, Jr., Hematologiceffects of a novel hemoglobin-based oxygen carrier in normal male and female subjects, J. Lab. Clin. Med. 126 (1995) 444–451.

[126] L.R. Sehgal, S.A. Gould, A.L. Rosen, H.L. Sehgal, G.S. Moss, Polymerized pyridoxylated hemoglobin: A red cell substitute with normal oxygen capacity, Surgery 95 (1984) 433–438.

[127] Y. Ogata, H. Goto, T. Kimura, H. Fukui, Development of neo red cells (NRC) with the enzymatic reduction system of methemoglobin, Artif. Cells Blood Substit. Immobil. Biotechnol. 25 (1997) 417–427.

[128] P. Laverman, A.H. Brouwers, E.T. Dams, W.J. Oyen, G. Storm, N. van Rooijen, F.H. Corstens, O.C. Boerman, Preclinical and clinical evidence for disappearance of long-circulating characteristics of polyethylene glycol liposomes at low lipid dose, J. Pharmacol. Exp. Ther. 293 (2000) 996–1001.
[129] M.C. Woodle, M.S. Newman, P.K. Working, Biological properties of sterically stabilized liposomes, in: D.D. Lasic, F. Martin (Eds.), Stealth Liposomes, CRC Press, Boca Raton, FL, 1995, pp. 103–117.
[130] Y. Izumi, H. Sakai, T. Kose, K. Hamada, S. Takeoka, A. Yoshizu, H. Horinouchi, R. Kato, H. Nishide, E. Tsuchida, K. Kobayashi, Evaluation of the capabilities of a hemoglobin vesicle as an artificial oxygen carrier in a rat exchange transfusion model, ASAIO J. 43 (1997) 289–297.
[131] V. Awasthi, S.H. Yee, P. Jerabek, B. Goins, W.T. Phillips, Cerebral oxygen delivery by liposome-encapsulated hemoglobin: A positron-emission tomographic evaluation in a rat model of hemorrhagic shock, J. Appl. Physiol. 103 (2007) 28–38.

ELECTRIC CONDUCTANCE OF PLANAR LIPID BILAYER AS A TOOL FOR THE STUDY OF MEMBRANE PORE SELECTIVITY AND BLOCKADE

Valery F. Antonov, Vladimir P. Norik, *and* Elena Yu. Smirnova*

Contents

---

* Corresponding author. Fax: (499)2480181;
E-mail address: h.smirnova@gmail.com

Department of Medical and Biological Physics, Moscow Sechenov Medical Academy,
119992 ul.Trubetskaja, 8 Moscow, Russia

Advances in Planar Lipid Bilayers and Liposomes, Volume 9
ISSN 1554-4516, DOI: 10.1016/S1554-4516(09)09002-4

Abstract

Despite the very low thickness, the lipid bilayer of biomembrane presents an efficient permeability barrier to polar substances such as water or ions. Biophysical approach to membrane permeability study includes among others the pure lipid pores appeared at the membrane lipid phase transition [Antonov *et al.* in: A. Leitmannova Liu, H.T. Tien (Eds.) Advances in Planar Lipid Bilayers and Liposomes, Academic Press, Amsterdam, 2005 pp. 151–173)] [1]. This approach belongs to the methods of soft poration of planar BLM (pBLM) based on the structural rearrangement of the lipid bilayer at the phase transition of membrane lipid from liquid crystalline state to the gel one. This allows us to avoid the unexpected influence of high electrical field at electroporation on chemical components of the BLM. This chapter is aimed an experimental and theoretical study of soft poration method and its application to the problem of lipid pore ion selectivity and conductance blockade. It was shown recently [V.F. Antonov, A.A. Anosov, V.P. Norik, E.Yu. Smirnova, Eur. Biophys. J. 34 (2005) 155–162)] [2] that the dependence of electric conductance in single lipid pore on the poly (ethylene)glycols (PEGs) size in water solution resembled the behavior of reconstructed protein pores like alamethicin channel [S.M. Bezrukov, I. Vodyanoy, Biophys. J. 64 (1993) 16–25] [3]. When a PEG with a low molecular weight was added to the medium, the pore conductance dropped by the same factor as the bulk conductivity. Increasing of the PEG molecular weight was followed by a nearly complete blockade of single lipid pore conductance in 1 M LiCl. However, as the size of the PEG added was increased more, there was a recovery in conductance as the PEG was progressively excluded from the pore interior. It is shown that PEG-1450 being added to bulk solution strongly influences the cation selectivity of BLM: while PEG-1450 completely blocks ion conductance in 1 M LiCl, it does not block ion conductance in 1 M CsCl. Experimentally observed in our study, complete blockade of lipid pores in the presence of PEGs, and change of ion selectivity could be attributed to prevent the conversion of hydrophobic lipid pore into hydrophilic one in evolution of lipid pore occurred at lipid phase transition.

1. INTRODUCTION

It has been known long ago [4] that at temperatures well above the lipid transition temperature liposomes exhibited osmotic shrinkage, which was dependent on the cationic size of the solute used to bring about the osmotic gradient. It indicated that the permeation through these less stable bilayers took place mainly via individual diffusion of the permeating ions. An enhanced release of trapped K^+ from liposomes was demonstrated in the vicinity of transition temperature. The extent of the increase, however, depended strongly on the length of paraffin chain. From measurements of the shrinkage behavior of liposomes in the vicinity of the transition temperature, it was concluded that the increased permeability decreased with increasing diameter of the permeating ion. This finding implies that the increased permeability at the transition temperature cannot be ascribed to macroscopic rupture of the membrane. It was concluded that the maximum permeability in the vicinity of the transition temperature should be discussed in terms of probability and size distribution of statistical pore formation at the boundaries of liquid and solid domains [4]. Just the reverse conclusion has been made later by Cruzeiro-Hansson and Mouritsen [5], who studied the passive ion permeability of lipid membrane via lipid-domain interfacial area determined more closely using computer simulation. They conclude that there is no need for aqueous pore formation to explain the experimental observation of a dramatic increase in ion conductance at the lipid phase transition. This evident discrepancy has been discussed in this chapter based on the data obtained by soft poration of pBLM.

Water soluble polymers like poly(ethylene)glycols (PEGs) widely used in membrane biophysics for the study of structural and functional state in reconstructed protein ionic channels (see for review [6]). Recent usage of the PEGs for ionic pore calibration in our study reveals the ability of polymer molecules to induce nearly complete blocking of pore conductance [2]. Observed property of PEG allows us to extend the application of pure lipid pores in pBLM itself as a model for ion channel blocking effect in biomembranes. The advantage of novel biophysical approach consists in evident simplicity of lipid pore in comparison with protein pores with respect to chemical composition, local electrostatics, and flexibility.

The application of pure lipid pore appeared at the lipid phase transition as an adequate model for the pore in biological membranes has a relatively long history [7]. In 1980 we presented [8] the first observation of single-ion channels in unmodified lipid bilayers at the phase transition temperature of individual phospholipids. In our experiments we observed transmembrane current fluctuations when the temperature of pBLM was near the phase transition of the lipid. The obtained histogram like that shown in Figs. 6–8 revealed the discrete character of the current distribution. It was found no current fluctuation at temperatures higher or lower than the phase transition temperature and a reversible change between the fluctuating and nonfluctuating states. The current fluctuations were related to the lipid phase transition. It was suggested that the appearance of current fluctuations could be linked to the formation of domains in the membrane. Impurities as the reason for the current fluctuations were ruled out by repeatedly moving the system through the phase transition temperature. After a sufficient amount of cycles, we concluded that most of the impurities should be released into the water solvent. Experimental data in this case remained with no change.

Later Boheim *et al.* [9] presented their results on pore-mediated transport in pBLM prepared from synthetic saturated phospholipids. They also found conductance fluctuations in unmodified pBLM, coinsiding with phase transition regime. Authors related these fluctuations to the presence of few defects of extended size.

In 1989, Kaufmann and Singer [10] published their observations on ion channel fluctuations in pure lipid membranes. They could present a variety of phase transition induced phenomena in lipid bilayers including the occurrence of current fluctuations in the phase transition regime and quantization of the events. Kaufmann and coworkers [10, 11] related these phenomena to fluctuations both in lipid area and bilayer thickness that could be directly connected to the thermodynamics of lipid bilayer. From these fluctuations they concluded that the appearance of hydrophilic defects in a two-dimensional lipid lattice become unavoidable after sufficient time interval. Such defects would then allow for transmembrane currents. Still the bilayer lattice remained stable despite of the increased probability of formation of defects. Only if the external compression was too large, the membrane would break. It could therefore be expected that discrete defect sizes appeared in the bilayer lattice. In any stable state the thermodynamic fluctuations then imply the spontaneous and reversible formation of discrete conductive defects in the lipid bilayer lattice.

1.1. Theoretical Background

Theoretical consideration includes a number of problems, among them we focus on the appearance of structural defects in form of hydrophobic pore at the temperature of lipid phase transition and evolution of the formed pore. The first problem could be solved by analysis of surface tension change of planar BLM (pBLM) at the temperature of the main phase transition. For two main membrane phospholipids—dipalmitoylphosphatidylcholine (DPPC) and distearoylphosphatydilcholine (DSPC)—the area per molecule has been determined by X-ray examination [12]. By transition from liquid state to the gel, the area per molecule decreases by $\sim 0.1\ \mathrm{nm}^2$. At the transition, molecules in gel domain were compressed in relation to equilibrium state and molecules in liquid crystal state were extended. As a result, some tension appeared which could be resolved by appearance of transmembrane pore. To estimate free energy change, the formula derived earlier by Kozlov and Markin [13] for osmotic lysis of liposome has been used. The formula is adapted to the lipid phase transition in pBLM. The adaptation takes account of a molecular area change due to lipid phase transition $L_\alpha \rightarrow L_\beta$ (Δa) and the size of the lipid cluster (domain) appeared at the phase transition (N).

Involvement of these parameters in the model has been made possible partly by the theory of Ipsen *et al.* [14], who elaborated it for explanation of Na^+-permeability enhancement in DPPC bilayer at the phase transition. They took into account that the main phase transition in lipid bilayer followed by strong density fluctuations. These fluctuations manifest themselves in terms of a lipid-cluster (domain) formation by which the equilibrium bulk phase is invaded clusters of the opposite phase, that is, fluid clusters in the gel state for $T < T_m$ and gel clusters in the fluid phase for $T > T_m$. The cluster formation leads to the creation of an interfacial environment which is defined by the borders between the clusters and the bulk. This phenomenon is a dynamic one: clusters are continuously created and annihilated and they persistently fluctuate in size. However, they are characterized by an equilibrium size distribution function.

Corrected formula for free energy change has been used by us in the form:

$$\Delta G = \Gamma \frac{(N\Delta a - \pi r^2)^2}{Na^{\varsigma}} + 2\pi\gamma r \tag{1}$$

where Γ is an elasticity coefficient of lipid bilayer equaled 50 mN/m, N is the number of phospholipid molecules in a domain, Δa is an area change per single phospholipid molecule at the transition, r is the pore radius, a^{ς} is an area of single phospholipid molecule in the liquid crystalline state, and γ is an edge tension of the pore. The size of the domain N, appeared at the transition, assumed to be close to the cooperative unit determined calorimetrically at the phase transition. These units for DPPC and DSPC are equaled 260 and 130, respectively [15]. One can see in Eq. (1) that the pore occurrence is followed by a decrease of the first term which is responsible for elastic tension in membrane. However, concurrently with this process the new process is developing due to appearance of linear tension in the pore edge which gives the positive contribution in the energy of the pore.

The results of calculations are presented in Fig. 1. One can see that the curves for the dependence of free energy on pore radius have a minimum at 2.5 and 1.6 nm for DPPC and for DSPC, respectively. It means that the more is the length of phospholipids molecule the less the radius of the pore appeared at the phase transition. This conclusion agrees with experimental data shown in Figs. 6 and 7, where the experimental results of the pore conductance have shown for DSPC and DPPC, respectively. The conductance of pores in pBLM formed of DPPC is higher than the conductance of the lipid pores formed from DSPC.

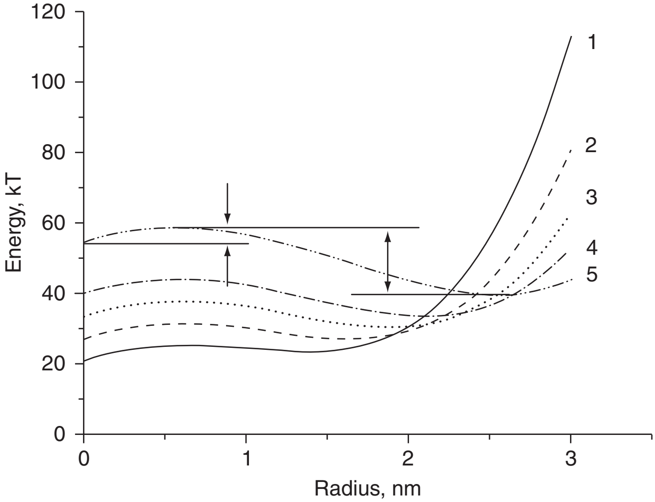

Figure 1 Free energy change of pore-contained pBLM as a function of lipid pore radius (Eq. (1)) at the lipid phase transition. Δa is fixed at 0.1 nm^2: (1) lipid cluster (domain) contains 260 molecules, (2) 190 molecules, (3) 160 molecules, (4) 130 molecules, (5) 100 molecules. First two arrows show the energy change due to hydrophobic pore occurrence. Second two arrows show the energy change at the pore resealing.

We suppose further that hydrophilic pore birth starts with creation of hydrophobic pore due to thermal motion of lipid molecules at the lipid phase transition. As shown in Fig. 1, the probability of hydrophobic pore occurrence is determined by the height of energetic barrier equaled the difference between the energy value at maximum and point $r = 0$. From this figure we notice that energy barrier for hydrophobic pore appeared at 0.5 nm equals to 5 kT, the energy needed for the pore resealing reaches about 18 kT. The significant change of energy in the resealing process implies the work done for transformation of hydrophobic pore into the hydrophilic one. The maximum in the curves corresponds to the occurrence of hydrophobic pore at $r = 0.6$ nm. It differs essential from the model which proposes an obligatory transformation of hydrophobic pore into hydrophilic one at this state of pore evolution. From geometrical constriction it is evident that the transformation is possible only at $r > 2.5$ nm if the thickness of bilayer equals to 5 nm. We suppose instead the occurrence of long-lived hydrophobic pore-filled with water.

In 1999, Zhi Qi *et al.* [16] first described the ion-conducting properties of a *de novo* synthesized channel, formed from cyclic octa-peptides consisting of four alternate L-alanine and benzoic acid moieties. The reconstruction of the hydrophobic channel in the BLM allows to register single channel conductance of 9 nS, which corresponds to pore diameter ~0.6 nm.

This size is close to our data shown in Fig. 1 for hydrophobic pore. Therefore, in the model of lipid, pore occurrence should be included as a transient step the long-lived water-filled hydrophobic pore.

The alternative way of energy barrier estimation is based on calculation of free energy change resulting from the formation of cylindrical hydrophobic pore of the radius r in a lipid bilayer formed above phase transition temperature. The pore is filled with water. The corresponding formula has been derived by Petrov *et al.* [17]:

$$\Delta G = 2\pi r h \Gamma(\infty) \tag{2}$$

where h is the thickness of the membrane and $\Gamma(\infty)$ is the interface tension between hydrophobic lipid tails and water. From this equation the energy of a hydrophobic pore was calculated in the order of 200 kT (with $h = 5$ nm and $\Gamma(\infty) = 50$ mN/m). It is evident that the spontaneous formation of hydrophobic pores in this case is highly improbable.

To resolve the problem, Glaser *et al.* [18] considered this discrepancy more closely. They took into account the interaction between the walls of the pore. According to Israelachvili and Pashley [19], the interaction of two hydrophobic surfaces separated by a thin layer of water significantly reduces the interface tension. The reduction of tension was attributed to changes in water structure near the interface with hydrophobic substances as follows. From the interface to the bulk phase, the properties of water undergo a gradual transition with a characteristic length of 1 nm. The high interface tension originates from the excess energy of this thin layer with disturbed water structure. When two hydrophobic surfaces come to a distance of a few nanometers, the overlapping of these layers reduces the effective surface tension and causes hydrophobic attraction between the surfaces. Taking into account this correction, Glaser *et al.* [18] estimated the free energy for hydrophobic pore of 0.5 nm in radius being equal to 40 kT.

Despite the correction, it means that the existence of hydrophobic pores in liquid crystalline state of lipid bilayer is highly improbable. It should be noted that taking into consideration the lipid domain occurrence at lipid phase transition (Eq. (1)) makes the model more realistic.

The dependence of pore energy on pore radius at different molecular area changes is demonstrated in Fig. 2. The set of curves reveals the first local minimum for DSPC at the pore radius of 1.7 nm (Fig. 2, curve 3) with energy depth about 5 kT. As a whole the free energy change does not exceed 10 kT that has made possible the reverse transformation of hydrophilic pore into hydrophobic one at small radius decrease.

The next problem to be resolved theoretically concerns the evolution of hydrophilic pore. It was discussed in many papers devoted to membrane electroporation (see for review [18]). However, taking into account the

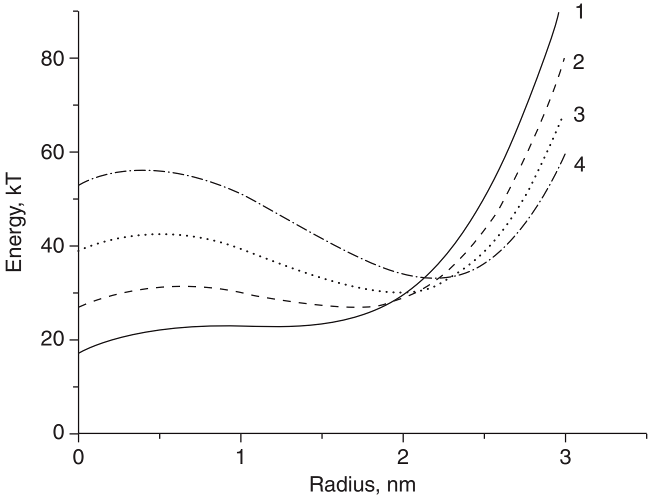

Figure 2 Free energy change of pore-contained pBLM as a function of lipid pore radius (Eq. (1)) at the lipid phase transition. N is fixed equaled 100 molecules: (1) $\Delta a = 0.14\ \mathrm{nm}^2$, (2) $\Delta a = 0.12\ \mathrm{nm}^2$, (3) $\Delta a = 0.1\ \mathrm{nm}^2$, (4) $\Delta a = 0.08\ \mathrm{nm}^2$.

evident difference between the soft poration approach and the electroporation, we return to the theory based mainly on Derjagin–Gutop–Prokhorov's conception of critical pore derived for soap bubble stability [20]. According to the theory of stability, the pore-contained lipid bilayer depends on the balance between the surface tension of lipid bilayer and an edge tension of the pore wall. The free energy of a hydrophilic pore is generally calculated from:

$$\Delta G = 2\pi\gamma r - \pi\sigma r^2 \tag{3}$$

where γ is the linear pore edge tension and σ is the mechanical tension of the bilayer. Some comments are needed to this simple formula. It is inapplicable for pores of small radius (much less than bilayer thickness) because the packing of lipids along the wall side of a narrow pore leads to substantial deformation of molecular order. The contribution of this deformation to pore energy steeply rises when pore radius approaches the size of lipid heads. In addition, strong hydration interaction causes repulsive forces between the hydrophilic compounds of the pore wall. Since the precise dependence of pore energy on small radii is unknown, only qualitative description could be done. The dependence is assumed to have the form shown in Fig. 3. One can see that the energetic profile for hydrophilic pore contains a number of extremes.

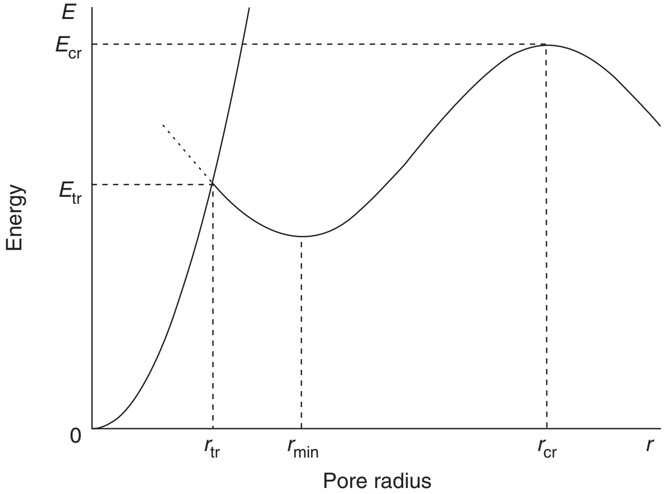

Figure 3 Comparison of the energy of hydrophobic and hydrophilic lipid pores in pBLM at different pore radii: (A) hydrophobic pore, (B) hydrophilic pore. E_{tr} is the energy change at the transformation of hydrophobic pore into hydrophilic one, E_{cr} is the energy barrier which prevents the conversion of pores with r_{min} to pores with r_{cr}. Overcoming of energetic barrier is followed by complete destruction of lipid bilayer. r_{min} is the radius of the pore at energetic minimum. r_{tr} must be close to 2.5 nm because of geometrical restriction [16].

Figure 3 analyzes the energy of hydrophilic pores as a function of pore radius r. The energetic profile reflects the existence of three critical points: r_{tr} corresponds to transformation of hydrophobic pore into hydrophilic one, r_{min} corresponds to the local energy minimum of pore, and r_{cr} is the critical radius of the hydrophilic pore, after which the lipid membrane is disrupting. As indicated the formation of hydrophobic pore is energetically more favorable for the pore of small radius. These hydrophobic pores are formed spontaneously by lateral thermal fluctuations of the lipid molecules. However, when their radius exceeds a critical value, a reorientation of the lipids becomes energetically favorable. This reorientation resulting in the formation of a hydrophilic pore is called the inversion of the pore.

Accumulation of pores in the minimum (Fig. 3) depends on the heights of two energetic barriers E_{tr} and E_{cr}. The height of the latter can be determined at $r_{cr} = \gamma/\sigma$ as $E_{cr} = \pi\gamma^2/\sigma$. As indicated (Table 2) in Section 2, we can take $\gamma = 0.88 \times 10^{-11}$ N and $\sigma = 1.7$ mN/m and find the barrier height equaled 34 kT. Thus, the energetic barrier E_{cr} is pretty high to prevent the pore disappearance. Energetic barrier E_{tr} has been estimated above as equaled 18 kT. The existence of high energetic barriers provides the accumulation of quasistationary pores in vicinity of energetic minimum.

To accomplish the energetic profile analysis of hydrophilic pore, lets consider the second energetic barrier more closely. Recently, we were succeeded in experimental study of subcritical pores [1]. The average radius of these pores was found to be 5.1 ± 1.3 nm. The lifetime of subcritical pores reached 1 s and more. Creation of such pores in lipid bilayer implies the loss of membrane selectivity and barrier function at all. They are responsible for complete disruption of the membrane at the electric breakdown and osmotic lysis in the living cell.

From the theoretical point of view, the subcritical pores should be referred to the macroscopic pores because their radius is more than the membrane thickness. The size of subcritical pore is close to r_{cr} defined above as $r_{\mathrm{cr}} = \gamma/\sigma$. Taking the literature data for $\gamma = 1 \times 10^{-11}$ N and $\sigma = 2 \times 10^{-3}$ N/m [17], we obtained the radius of the critical pore equaled ~5 nm, which is close to the radius of subcritical pore [1].

The original theory of macroscopic lipid pore at the soft poration has been proposed by Bronstein and Iserovich [21]. On the assumption of phase coexistence at the lipid phase transition, they focus on the area per molecule change as a main cause of bilayer stretch. Their theory is kinetic by origin. If liquid lipid domain is located within the solid lipid bilayer, it exhibits the tension which is accomplished by relaxation and pore appearance. After accomplishment of the phase transition, the lipid pore could be found in solid bilayer with radius

$$r^2 = r_1^2 \frac{\Delta a}{a}$$

where r_1 is an area of lipid bilayer in solid state, $\Delta a/a$ is a relative decrease of membrane area at solidification.

The lifetime of the pore is limited because there is an energetic advantage for lipid molecules to diffuse into the pore that is accomplished by closing of the pore. The authors [21] found the expression for volume flow (I) of lipids into the pore as a function of r in the form as:

$$I = \frac{A}{r \ln(r/r_1)} = 2\pi r \frac{\mathrm{d}r}{\mathrm{d}t}$$

where $A = 2\pi D\gamma\omega/fkT$, D is a lateral diffusion coefficient of lipid, γ is line tension coefficient for pore edge, ω is an area of lipid bilayer in solid state, f is the reflection coefficient, k is Boltzmann's coefficient, and T is absolute temperature.

The integration of the equation allows calculating of the lifetime of the pore (t).

$$t = \frac{fkTr^3(\ln r/r_1 - 1/3)}{3\omega D\gamma}$$

The approximate evaluation of t is accessed if the expression $f(\ln r/r_1 - 1/3)$ assumed to be close to 1. Taking the well-known values for $kT = 4 \times 10^{-21}$ J, for $\gamma = 2 \times 10^{-11}$ N, for $\omega = 3 \times 10^{-15}$ cm^2, for $D = 10^{-11}$ cm^2/s, we obtain the lifetime of the lipid pore equaled several seconds if the pore radius would be approximately 10 nm. This result is in a good agreement with experimental data discussed in this chapter with respect of subcritical pores.

1.2. Formulation of the Experimental Problem

Based on theoretical predictions, we can formulate the main purposes of the experimental study as follows:

- Elaborate experimental conditions for obtaining of lipid pore population in pBLM from disaturated phospholipids at the temperature of lipid phase transition to study the electric conductance of single pores;
- Estimate the size of single lipid pores appeared at the lipid phase transition and their ion selectivity;
- Investigate the blocking effect of PEGs in pure lipid pores in comparison with blocking effect performed by Pegs in reconstructed protein ion channels.

2. EXPERIMENTAL

2.1. Lipids

Three disaturated phospholipids have been used in experiments:

- 1,2-Distearoyl-*sn*-glycero-3-phosphocholine (Avanti Polar Lipids);
- 1,2-Dipalmitoyl-*sn*-glycero-3-phosphocholine (Avanti Polar Lipids);
- Hydrogenated egg lecithin (Avanti Polar Lipids).

All lipid samples obtained from Avanti Polar Lipids have been used without additional purification. The membrane forming solution contained 25 mg of lipid dissolved in 1 ml of a mixture of *n*-decane/chloroform/methanol (7:2:1 v/v/v).

2.2. Poly(ethylene)glycols

A series of PEGs includes PEG-300, PEG-600, PEG-1450, PEG-2000, PEG-3350, PEG-6000, and PEG-20000. Except PEGs the sample of glycerol has been used. All samples were obtained from Sigma.

2.3. Differential Scanning Calorimetry

To determine the phase transition temperature of lipids, differential scanning calorimeter (DASM-4, Puschino, Russia) has been used. To prepare a sample of multilayer liposomes, the dry lipids were suspended in aqueous solution of appropriate salt by mechanical shaking.

2.4. Planar BLMs

The pBLM were formed over a circular hole in a vertical wall of a Teflon pot as described by Mueller *et al.* in 1962 [22]. Before each experiment, the vertical wall in the vicinity of the hole was covered with a thin layer of membrane-forming solution and dried. To carry out experiments at constant temperature, the measuring cell was placed in a water jacket connected to a thermostat. The temperature near the pBLM was measured by a thermocouple. The details of experiments with pBLM were described earlier [1, 2].

2.5. Electrical Measurements

The membrane current fluctuations in the pBLM were recorded at voltage-clamp condition by an ion operational amplifier (Puschino). The details of the measurements were described earlier [2]. The specific electric conductivity of the bulk solution was measured in electrolytic cell equipped with pair of Pt-electrodes.

2.6. Lipid Pore Size Evaluation

The pore size has been calculated according to Hille [23] from the formula:

$$R = \frac{\rho G}{2\pi}\left(\frac{\pi}{2} + \sqrt{\left(\frac{\pi}{2}\right)^2 + \frac{4\pi l}{\rho G}}\right) \tag{4}$$

where R is the pore radius; G is the conductance of single lipid pore; l is the length of the pore, assumed to be 5 nm; and ρ is resistivity of bulk solution with correction factor introduced by Smart *et al.* [6].

2.7. Poly(ethylene)glycol Method

The method allows to measure the pore size [3,24,25] by recording of transmembrane ion current in the presence of PEGs in the bulk solution. The effect of PEG addition (20% w/w) on pore conductance at clamp-voltage has been studied. PEGs are sphere-like, neutral polymers and their hydrodynamic radii are given in the diagram in Fig. 3. The application of this method to size determination of protein channels has been discussed recently by Hinnah *et al.* [26]. Their approach was based on the theory elaborated by Bezrukov *et al.* [27]. Earlier we obtained the experimental data which showed the principal resemblance of conductance-blocking procedure between the many protein pores reconstructed in pBLM and pure lipid pores [1]. The principle of the measurement is a follows. The electric conductivity of the bulk solution is lowered in the presence of PEGs. At low hydrodynamic radius, polymer molecule can enter the pore and lower the conductance of the pore by the same factor as the bulk conductivity, but as their radius increases the PEG molecules are progressively excluded from the pore interior and the conductance begins to recover. One aspect of this chapter aims to demonstrate the applicability of quantitative approach of this method to ion-blocking effect irrespective of what material is used to build the pore wall. The formula derived by Bezrukov *et al.* [27] is of the form:

$$\frac{g_{\mathrm{PEG}}}{g_0} = \beta\left(1 - \frac{1-\chi_{\mathrm{PEG}}}{\chi_0\beta}\right)\exp\left(-\frac{w^2}{w_0^2}\right)^{\alpha} \tag{5}$$

where g_{PEG}/g_0 is the ratio of pore conductance in the presence and absence of polymer, $\chi_{\mathrm{PEG}}/\chi_0$ is ratio of bulk solution conductivity in the presence and absence of polymer, β is the maximal conductance of solution, w/w_0 is the ratio of the average monomer density inside the pore to that in the bulk solution, and α is set as 1.

The equation yields the characteristic cutoff polymer radius w_0. At this radius the concentration of PEGs in the pore is reduced to $1/e$ of the original concentration. Therefore, w_0 is the characteristic radius of the pore.

2.8. Estimation of Membrane Surface Tension σ

The surface tension of pore-contained pBLM can be determined by bulging of membrane by applied hydrostatic pressure under the control of electric capacitance measurement. According to Moran and Ilani [28], computation of membrane surface tension is based on the following assumptions: (i) the increase in membrane capacitance above the minimum reflects only an increase in membrane area; (ii) due to homogeneity, the bulged membrane has a constant radius of curvature (depending only upon the degree of bulging); and (iii) the membrane is anchored at the circumference of the hole punched in the Teflon. The increase in membrane area in response to applied pressure would reach an equilibrium when

$$P = \frac{2\sigma}{R}\,(\text{computation based})$$

where P is the pressure difference across the membrane, σ is membrane surface tension, and R is the radius of curvature of the bulged membrane. The radius of the curvature of the bulged membrane could be calculated from the increase in membrane area as follows:

$$R = \frac{1}{2}\left[\frac{A^2}{\pi A - \pi^2 a^2}\right]^{1/2} \tag{6}$$

where A is an expression $(C/C_{\mathrm{min}})\pi a^2$ where in turn C is the electric capacitance of the membrane, C_{min} is a minimal capacitance of the membrane, and a is the radius of the hole in the Teflon wall. Thus, knowing C, C_{min}, and P, it is possible to calculate σ.

The capacitance changes were measured by applying a voltage pulse of triangle form on the pBLM and registration of the resulting cyclic current–voltage (I–V) curves. It is well known that the measured current is the sum of the ohmic and the capacitance currents. The capacitance of the pBLM has been calculated using the formula:

$$C_{\mathrm{m}} = \frac{I_{\mathrm{c}}}{4f\,U_{\mathrm{max}}}$$

where I_{c} is the capacitance current, f is the frequency of applied voltage pulse, and U_{max} is the amplitude of the applied voltage.

Experiments were carried out with pBLM formed from hydrogenated egg lecithin (HEL) at temperatures above and below T_{m} [1]. The capacitance growth due to bulging of pBLM was sensitive to the phase state of lipids. The high rate of capacitance growth corresponded with liquid state of lipids when slow rate was inherent with the gel state. Those results were in complete agreement with experiments conducted by Evans *et al.* [29] with lipid bilayer from DMPC in experiments based on aspiration technique. Indeed, the surface tension of the pBLM from the HEL in our experiment reached of 5.0 ± 0.2 mN/m for the gel state and of 1.7 ± 0.1 mN/m for the liquid crystalline phase.

2.9. Estimation of Single Lipid Pore Edge Tension γ

The principal advantage of soft poration of the pBLM is the possibility of obtaining a small population of single lipid pores at small voltage applied to membrane. It allows directly to count the number N of the pore in pBLM. According to Freeman *et al.* [30], the number of the lipid pores N existed in pBLM under small applied voltage depends only on the pore edge energy as follows:

$$N = n_0 \lambda \exp\left(\frac{-r_{\min}}{\lambda}\right) \tag{7}$$

where n_0 is a constant, numerically equals to $1.2 \times 10^{24}\ \mathrm{m}^{-1}$, λ is the characteristic length determined as $kT/2\pi\lambda$, and $r_{\min}$ is the radius of minimal pore. This approach greatly simplifies the experimental determination of γ for conducting lipid pores.

3. RESULTS

The order of experimental data presentation includes three diagrams for each phospholipid: thermogram of relevant phospholipids in liposome suspension, a set of ion current fluctuation records in pBLM from this phospholipid and corresponding histogram for current fluctuation distribution.

3.1. Registration of Lipid Pore Population Appeared in pBLM from DPPC at the Lipid Phase Transition Temperature

Figure 4 demonstrates the records of current fluctuations in pBLM formed from DPPC observed at different membrane voltage. To avoid the electroporation of the membrane, the voltage does not exceed of 100 mV which is far below the threshold voltage of electroporation about 400 mV [18]. It is seen a number of time-resolved fluctuation with average amplitude about 1.5 nA at 100 mV and dwell time in the range 0.3–1 s. The decrease of voltage is followed by dropping of fluctuation amplitude up to the noise level. *I*–*V* dependence is symmetrical and the increase of negative voltage is followed by appearance of current pulses of opposite sign. Insertion shows the *I*–*V* characteristic for the single current fluctuations which is really linear with the slope about 30 nS.

The ion selectivity of the pBLM formed from individual phospholipids at the phase transition has been carried out in experiments with a series of alkaline chlorides. The selective cationic conductance of the pBLM at the lipid phase transition was observed earlier [2]. The results of present experiments are shown in Table 1. Cationic selectivity measured by *I*–*V* characteristics reveals the relatively high conductance for Li^+ and Na^+ and more modest for others. Selectivity order is as follows: $G_{\mathrm{Li}+}:G_{\mathrm{Na}+}:G_{\mathrm{K}+}:G_{\mathrm{Rb}+}:G_{\mathrm{Cs}+} = 1:0.9:0.4:0.4:0.3$. It should be noted that this selectivity order is opposite to that known for wide hydrophilic membrane pores while this order is close to selectivity of excited cell membranes like nerve axon [31]. According to Eisenman's classification, the existence of such pores requires the location inside the pore hole the chemical groups with high anionic field [32]. However, the polar heads of lecithin are in general sense electroneutral (see Section 4).

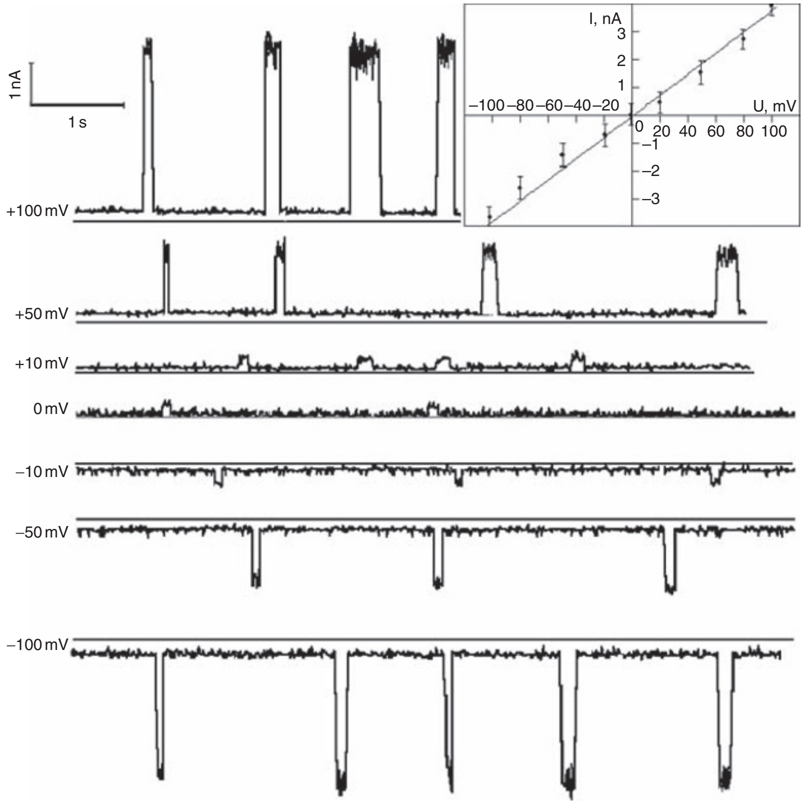

Figure 4 Current fluctuations in the pBLM from DPPC formed in 1 M LiCl at the temperature of the main phase transition corrected for Li^+ presence (43 ± 0.5 °C). Records observed at the clamp-voltage indicated in picture. Horizontal lines correspond to zero level. The insert demonstrates typical current–voltage characteristics of a single pore averaged over 150 experimental points.

Table 1 Experimental data of single lipid pore conductance and pore number for the pBLM from DPPC in 1 M solutions of LiCl, NaCl, KCl, RbCl, CsCl at the temperature of the main phase transition

Cation	Radius of hydrated cation (nm)	Lipid pore conductance (nS)	Pore radius (nm) calculated by Eq. (4)
Li^+	0.237	31 ± 15 (250)	2.1
Na^+	0.183	28 ± 16 (90)	1.9
K^+	0.125	12 ± 2 (100)	1.0
Rb^+	0.121	12 ± 4 (50)	1.0
Cs^+	0.119	10 ± 6 (50)	0.9

Numbers in parentheses indicate a total amount of studied membranes.

3.2. Lipid Phase Transition in pBLM and Electric Current Fluctuations

Experimental approach used in this study allows to observe the correlation between current fluctuations and the temperature of lipid phase transition in pBLM. In Fig. 5 a set of current fluctuations, recorded at different temperatures, is shown. The temperature change is shown for three different regions: far above the temperature of phase transition T_m (50 °C); middle record corresponds to the temperature of the main phase transition of DPPC corrected on Li^+ effect (43 °C); and last record obtained by the temperature well below T_m (33 °C). One can see that there is no any current fluctuation well above and well below the temperature of main phase transition. At the temperature T_m supported by thermostat with accuracy of ±0.5 °C, a number of discrete current fluctuations are observed of one-, two- and threefold levels with basic amplitude of 1.5 nA. The duration of separate fluctuations is widely dispersed in the range of one second. The histogram reveals three levels of fluctuations concentrated close to 0, 1.5, and 3 nA. The prevalence of zeroth current means that appearance of current fluctuation is a relatively rare event. The appearance of current fluctuations in the vicinity of the temperature of the main phase transition of the phospholipids and absence of any fluctuations well above and well below the transition must not be unnoticed. It reveals the correlation between membrane current fluctuation appearance and lipid phase transition.

First evidence in favor of such suggestion has been obtained in 1980 in experiments with pBLM formed from the DSPC [8]. In this study the experiments with DSPC have been proceeded (Fig. 6). It is shown that in pBLM formed from DSPC single fluctuations are registered while the temperature in the experimental cell reached the temperature of phase transition of DSPC. The amplitude of current fluctuation was changed in diapason 0.8–2.4 pA. The histogram revealed the discrete distribution of fluctuations.

It should be noted that there is an existence of great difference in the amplitudes of current fluctuations between pBLMs from DSPC (Fig. 6) and DPPC (Fig. 7). Thermograms for DPPC were obtained in 1 M chloride solutions of a monovalent cations Li^+, Na^+, K^+, Rb^+, and Cs^+ (not shown). It should be noted that the thermograms in all alkaline solutions except Li^+ are typical for the DPPC at endothermic phase transition of (L_α–L_β)-type. Their common thermograms demonstrate two peaks at 35.5 °C (pretransition) and 41 °C (main phase transition) while in 1 M LiCl (Fig. 7), there is a shift of both peaks toward the higher temperatures of 40 °C (pretransition), and 43 °C (main phase transition). Earlier the same effect of LiCl has been observed by Cunningham *et al.* [33]. In their experiments, the effects of various monovalent cations on bilayer packing and structure of DPPC were studied using X-ray diffraction and differential

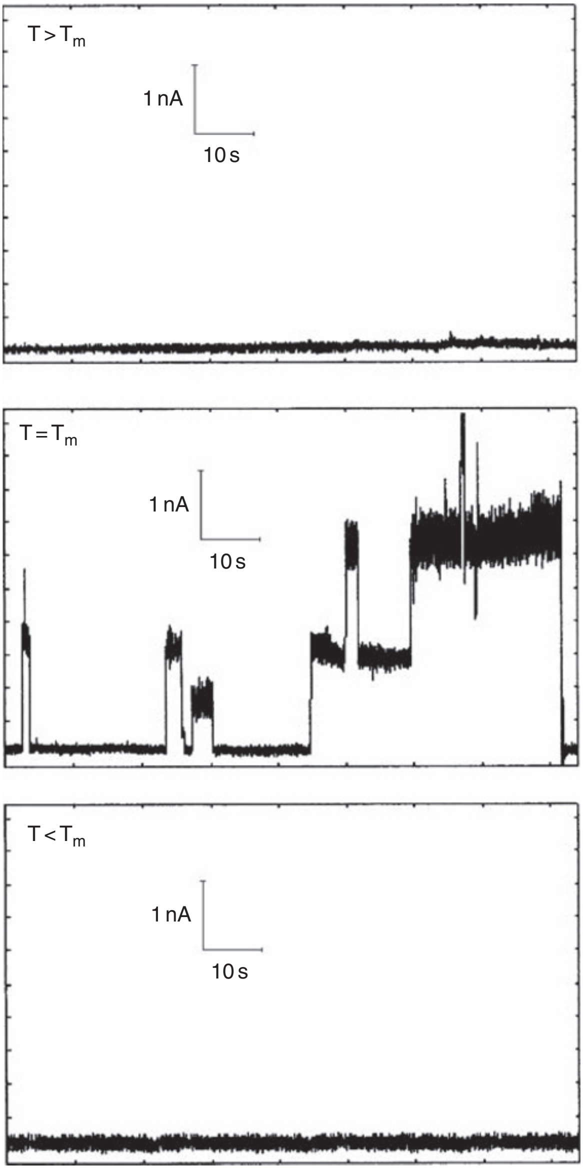

Figure 5 Typical electric current fluctuations recorded in pBLM from DPPC in 1 M LiCl at different temperatures: (A) temperature well above the temperature of the main phase transition of DPPC (50 °C), (B) temperature maintained at the temperature of main phase transition of DPPC corrected for Li^+ presence (43 °C), (C) temperature well below the main phase transition of DPPC (35 °C). The transmembrane potential has been clamped at 50 mV (source: adapted from Ref. [2]).

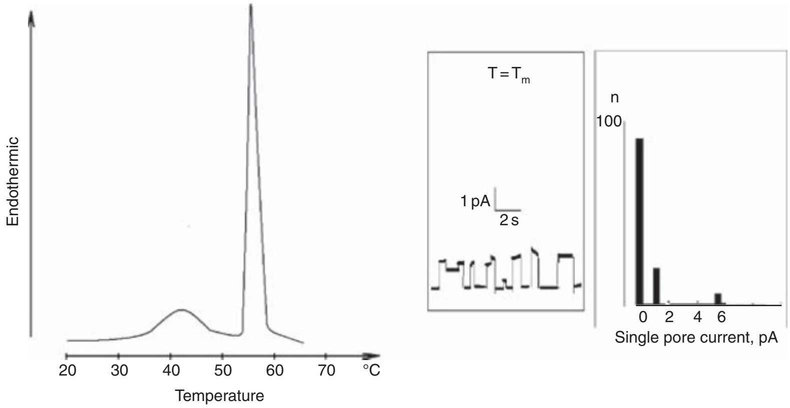

Figure 6 Soft poration of pBLM from DSPC in 0.1 M KCl: *left*, thermogram of DSPC vesicles in 0.1 M KCl with the main phase transition at 58 °C and pretransition at 41 °C; *middle*, typical record of current fluctuations in pBLM from DSPC at the temperature of the main phase transition, clamp-voltage of 50 mV; *right*, histogram of current fluctuation distribution with two maximums at 1 and 6 pA, respectively.

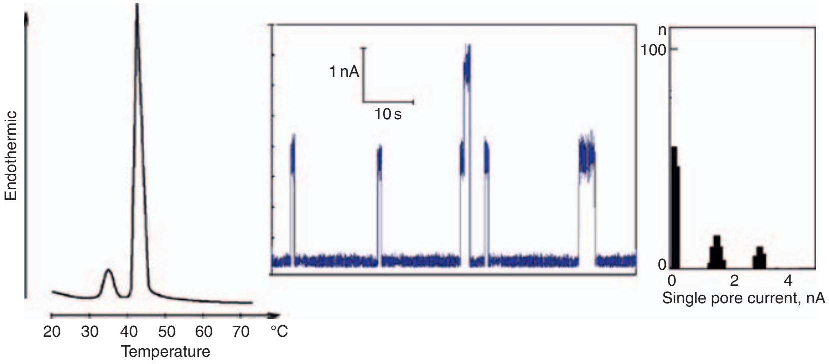

Figure 7 Soft poration of pBLM from DPPC in 1 M LiCl: *left*, thermogram of DPPC vesicles obtained with differential scanning calorimeter: main phase transition at 43 °C and pretransition at 37 °C; *middle*, typical record of electric current fluctuations in pBLM from DPPC at the temperature of main phase transition, clamp-voltage of 50 mV; *right*, histogram of current fluctuation distribution with two maximums at 1.5 and 3 nA, respectively.

scanning calorimetry. They observed the same effect as shown in Fig. 5 and made conclusion that Li^+ particularly involved in binding to DPPC bilayers.

It is shown in Figs. 6 and 7 that the difference in single pore conductance between DSPC and DPPC reaches as much as three orders. We suggest that this difference is conditioned by the difference in the edge energy of lipid pore, which in turn is strongly dependent on lipid molecule length. The dependence of many permeability effects observed at the lipid phase transition on the acyl-chain length has been discussed by Ipsen *et al.* [14]. A systematic computer simulation study has been conducted for a model of the main phase transition in bilayers of saturated diacyl phosphatidylcholines (DMPC, DPPC, DSPC). Among others, effect of transmembrane transport of Na^+ has been analyzed. Authors showed that the lateral density fluctuations and hence the correlated effects such as lipid domain size change and sodium ion permeability increase as the acyl-chain length decreased. The conception formulated by Ipsen *et al.* [14] on the basis of computer simulation study allows giving a qualitative explanation of transmembrane current difference between DSPC and DPPC membranes obtained in our experimental study of current fluctuation in pBLM (Figs. 6 and 7).

3.3. The Appearance of Single Lipid Pores in the pBLM from Natural Phospholipids

As a source of natural phospholipids, the HEL has been used. Before proceeding to study the electric conductance of the pBLM, the thermogram of the lipid was investigated. The thermogram in Fig. 8 shows an endothermic wide phase transition with a single peak near 52 °C. It should be noted that the pretransition peak revealed for synthetic DSPC and DPPC escaped detection in the HEL. These data are in agreement with the results obtained earlier by Nuhn *et al.* [34]. The HEL belongs to mixed-chain phospholipids enriched with palmitoyl and stearoyl fatty acid residues. A series of current fluctuations shown in Fig. 7 indicate the appearance of lipid pores in pBLM at the temperature of phase transition. The duration of each pulse is close to that indicated for DPPC (Fig. 7). As to the amplitude of current fluctuation, it is to be found at three discrete current levels at 40, 60, and 80 pA. The maximum at 60 pA corresponds to an intermediate position between the DPPC and DSPC, which correlates with nearly equal distribution of palmitoyl and stearoyl fatty acid tails in the HEL.

3.4. Line Edge Tension of Lipid Pore

Soft poration of pBLM allows measurement of single current fluctuation at a very low voltage applied to membrane. Lipid pore existence in this case is controlled predominantly by line edge tension. Equation (7) enables the calculation of edge tension if the number of single pores is known. The number of single pores in the pBLM of DPPC does not exceed 3 as shown in Fig. 5. For approximate evaluation of edge tension, we suppose the existence of one pore in 1 M LiCl with average radius 2.1 ± 0.7 nm (Table 1). The calculation gives the estimation for lipid pore edge tension equaled 8.8 pN. For comparison of our experimental data with others, obtained by different soft poration methods, we summarize them in the Table 2. Comparison indicates the good agreement between the

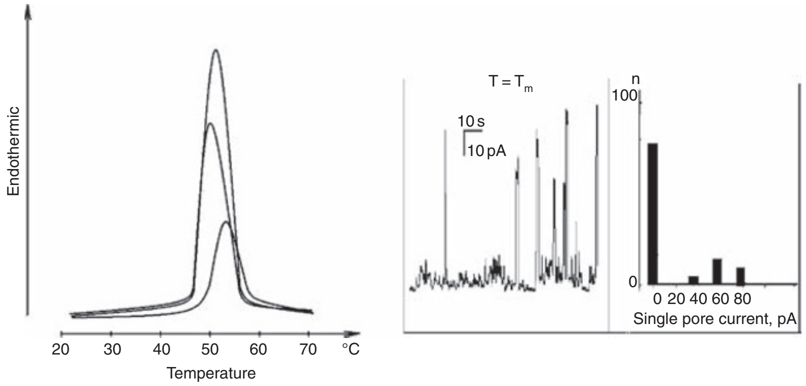

Figure 8 Soft poration of pBLM from hydrogenated egg lecithin in 0.1 M KCl: *left*, thermogram of HEL vesicles with single maximum at 52 °C (the disposition of two mixed-chain components inside is reconstructed according to Keough *et al.* [50]); *middle*, typical record of current fluctuations in pBLM from HEL at the temperature of phase transition, clamp-voltage of 50 mV; *right*, histogram of current fluctuation distribution with three peaks at 30, 60, and 80 pA.

Table 2 Comparison of lipid pore line tension determined in this study with other data obtained in experiments with soft poration

System	Line tension (pN)	Reference	Methods
DPPC	8.8	This work	Soft poration at the lipid phase transition
DOPC	6.9 ± 0.4	Karatekin *et al.* [35]	Vesicle pore closure dynamics
SOPC	9.2 ± 0.7	Zhelev and Needham [36]	Micropipette aspiration
DPPC	6.5	Taupin *et al.* [37]	Vesicle response to osmotic stress
Egg lecithin	20	Harbich and Helfrich [38]	Observation of open Cylindrical vesicles
Egg lecithin	8.6 ± 0.4	Chernomordik *et al.* [39]	Electroporation

experimental data obtained with different methods of soft poration. It is of interest to note that data obtained by the electroporation method [39] also give close estimation for the line edge tension. For theoretical estimation of line tension, formula $r_{cr} = \gamma/\sigma$ has been used. Substituting critical pore radius by experimentally determined subcritical pore radius equaled 5.1 nm, we can calculate γ if we take σ equaled 1.7 mN/m (liquid crystalline state of lipid bilayer). The result would be equal to 9.4 pN, which is close to experimental data shown in Table 2.

3.5. Evaluation of Lipid Bilayer Stability

The main criteria for bilayer stability, as shown above in theoretical background, are the critical radius pore r_{cr} and the barrier height E_{cr} (Fig. 3). Barrier height can be calculated as $E_{cr} = \pi\gamma^2/\sigma$. Taking $\gamma = 8.8$ pN and $\sigma = 1.7$ mN/m, we can calculate the energy barrier equaled of 34 kT in liquid crystalline state. This barrier is pretty high to provide the lipid bilayer stability.

The calculated critical pore radius equals to 5.1 nm. It is greater than r_{min} as much as twice. It should be remarked that there is a complete coincidence between the theoretical and experimental values of r_{cr} determined in Ref. [1].

The stability of lipid bilayer is decreased at the temperature below T_m due to increase of σ. The calculation shows that E_{cr} is lowered up to 11.6 kT. However, the experimental observation of pBLM well below T_m indicates that this barrier is sufficient to prevent bilayer rupture.

Based on obtained data, we can support the kinetic model elaborated by Bronstein and Iserovich [21] for lipid pore occurrence mentioned above. The calculated critical radius of the lipid pore depends on lipid phase state being equal to 5.1 nm in the liquid crystalline state and to 1.8 nm in the gel. The latter predicts the destabilization of the pBLM from DPPC in LiCl (Table 1) because the experimental radius is 2.1 nm. This discrepancy implies that the pore in frozen bilayer would be maintained in liquid environment (see Fig. 9D). As shown in Figs. 6 and 7, each bilayer at the phase transition contains a few if only one pores that conforms, in general, to precondition of kinetic model. The last argument in favor of that model consists in suggestion about an additional surface tension appearance which would exert the liquid lipid inclusion surrounded by frozen lipids. We experimentally determine σ to be equaled 5 mN/m in the gel state and 1.7 mN/m for the liquid crystalline state of lipid [1]. Therefore, the liquid lipid cluster (domain) captured by frozen lipid environment would experience some additional tension. The value of additional tension would be as high as three times. It could be able to provide the opening of the wide lipid pore.

The schematic picture of lipid pore evolution at the lipid phase transition of $L_\alpha \rightarrow L_\beta$-type is shown in Fig. 9. It is seen that the main precondition for lipid pore occurrence is a coexistence of liquid and gel lipid domains at the temperature of phase transition. The fluid cluster captured by solid one experiences the tension increase due to suction pressure and additional

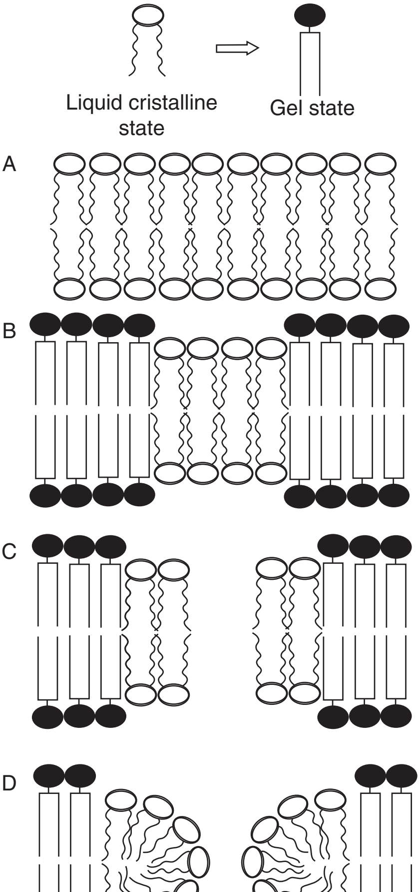

Figure 9 Diagram of phospholipid pore evolution at the phase transition of $L_\alpha \rightarrow L_\beta$-type: (A) a lipid bilayer in liquid crystalline state, (B) coexistence of liquid crystalline and gel phase states (it is assumed that liquid domain is captured by surrounding gel domain in pBLM), (C) hydrophobic pore occurrence (pore is filled with water), (D) the conversion of hydrophobic pore into hydrophilic one with reorientation of phospholipid molecules at the pore edge, and (E) a lipid bilayer in the gel state. Parts (A), (B), and (C) are referred to the main phase transition.

lateral pressure as mentioned above (Fig. 9B). The next step of hydrophobic pore evolution needs a significant growth of the initial pore size from $r = 0$ to 2.5 nm. The last limit is dictated by requirement to reorient of lipid molecules from vertical position to horizontal one. Experimental data of pore radius obtained in our measurements (2.1 ± 0.9 nm (Table 1)) well agree with prediction in 1 M LiCl. It should be noticed, however, that this value of pore radius is cation dependent, and for 1 M CsCl it closes to 0.9 ± 0.4 nm. Taking into account this discrepancy, we would have to suggest belonging of the pore to amphipathic type [40]. Amphipathic pore presents a partly hydrophobic pore filled with water.

Recently, Roth *et al.* [41] noted the remarkably new feature of hydrophobic pore that was existence of hydrophobic pore filled by a vapor. They supposed that hydrophobic regions of the channel wall helped control bubble formation much as hydrophobic surfaces control wetting and dewetting; a hydrophobic surface allowed the cohesive forces of water to pull the fluid away from the wall. The main advantage of this approach concludes in simple explanation of specific rectangular form of current fluctuations seen in many experimental records (Figs. 4–6). In fact, the current flow through an open channel is blocked when a bubble forms in a hydrophobic region of the pore. To advance the argument in favor of these conclusions, we attract the data obtained in experiments with cation selectivity of lipid pores (Table 1). One argument is based on comparison of data obtained by us in experiments with PEGs and the behavior of fully hydrophobic protein pore synthesized *de novo* by Zhi Qi *et al.* [16]. They showed that the selectivity sequence among monovalent cations based on permeability ratio fell into an order: $Cs^+ \geq K^+ > Na^+ \gg Li^+$. The Li^+-permeability was close to zero. Based on our experimental data with PEGs (Fig. 10), we suggest that complete blockade of ion conductance observed in 1 M LiCl could be explained by conversion of amphipathic pore into the fully hydrophobic pore due to high hygroscopicity of several PEGs used in the research. Verification of this suggestion needs an additional study.

3.6. Blocking Effect of PEGs on Single Lipid Pore Conductance

Except pore size calibration, water soluble molecules of PEGs allow to study the blocking effect in narrow ion-conducting pore whether it be the protein or lipid origin. According to Smart *et al.* [6], the standard experiment measures the effect of the presence of high concentration (20% w/w) of neutral polymers such as PEGs on the conductance of the pore of interest. The variation of conductance is measured as a function of the molecular weight of PEG at a constant weight fraction. In bulk solution, the conductivity of ionic solutions is reduced in the presence of PEG. This is due to the increase in the viscosity of the solution, with a consequent decrease in the ionic diffusion coefficients and conductivity. Krasilnikov *et al.* [24] showed

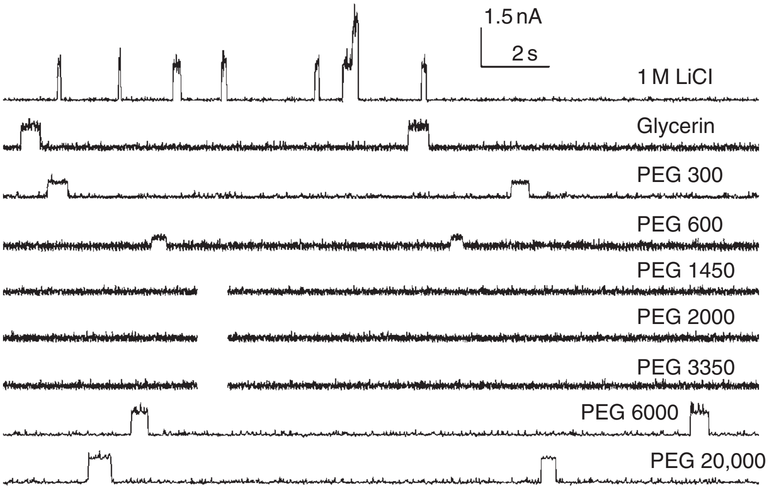

Figure 10 Current fluctuations in the pBLM at a voltage clamped at 50 mV in 1 M LiCl after addition of 20% PEGs of different molecular size: (A) without added PEG, (B) glycerol, (C) PEG-300, (D) PEG-600, (E) PEG-1450, (F) PEG-2000, (G) PEG-3350, (H) PEG-6000, (I) PEG-20000. Each blank in (E), (F), (G) lasts 5 min. Adapted from Ref. [2].

that this reduction is broadly independent of the molecular weight of the PEG used, provided a constant weight fraction is maintained.

The exclusion effect has been linked to the hydrodynamic radius of polymer. Polymers such as PEGs have been shown to be approximately spherical in solution. The hydrodynamic radius is obtained from the diffusion coefficient of the polymers in solution and it is found to vary with the square root of molecular weight of polymer. Different workers take distinct approaches to obtain a characteristic radius of a particular pore, from the measured the conductance profile inside the pore. Some take the 50% effect for radius [3]. In contrast, Krasilnikov *et al.* [24] prefer to fit two straight lines to the data: one when the conductance plateaus at high radius/molecular weight and another at lower radius. The characteristic radius is taken as the intersection point between these lines.

When very large PEGs are added to the conductance medium, there is normally an increase in protein pores conductance compared to the PEG-free measurements. Such behavior has been observed for reconstructed *Vibrio cholera* cytolysin [24] and for three different conductance states of the alamethicin channel [3]. An explanation for this increase has been offered by Krasilnikov *et al.* [24] and Bezrukov and Vodyanoy [3]. This indicates that PEG is hygroscopic—as the polymer is excluded from the interior of the channel, the water activity of the solution is increased in this space and the conductivity of the permeant ions consequently increases.

This effect can also be shown to occur in bulk solutions using a sodium electrode. Bezrukov and Vodyanoy [3] show how such measurements can be linked to access resistance considerations and an effective end radius can be assigned to a pore. This is because although the polymer is excluded from the interior of the pore, it is still present at the approach to both mouths. These authors also show that similar results can be obtained using nonhygroscopic polymers such as dextrans. This is important as it reduces the possibility that specific interactions between the polymer and ion channel could affect the result.

In the work presented here, we show how the results of the conductance experiments with PEGs can be linked to structural arrangement in the pure lipid pore appeared in unmodified pBLM at the lipid phase transition. Experimental data represented in Fig. 10 were obtained in experiments with the pBLM of DPPC, formed in 1 M LiCl. The concentration of added PEG was 20% (w/w). First record reflects the control experiment carried out in the absence of PEG. It corresponds to the data shown above in Fig. 6. Other records are obtained by addition in the bulk solution of the PEG molecules of different molecular size kept at the same weight fraction. One can see that all PEGs could be arranged in three groups where the first group includes PEG-300, PEG-600, and glycerol; second group includes PEG-1450, PEG-2000, and PEG-3350; and third group is represented by PEG-6000 and PEG-20000. In Fig. 10B the effect of glycerol (hydrodynamic radius 0.31 nm) is shown. Comparison with control experiment (Fig. 10A) demonstrates a decrease of current fluctuation amplitude and an increase of a dwell time, the number of fluctuation is lowered. The effect of PEG-300 (with radius of 0.6 nm) and PEG-600 (with radius of 0.7 nm) is followed by proportional decrease of amplitude. The further increase of molecular size of added PEG is followed by total absence of current fluctuations. The second group of PEG molecules included PEG-1450, PEG-2000, and PEG-3350 covers the hydrodynamic molecular radii from 1.05 nm (PEG-1450) up to 1.63 nm (PEG-3350). Extending the exposition time up to 5 min did not change the situation. It was concluded that we dealt with full blocking of lipid pore conductance. The further increase of the molecular size of PEG (PEG-6000 with a radius of 2.1 nm and PEG-20000 with a radius of 3.1 nm), added to the solution (Fig. 10H and I), led to unexpected result. We observed the reappearance of current fluctuation resembled that shown above in Fig. 10B, which were found to belong to the first group of PEGs namely to glycerol with molecular radius of 0.3 nm. Despite the great difference in molecular mass between PEG-6000 and PEG-20000, there was no significant difference in current fluctuations between them.

In this study the role played by conductivity of the bulk solution is very important because the electric circuit for transmembrane current measurement is completed through the electrodes placed in bulk electrolyte solution. In narrow pore the added PEGs influence the conductance inside the pore and surrounding bulk solution in a different way. In Fig. 11 the dependence of both bulk conductivity and lipid pore conductance on the molecular size of PEG is represented. As shown in the figure, there is a synchronization in conductance change between the bulk solution and pore by addition of glycerol and PEG-300. By this is meant that the pore is a hydrophilic hole filled with a bulk solution and accessed for glycerol and PEG-300. Starting with PEG-600, one can see the slight divergence between conductance change curves. This divergence sharply increases by addition of PEG-1450, PEG-2000, and PEG-3350. Conductance of modified pore drops up to the level of a noise while the conductance of the bulk solution remains constant. These three PEGs cover the pore size range from 1.05 to 1.63 nm. The final lapse of the curve is very important because it allows comparing the observed effect of polymer exclusion in pure lipid pores with analog effects in protein channels [38].

This lapse demonstrates the restoration of pore conductance due to exclusion of PEG-6000 and PEG-20000 with high steepness. The intersection between two curves gives the cutoff value for the PEG in pure lipid pore.

To compare polymer partitioning into the pore, Bezrukov *et al.* [27] apply a more simple scaling law that indicated above (see Experimental):

$$p(w) = \exp\left(-\left(\frac{w}{w_0}\right)^{\alpha}\right) \tag{8}$$

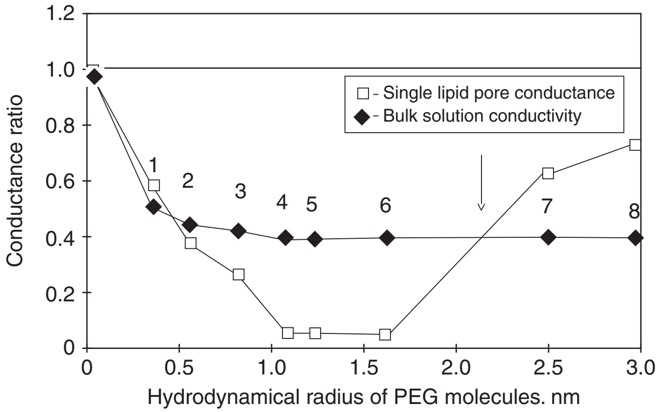

Figure 11 The dependence of a PEG-induced pore conductance (open square) and bulk solution conductivity (black diamond) on the polymer molecule size: (1) glycerol, (2) PEG-300, (3) PEG-600, (4) PEG-1450, (5) PEG-2000, (6) PEG-3350, (7) PEG-6000, (8) PEG-20000. In (4), (5), and (6), pore conductance has been registered at the noise level. Arrow shows the point where the pore conductance equals to the conductivity of bulk solution.

for the partitioning coefficient $p(w)$ with adjustable α and w_0. The first parameter characterizes the sharpness of transition between regimes of exclusion and penetration. Sharper transitions correspond to larger α value. The second parameter w_0 is the characteristic polymer molecular weight ("cutoff size") that separates these two regimes. Assuming a linear relationship between the polymer monomeric concentration in the pore and the reduction in the pore conductance, we can write:

$$p(w) = \frac{1 - g_{\mathrm{w}}/g_0}{1 - \chi_{\mathrm{w}}/\chi_0} \tag{9}$$

where g_{w} is the conductance of the pore in the presence of the PEG, g_0 is the conductance of the pore in the absence of the PEG, χ_{w} is the conductivity of bulk solution in the presence of the PEG, and χ_0 is the conductivity of the bulk solution in the absence of the PEG. The experimental data are summarized in Table 3. The first peculiarity of the lipid pore resides in the fact that the calculated values of PEG partitioning exceed 1.0 for at least several PEGs (PEG-300, PEG-600). According to Merzlyak *et al.* [42], this effect is attributed to strengthening of hydrophobic interaction between the PEG molecule and lumen wall in the pore at high salt concentration. In spite of very high water solubility of PEG, it is essentially nonpolar [43]. Remembering that the lipid pore surface is lined by polar heads in contact with water and the PEG avoids charged species, it is plausible to assume that attraction of PEG to the pore lumen will increase with ion strength of solution. Merzlyak *et al.* [42] showed in experiments with reconstructed α-toxin pore that the increase of the salt concentration from 0.1 M KCl to 1.0 M KCl was followed by significant rise of portioning coefficient from 1 to 1.7 for PEG-300, PEG-400, PEG-600, PEG-1450, and PEG-2000. They explained this effect by hydrophobic attraction of PEG molecules inside the pore. It should be noted that the polar molecule of glycerol (Table 3) possesses the partitioning coefficient less than 1.

Next effect demonstrated in Table 3 concerns PEG-1450, PEG-2000, and PEG-3350. They give anomalously high partitioning coefficient much more than 1. This result corresponds the absence of any current fluctuations in the pBLM (Fig. 10). Following arguments given before we can conclude that this effect is due to hydrophobic interaction of these PEGs with lipid pore wall.

The polymer exclusion effect shown in Table 3 starts in the lapse between PEG-3350 and PEG-6000. This point called "cutoff size" could be detected in Fig. 10 as an intersection point at PEG-4800 with hydrodynamic radius of 2.1 nm. Equation (8) could be used for estimation of steepness of polymer exclusion process widely used in membrane biophysics to compare experimental data of different pores in frame of

Table 3 Comparative effect of PEGs on the lipid pore conductance and the conductance of the bulk solution

PEGs	Hydrodynamic radii of PEG molecules	Conductivity of bulk solution, χ (S/m)	Single lipid pore conductance, G (S)	G_{PEG}/G_0	χ_{PEG}/χ_0	$p(\omega)$
Control	–	7.9	29.8 ± 1.3	1	1	
Glycerol	0.31	4.1	18.1 ± 0.7	0.61	0.51	1.79
PEG-300	0.61	4.3	12.3 ± 1.3	0.41	0.54	1.29
PEG-600	0.78	4.1	10.1 ± 0.5	0.33	0.51	1.34
PEG-1450	1.05	4.4	0 ± 0.5	0	0.56	2.26
PEG-2000	1.22	4.4	0 ± 0.5	0	0.56	2.26
PEG-3350	1.63	4.1	0 ± 0.5	0	0.56	2.26
PEG-6000	2.51	4.1	19.1 ± 0.6	0.64	0.52	0.33
PEG-20000	3.21	4.1	21.1 ± 0.4	0.70	0.52	0.15

The conductance of pBLM of DPPC has been studied in 1 M LiCl at the temperature 43 ± 0.5 °C. PEGs were added symmetrically in concentration 20% (w/w). $p(\omega)$ is calculated from Eq. (9).

scaling theory [42]. At the cutoff point $p(w)$ close to 1, the ratio w/w_0 equals to 1.3, and α would be close to 4. It means the very high sharpness of transition from penetration state to the exclusion state in lipid pore which is much higher than in a number of protein pores like OmpF porin with α equaled 1.65 [25], α-toxin with $\alpha = 3.2$ [42], and alamethicin with $\alpha = 1.3$ [27].

The transition sharpness characterized by parameter α exceeds those predicted by the scaling approach [44] and hard sphere partitioning [45]. These two models are tempting to use because they give the analytical expression for partition coefficient. Based on it one can estimate the risk of some complications to be ignored. One of them is the high polymer concentration used in our experiments. At 15% concentration, the PEG-1000 solution is on the border between diluted and semidiluted regimes, where interactions between polymer molecules can no longer be neglected. It was shown [42] that only the hard-sphere model is able to give an appreciably sharper transition. One of the most important peculiarities of pure lipid pore is a high elasticity of the wall in comparison with the rigid wall in protein pore. We can suggest therefore that this model is more suitable for the quantitative description of PEG interaction with pure lipid pore. In favor of this suggestion, the fact of current fluctuation absence in the presence of three different sized PEGs is indicated.

It should be noted that corrections for the finite access resistance mentioned above do not influence the transition sharpness and characteristic cutoff polymer size significantly. However, it could be obligatory in an attempt to determine the pore size with high precision. Based on theory derived by Hall [46], we can calculate the value of access resistance of lipid pore in our study. The formula is:

$$R_{\mathrm{acc}} = \frac{\rho}{4r}$$

where ρ is the resistivity of the solution and r is the radius a circular pore. Taking a resistivity of 1 M LiCl (with addition of glycerol, see above the comments to Fig. 11) as 0.25 Ω m, and the radius of the lipid pore equaled 2.1 nm (determined in Fig. 11 as cross-section point), we calculated R_{acc} as equaled $3 \times 10^7\ \Omega$. The corrected total resistance of the pore immersed in the electrolyte solution with excluded PEG is given as:

$$R_{\mathrm{tot}} = R_{\mathrm{pore}} + 2R_{\mathrm{acc}}$$

Calculation gives the corresponding effective radius of pore entrances equaled 1.4 nm. This value is very close to the results obtained independently in experiments with a series of monovalent cations (Table 2). Monovalent cation selectivity in the pBLM modified with PEGs.

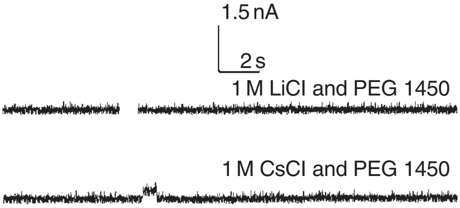

Figure 12 Comparison of typical records of current fluctuations in the pBLM at a voltage clamp at 50 mV in 1 M LiCl after addition of 20% PEG-1450 (A) with the same in 1 M CsCl. The blank in (A) lasts 5 min. The amount of experiments in both solutions numbers 5.

The experimental results with PEGs allow to return to the discussion of cation selectivity of pBLM modified with PEGs. We focus on Li^+- and Cs^+-selectivity because both ions locate at the ends of each selectivity order classified by Eisenman *et al.* [32]. From three blocking PEGs, we concentrate on PEG-1450 with hydrodynamic radius of 1.05 nm. As illustrated in Fig. 12, the modification of pBLM with PEG-1450 in 1 M LiCl is followed by full blockade of Li^+-selectivity. In contrast, the modified pBLMs formed in 1 M CsCl demonstrate the appearance of current fluctuations. The amplitude of current fluctuation equals in average to 0.5 nA with dwell time ~1 s. Calculation of pore radius gives 1.1 nm. Taking into account the radius of the pore and hydrodynamic radii Li^+ (0.24 nm) and Cs^+ (0.12 nm), we could explain obtained result in a context of simple diffusion rate difference between monovalent cations. It is reasonable to suggest that the observed full blockade of lipid pores in 1 M LiCl is attributed to exclusively feature of Li^+ to bind by pore wall. The ability of Li^+ to bind the lipid bilayer surface has been observed in thermogram while the T_m for DPPC was shifted from 41 to 43 °C [2].

4. DISCUSSION

Many experiments on pore formation avoid the complexity of biological membranes by using one-component lipid bilayers, either artificial vesicles or pBLM. Soft poration of the BLM deals with thermally generated transient defects occurred due to lipid phase transition [1] or osmotic pressure [37]. The former is the main subject of discussion in this chapter. Thermally generated transient defects, in which lipid headgroups fluctuate apart, exposing their hydrocarbon tails to the aqueous medium, are encouraged. It happened so that most studies of passive ion transport at the lipid phase transition were carried out on liposomes and only a few were conducted with pBLM (see Section 1). It should be noticed that there is a significant difference between them concerning the very important feature of pore creation process as a surface tension. In the absence of osmotic pressure gradient or aspiration, the surface tension in vesicles lacks while pBLM experiences the suction tension due to torus. Additional source of surface tension in pBLM aroused at lipid phase transition is provided by Bronstein and Iserovich [21]. They analyzed the pore creation in fluid lipid trapped by frozen lipid environment.

The criterion of critical pore could account for discrepancy between monovalent cation selectivity at soft poration in free standing liposomes [4] and absence of significant selectivity in our experiments with pBLM (Table 1). At $\sigma = 0$, the r_{cr} is tending to infinity and any pore appeared in liposome bilayer would exist without rupture of bilayer. The existence of lipid pore in liposome is governed presumably by line edge tension [35]. This explanation is agreed with theory of Petrov *et al.* [17]. They suppose that γ depends on σ and r. Even though $\sigma = 0$, the line edge tension of the pore is saved and this permits the existence of metastable or stable toroid pores.

Based on this consideration, we can suggest that population of lipid pores in liposome at the lipid phase transition could be enriched with pores which are tending to close while the population of lipid pores in pBLM contains at least a number of pores with radius close to r_{cr}. In model experiments, Bekstein and Sansom [40] stated that the size of hydrophobic pore plays the key role in pore blockade and cation selectivity. They referred both phenomena to the process of conversion of hydrophilic pore into hydrophobic one and vice versa. Based on molecular dynamic simulation, they show that a short hydrophobic pore in protein channel is closed to water for radii smaller than 0.45 nm. Ions behave similarly but the transition from conducting to nonconducting pores is even steeper and occurs at a radius of 0.65 nm for hydrophobic pores. We suppose that partition of PEG molecules into lipid pore lead to a decrease of intrapore space and provide the conversion hydrophilic pore into hydrophobic one. This prediction is tested in our experiments with PEG-1450 (Fig. 12). As would be expected, the penetration of PEG molecule should be followed by significant increase of selectivity in favor of Cs^+ over Li^+ either due to occupation of the pore by polymer molecule or its exclusion from the pore. In the case of Cs^+-pore, it could be accounted for by exclusion of PEG molecule with hydrodynamic radius of 1.05 nm (Table 3) from the pore whose radius is of 0.9 nm (Table 1). In the case of Li^+-pore, the size of the pore (2.1 nm) is sufficient for PEG molecule to penetrate inside the pore. The remaining free space with radius of 1.05 nm would be enough for Li^+ to diffuse. However, the effect of PEG-1450 is followed by full blockade of Li^+ permeability. We prone to explain this contradiction by capability of Li^+

to induce the ‘‘salt out’’ effect [19]. The exclusion of PEG molecules from the Li^+-pore starts with PEG-4800 (Fig. 11) and continues with PEG-6000 and PEG-20000. As a result we observe a complete restoration of Li^+ permeability. The mechanism of PEGs interaction with the pore wall remains to be elucidated. Taking into account the high hygroscopes of PEGs, we can suppose that the blocking effect should involve dewetting of pore lumen. As a result the conversion of hydrophobic lipid pore into hydrophilic one would be prevented (Fig. 9C and D).

The energy cost of structural defects, referred to as hydrophobic pores, is essential for the energy of the exposed hydrocarbon–water interface [45]. It is evident that it is energetically favorable for the lipids in the rim of a large hydrophobic pore to reorient, overcoming an energy barrier so that their headgroups point into the pore lumen, and form a hydrophilic pore. This transformation is provided in Fig. 9. A new aspect concerns the possibility of sufficiently long time existence of hydrophobic pore filled with water [16] or amphipathic pore filled with vapor [40,47]. More adequate for hydrophobic lipid pore is a model membrane formed of hexagonally packed carbon nanotubes [47]. Molecular dynamic simulation shows that a narrow hydrophobic pore of subnanometer radius pose a huge free-energy barrier for ions, but a small increase in the pore diameter to ∼1 nm nearly eliminates that barrier. This pore model is able to mimic high ion selectivity and gating effect known for a number of biological ion channels [23].

5. CONCLUSION

Soft poration of lipid bilayer occurred at the lipid phase transition allows to trace the phenomenon of membrane pore conductance from molecular perturbation of bilayer up to formation of long-lived transmembrane channel. In contrast to reconstructed proteinous channels, this model is much simpler but reproduce many characteristics of ion-conducting channels: current fluctuations, ionic selectivity, channel blockade, etc. Recently, we discovered a model for self-sustained potential oscillation of lipid bilayer membranes induced by the gel–liquid crystal phase transition, published by Yagisava *et al.* [48]. In his replay, Dr. M.J. Zuckerman [49] wrote: ‘‘If the excellent work of Yagisava *et al.* is to bear fruit in he realm of biophysics, it will be necessary o go beyond the case of repeated bilayer phase transitions. One possibility is to move to phase coexistence in lipid mixture or to examine the effect of protein–lipid interactions on self-sustained oscillations or both.’’ Our chapter has been devoted to another aspect of nerve excitation—modeling of gating process which is studied in more than one hundred protein channels (see for review [41]). We showed that certain of the calibrated PEGs may control ion selectivity and blocking effect in pore occurred at the main lipid phase transition. The key stone in the gating problem is the hydrophobic–hydrophilic transition in the pore wall which is accessible for the study at the lipid phase transition.

ACKNOWLEDGMENTS

We are grateful for the interest and encouragement of all our colleagues. The authors are grateful to Prof. D.P. Kharakoz for fruitful discussion. V.A. thanks Matthias Schneider, Konny Kaufmann, Misha Kozlov, and Lenja Chernomordik for stimulating discussion at workshop in Gomadingen. This study has been supported by grants from the Russian Fund for Basic Research.

REFERENCES

[1] V.F. Antonov, A.A. Anosov, O.Yu. Nemchenko, E.Yu. Smirnova, Pure lipid pores in unmodified planar lipid membrane at the phase transition from the liquid crystalline state to the gel state, in: A. Leitmanova, Liu, H.T. Tien (Eds.), Advances in Planar Lipid Bilayers and Liposomes Academic Press, New York, 2007, pp. 151–173.
[2] V.F. Antonov, A.A. Anosov, V.P. Norik, E.Yu. Smirnova, Soft perforation of planar bilayer lipid membranes of dipalmitoylphosphatidylcholine at the temperature of the phase transition from the liquid crystalline to the gel state, Eur. Biophys. J. 32 (2003) 55–59.
[3] S.M. Bezrukov, I. Vodyanoy, Probing alamethicin channels with water-soluble polymers. Effect on conductance of channel states, Biophys. J. 64 (1993) 16–25.
[4] M.C. Blok, E.C.M. van der Neut-Kok, L.L.M. van Deenen, J. de Gier, The effect of chain length and lipid phase transitions on the selective permeability properties of liposomes, BBA 406 (1975) 187–196.
[5] L. Cruzeiro-Hansson, O.G. Mouritsen, Passive ion permeability of lipid membranes modeled via lipid-domain interfacial area, BBA 944(1) (1988) 63–72.
[6] O.S. Smart, J. Breed, G.R. Smith, M.S.P. Sansom, A novel method for structure-based prediction of ion channel conductance properties, Biophys. J. 72 (1997) 1109–1126.
[7] B. Wunderlich, Role of Thermodynamics for the Pore Formation in Membranes Inst. fur Physik, Universitat Augsburg, 2007, pp. 43–49.
[8] V.F. Antonov, V.V. Petrov, A.A. Molnar, D.A. Predvoditelev, A.S. Ivanov, The appearance of single ion channels in unmodified lipid bilayer membrane at the phase transition, Nature 283 (1980) 585–588.
[9] G. Boheim, W. Hanke, H. Eibl, Lipid phase transition in planar lipid membrane and its effect on carrier- and pore-mediated ion transport, Proc. Natl. Acad. Sci. USA 77 (1980) 3403–3407.
[10] K. Kaufmann, I. Singer, The induction by protons of ion channels through lipid bilayer membranes, Biophys. Chem. 18 (1983) 89–99.
[11] K. Kaufmann, I. Silman, The induction of ion channels through excitable membrane by acetylcholineesterase, Naturwissenschaften 67 (1980) 608–610.
[12] J.K. Levine, M.H.F. Wilkins, Structure of oriented lipid bilayers, Nat. New Biol. 230 (1971) 69–72.
[13] M.M. Kozlov, V.S. Markin, The theory of osmotic lysis of lipid vesicles (in Russian), Biol. Membranes 1 (1984) 74–89.

[14] J.H. Ipsen, K. Jorgensen, O.G. Mouritsen, Density fluctuations in saturated phospholipids bilayers increase as the acyl-chain length decreases, Biophys. J. 58 (1990) 1099–1107.

[15] S. Mabrey, J.M. Surtevant, Investigation of phase transitions of lipids and lipid mixtures by high sensitivity differential scanning calorimetry, Proc. Natl. Acad. Sci. USA 73 (1976) 3862–3866.

[16] M. Zhi Qi, K.D. Sokabe, H. Ishida, Structure–function study on a *de novo* synthetic hydrophobic ion channel, Biophys. J. 76 (1999) 631–641.

[17] A.G. Petrov, M.D. Mitov, A.I. Derzhanski, Edge energy and pore stability in bilayer lipid membranes, in: L. Bata (Ed.) Advances in Liquid Crystal Research and Applications, Pergamon Press, Oxford—Akademiai Kiado Budapest, 1980, pp. 695–737.

[18] R.W. Glaser, S.L. Leikin, L.V. Chernomordik, V.F. Pastushenko, I. Sokirko, Reversible electrical breakdown of lipid bilayers: formation and evolution of pores, BBA 940 (1988) 275–287.

[19] J.N. Israelachvili, R.M. Pashley, Measurements of the hydrophobic interaction between two hydrophobic aqueous-electrolyte solutions, J. Colloid. Interface Sci. 98 (1984) 500–514.

[20] B.V. Derjagin, A.V. Prokhorov, On the theory of the rupture of black films, J. Colloid. Interface Sci. 81 (1980) 108–115.

[21] V.L. Bronstein, P.G. Iserovich, Physical and mathematical model of macroscopic pore appeared in lipid bilayer at phase transition (in Russian), Cryobiology 20 (1983) 22–24.

[22] P. Mueller, D.O. Rudin, H.T. Tien, W.C. Wescott, Reconstruction of cell membranes structure *in vitro* and its transformation into an excitable system, Nature 194 (1962) 979–980.

[23] B. Hille, Ionic Channels of Excitable Membranes, Sinauer Associates Inc., Sunderland, 2001, pp. 1–814.

[24] O.V. Krasilnikov, R.Z. Sabirov, V.I. Ternovsky, P.G. Merzliak, J.N. Muratkhodjaev, A simple method for determination of the pore radius of ion channels in planar lipid bilayer membranes, FEMS Microbiol. Immunol. 105 (1992) 92–100.

[25] T.K. Rostovtseva, E.M. Nestorovich, S.M. Bezrukov, Partitioning of differently sized poly(ethylene glycols) into OmpF porin, Biophys. J. 82 (2002) 160–169.

[26] S.C. Hinnah, R. Wagner, N. Sveshnikova, R. Harrer, J. Soll, The chloroplast protein import chanel Toc75: Pore properties and interaction with transit peptides, Biophys. J. 83 (2002) 899–911.

[27] S.M. Bezrukov, I. Vodyanoy, R.A. Brutyan, J.J. Kasianowicz, Dynamics and free energy of polymer partitioning into a nanoscale pore, Macromolecules 29 (1996) 8517–8522.

[28] A. Moran, A. Ilani, Surface tension of an artificial bileaflet membrane in comparison to parent lipid solution–water interfacial tension, Chem. Phys. Lipids 4 (1970) 169–180.

[29] E. Evans, V. Heihrich, F. Ludwig, W. Rawicz, Dynamic tension spectroscopy and strength of biomembranes, Biophys. J. 85 (2003) 2342–2350.

[30] S.A. Freeman, M.A. Wang, J.C. Weaver, Theory of electroporation of planar bilayer membranes: predictions of the aqueous area, change in capacitance, and pore-pore separation, Biophys. J. 67 (1994) 42–56.

[31] W.K. Chandler, H. Meves, Sodium and potassium currents in liquid axons perfused with fluoride solutions, J. Physiol. (Lond.) 211 (1970) 623–652.

[32] G. Eisenman, G. Szabo, S.M. Ciani, S. McLauglin, S. Krasne, Ion binding and ion transport produced by neutral lipid-soluble molecules, in: Richard Durst (Ed.), Progress in Surface and Membrane Science, Academic Press, New York, 1973, pp. 139–241.

[33] B.A. Cunningham, J.E. Shimotake, W. Tamura-Lis, T. Mastran, W.M. Kwok, J.W. Kauffman, L.G. Lis, The influence of ion species on phosphatidylcholine bilayer structure and packing, Chem. Phys. Lipids 39(1–2) (1986) 135–143.

[34] P. Nuhn, P. Schenk, H. Richter, Untersuchungen an liposomen aus hydrierten eilecithin, Pharmazie 40 (1985) 705–709.

[35] E. Karatekin, O. Sandre, H. Guitouni, N. Borghi, P. Puech, F. Brochard-Wyart, Cascades of transient pores in giant vesicles: line tension and transport, Biophys. J. 84 (2003) 1734–1749.

[36] D.V. Zhelev, D. Needham, Tension-stabilized pores in giant vesicles: Determination of pore size and pore line tension, BBA 1147 (1993) 89–104.

[37] C. Taupin, M. Dvolatzky, C. Sauterey, Osmotic-pressure induced pores in phospholipids vesicles, Biochem. USA 14 (1975) 4771–4775.

[38] W. Harbich, W. Helfrich, Alignment and opening of giant lecithin vesicles in electric fields, Naturforsch. A 34 (1979) 1063–1065.

[39] L.V. Chernomordik, M.M. Kozlov, G.B. Melikjan, I.G. Abidor, V.S. Markin, Yu.A. Chismadzhev, The shape of lipid molecules and monolayer membrane fusion, BBA 812 (1985) 643–655.

[40] O. Beckstein, M.S.P. Sansom, The influence of geometry, surface character, and flexibility on the permeation of ions and water through biological pores, Phys. Biol. 1 (2004) 42–52.

[41] R. Roth, D. Gillespie, W. Nonner, R.E. Eisenberg, Bubbles, gating, and anesthetics in ion channels, Biophys. J. 94 (2008) 4282–4298.

[42] P.G. Merzlyak, L.N. Yuldasheva, C.D. Rodrigues, C.M.M. Carneiro, O.V. Krasilnikov, S.M. Bezrukov, Polymeric nonelectrolytes to probe pore geometry: Application to the α-toxin transmembrane channel, Biophys. J. 77 (1999) 3023–3033.

[43] J. Israelachvili, Commentary. The different faces of poly(ethylene glycol), Proc. Natl. Acad. Sci. USA 94 (1997) 8378–8379.

[44] A.Yu. Grosberg, A.R. Khokhlov, Statistical Physics of Macromolecules AIP Press, New York, 1994.

[45] R.H. Boyd, R.R. Chance, G. Ver Strate, Effective dimensions of oligomers in size exclusion chromatography. A molecular dynamics simulation study, Macromolecules 29 (1996) 1182–1190.

[46] J.E. Hall, Access resistance of a small circular pore, J. Gen. Physiol. 66 (1975) 531–532.

[47] C. Peter, G. Hummer, Ion transport through membrane-spanning nanopores studied by molecular dynamics simulations and continuum electrostatics calculations, Biophys. J. 89 (2005) 2222–2234.

[48] K. Yagisawa, M. Naito, K. Gondairo, T. Kambara, A model for self-sustained potential oscillations of lipid bilayer membranes induced by the gel-liquid crystal phase transitions, Biophys. J. 64 (1993) 1461–1475.

[49] M.J. Zuckermann, Self-sustained potential oscillations and the main phase transition of lipid bilayers, Biophys. J. 64 (1993) 1369–1370.

[50] K.M.W. Keough, P.J. Davis, Gel to liquid-crystalline phase transitions in water dispersion of saturated mixed-acid phosphatidylcholines, Biochemistry 18 (1979) 1453–1459.

CHAPTER THREE

PHYSICOCHEMICAL AND PHARMACOKINETIC CHARACTERIZATION OF ULTRADEFORMABLE VESICLES USING CALCEIN AS HYDROPHILIC FLUORESCENT MARKER

Ana Paula Corrêa Oliveira Bahia,[1] Larissa Barbosa Rabelo,[1]
Warley Cristiano Souza,[1] Lucas Antonio Miranda Ferreira,[2]
and Frédéric Frézard[1,*]

Contents

[*] Corresponding author. Tel.: +55 31 34092940; Fax: +55 31 34092924;
E-mail address: frezard@icb.ufmg.br

[1] Departamento de Fisiologia e Biofísica, ICB, Universidade Federal de Minas Gerais, Av. Antônio Carlos 6627, Pampulha, 31270-901 Belo Horizonte, MG, Brazil
[2] Faculdade de Farmácia, Universidade Federal de Minas Gerais, Av. Antônio Carlos 6627, Pampulha, 31270-901 Belo Horizonte, MG, Brazil

Advances in Planar Lipid Bilayers and Liposomes, Volume 9
ISSN 1554-4516, DOI: 10.1016/S1554-4516(09)09003-6

Abstract

Appropriate mixtures of phospholipid and surfactant were found to produce ultradeformable vesicles which were claimed to pass through nanometer pores of the stratum corneum (SC), allowing transdermal drug delivery. However, the precise *in vivo* fate of encapsulated drug and whether ultradeformable vesicles pass intact through the SC and can promote the transdermal delivery of any substance remain open questions. Indeed, systematic physicochemical and pharmacokinetic studies are still needed to define the mode of action and the range of applications of these vesicles. This chapter presents different experimental approaches, based on the use of calcein as hydrophilic fluorescent marker, for probing the physicochemical and pharmacokinetic characteristics of these vesicles. The ability of Co^{2+} ion to quench the fluorescence of calcein allowed determining the drug encapsulation efficiency and the membrane permeability to calcein of ultradeformable vesicles. Ultradeformable membranes made from natural phosphatidylcholine and sodium cholate were found to be highly permeable to calcein, the resulting vesicles being therefore unable to effectively retain the encapsulated marker. Both *in vitro* skin permeation and *in vivo* transdermal (percutaneous) absorption studies were performed. *In vitro* experiments used Franz diffusion cells mounted with hairless mouse skin. *In vivo* experiments were carried out by applying calcein formulations onto the dorsal skin of hairless mice and determining fluorimetrically the plasma calcein concentration at different time intervals. Surprisingly, both *in vivo* and *in vitro* skin permeation studies indicated that deformable vesicles reduced the transdermal flux of calcein, when compared to a solution containing or not sodium cholate. Importantly, fluorescence measurements of the receptor fluid of the Franz diffusion cell in the absence and presence of Co^{2+} revealed that the permeated calcein existed essentially under the nonencapsulated form. In conclusion, the high membrane permeability of deformable vesicles and the nonencapsulated state of calcein after *in vitro* skin permeation argue against the passage of calcein through the SC under the encapsulated form.

1. INTRODUCTION

The skin represents an ideal route of drug administration in terms of accessibility and ease of application. However, the range of molecules that can achieve therapeutic amounts at their target site following application to the skin is severely limited. This is due to the effective barrier properties of intact skin, which is primarily associated with the outermost layers of the epidermis, namely the stratum corneum (SC). Lipid vesicles have been extensively studied to carry drugs and enhance their penetration through the skin. Classical liposomes, such as those made from lecithin, are generally reported to accumulate in the SC, upper skin layers and in the appendages, with minimal penetration to deeper tissues or the systemic circulation [1–4]. Therefore, classical liposomes are too large and rigid to fit within the intercellular lipid domains of the SC and are not useful as transdermal delivery systems.

Other vesicle compositions have been investigated to develop systems that are capable of carrying drugs and macromolecules to deeper tissues and/or systemic circulation. These belong to the category that is variously termed as deformable, highly deformable, elastic, or ultra-flexible liposomes or vesicles. Transfersomes® (Idea AG) are a form of deformable vesicles, which were first introduced in the early 1990s by Cevc and Blume [5]. Elasticity is generated by incorporation of an edge activator in the lipid bilayer structure. The original composition of these vesicles was soybean phosphatidylcholine (SPC) incorporating sodium cholate. The incorporation of ethanol in lipid vesicles is an alternative approach to fluidize the lipid membrane [6], generating the so-called Ethosomes. Transfersomes® and Ethosomes were reported to improve the penetration of a range of small hydrophilic and lipophilic molecules, peptides, proteins, hydrophilic macromolecules to deep peripheral tissues and/or to the systemic blood circulation [7–9].

The mechanism proposed by Cevc [7] is that the high deformability of these vesicles facilitates their penetration through the intercellular lipid pathway of the SC. The osmotic gradient, caused by the difference in water concentrations between the skin surface and interior, has been proposed as the major driving force for the penetration of the vesicles [5]. A lipid suspension applied nonocclusively to the skin is subject to evaporation and, to avoid dehydration, ultradeformable vesicles must penetrate to deeper tissues.

Despite the substantial interest in the mechanism of vesicular delivery over the past decade, there is still considerable debate as to whether ultradeformable vesicles behave as a true carrier system by penetrating intact through the skin or act as a permeation enhancer [10–12]. Either drug deposition into the skin or transdermal drug delivery to deep tissues or/and the blood circulation has been reported following the topical application of drugs in ultradeformable vesicles. However, the factors that determine the depth of drug penetration remain to be elucidated. Indeed, different drugs, vesicle compositions, and methods of preparation have been employed, resulting in deformable vesicles having diverse characteristics with respect to size, lamellarity, charge, membrane fluidity, permeability, elasticity, and drug entrapment efficiency. This fact, in addition to the variety of skin models used (man or animal, *in vivo* or *in vitro*) probably account for the lack of understanding of the mode of action of these vesicles. In this context, systematic physicochemical and pharmacokinetic studies are still needed to define the mode of action and the range of applications of these vesicles.

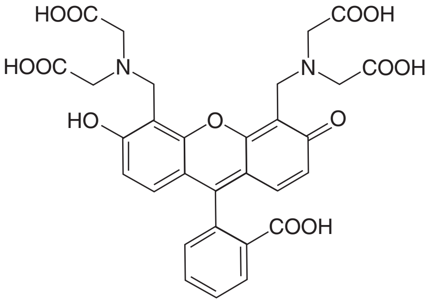

Figure 1 Structure of calcein.

This chapter presents different experimental approaches, based on the use of 4′,5′-bis[*N*,*N*-bis(carboxymethyl) aminomethyl] fluorescein (calcein) as hydrophilic fluorescent marker (Fig. 1), for probing the physicochemical and pharmacokinetic characteristics of deformable vesicles.

Calcein was also considered as a model of low molecular weight, hydrophilic, and polyanionic drug. Importantly, new insights into the mode of action of deformable vesicles were achieved through the determination of calcein encapsulation efficiency and membrane permeability as well as *in vitro* and *in vivo* skin permeation studies.

2. PHYSICOCHEMICAL CHARACTERIZATION OF ULTRADEFORMABLE VESICLES

2.1. Composition and Process of Preparation

Ultradeformable vesicles were made from phosphatidylcholine (PC), sodium cholate, and ethanol, according to Cevc and Blume [5]. PC was either soybean PC (SPC, 95%) or egg yolk PC (EPC, 100%) obtained from Avanti Polar Lipids Inc. and Lipoid GmbH, respectively.

The vesicles were prepared through injection of an ethanolic solution of PC in NaCl 0.15 M and HEPES 0.02 M buffer at pH 7.4 containing sodium cholate and calcein, under stirring at 25 °C. The size of vesicles was calibrated by repeated extrusions through two stacked polycarbonate membranes with pore diameter of 100 mm, as described previously [13].

The formulation used for *in vitro* and *in vivo* skin permeation studies had final concentrations of PC, sodium cholate, and ethanol of 8.8% (w/v), 1.2% (w/v), and 9% (v/v), respectively.

The final concentration of calcein was 0.1 mM for physicochemical studies and 10 or 30 mM for *in vitro* and *in vivo* skin permeation studies.

2.2. Mean Hydrodynamic Diameter and Deformability

Ultradeformable vesicles made from SPC showed a mean hydrodynamic diameter of 90.1 ± 2.9 nm ($n = 11$) and were monodisperse (polydispersity index of 0.073 ± 0.009), as determined by photon correlation spectroscopy. Ultradeformable vesicles made from EPC showed a mean hydrodynamic diameter of 99.9 ± 2.7 nm and a polydispersity index of 0.064 ± 0.008 ($n = 7$).

The high deformability of these vesicles was supported by the observation that extrusion of the suspension through polycarbonate membrane with 30 nm pore size did not change significantly the mean vesicle hydrodynamic diameter. Moreover, the flux of the suspension across the 30 nm polycarbonate membrane was significantly higher than that of a suspension of PC vesicles prepared without sodium cholate. It is also noteworthy that SPC and EPC deformable vesicles did not show significantly different deformabilities (data not shown).

2.3. Encapsulation Efficiency of Calcein: Influence of the Formulation Final Concentration

Two different methods were employed to determine the fraction of encapsulated calcein in ultradeformable vesicles.

The first method used the minicolumn technique [14] based on the purification of liposomes by Sephadex G50 gel filtration without dilution, followed by the fluorometric determination of the amount of calcein associated to the liposome fraction (excitation and emission wavelength of 490 and 515 nm, respectively; Varian spectrofluorimeter, Eclypse).

The second method, as illustrated in Fig. 2, exploited the ability of Co^{2+} ion to form a nonfluorescent complex with calcein [15]. The liposome suspension was first diluted 100-fold in NaCl 0.15 M and HEPES 0.02 M buffer at pH 7.4, and fluorescence intensity was measured before (F_{Total}) and after the addition of $CoCl_2$ (0.18 mM) ($F_{\mathrm{Encapsulated}}$) and Triton X-100 (0.1%, w/v) (F_{Basal}). The encapsulation efficiency was then given by:

$$\text{encapsulation efficiency}(\%) = 100 \times \frac{F_{\mathrm{Encapsulated}} - F_{\mathrm{Basal}}}{F_{\mathrm{Total}} - F_{\mathrm{Basal}}}.$$

The values obtained for calcein encapsulation efficiency in ultradeformable vesicles were 17.5 ± 1.2% ($n = 9$) and 14.4 ± 3.1% ($n = 4$), according to the Co^{2+} and minicolumn methods, respectively.

Since the suspension of ultradeformable vesicles suffers evaporation and becomes more concentrated following a topical application under nonocclusive conditions, an important question to be answered is how this increase in concentration would affect the drug encapsulation efficiency.

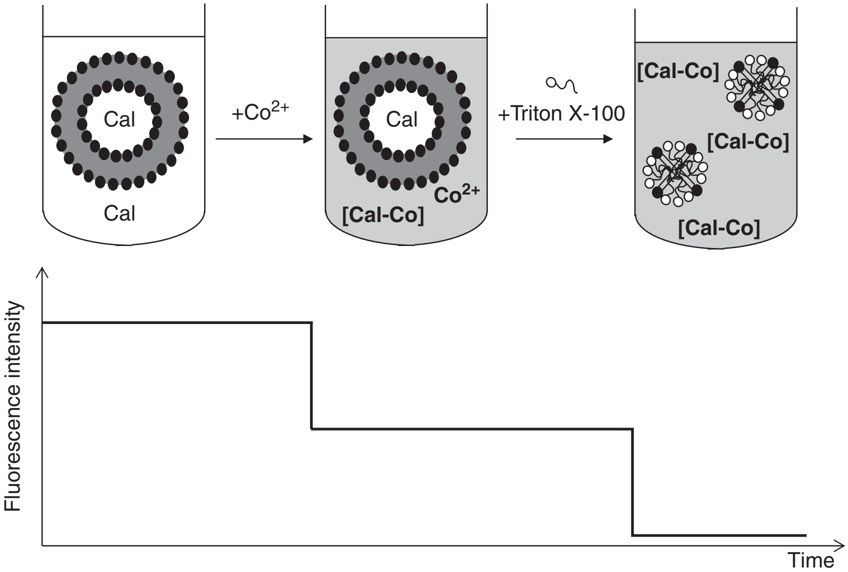

Figure 2 Fluorometric determination of encapsulated calcein (Cal), exploiting the ability of Co^{2+} ion to form a nonfluorescent complex with calcein (Cal-Co).

Two different experiments were performed to address this question. In the first experiment, the suspension of ultradeformable vesicles was prepared with twofold higher concentrations of both cholate and SPC, when compared to the original formulation. In the second experiment, the conventional suspension of ultradeformable vesicles was submitted to evaporation under vacuum, resulting in a threefold volume reduction. In both cases, the change in encapsulation efficiency was evaluated using the Co^{2+} method. The results displayed in Table 1 show that both processes promoted a marked increase of calcein encapsulation efficiency, supporting the model that the drug encapsulation efficiency increases gradually during the drying of the formulation on skin surface.

This interpretation is consistent with a recent report by Cevc *et al.* [8] that the extent of association of the amphiphilic drug ketoprofen with ultradeformable vesicles increased following partial carrier drying. These authors attributed this effect to the drug association to the membrane surface of vesicles. The present study, however, reports for the first time that such phenomenon can also take place in the case of a highly hydrophilic compound.

The model described here also provides an alternative explanation for two previous observations which were claimed to support the permeation enhancer effect of Transfersomes®. As a first observation, ultradeformable liposomes carried not only the entrapped hydrophilic drug model (carboxyfluorescein) into the SC but also the nonentrapped compound [16]. As a

Table 1 Encapsulation efficiencies of calcein in ultradeformable vesicles prepared at different concentrations and with different compositions

Formulation	PC (w/v)	% Encapsulated calcein ± S.D. ($n = 3-9$)
Conventional	8.8% SPC	17.5 ± 1.2
Twofold concentrated	17.6% SPC	35 ± 6
Threefold concentrated[a]	26.4% SPC	43 ± 5
Conventional	8.8% EPC	17.2 ± 1.5

[a] Obtained by evaporation of conventional formulation under vacuum.

second observation, the percentage of 5-fluorouracil permeated through the skin from Transfersomes® was higher than the drug entrapment efficiency in the original formulation [17]. Finally, this phenomenon may also account for the negative impact of occlusive conditions on the effectiveness of Transfersomes® [5,7].

The model that the calcein encapsulation efficiency increases as the suspension of vesicles is submitted to evaporation also assumes that ultradeformable membranes exhibit a high permeability to calcein, allowing for its rapid equilibration across the membrane. To validate this assumption, the membrane permeability of ultradeformable membranes to calcein has been investigated.

2.4. Membrane Permeability to Calcein

The permeability of ultradeformable membrane to calcein was evaluated, as illustrated in Fig. 3, by adding calcein to preformed empty ultradeformable vesicles and evaluating at different time intervals the fraction of encapsulated calcein. The fraction of encapsulated calcein was determined by the Co^{2+} assay, as described in Fig. 2.

Figure 4 shows the kinetics of incorporation of calcein in ultradeformable vesicles at 25 °C, when those were prepared at different cholate/PC ratios or with different phospholipid compositions (EPC or SPC).

Table 2 also summarizes the results obtained with different formulations prepared at different cholate/PC ratios, phospholipid compositions, and concentrations.

Surprisingly, the membrane permeability to calcein of ultradeformable cholate/SPC vesicles, in the original suspension, was so high that it could not be determined experimentally. This high permeability could be attributed to the effect of cholate, since a twofold reduction of its concentration resulted in membranes of very low permeability.

When the total concentration of the formulation was decreased by twofold when compared to original one, while maintaining constant the cholate/SPC

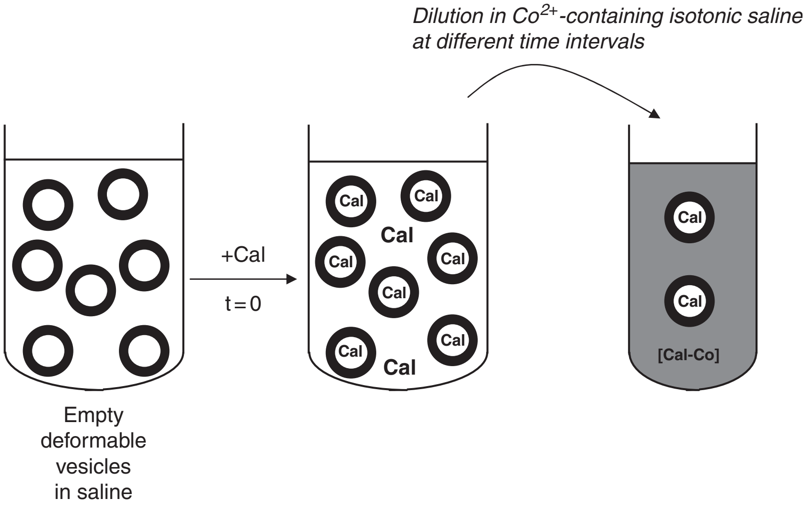

Figure 3 Illustration of the fluorometric method used to determine the kinetic of permeation of calcein (Cal) into ultradeformable vesicles.

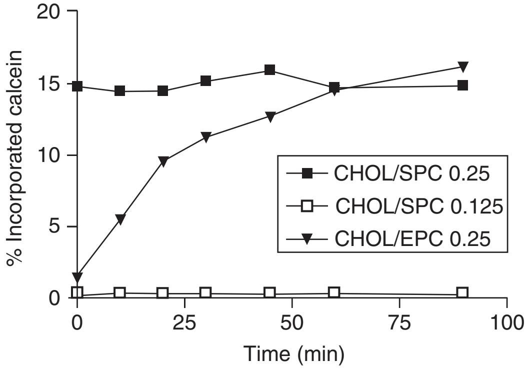

Figure 4 Kinetics of incorporation at 25 °C of 0.1 mM calcein in ultradeformable vesicles of different compositions: sodium cholate/SPC 0.25 (mol/mol), sodium cholate/SPC 0.125 (mol/mol), and sodium cholate/EPC 0.25 (mol/mol). The final PC concentration was 8.8% (w/v).

ratio, ultradeformable membranes exhibited a low permeability to calcein. This is consistent with the observation of Cevc *et al.* [8] that the deformability of the elastic vesicles was reduced following dilution in water.

Interestingly, deformable vesicles made from EPC exhibited a membrane permeability lower than those made from SPC, allowing the determination of permeability coefficient for calcein. It is also noteworthy that a twofold increase of both cholate and EPC concentrations in the formulation

Table 2 Membrane permeability to calcein of ultradeformable vesicles at 25 °C: influence of the cholate/PC ratio, the total lipid concentration and the lipid composition

PC (w/v)	Sodium cholate (w/v)	Cholate/PC (mol/mol)	Permeability coefficient of calcein[a] (cm/s)
8.8% SPC	1.2%	0.25	High
8.8% SPC	0.9%	0.19	High
8.8% SPC	0.6%	0.125	Low
4.4% SPC	0.6%	0.25	Low
8.8% EPC	1.2%	0.25	$1.5 \pm 0.6 \times 10^{-9}$
17.6% EPC	2.4%	0.25	High

[a] "High" means that the permeability coefficient was higher than 25×10^{-9} cm/s; "Low" means that the permeability coefficient was lower than 0.01×10^{-9} cm/s. The permeability coefficient (P) was determined from equation: $\ln[1 - F \times (V_e/V_i)] = -(3P/R)t$, where F is the fraction of encapsulated calcein at time t, V_e is the external aqueous volume of vesicle suspension, V_i is the total internal aqueous volume of the vesicle suspension, and R is mean vesicle radius.

promoted an increase of the membrane permeability to calcein by a factor higher than 15, suggesting that the drying of the formulation would result in even more leaky vesicles.

This data supports the model that the permeability to calcein is influenced by the amount of cholate associated to the vesicle membrane which, in turn, depends on both the dilution and the cholate/PC ratio.

It can be anticipated from this data that the drying of the vesicle suspension on the skin surface may promote an increase of the membrane permeability to calcein and of its encapsulation efficiency. This data also supports the idea that ultradeformable vesicles may be too leaky to act as a true carrier system. On the other hand, the transfer of cholate from the formulation to the SC may occur during the penetration of the formulation within the SC. This phenomenon should result in a change of the vesicle characteristics, those being gradually less deformable and leaky.

3. PHARMACOKINETICS OF CALCEIN FROM ULTRADEFORMABLE VESICLES

3.1. *In Vitro* Skin Permeation of Calcein

In vitro skin permeation of calcein was determined using an open-cap, ground-glass surface, Franz diffusion cells (membrane surface area of 1.77 cm^2 and a receptor fluid volume of 6.7 ml). Full thickness skin was excised from the abdominal surface of hairless mice (HRS/J strain, originally obtained from Jackson Laboratories, Bar Harbor, ME, USA), as described previously [18]. The skin fragments were kept horizontally, dividing the cell into two compartments: the donor and the receiver. The receiver compartment was filled with 5 mM HEPES buffered isotonic saline at pH 7.4. The skin, mounted in the diffusion cell, was allowed to equilibrate with the receptor fluid and the environment for 1 h, in order to maintain an *in vivo* transepidermal hydration gradient which has been proposed as generating the driving force for the skin penetration of deformable vesicles [5]. After this period, the receiver content was totally removed and this compartment was filled with fresh HEPES buffer. The buffered solution was continuously stirred with a small magnetic bar to ensure homogeneity. Experiments were conducted maintaining the skin surface temperature at 32 ± 1 °C, which was achieved by maintaining the receptor phase, by means of cell jackets, at the correct temperature (37 °C).

To simulate the conditions of use, the upper chamber (donor compartment) was left open (nonocclusive conditions) and a dose of the calcein formulation (100 μL at 10 mM calcein) was applied to the skin. The receptor fluid was collected through total removal of the receptor fluid at 2, 4, 6, and 8 h, and refilling of the receiver compartment with fresh isotonic HEPES-buffered saline. The calcein concentration was determined by fluorescence measurement of the receptor fluid at excitation and emission wavelengths of 490 and 515 nm, respectively, and by establishing a calibration curve using the fluid receptor obtained from a control diffusion cell that did not received any formulation.

Figure 5 shows the kinetics of permeation of calcein across hairless mouse skin, when calcein was applied topically either in the form of a suspension of deformable vesicles (CHOL/SPC or CHOL/EPC) or in the form of a solution containing sodium cholate and ethanol at the same concentrations as in the vesicle suspension (CHOL). In the case of all preparations, the flux of calcein was found to be higher during the first 4 h of permeation than on the subsequent 4–8 h period. Whereas CHOL/SPC and CHOL/EPC showed similar kinetics, those differed significantly from that obtained with CHOL ($P < 0.01$, two-way ANOVA). Importantly, the flux of calcein from CHOL was approximately 10-fold higher (on the 0–4-h period) than that from CHOL/SPC and CHOL/EPC. It is also noteworthy that the cumulative amount of transported calcein after 8 h in the receiver compartment was less than 0.4% of the total applied amount in the case of CHOL/SPC and CHOL/EPC and higher than 1.2% in the case of CHOL. This data clearly establishes that the incorporation of PC into the cholate/ethanol formulation, at a proportion that leads to the formation of ultradeformable vesicles, considerably reduces the transcutaneous flux of calcein across mouse skin.

Even though the present data seems contradictory with the classical model that ultradeformable vesicles improve the skin permeation of

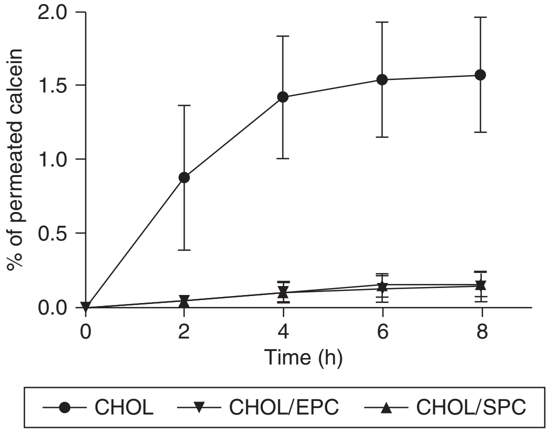

Figure 5 Kinetics of *in vitro* permeation of calcein across hairless mouse skin from different formulations applied topically. CHOL/SPC, 100 μL of deformable sodium cholate/SPC vesicles containing 10 mM calcein; CHOL/EPC, 100 μL of deformable sodium cholate/EPC vesicles containing 10 mM calcein; CHOL, 100 μL of 10 mM calcein solution containing sodium cholate and ethanol. Data are given as the percentages of permeated calcein in relation to the total amount of applied calcein ± S.E.M. ($n = 3$). A significant difference between CHOL and the other groups was detected using two-way ANOVA ($P < 0.01$).

drugs [7], it is consistent with two recent reports from Cevc *et al.* [8] and El Maghraby *et al.* [17] for ketoprofen and 5-fluorouracil, respectively. The transcutaneous flux of ketoprofen was much lower from deformable vesicles than from conventional topical formulations. Ultradeformable vesicles improved the skin deposition of 5-fluorouracil with little or no effect on the drug transcutaneous flux. According to Cevc *et al.* [8], the drying of the formulation of ketoprofen on the skin surface would increase the drug binding to the carrier, resulting in a decrease of the free drug concentration and of its transcutaneous flux.

In the case of the highly hydrophilic and polyanionic calcein, membrane binding is not expected to be favored and one may propose that vesicle encapsulation and retention contributed to the decreased transcutaneous flux. However, since deformable vesicles were found to be leaky for calcein, one should assume that deformable vesicles suffer a maturation process during their migration through the skin layers, consisting of the gradual loss of cholate and resulting decrease of membrane permeability.

Taking into account that both cholate and ethanol are known skin permeation enhancers [19, 20], an alternative explanation for the reduced flux of calcein from deformable vesicle may be that the association of cholate with PC vesicles inhibited the permeation enhancer effect of cholate.

Table 3 Percentage of encapsulated calcein in the receptor fluid (nonaccessible to Co^{2+} ion and released by Triton X-100) at different periods of time, following *in vitro* permeation across hairless mouse skin from different formulations applied topically

	Encapsulation efficiency (%) (mean ± S.D.)	
Formulation	**0–2 h period**	**6–8 h period**
CHOL	0.15 ± 0.21	0.15 ± 0.14
CHOL/SPC	0.33 ± 0.37	0.40 ± 0.38
CHOL/EPC	0.44 ± 0.49	0.10 ± 0.12

In order to address the important question as to whether calcein exists in the free or in the encapsulated form following permeation across the skin, fluorescence measurements of the receptor fluid were performed before and after the addition of $CoCl_2$ and Triton X-100, as described in Fig. 2, such as to determine the fraction of encapsulated calcein. This assay was carried out with the receptor fluids arising from both the early phase (0–2 h) and the late phase (6–8 h) of the kinetics, immediately after being collected. Following the addition of both $CoCl_2$ and Triton X-100, more than 95% of calcein fluorescence was quenched. The mean values of calcein encapsulation efficiency, as displayed in Table 3, were very low, typically less than 1%, and did not differ significantly between the groups, indicating that permeated calcein does not exist in the encapsulated form.

3.2. *In Vivo* Studies of the Transdermal Absorption of Calcein to the Blood Circulation

3.2.1. Validation of fluorometric method for determination of calcein in plasma

The fluorometric method for determination of calcein in plasma was validated according to FDA recommendations for bioanalytical methods (http://www.fda.gov/cder/guidance/4252fnl.htm).

Figure 6 shows the relationship between the fluorescence intensity and the calcein concentration in mouse plasma. The method was found to be linear for plasma concentrations of calcein in the range of 0.022–0.18 μM, showing a linear regression coefficient equal to 0.996.

The following equation was used to determine the plasma calcein concentration from fluorescence intensity:

$$[\text{calcein}](\mu\text{M}) = \frac{\text{fluorescence intensity} - 0.1291}{20.21}.$$

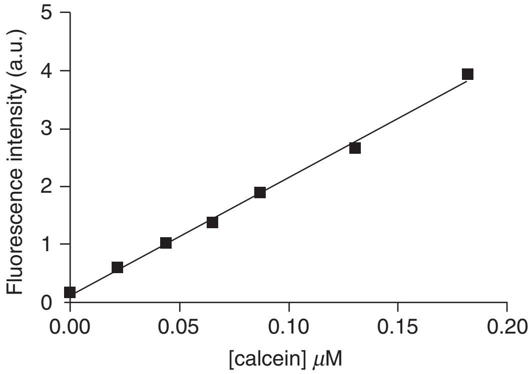

Figure 6 Relationship between fluorescence intensity and calcein concentration in mouse plasma. Calcein was added to mouse plasma at different concentrations (25 μL of calcein solution added to 30 μL plasma). After 1 h of incubation at 37 °C, samples were diluted in NaCl 0.15 M solution and fluorescence intensity was measured at $\lambda_{exc} = 490$ nm and $\lambda_{em} = 515$ nm. Data at each concentration represent the mean fluorescence intensity of seven independent samples.

Table 4 Data related to the precision of the fluorometric method for the determination of calcein in mouse plasma ($n = 7$, at each concentration)

Plasma calcein concentration (μM)	Mean fluorescence intensity (a.u.)	Standard deviation	Relative standard deviation (%)
0.0218	0.608	0.174	28.6
0.0436	1.022	0.144	14.1
0.0654	1.386	0.138	9.9
0.0872	1.887	0.205	10.9
0.1308	2.642	0.248	9.4
0.1817	3.912	0.226	5.8

Table 4 shows the data related to the precision of the fluorometric method for the determination of calcein in mouse plasma. Considering the limit of 15% for the relative standard deviation in bioanalytical methods, one can conclude that the fluorometric method presented here is precise for the determination of calcein in the concentration range of 0.044–0.18 μM.

The lower limit of quantification of the fluorometric method could be estimated as 0.044 μM, since this concentration gave a precision lower than 20% and an analyte response higher than five times the response compared to the blank response.

3.2.2. Pharmacokinetic of calcein in the plasma of hairless mice after topical application

Hairless mice (HRS/J strain) were used in this study. Animals were first anesthetized with a mixture of ketamine hydrochloride (57 mg/kg) and xylazin (8.6 mg/kg) by i.p. route and the dorsal skin was cleaned with distilled water. One hundred microliters of the formulations containing either 10 or 30 mM of calcein were applied in a delimited area of 2.25 cm^2 under nonocclusive conditions. At different time intervals, blood samples (15 μL) were collected from the tail with heparinized tip and diluted in 3 mL of isotonic saline. After homogenization and centrifugation for 5 min at $1000 \times g$ and 4 °C to sediment the red blood cells, supernatants were used for fluorescence measurements at excitation and emission wavelengths of 490 and 515 nm, respectively. In all assays, a calibration curve relating the fluorescence intensity to the plasma calcein concentration was established.

In a first experiment, the ability of a suspension of cholate/SPC deformable vesicles (CHOL/SPC) to promote the absorption of calcein to the blood circulation was compared to that of a solution containing the cholate/ethanol mixture (CHOL) at the same concentrations as those in the vesicle suspension. A control group receiving empty cholate/SPC deformable vesicles was also evaluated. Data are presented in Fig. 7, as (A) the mean fluorescence intensity of diluted plasma ($n = 6$) and (B) the mean plasma calcein concentration, at different time intervals. Importantly, the bioavailability of calcein was found to be significantly lower from CHOL/SPC than from CHOL. One-way ANOVA analysis indicated a significant increase of the fluorescence intensity as a function of time only in the group that received nonencapsulated calcein. Two-way ANOVA analysis of the fluorescence data shows statistically significant differences between the group that received CHOL and those receiving CHOL/SPC and empty CHOL/SPC. Comparison of the plasma calcein concentrations between CHOL/SPC and CHOL groups revealed significant differences at 1, 2, and 4 h postapplication ($P < 0.05$, Student's *t*-test).

The lower absorption of calcein to the blood circulation from deformable vesicles is consistent with the reduced transcutaneous flux of calcein, as evidenced by our *in vitro* permeation study. It is also noteworthy that the higher plasma calcein concentration over the 0–2-h period correlates well with the higher transcutaneous flux of calcein over the 0–4-h period. This data also supports the model that the rate-limiting step for the transdermal delivery of calcein to the blood circulation from both formulations is its passage through the skin.

To evaluate whether the cholate/ethanol mixture, at the concentration used in the deformable vesicle suspension, may act as a skin permeation enhancer for calcein, the transdermal absorption of calcein in HEPES-buffered saline containing cholate/ethanol (CHOL) was compared to that of calcein in the same buffer (Control). As illustrated in Fig. 8A, a significant

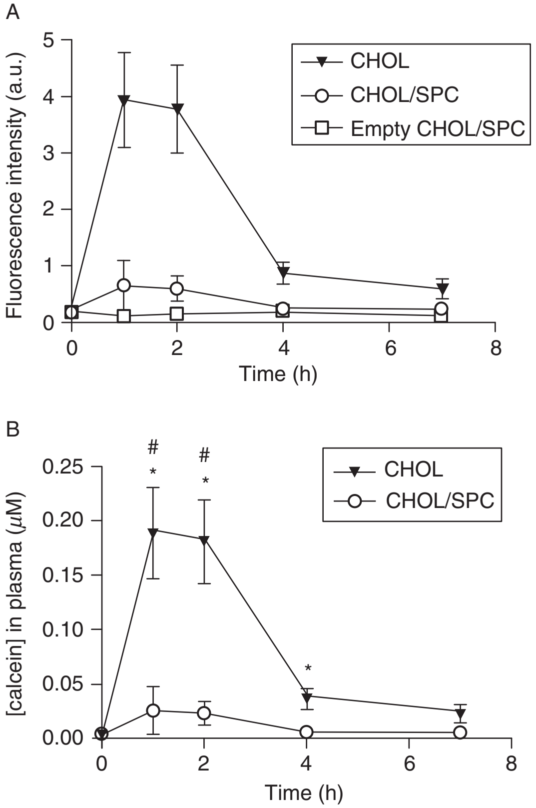

Figure 7 Transdermal absorption of calcein to the blood circulation of hairless mice, as determined fluorimetrically, from different formulations applied topically. CHOL/SPC, 100 µL of sodium cholate/SPC deformable vesicles containing 10 mM calcein; CHOL, 100 µL of 10 mM calcein solution containing sodium cholate and ethanol at the same concentrations as those in deformable vesicles; empty CHOL/SPC, 100 µL of sodium cholate/SPC deformable vesicles prepared in the absence of calcein. Data are presented as (A) mean fluorescence intensities of diluted plasma at $\lambda_{exc} = 490$ nm and $\lambda_{em} = 515$ nm ($n = 6$) and (B) mean calcein concentrations, as a function of time (± S.E.M.). $^{\star}P < 0.05$ for comparison between COL and CHOL/SPC, Student's *t*-test ($n = 5$–6). $^{\#}P < 0.05$ for comparison with the mean value at time zero, one-way ANOVA followed by Dunnett posttest.

increase of calcein bioavailability was observed in the presence of the cholate/ethanol mixture, confirming that this composition acts as skin permeation enhancer.

On the other hand, as shown in Fig. 8B, the transdermal absorption of calcein from CHOL/SPC was still significantly reduced when compared to that from calcein in buffer.

Accordingly, ultradeformable vesicles and cholate micelles exert opposite effects on the transdermal flux of calcein. The latter data also supports

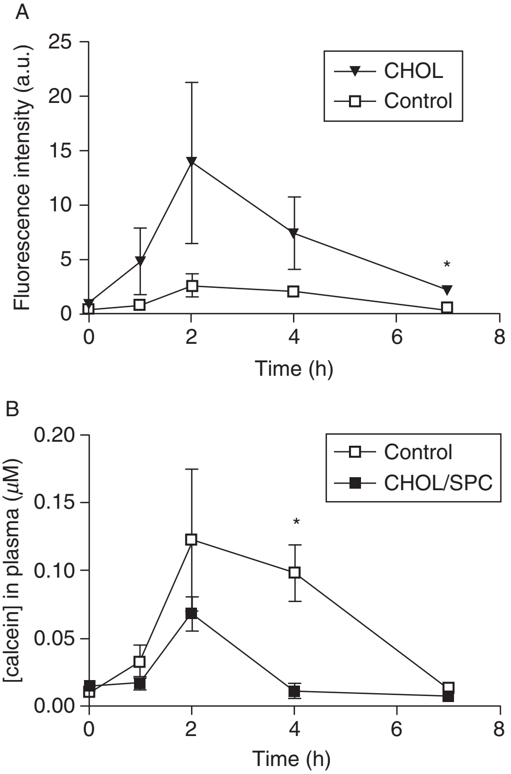

Figure 8 Transdermal absorption of calcein to the blood circulation of hairless mice, as determined fluorimetrically, from different formulations applied topically. (A) CHOL, 100 μL of 30 mM calcein in buffer containing sodium cholate and ethanol at the same concentrations as those in deformable vesicles; Control, 100 μL of 30 mM calcein in buffer. (B) CHOL/SPC, 100 μL of sodium cholate/SPC deformable vesicles containing 30 mM calcein; Control, 100 μL of 30 mM calcein in buffer. Data are presented as (A) mean fluorescence intensities of diluted plasma at $\lambda_{exc} = 490$ nm and $\lambda_{em} = 515$ nm ($n = 3$) and (B) mean plasma calcein concentration (± S.E.M.), as a function of time. $^{\star}P < 0.05$ for comparison with Control using Student's *t*-test.

the idea that the reduction of the transdermal flux of calcein by deformable vesicles cannot be attributed solely to the inhibition of the permeation enhancer effect of the cholate/ethanol mixture.

As an attempt to uncover the occurrence of a late absorption phase of calcein, plasma samples were collected at longer time points. Figure 9 shows the mean fluorescence intensities of diluted plasma 48 h after application of calcein in a suspension of deformable cholate/SPC vesicles, in a solution containing cholate/ethanol and in the HEPES-buffered saline vehicle. Although the values of fluorescence intensity were below to the method quantification limit, those was significantly higher after calcein in

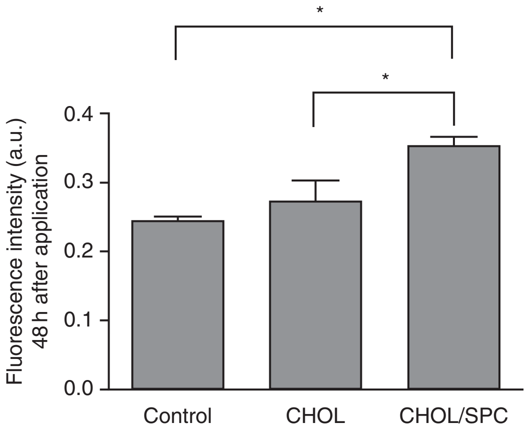

Figure 9 Fluorescence intensities of diluted plasma of hairless mice, 48 h after administration of different formulations of calcein. CHOL, 100 μL of 30 mM calcein in buffer containing sodium cholate and ethanol at the same concentrations as those in deformable vesicles; CHOL/SPC, 100 μL of sodium cholate/SPC deformable vesicles containing 30 mM calcein; Control, 100 μL of 30 mM calcein in buffer. Data are presented as mean fluorescence intensity at $\lambda_{exc} = 490$ nm and $\lambda_{em} = 515$ nm ± S.E.M. ($n = 3$). $^{\star}P < 0.05$, one-way ANOVA, followed by Newman–Keuls multiple comparison.

deformable cholate/SPC vesicles, suggesting the existence of slow absorption phase specifically in the case of this formulation ($P < 0.05$, one-way ANOVA, followed by Newman–Keuls posttest).

In a second set of experiments, the extent of transdermal absorption of calcein from SPC deformable vesicles was compared to that from EPC ones (data not shown). No significant variation of the fluorescence intensity was found in each group, according to one-way ANOVA statistical analysis. Moreover, comparison of fluorescence intensities between the different groups showed no significant difference. One can infer that deformable vesicles made from EPC and SPC exhibit similar properties with respect to their ability to reduce the transdermal flux of calcein to the blood circulation.

4. CONCLUDING REMARKS: NEW MODEL FOR THE MODE OF ACTION OF ULTRADEFORMABLE VESICLES

The experimental approaches presented in this chapter bring new insight into the mode of action of ultradeformable vesicles for transdermal drug delivery.

This work provides, for the first time, information on the membrane permeability of ultradeformable vesicles. Our permeability data indicates that the presence of cholate in deformable vesicles turns the membrane highly permeable to calcein and supports the idea that these vesicles, at least in their original form, are unable to act as a true carrier system. Our data also suggests that the drying of the formulation on the skin surface enhances the drug encapsulation efficiency, a fact that may explain, at least in part, the impact of nonocclusive conditions on the effectiveness of deformable vesicles.

Both *in vivo* and *in vitro* skin permeation studies indicated that deformable vesicles reduced the transdermal flux of calcein, when compared to solutions containing or not a cholate/ethanol mixture. These results are quite surprising in the light of the classical model for deformable vesicles action [7]. In fact, a similar effect of ultradeformable vesicles was recently reported for the amphiphilic drug ketoprofen [8]. However, the present study provides the first clear demonstration that deformable vesicles can reduce the transdermal flux of a hydrophilic compound to the blood circulation. These data also suggest that deformable vesicles promote a sustained release system for calcein. Even though deformable vesicles are initially very leaky for calcein, one can reasonably propose that these vesicles suffer a maturation process during their penetration through the SC, consisting of the gradual loss of cholate and decrease of membrane permeability. Ultimately, these nonleaky vesicles would serve as a slow release depot system, located in the deep layers of the SC, and may be responsible for the late phase of calcein absorption. The proposal of an improved skin deposition of calcein after application with deformable vesicles is supported by the observation by Touitou *et al.* [21] that Ethosomes increased the amount and depth of calcein penetration within the mouse skin, when compared to conventional liposomes and hydroethanolic solution.

Another important contribution of the present work is the report that calcein, following permeation through the skin from deformable vesicles, exists essentially under the nonencapsulated form. This observation argues against the passage of calcein through the SC under the encapsulated form and the model that deformable vesicles would permeate intact through the skin to the blood circulation. Nevertheless, one cannot completely exclude the possibility that vesicles may be released from the skin at a latter stage (time longer than 8 h).

These data taken altogether allow us to propose a new model to the mode of action of deformable vesicles. According to this model, illustrated in Fig. 10 as model 2, the drying of the drug-containing suspension of deformable vesicles on the skin surface would lead to a highly concentrated drug–lipid gel capable of penetrating deeply within the SC. During the migration of the gel through the SC, the gradual transfer of cholate from the gel to the SC would result in less deformable and leaky vesicles which,

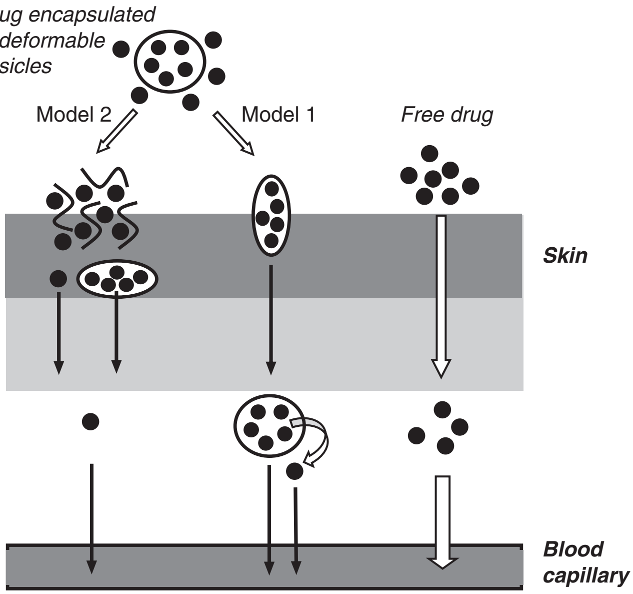

Figure 10 Proposed models for the pathways used by deformable vesicle-associated calcein and free calcein for reaching the blood circulation when applied to the skin. Model 1 represents the classical model proposed by Cevc [7]. Model 2 represents the model supported by our results. The width of the sets is related to the intensity of calcein flux.

ultimately, would accumulate within the deep layers of the SC, where they would act as a slow drug release system. This model differs markedly from the classical model proposed by Cevc *et al.* [7] and illustrated in Fig. 10 as model 1. The main difference is that, according to our model, the drug would be released from the skin in the free form but not in the encapsulated form.

Future studies varying the lipid composition and the total amount of applied formulation should help answering to the question as to whether this model is valid for any deformable vesicles and any dose of formulation. Furthermore, the present work refers to the effect of deformable vesicles on the skin permeation of a highly hydrophilic molecule and it is possible that the mechanism of drug penetration may depend on the physicochemical characteristics of encapsulated compound. Indeed, the effect of deformable vesicles on the transdermal flux of a hydrophilic compound is expected to depend on its molecular weight. In the case of high molecular weight compounds with very low membrane permeability, one may expect an increase rather than a decrease of the transcutaneous flux when applied as deformable vesicles.

ACKNOWLEDGMENTS

We thank Fernanda O. Lemos and Dr. Erly G. Azevedo for technical support in the *in vitro* skin permeation studies and Prof. Dr. Silvia P. Andrade for her valuable technical suggestions for the *in vivo* assay. This research was supported by the Brazilian agencies, CNPq (472032/2004-6, 307726/2006-1, 501181/2007-5) and FAPEMIG (Nanobiotechnology Network, REDE 2825/05, REDE 221/08), and performed by the National Institute of Science and Technology in Nanobiopharmaceutics.

REFERENCES

[1] M. Mezei, V. Gulasekharam, Liposomes—A selective delivery system for the topical route of administration, Life Sci. 26 (1980) 1473–1477.
[2] M. Fresta, G. Puglisi, Application of liposomes as potential cutaneous drug delivery system. *In vitro* and *in vivo* investigation with radioactively labeled vesicles, J. Drug Target. 4 (1996) 95–101.
[3] M. Kirjavainen, A. Urtti, R. Valjakka-koskela, J. Kiesvaara, J Monkkonen, Liposome–skin interactions and their effects on the skin permeation of drugs, Eur. J. Pharm. Sci. 7 (1999) 279–286.
[4] D.D. Verma, S. Verma, G. Blume, A. Fahr, Particle size of liposomes influences dermal delivery of substances into skin, Int. J. Pharm. 258 (2003) 141–151.
[5] G. Cevc, G. Blume, Lipid vesicles penetrate into intact skin owing to the transdermal osmotic gradients and hydration force, Biochim. Biophys. Acta 1104 (1992) 226–232.
[6] E. Touitou, N. Dayan, L. Bergelson, B. Godin, M. Eliaz, Ethosomes-novel vesicular carriers: Characterization and delivery properties, J. Control. Release 65 (2000) 403–418.
[7] G. Cevc, Lipid vesicles and other colloids as drug carriers on the skin, Adv. Drug Deliv. Rev. 56 (2004) 675–711.
[8] G. Cevc, U. Vierl, S. Mazgareanu, Functional characterisation of novel analgesic product based on self-regulating drug carriers, Int. J. Pharm. 360 (2008) 18–28.
[9] B. Godin, E. Touitou, Ethosomes: New prospects in transdermal delivery, Crit. Rev. Ther. Drug Carrier Syst. 20 (2003) 63–102.
[10] G. Cevc, A. Schatzlein, H. Richardsen, Ultradeformable lipid vesicles can penetrate the skin and other semi-permeable barriers unfragmented. Evidence from double label CLSM experiments and direct size measurements, Biochim. Biophys. Acta 1564 (2002) 21–30.
[11] H.A.E. Benson, Transfersomes for transdermal drug delivery, Expert Opin. Drug Deliv. 3 (2006) 1–11.
[12] M.M.A. Elsayed, O.Y. Abdallah, V.F. Naggar, N.M. Khalafallah, Lipid vesicles for skin delivery of drugs: Reviewing three decades of research, Int. J. Pharm. 332 (2007) 1–16.
[13] L.D. Mayer, M.J. Hope, P.R. Cullis, Vesicles of variable sizes produced by rapid extrusion procedure, Biochim. Biophys. Acta 858 (1986) 161–168.
[14] D.W. Fry, J.C. White, I.D. Goldman, Rapid separation of low molecular weight solutes from liposomes without dilution, Anal. Biochem. 90 (1978) 809–815.
[15] D.A. Kendall, R.C. MacDonald, Characterization of a fluorescence assay to monitor changes in the aqueous volume of lipid vesicles, Anal. Biochem. 134 (1983) 26–33.
[16] D.D. Verma, S. Verma, G. Blume, A. Fahr, Liposomes increase skin penetration of entrapped and non-entrapped hydrophilic substances into human skin: A skin penetration and confocal laser scanning microscopy study, Eur. J. Pharm. Biopharm. 55 (2003) 271–277.

[17] G.M.M. El Maghraby, A.C. Williams, B.W. Barry, Skin delivery of 5-fluorouracil from ultradeformable and standard liposomes *in vitro*, J. Pharm. Pharmacol. 53 (2001) 1069–1077.

[18] W. Diembeck, H. Beck, F. Benech-Kieffer, P. Courtellemont, J. Dupuis, W. Lovell, M. Paye, J. Spengler, W. Steiling, Test guidelines for in vitro assessment of dermal absorption and percutaneous penetration of cosmetic ingredients. European Cosmetic, Toiletry and Perfumery Association, Food Chem. Toxicol. 37 (1999) 191–205.

[19] T.M. Borg, Bile salts as skin permeation enhancers, Pharmazeutishe Industrie 62 (2000) 157–160.

[20] B. Berner, P. Liu, Alcohols, in: E.W. Smith, J.I. Maibach (Eds.), Percutaneous Penetration Enhancers CRC Press, Boca Raton, FL, 1995, pp. 45–60.

[21] E. Touitou, B. Godin, N. Dayan, C. Weiss, A. Piliponsky, F. Levi-Schaffer, Intracellular delivery mediated by an ethosomal carrier, Biomaterials 22 (2001) 3052–3059.

CHAPTER FOUR

ELECTRICAL METHODS FOR DETERMINING SURFACE CHARGE DENSITY AND ELECTROLYTE COMPOSITION AT THE LIPID BILAYER-SOLUTION INTERFACE

Derek Laver*

Contents

Abstract

In this chapter I will review electrical methods for inferring the surface potential and surface charge density on lipid bilayers and the electrolyte composition at the bilayer interface. I will review the early studies which measured electrostatic potentials between the bilayer interior and the external solution. These include methods based on ionophores, open circuit potential measurements, the inner field compensation and measurements of the ionic double-layer capacitance. I will then go on to review two methods which I developed for inferring changes in solute concentrations (solution transients) at a bilayer

---

* Corresponding author. Tel.: +61 2 4921 8732; Fax: +61 2 4921 7903;
E-mail address: Derek.Laver@newcastle.edu.au

School of Biomedical Sciences, University of Newcastle, Callaghan, NSW 2308, Australia

Advances in Planar Lipid Bilayers and Liposomes, Volume 9
ISSN 1554-4516, DOI: 10.1016/S1554-4516(09)09004-8

surface during solution changes which also allows simultaneous measurement of single channel activity. These methods (1) use fast solution changes with induce a shift in bilayer potential that can generate a transient, capacitive current through the bilayer under voltage-clamp conditions and (2) use ion channels embedded in the bilayer to sense solute concentrations during solution exchange.

1. INTRODUCTION

The modern concept of cell membrane structure is that membranes are two dimensional, oriented, viscous solutions of proteins and lipids (the fluid mosaic model championed by Singer and Nicolson [1]). In the original formulation of the fluid mosaic model it was believed that, on the whole, the membrane structure is quite fluid in the plane of the membrane while there are ''islands'' of restricted mobility associated with the occurrence of phase separations of membrane components [2, 3]. However, even before the proposal of the fluid mosaic model it was recognized that protein function critically depends on the lipid environment [4]. It is well understood that proper function of membrane proteins relies on the fluidity of the lipid hydrocarbon chains and the chemical residues in the lipid polar heads. Electrostatic charge on the lipid head groups is known to regulate a wide range of biological processes including membrane adhesion, binding of peptides, protein trafficking, and membrane transport [5].

The study of cell membrane structure using artificially produced bilayers as an *in vitro* model began in 1962 with the work of Mueller *et al.* [6]. Though, the significance of such studies was realized much earlier by Langmiur and Waugh [7]. The large area and planar geometry of these structures allowed easy access to the aqueous phases on both sides of the membrane and thus proved to be convenient membrane models in mechanical, electrical, and permeability studies. Basically, the technique of Mueller *et al.* [6] was to disperse the lipid components of the membrane in a hydrophobic solvent and form a film of this solution across a circular support submerged in an aqueous solution. The surface active lipid components form monolayers at each oil–water interface. The hydrophobic solution drains away from between the two monolayers allowing them to form a bilayer. Such model membranes have been extensively used to study the origin of electrostatic potentials on lipid surfaces (surface potentials, see studies cited by Refs. [8, 9]). Several methods have been used to measure surface potential, each probing the electrostatic potential from different parts of the membrane solution interface [10]. Gouy–Chapman theory has been effectively used to understand how surface potentials depend on ion concentration, the presence of charged moieties on the lipid polar heads and the adsorption of hormones, peptides, and drugs to the bilayer surface [8, 11].

MacDonald and Bangham [11] were able to measure the surface potential on a lipid bilayer by rapidly establishing an electrolyte gradient across a membrane held under open circuit conditions. The idea was to induce a change in the surface potential on only one side of the membrane which could be measured as a change in the potential difference between the bulk aqueous phases on each side of the membrane. The rationale for this approach is demonstrated in Fig. 1B. They were able to show that Gouy–Chapman theory was indeed able to account for the magnitude of surface potential and further went on to show that bilayer composition is very similar to the composition of the lipid solutions from which they were generated.

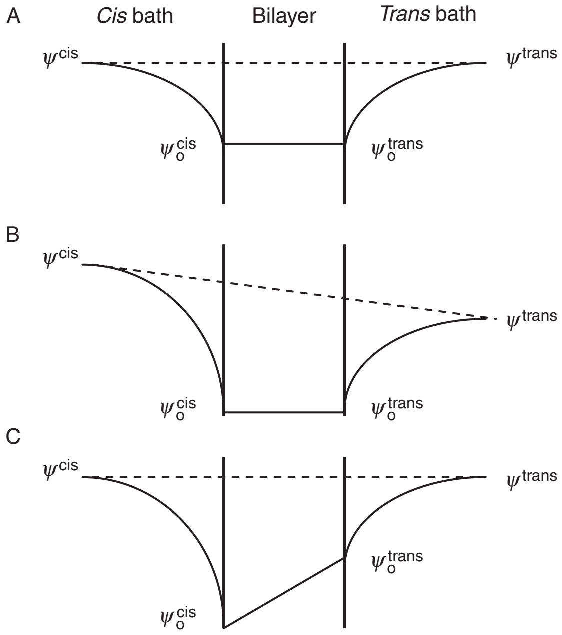

Figure 1 The effect of surface potential on the trans-bilayer potential difference. A hypothetical electrostatic potential profile across an electrolyte–bilayer–electrolyte system. (A) In symmetric solutions the surface potentials ($\Psi_0^{cis} - \Psi^{cis}$and $\Psi_0^{trans} - \Psi^{trans}$) at the bilayer–solution interfaces are equal so that the bilayer potential difference, ($\Psi_0^{cis} - \Psi_0^{trans}$) is equal to the applied potential difference in the bulk solution ($\Psi^{cis} - \Psi^{trans}$). (B) Under open circuit conditions, a change in surface potential on the *cis* side of the bilayer causes a change in the potential difference between the bulk solutions. (C) Under voltage-clamp conditions, a change in surface potential on the *cis* side of the bilayer shifts the bilayer potential difference even though the applied potential between the bulk solutions is unchanged.

Both the capacitance and conductance of lipid bilayers have been used to probe the surface charge on lipid bilayers. McLaughlin *et al.* [12] used the sensitivity of bilayer ion permeability to electrostatic potential within the membrane to measure the surface potential. To this end they developed a model to explain how voltage influences both the partitioning of charged molecules into the bilayer and their rate of transport within the membrane. Several studies [13, 14] used the voltage-dependence of bilayer capacitance to measure bilayer surface potential. These measurements were based on the principle enunciated by Frankenhaeuser and Hodgkin [15], that asymmetric surface potentials cause an offset between the potential difference across the bilayer and the potential difference between the bulk aqueous phases. The mechanism for this is explained in Fig. 1C. The potential difference between the aqueous phases can be directly measured via electrodes in the bulk solution whereas the bilayer potential difference must be measured by other means. For example, one method makes use of the fact that bilayer capacitance is increases as an even power (~2) of voltage [16] because of electrostriction. By adjusting the potential difference applied to the aqueous phases to minimize the bilayer capacitance, one can determine when the bilayer potential difference is zero. Under that condition, the applied voltage is equal to the difference in the surface potentials on each side of the bilayer.

A similar rationale underlay a much improved method which could track rapid changes in bilayer surface potential, referred to as "inner field compensation" [17]. A sinusoidal voltage was applied to the membrane and the second harmonic of the current response indicated the presence of a potential difference across the bilayer. The externally applied DC voltage required to null the second harmonic was used to calculate the bilayer "inner field". This technique made use of the fact that both bilayer capacitance and conductance increases as even powers of membrane potential. Thus, by changing the electrolyte on one side of the bilayer they could calculate the change in the bilayer surface potentials using the same logic as MacDonald and Bangham [11] (see above).

A further step in the development of the method for measuring surface potentials on lipid bilayers came with the observation that a fast change in the ionic composition of the aqueous phase on one side of a lipid bilayer caused the occurrence of a current transient under voltage-clamp conditions [18]. It was realized that this was due to an ion induced change in the surface potential on that side of the membrane. An asymmetric change in surface potential shifts the bilayer potential relative to the voltage-clamp potential and so induces a capacitive current through the bilayer and voltage-clamp system. This method is very similar to that used by MacDonald and Bangham [11] except that the measurement is simplified by using voltage-clamp conditions rather than open circuit.

2. BILAYER CAPACITANCE AS A PROBE FOR BILAYER SURFACE POTENTIAL

Studies of the AC electrical properties of lipid bilayers have obtained values of membrane capacitances ranging from 3 to 8 $\mathrm{mF/m^2}$ depending on bilayer composition. The first accurate measurement of the thickness of a lipid bilayer came from measurements of the membrane capacitance using Eq. (1) [19]:

$$C_\mathrm{m} = \frac{\varepsilon_0 \varepsilon_\mathrm{m}}{\delta} \tag{1}$$

where δ is the membrane thickness and ε_m is the dielectric constant of the region containing the fatty acid chains which is ~2.1 [20]. The effects of ionic double layers on bilayer capacitance were first considered by applying Gouy–Chapman theory to the bilayer water interface [21, 22]. These studies showed that the ionic double layers have a capacitance (C_d) that acts in series with the bilayer capacitance. The capacitance of the double layer depends on the surface potential on the bilayer and is given by:

$$C_\mathrm{d} = \frac{\varepsilon_0 \varepsilon_\mathrm{w}}{\lambda} \cosh\left(\frac{ze\Psi_0}{2kT}\right) \text{which reduces to } C_\mathrm{d} = \frac{\varepsilon_0 \varepsilon_\mathrm{w}}{\lambda} \text{ when } \Psi_0 = 0 \tag{2}$$

The total capacitance of the electrolyte–membrane–electrolyte system is given by

$$\frac{1}{C_\mathrm{T}} = \frac{1}{C_\mathrm{d}} + \frac{2}{C_\mathrm{m}} \tag{3}$$

In effect, the double-layer capacitance is equal to what is expected from a slice of electrolyte on each side of the membrane with a thickness of one "hypothetical" Debye length. The "hypothetical" Debye length here refers to the Debye length of a bulk solution with an ion concentration equal to that present at the membrane surface. Therefore, increasing either the ionic strength of the bath or the surface potential of the bilayer will increase C_d and hence C_T. Consequently the total capacitance of the electrolyte–membrane system increases with ion concentration to an upper limit given by C_m (Fig. 2). These predictions were verified experimentally for neutral bilayers formed from glycerol monooleate [23, 24] and from zwitterionic (dipolar) phosphatidylcholine [25]. Therefore, one should be able

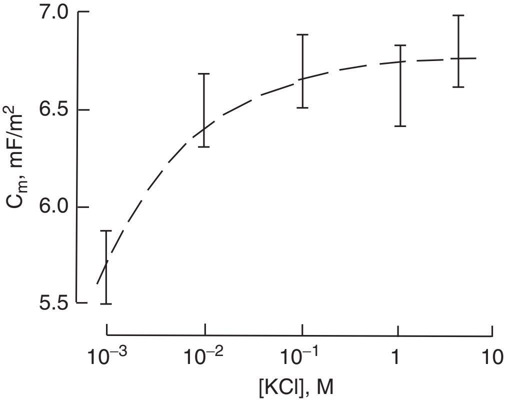

Figure 2 Effect of ionic double layers on bilayer capacitance. The dependence of bilayer capacitance neutral bilayers formed from glycerol monooleate/*n*-hexadecane solutions. The dashed lines show the theoretical dependence expected from a double layer–bilayer–double layer sandwich for the case when $\Psi_0 = 0$ using Eqs. (2) and (3) (after Ref. [24]).

to estimate the absolution value of Ψ_0 under a specific condition by comparing the comparing the bilayer capacitance with the capacitance obtained in the limit of high ionic strength.

3. APPARATUS FOR MEASURING PERFUSION INDUCED CURRENT TRANSIENTS IN LIPID BILAYERS

Bilayers separating two aqueous baths (*cis* and *trans*) were formed from mixtures of palmitoyl-oleoyl-phosphatidylethanolamine (PE), palmitoyl-oleoyl-phosphatidylserine (PS), palmitoyl-oleoyl-phosphatidylcholine, and palmitoyl-oleoyl-phosphatidylinositol-4,5-bisphosphate (PIP_2) in *n*-decane using a modification of the film drainage technique of Mueller *et al.* [6]. Lipids were obtained in chloroform from Avanti Polar Lipids (Alabaster, AL, USA). Bilayers were formed across an aperture of ~100 μm by spreading the lipid solution across the hole using a glass bead (~1 mm diameter) on the end of a flamed pasture pipette. Thinning of the lipid film to a bilayer was monitored visually with 20× magnification and electrically, using measurements of bilayer capacitance. Interference of white light reflecting from both membrane solution interfaces of the bilayer produced colored fringes on the unformed bilayer which vanished upon bilayer formation giving its characteristic “black” appearance. Although spontaneous formation of the bilayer would occur within 5–10 min we found that thinning could be triggered sooner by careful dabbing of the film with a clean glass bead. The bilayer chamber and schematic of the recording apparatus is shown in Fig. 3.

Rapid exchange of solutions at the *cis* face of the bilayer was achieved by puffing solutions from a tube introduced into the *cis* chamber such that it covered the bilayer (Fig. 3). The methods for rapid exchange of solutions at the *cis* face of the bilayer evolved during the course of these studies. Initially solutions were introduced from a single reservoir through a PVC tube to a stainless steel nozzle near the bilayer. Solution flow was initiated by releasing

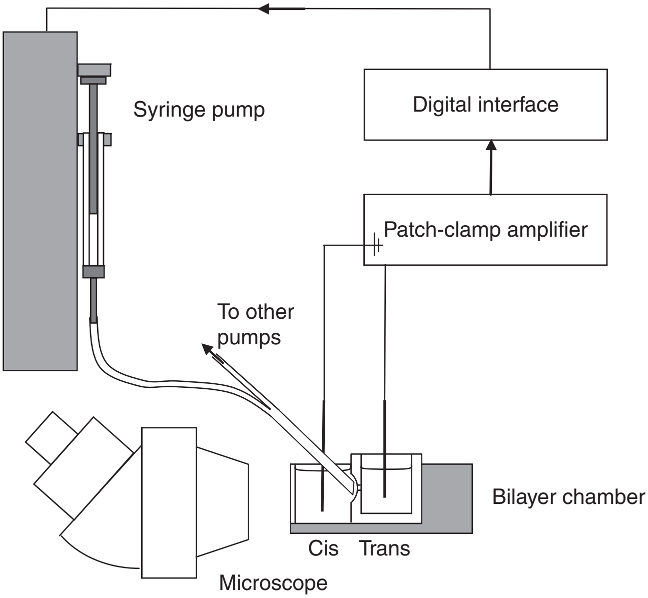

Figure 3 A schematic of the bilayer apparatus. The bilayer chamber consisted of *cis* and *trans* baths separated by a partition on which the bilayer was formed. A Delrin cup formed the inner compartment and contained the *trans* bath. The outer compartment (*cis* bath) was made from either glass or Delrin. A hole formed by spark discharge was punched into the side of the inner chamber to produce the support for the bilayer. The beveled PVC nozzle of the perfusion tube was positioned over the bilayer using a micromanipulator. The nozzle was connected via quartz tubing (300 μm i.d.) and micro manifold (2 μl dead space) to 12, glass syringes with Teflon pistons. The bath partition near the bilayer aperture had a great deal of the lateral wall machined away to provide adequate access for the perfusion tube and flow solution. The bilayer membrane and perfusion tube was viewed under a 10–40× binocular microscope. Electrical connection with the bath was made using silver chloride coated silver wire. The *cis* chamber was electrically grounded to prevent the tubing leading to the flow nozzle, the reservoir and the solution they contained from becoming a source of electrical interference. Voltage was controlled and current recorded with an Axopatch 200A amplifier (Axon Instruments). During the experiments the bilayer current and voltage were recorded at a bandwidth of 5 kHz.

the pinch valve on the flexible PVC tubing. The pinch valve was fitted with a micro switch that allowed a capacitor discharge to be recorded on the voltage recording channel of the recording system to mark the beginning of flow. Solution flow rate was set in the range 1–5 μl/s by adjusting the height of the reservoir above the bilayer chamber. Lower flow rates allowed moderate rates of solution exchange whilst conserving bilayer integrity whereas faster rates were used to achieve rapid solution changes. Recent experiments used more sophisticated apparatus in which perfusion could be switched between twelve reservoirs in random sequence under computer control. Desired flow rates were achieved using a pressure driven syringe injection system (produced in-house).

In some experiments, ion channels were incorporated into bilayers by adding vesicles of sarcoplasmic reticulum membrane from rabbit skeletal muscle to the *cis* bath [26]. Due to the orientation of the vesicles, the cytoplasmic side of the sarcoplasmic reticulum membrane, and the ion channels in that membrane, face the *cis* solution when they fuse with the bilayer [27].

During the experiments the bilayer current and potential were recorded at a bandwidth of 5 kHz. Bilayer capacitance measurements (∼ 5% precision using a two terminal method) were made by measuring the amplitude of the rectangular current response to voltage ramps. Background capacitance attributable to the delrin cup was measured from the capacitance of the cup when the bilayer hole was occluded by a thick lipid/*n*-decane film. Bilayer capacitance (∼200 pF) was calculated by subtracting the background capacitance (∼50 pF) of the thick lipid/*n*-decane film from the total capacitance (∼250 pF) once the bilayer had formed.

4. EXCHANGE OF SOLUTIONS INDUCED BILAYER CURRENT TRANSIENT

Triggering solution changes at the bilayer surface elicited a transient current through the bilayer as shown in Fig. 4. The current depended on the changes in ion concentration in the bath (e.g., changes in [Na^+], [Cs^+], and [Ca^{2+}], see Fig. 4A and B) and it was proportional to the bilayer capacitance (not shown). The current transient was also sensitive to the exchange of ion species at constant ionic strength (Na^+ for Cs^+—Fig. 4B) indicating that it arose, in part, from ion specific (i.e., ion binding at specific sites on the lipids) as well as ionic strength-dependent mechanisms. This phenomenon could not be attributed merely to a mechanical distortion of the bilayer which would induce a microphonic current because it was not present during solutions changes that did not involve changes in ion composition (Fig. 4C and D). The current transient also depended on the

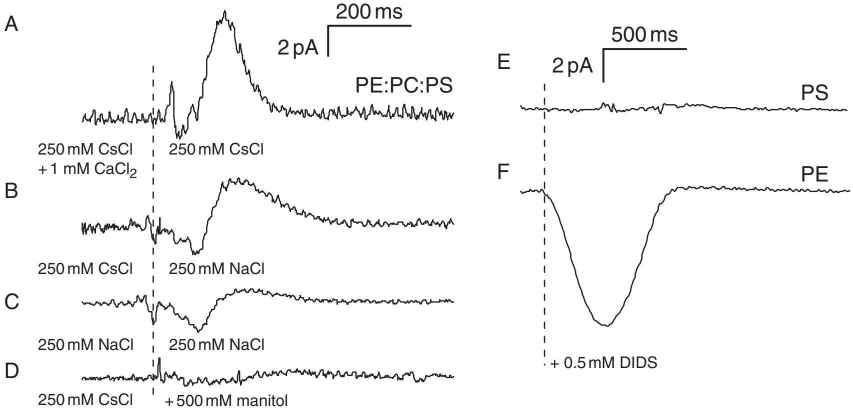

Figure 4 Individual current transients induced by changing the composition of the *cis* bath. Records are filtered at 100 Hz. The solution exchange begins at 200 ms after the beginning of each trace (vertical dashed line). The bath solution (beginning of each trace) is replaced by the perfusion solution during the transient. (A–D; bilayers composed of 30% PS, 20% PC and 50% PE (by weight), data from [18] (A) 250 mM CsCl + 500 mM mannitol replaced 250 mM CsCl. (B) [Ca^{2+}] decreased from 1 mM to 0.1 μM whilst [CsCl] remained at 250 mM. (C) 250 mM NaCl + 0.1 mM $CaCl_2$ replaced 250 mM CsCl + 0.1 mM $CaCl_2$. (D) The same record as in Part (B) except that the flow valve was opened before the 250 mM NaCl from the previous puff had a chance to dilute into the 250 mM CsCl of the *cis* bath. (E, F; data from [33]) (E) Addition of 0.5 mM DIDS in the presence of 250 mM CsCl to bilayers composed of PS or (F) PE.

lipid composition of the bilayers. A striking example of this was found for the divalent anion, diisothiocyanostilbene-2′,2′-di-sulfonic acid (DIDS) which produced a large current transient in bilayer composed of PE but had no effect on bilayers composed of PS (cf. Fig. 4E and F).

The brief spikes near the onset of solution exchange in Fig. 4 probably do arise from acoustic effects (microphonic current) because they were present during all solution changes and did not depend on the composition of the bilayer of bathing solutions. In Fig. 4 the rate of solution exchange was at the high end of the experimental range. The microphonic current was substantially reduced when the rate of perfusion was slowed.

The way in which the current transients depended on changes in ion concentrations suggests that they result from a change in the surface potential on the side of the bilayer facing the nozzle. An asymmetric change in bilayer surface potential shifts the bilayer potential relative to the voltage-clamp potential as previously proposed by others [8, 11]. This change in bilayer potential will induce a capacitive current through the bilayer and voltage-clamp system. We consider the possibilities that the current transients provide information about the bilayer surface potential and the time course of solution exchange at the bilayer surface.

5. DERIVING SURFACE POTENTIAL AND SURFACE CHARGE DENSITY FROM CAPACITIVE CURRENT

A change in the bilayer surface potential by $\Delta\Psi_0$ ($\Delta\Psi_0^{\text{after}} - \Delta\Psi_0^{\text{before}}$) on only one side of the membrane shifts the bilayer potential relative to the voltage-clamp potential by the same amount (Fig. 1). One can calculate the size of this shift from the capacitive current, I and the bilayer capacitance, C, as follows:

$$\Delta\Psi_0 = \frac{1}{C}\int_0^t I\,\mathrm{d}t \tag{4}$$

In other words, the total shift in bilayer potential is equal to the area under the current transient divided by the bilayer capacitance. In most instances the acoustic current was relatively small so that integrating the total current did not incur a significant error in estimates of $\Delta\Psi_0$.

The origin of electrostatic potentials on lipid surfaces has been the subject of many studies and these have been reviewed by McLaughlin [8, 9]. There are at least two ways in which ions in the aqueous baths can alter the bilayer surface potential. Firstly, ions can bind to the head groups of lipids, becoming part of the bilayer and so contribute to the bilayer surface charge density. Competitive binding of alkali metal ions to the polar groups of lecithin has been detected using ^{23}Na NMR spectroscopy [28]. Furthermore, the effects of ion binding have been shown to depend on the chemical nature both the ions and the lipid polar head groups [29]. Secondly ions in the electrolyte will be distributed according to the electric field associated with the surface charge on the bilayer. This has the effect of screening the surface charge and reducing the bilayer surface potential.

Consider competition between two ion species, *a* and *b*, for a lipid head group. The probability that the lipid is bound to *a* is given by

$$P_\mathrm{a} = \frac{K_\mathrm{a} C_\mathrm{a}(0)}{1 + K_\mathrm{a} C_\mathrm{a}(0) + K_\mathrm{b} C_\mathrm{b}(0)} \tag{5}$$

where K and $C(0)$ are the association constants for each ion species and their concentrations at the bilayer surface. The concentrations of ions at the surface are related to their bulk values by

$$C_i(0) = C_i \exp\left[\frac{-z_i e\psi_0}{RT}\right] \tag{6}$$

where z_i are the valences of ion species, i. The net charge on each head group is then given by

$$Q + z_a P_a + z_b P_b \tag{7}$$

For an arbitrary number of ions the surface charge per lipid is given by (each lipid molecule has a net charge of Q):

$$\frac{Q + \sum_i z_i K_i C_i(0)}{1 + \sum_i K_i C_i(0)} \tag{8}$$

Using this approach, McLaughlin [30] derived the surface charge density, σ, for a lipid bilayer composed of negatively charged lipids (PS) and zwitterionic lipids (PC and PE).

$$\sigma = \frac{-P^-[1 - K_2 C^{2+}(0)]}{[1 + K_1 C^+(0) + K_2 C^{2+}(0)]} + \frac{2K_3 P C^{2+}(0)}{[1 + K_3 C^{2+}(0)]} \tag{9}$$

where

$$C^{2+}(0) = C^{2+} \exp\left[\frac{-2e\psi_0}{RT}\right] \tag{10}$$

$$C^+(0) = C^+ \exp\left[\frac{-e\psi_0}{RT}\right] \tag{11}$$

where C^{2+} and C^+ (mol/m^3) are the bulk concentrations of divalent and monovalent cations, respectively, P^- and P are the concentrations (mol/m^2) of negatively charged lipids ($Q = -1$) and zwitterionic lipids ($Q = 0$), respectively. K_1 and K_2 (m^3/mol) are the intrinsic association constants for monovalent and divalent ions to PS head groups. K_3 is the association constant for divalent cations and the headgroups of PE and PC. The values of K_1, K_2, and K_3 have been determined from electrophoresis studies [30] and their values are given in the caption of Fig. 5.

As previously stated, mobile ions in the bath screen the bilayer surface charge and affect the surface potential. The Grahame [31] equation (Eq. (12)) relates the surface charge density to the surface potential:

$$\sigma = \pm\left\{2\varepsilon_r\varepsilon_0 RT \sum_i C_i \left[\exp\left(\frac{-z_i F\psi_0}{RT}\right) - 1\right]\right\}^{1/2} \tag{12}$$

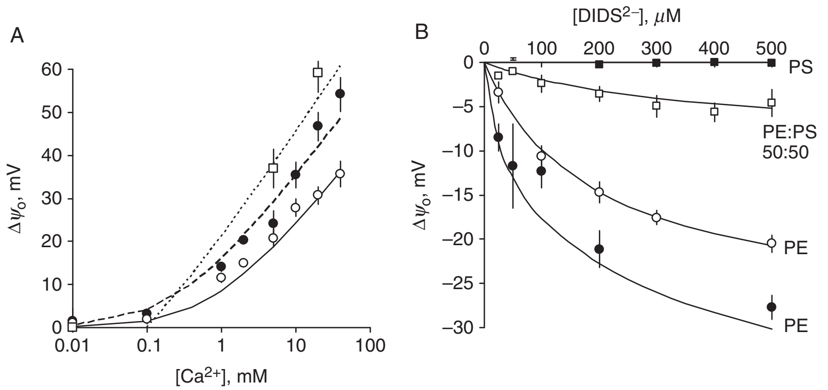

Figure 5 Measured changes in surface potential $\Delta\psi_0$ compared with Gouy–Chapman theory. $\Delta\psi_0$ at the *cis* bilayer surface in response to electrolyte substitution in the *cis* bath, shown as $\Psi_0^{\text{before}} - \Psi_0^{\text{after}}$ (symbols, mean of at least three measurements). (A) $\Delta\psi_0$ values, calculated from the capacitive transients induced by solution changes in which Ca^{2+} was rapidly removed flowing nominally Ca^{2+} free solutions (i.e., containing ~1 μM for circles and ~100 μM for squares). The circles show the data obtained from bilayers composed of 30% PS, 20% PC, and 50% PE (by weight) and the squares show data from 100% PS bilayers. The lines show theoretical predictions using Eqs. (9)–(12). (●) $\Delta[Ca^{2+}]$ in the presence of 250 mM CsCl. (cf. dashed line). (○) $\Delta[Ca^{2+}]$ in the presence of 500 mM CsCl. (cf. solid line) (□) Δ $[Ca^{2+}]$ in the presence of 500 mM CsCl. The model parameters are those determined by McLaughlin *et al.* (1981). $K_1 = 5 \times 10^{-5}$, $K_2 = 1.2 \times 10^{-2}$, $K_3 = 3 \times 10^{-3}$. Lipid concentrations P^- and P were calculated from the lipid weight-fraction multiplied by 2.28×10^{-6}. (B) $\Delta\psi_0$ upon rapid application of DIDS to bilayers containing only zwitterionic lipids (PE, ○, ●) and those also containing negatively charged bilayers (PS, □, ■). In the presence of 250 mM CsCl, the surface potentials generated by application of DIDS are smaller than those in the presence of 25 mM CsCl. Bilayers composed of PS had reduced response to DIDS application suggesting that DIDS does not bind to PS. The model parameters from part A were used and in addition the following parameters were determined from fits of Eqs. (12)–(16) to the data (curves). The association constant for DIDS, $K_4 = 5$ m^3/mol and $F = 0.077$.

In the case of a binary, monovalent electrolyte this reduces to the well known Gouy equation. Both equations for surface charge (Eqs. (9) and (12)) can be solved numerically to give the bilayer surface potential under various experimental conditions and so calculate the voltage shifts, $\Delta\Psi_0$, that occur when solutions are changed.

To test the utility of the capacitive current method for determining $\Delta\Psi_0$, we compared these measured values to those predicted by solving Eqs. (9)–(12). It is noteworthy that theoretical predictions are based on parameters that have been measured independently and do not involve any adjustable parameters. Figure 5A shows $\Delta\Psi_0$ obtained when Ca^{2+} was removed from the solution bathing the *cis* side of bilayers composed of PS, PC, and PE (data from Laver and Curtis [18]). Ca^{2+} was added to solutions with ionic strengths of 250 mM (●, □) or 500 mM (○) and the experimental determination of $\Delta\Psi_0$ was in good agreement with predictions of the theory.

We also investigated the binding of stilbene derivatives such as DIDS for which the binding parameters had not been previously determined. Stilbene derivatives are well known blockers of anion channels [32] and agonists for cation channels such as the calcium release channel from the sarcoplasmic reticulum of muscle [33]. In fact, it was during experiments measuring the effects of these compounds on ion channels that it was first apparent that stilbene derivatives bind to lipid bilayers. Addition of DIDS to the *cis* solution causes a substantial capacitive transient in bilayers composed of zwitterionic lipids (PE and PC, Fig. 4F). This occurred even when the DIDS concentration (~100–500 μM) was much less than the ionic strength of the bath (250 mM). At these low concentrations, DIDS will not contribute significantly to charge screening so $\Delta\Psi_0$ is likely to be due to a change in surface charge as a result of the adsorption of DIDS to the bilayer surface. The presence of negative charged lipids in the bilayer could completely abolish the capacitive currents indicating that these negative charges repel DIDS from the bilayer (Figs. 4E and 5B). The effects of DIDS application on surface potential is shown in Fig. 5B where it can be seen that the dependence of $\Delta\Psi_0$ on [DIDS] is markedly sub linear. The ability of 50% and 100% mole fractions of PS in bilayer the to decrease $\Delta\Psi_0$ induced by DIDS is shown in the presence of 250 mM CsCl. Decreasing the ionic strength increased $\Delta\Psi_0$ induced by DIDS as would be expected from Gouy–Chapman theory.

Equation (8) was applied to model the experimental situation with DIDS. In order to fit the data it was necessary to assume that DIDS only bound to a fraction, *F*, of the PE and PC lipid head groups. DIDS is a large molecule compared to the polar heads of the lipids so that it is possible that steric hindrances prevent DIDS from binding to every lipid. Equation (13) relates the surface charge density, σ, to the bilayer and bath composition:

$$\sigma = \frac{-P^{-}[1 - K_2C^{2+}(0)]}{[1 + K_1C^{+}(0) + K_2C^{2+}(0)]} + \frac{2FP[K_3C^{2+}(0) - K_4C^{2-}(0)]}{[1 + K_3C^{2+}(0) + K_4C^{2-}(0)]} + \frac{2[1 - F]PK_3C^{2+}(0)}{[1 + K_3C^{2+}(0)]} \quad (13)$$

where

$$C^{2+}(0) = C^{2+}\exp\left[\frac{-2e\psi_0}{RT}\right]$$

$$C^{+}(0) = C^{+}\exp\left[\frac{-e\psi_0}{RT}\right]$$

$$C^{2-}(0) = C^{2-}\exp\left[\frac{2e\psi_0}{RT}\right]$$

C^{2-} is the concentration of DIDS and K_4 is its association constants with PE and PC. The first term in Eq. (13) predicts the surface charge arising from the binding of Ca^{2+} to PS in competition with Cs^+. The second term predicts the charge from competitive binding of DIDS and Ca^{2+} to the fraction, F, of PE or PC head groups. The last term shows the charge contribution from Ca^{2+} binding to the fraction of neutral lipids that do not bind DIDS. The theory could fit the data very well when the association constant for DIDS, $K_4 = 5$ m^3/mol and $F = 0.077$. The value for F indicates that DIDS can only bind to ~8% of the available lipid head groups. The fits to the data are shown as solid curves in Fig. 5B.

6. BILAYER CAPACITIVE CURRENTS CAN BE USED TO MONITOR SOLUTION EXCHANGE

By examining Eq. (4) one can see how the capacitive current transient can be used to derive the time course of $\Delta\Psi_0$ and hence infer the time course of the ion concentrations at the bilayer surface. The accuracy of the capacitive current method for monitoring solution changes was tested by comparing the $[Cs^+]$ time course predicted by this method with that obtained independently from the Cs^+ current through a calcium release channel from the sarcoplasmic reticulum of rabbit skeletal muscle. In the experiment, shown in Fig. 6A, a calcium release channel was incorporated into a lipid bilayer as described above. The CsCl concentration in the *cis* bath was lowered from 500 to 100 mM over a period of 500 ms. The channel is well suited to sense the local $[Cs^+]$ because the unitary current through the channel has a linear dependence on $[Cs^+]$ between 100 and 500 mM at an applied voltage of 40 mV. Thus, the channel is being used as a biosensor for the local $[Cs^+]$ in the *cis* bath. Channel openings are seen as upward current steps from the baseline and during the solution exchange the channel current decreases. Figure 6B shows the time course of $[Cs^+]$ calculated from the channel current amplitude (■). The capacitive current induced by the solution change is seen as a negative deflection in the channel baseline current. Equation (4) was used to calculate $\Delta\Psi_0(t)$ and Eqs. (8)–(12) were used to infer $[Cs^+]$ using the parameters for monovalent ion binding to the bilayer listed in the caption to Fig. 5. Figure 6B shows the time course of $[Cs^+]$ calculated from the integral of the current transient is not significantly different to that determined from the channel Cs^+ current.

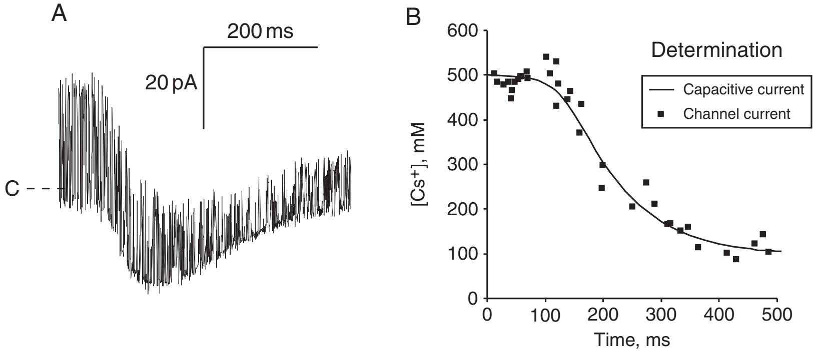

Figure 6 Tracking solution composition during perfusion using capacitive current and ion channels as biosensors. The effect of a rapid reduction of *cis* [Cs^+] from 500 to 100 mM on a bilayer (30% PS, 20% PC, and 50% PE) containing one sarcoplasmic reticulum, calcium release channel from skeletal muscle. The channel was activated by the presence of 100 μM Ca^{2+} in the *cis* bath which was present throughout the solution exchange. The bilayer potential was clamped at +40 mV and channel openings are seen as upward steps. The *trans* bath contained 50 mM CsCl plus 100 μM $CaCl_2$. (A) The dashed line labeled "C" indicates the level of the current baseline and the RyR closed state prior to the solution change. At time = 0 (time scale shown in part (B)) the flow valve was opened. The first sign of a baseline shift (capacitive current) and the onset of solution exchange are seen at time = 80 ms. During the solution change the channel current is reduced. (B) The time course of [Cs^+] inferred from the data in "A" using two independent approaches. (■) [Cs^+] time course predicted from the linear relationship between the RyR current and *cis* [Cs^+] under these experimental conditions. (Solid line) [Cs^+] time course predicted from the capacitive current induced by the solution change using Eqs. (9)–(12) (figure from Ref. [18]).

7. BILAYER CAPACITIVE CURRENTS CAN BE USED TO MONITOR CHANGES IN LIPID COMPOSITION

A number of important biological processes involve chemical modification of the lipids in the cell membrane. Inositol trisphosphate (IP_3) is intracellular second messenger molecule that triggers a wide range of Ca^{2+} signaling events in the cytoplasm. It is liberated from the membrane as a result of cleavage of the head group of phosphatidylinositol-4,5-bisphosphate (PIP_2) by the enzyme, phospholipase C (PLC). This reaction converts the negative lipid, PIP_2 to a neutral lipid called diacylglycerol (DAG). Therefore, one would expect to be able to change the surface charge density of bilayer composed of PIP_2 by exposing them to PLC. To see if such a process would cause a detectable capacitive current, PLC (10 μg/ml) was applied to bilayers composed of PIP_2 (30%), PS (20%), and PC (50%). PLC was added to the perfusing solution and was repeatedly applied to bilayers for periods lasting 8–15 s. Between each application the perfusion was stopped and the PLC was permitted to dilute into the *cis* bath. Three such experiments are shown in Fig. 7. The control experiment in Fig. 7A shows the current induced by PLC in bilayers that did not contain PIP_2 (the bars show periods of application). There were current peaks that coincided with application and removal of PLC but there was no current that correlated with the sustained presence of PLC during perfusion. In Fig. 7(B and C), two experiments are shown in which PLC was added to bilayer containing PIP_2. The application and withdrawal of PLC produced pronounced capacitive transients which presumably come from binding of PLC to the lipid bilayer since PLC was the only component that differed between the perfusion and bath solutions. What was also clear from these experiments was a sustained, 0.2 pA current that correlated with the presence of PLC at the bilayer surface. This current corresponds to a decrement of 1 mV/s in Ψ_0 which in turn equated to a loss of negatively charged lipids at a rate of ~ 1%/s.

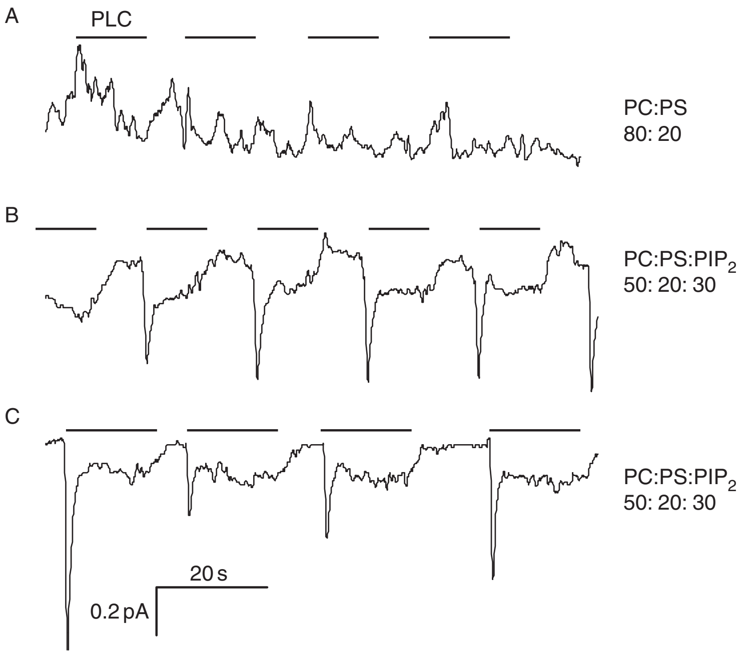

Figure 7 Changes in bilayer lipid composition during enzymatic treatment. Recordings of bilayer current during intermittent perfusion of the bilayers with solutions containing PLC (indicated by the horizontal bars). The *cis* bath solution contained 250 mM CsCl and the perfusing solution contained the same plus 10 μg/ml PLC. Bilayers were formed from solutions containing (A) PC and PS (80:20), (B, C) PC, PS, and PIP2 (50:20:30).

8. CONCLUSIONS

An electrical method for inferring rapid changes in the concentrations of bilayer surface charge and electrolyte concentrations was evaluated in the context of previous developments by other laboratories. Changes in surface potential were detected by the capacitive current they induced under voltage-clamp conditions. Using the ion binding properties of the bilayer lipids previously determined from electrophoresis experiments by McLaughlin [30], and the use of Gouy–Chapman theory it was possible to get a very close agreement between experimental and theoretical estimates of surface potential under a range of ionic conditions. These indicate that capacitive currents induced by changing the electrolyte composition on one side of the membrane is indeed suitable a method for obtaining $\Delta\Psi_0$. The capacitive transient method for predicting ion concentrations at the bilayer surface was cross checked with another method using the conductance of an ion channel to sense the concentration of conducting ions. The surprisingly good agreement between these two methods again indicates that bilayer capacitive current can be used to monitor solution exchange as the bilayer surface.

It appears that capacitive currents can be used to detect catalysis of lipid polar heads. However, the current induced by this process are extremely small and this limits the use of the methods for this purpose. The capacitive current method is better suited to situations where changes in the bilayer surface charge are rapid. For long-term effects such as lipid catalysis it would be better to measure bilayer voltage using the IFC method which has been successfully used to track the surface charge on PC bilayers under the action of phospholipase A_2 [34].

ACKNOWLEDGMENTS

I thank Ms. Katherine Bradley and Drs. Bonny Honen and Brian Curtis for assisting with the experiments. Derek Laver was supported by a Senior Brawn Fellowship from the University of Newcastle and by infrastructure grant from NSW Health through Hunter Medical Research Institute.

REFERENCES

[1] S.J. Singer, G.L. Nicolson, The fluid mosaic model of the structure of cell membranes, Science 175 (1972) 720.
[2] M. Edidin, Rotational and translational diffusion in membranes, Annu. Rev. Biophys. Bioeng. 3 (1974) 179.

[3] G.L. Nicolson, Transmembrane control of the receptors on normal and tumor cells. I. Cytoplasmic influence over surface components, Biochim. Biophys. Acta 457 (1976) 57.

[4] D.J. Triggle, A comment on "A Generalized Functional Role for Phospholipids", J. Theor. Biol. 25 (1969) 499.

[5] M. Langner, K. Kubica, The electrostatics of lipid surfaces, Chem. Phys. Lipids 101 (1999) 3.

[6] P. Mueller, D.O. Rudin, H.T. Tien, W.C. Westcott, Reconstitution of cell membrane structure *in vitro* and its transformation into an excitable system, Nature 194 (1962) 979.

[7] I. Langmiur, D.F. Waugh, The adsorption of proteins at oil-water interfaces and artificial protein-lipoid membranes, J. Gen. Physiol. 21 (1938) 745.

[8] S. McLaughlin, Electrostatic potentials at membrane—Solution interfaces, Curr. Top. Membr. 9 (1977) 71.

[9] S. McLaughlin, The electrostatic properties of membranes, Annu. Rev. Biophys. Biophys. Chem. 18 (1989) 113.

[10] V. Sokolov, V. Cherny, M.V. Simonova, V. Markin, Electrical potential distribution over the bilayer lipid membrane due to amphiphilic ion adsorption, Bioelectrochem. Bioenerg. 23 (1990) 27.

[11] R.C. MacDonald, A.D. Bangham, Comparison of double layer potentials in lipid monolayers and lipid bilayer membranes, J. Membr. Biol. 7 (1972) 29.

[12] S.G. McLaughlin, G. Szabo, G. Eisenman, S.M. Ciani, Surface charge and the conductance of phospholipid membranes, Proc. Natl. Acad. Sci. USA 67 (1970) 1268.

[13] O. Alvarez, R. Latorre, Voltage-dependent capacitance in lipid bilayers made from monolayers, Biophys. J. 21 (1978) 1.

[14] P. Schoch, D.F. Sargent, R. Schwyzer, Capacitance and conductance as tools for the measurement of asymmetric surface potentials and energy barriers of lipid bilayer membranes, J. Membr. Biol. 46 (1979) 71.

[15] B. Frankenhaeuser, A.L. Hodgkin, The action of calcium on the electrical properties of squid axons, J. Physiol. (Lond.) 137 (1957) 218.

[16] S.H. White, A study of lipid bilayer membrane stability using precise measurements of specific capacitance, Biophys. J. 10 (1970) 1127.

[17] V. Cherny, V. Sokolov, I. Abidor, 330-Determnination of surface change of bilayer lipid membranes, Bioelectrochem. Bioenerg. 7 (1980) 413.

[18] D.R. Laver, B.A. Curtis, Surface potentials measure ion concentrations near lipid bilayers during rapid solution changes, Biophys. J. 71 (1996) 722.

[19] T. Hanai, D.A. Haydon, J.L. Taylor, A investigation by electrical methods of lecithin-in-hydrocarbon films in aqueous solution, Proc. R. Soc. Lond. 281 (1964) 337.

[20] W. Huang, D.G. Levitt, Theoretical calculation of the dielectric constant of a bilayer membrane, Biophys. J. 17 (1977) 111.

[21] P. Lauger, W. Lesslauer, E. Marti, J. Richter, Electrical properties of bimolecular phospholipid membranes, Biochim. Biophys. Acta 135 (1967) 20.

[22] C.T. Everitt, D.A. Haydon, Electrical capacitance of a lipid membrane separating two aqueous phases, J. Theor. Biol. 18 (1968) 371.

[23] S.H. White, The surface charge and double layers of thin lipid films formed from neutral lipids, Biochim. Biophys. Acta 323 (1973) 343.

[24] D.R. Laver, J.R. Smith, H.G.L. Coster, The thickness of the hydrophobic and polar regions of glycerol monooleate bilayers determined from the frequency-dependence of bilayer capacitance, Biochem. Biophys. Acta 772 (1984) 1.

[25] H.G. Coster, J.R. Smith, The molecular organisation of bimolecular lipid membranes. A study of the low frequency Maxwell-Wagner impedance dispersion, Biochim. Biophys. Acta 373 (1974) 151.

[26] D.R. Laver, L.D. Roden, G.P. Ahern, K.R. Eager, P.R. Junankar, A.F. Dulhunty, Cytoplasmic Ca^{2+} inhibits the ryanodine receptor from cardiac muscle, J. Memb. Biol. 147 (1995) 7–22.

[27] C. Miller, E. Racker, Ca^{++}-induced fusion of fragmented sarcoplasmic reticulum with artificial planar bilayers, Cell 9 (1976) 283.

[28] N.O. Persson, G. Lindblom, B. Lindman, Deuteron and sodium-23 NMR studies of lecithin mesophases, Chem. Phys. Lipids. 12 (1974) 261.

[29] M.M. Sacre, J.F. Tocanne, Importance of glycerol and fatty acid residues on the ionic properties of phosphatidylglycerols at the air-water interface, Chem. Phys. Lipids 18 (1977) 334.

[30] S. McLaughlin, N. Mulrine, T. Gresalfi, G. Vaio, A. McLaughlin, Adsorption of divalent cations to bilayer membranes containing phosphatidylserine, J. Gen. Physiol. 77 (1981) 445.

[31] D.C. Grahame, The electrical double layer and the theory of electrocapillarity, Chem. Rev. 41 (1947) 441.

[32] D.R. Laver, K.M. Bradley, Disulfonic stilbene permeation and block of the anion channel from the sarcoplasmic reticulum of rabbit skeletal muscle, Am. J. Physiol. Cell Physiol. 290 (2006) C1666.

[33] E.R. O'Neill, M.M. Sakowska, D.R. Laver, Regulation of the Calcium Release Channel from Skeletal Muscle by Suramin and the Disulfonated Stilbene Derivatives DIDS, DBDS, and DNDS, Biophys. J. 84 (2003) 1674.

[34] V. Cherny, M.G. Sikharulidze, V. Mirsky, V. Sokolov, Potential distribution on the lipid bilayer membrane due to the phospholipase A2 actvity, Biol. Membr. 6 (1993) 971.

CHAPTER FIVE

MICROPATTERNED LIPID BILAYER MEMBRANES ON SOLID SUBSTRATES

Kenichi Morigaki*

Contents

Abstract

Micropatterned phospholipid bilayers on solid substrates offer an attractive platform for various applications, such as high throughput drug screening. We have developed a photopolymerization-based methodology for generating micropatterned bilayers composed of polymerized and fluid lipid bilayers. The polymeric bilayer acts as a framework that supports embedded lipid membranes with defined boundaries. The embedded lipid membranes, on the other hand, retain some important characteristics of the biological membrane such as fluidity, and are used as a model system. The fact that polymeric and fluid bilayers are integrated as a continuous bilayer membrane gives various unique features to the model membrane. For example, enhanced incorporation of fluid bilayers by preformed polymeric bilayer scaffold was observed. The lateral mobility of membrane-associated molecules could also be modulated by

---

* Corresponding author. Tel.: +81 727 514 142; Fax: +81 727 519 628;
E-mail address: morigaki-kenichi@aist.go.jp

Research Institute for Cell Engineering, National Institute of Advanced Industrial Science and Technology (AIST), Ikeda 563-8577, Japan

Advances in Planar Lipid Bilayers and Liposomes, Volume 9
ISSN 1554-4516, DOI: 10.1016/S1554-4516(09)09005-X

controlling the composition of polymeric and fluid bilayers, resembling the obstructed lateral diffusion in cellular membranes. Owing to these features, micropatterned composite membranes of polymeric and fluid lipid bilayers provide a versatile platform for constructing complex model systems of the biological membrane, which should be useful for basic biophysical studies as well as biomedical applications.

1. INTRODUCTION

1.1. Substrate-Supported Planar Lipid Bilayers

Artificial model membranes have a long history of playing important roles in the development of our understanding on the structure and function of the biological membrane [1–4]. Various types of model systems have been developed, including Langmuir monolayers, planar bilayers (black lipid membranes), liposomes (lipid vesicles), and substrate-supported planar bilayers (SPBs). SPBs are a relatively new type of model membranes introduced in the 1980s [5–7]. They typically comprise a single lipid bilayer adsorbed on the solid surface by physical interactions or chemical bonds. The lipid bilayer is trapped in the vicinity of the surface by colloidal interactions with an estimated separation of about 10 Å [8]. The presence of a water layer ensures lateral mobility of lipid molecules in the bilayer (fluidity), which is an important property of the biological membrane [7].

SPBs have some unique features compared with other formats of model membranes. First, they are mechanically stable due to the fact that the membrane is supported by a solid surface (in contrast to free-standing black lipid membranes). Second, there are various optical and electrochemical analytical techniques that can detect interfacial events with an extremely high sensitivity, such as surface plasmon resonance (SPR) and quartz crystal microbalance with dissipation monitoring (QCM-D) [9–12]. These features render SPBs highly attractive for the development of devices that utilize artificially mimicked cellular functions [7, 13]. One pertinent shortcoming of SPBs is, however, their inherent limited stability. Possible pathways to improve the stability include the use of self-assembled monolayers [14], tethered lipopolymers to the surface [15–17], and polymerizable lipids [2, 18, 19].

1.2. Micropatterning Substrate-Supported Planar Lipid Bilayers

One important feature of SPBs is the potential to generate micropatterned membranes on the substrate by utilizing various microfabrication techniques. As mentioned above, lipid molecules diffuse laterally in SPBs. Therefore, all components are randomly mixed in continuous SPBs, unless there is a spontaneous phase separation in the lipid membrane. However, one could also block mixing by imposing various types of diffusion barriers to the membrane, as pioneered by the group of S.G. Boxer [20, 21]. The separation of SPBs into distinct areas allows the creation of designed microarrays of model membranes and should facilitate various new applications, such as high throughput drug screening [22]. There have been several micropatterning approaches reported to date. Developed methods are summarized chronologically in Table 1. Some examples of patterning methods are schematically depicted in Fig. 1. The patterning principles can be categorized into three types. The first type is spatially controlled deposition or removal of lipid membranes. This approach includes the use of mechanical scratching [23], microcontact-printing [24, 25], microfluidics [26–28], micropipettes [29], scanning probe microscope tips [30–32], inkjet printer [22], and air bubble collapse [33]. The second type is the deposition of lipid membranes on prepatterned substrates. In this approach, materials on which lipid membranes do not adsorb or form SPBs (e.g., metals and polymeric materials) are prepatterned on the substrate and lipid membranes are subsequently introduced [20, 34, 35]. Materials such as self-assembled monolayers and proteins were reported to be an effective barrier to confine lipid bilayers [36–38]. The third type is photolithographic modification of lipid bilayers. This approach includes decomposition of lipid membranes by deep UV light and UV polymerization of lipid bilayers [39, 40]. Each type of micropatterned bilayer has pros and cons in various properties, such as the ease of fabrication, pattern size, stability, adsorption of biologically relevant molecules, etc. Therefore, a suitable technique is usually adopted for individual applications. Micropatterned lipid membranes have been applied to various basic biological studies such as immunological synapse formation [41] and signal transduction in cells [42]. They also provide an attractive platform for microarrays of membrane proteins [22].

1.3. Micropatterned Composite Membrane of Polymerized and Fluid Lipid Bilayers

We have recently developed a methodology to create micropatterned SPBs composed of polymerized and fluid lipid bilayers, where the polymerized bilayer forms an integrated matrix with the embedded fluid bilayers [40, 43–45]. Micropatterned SPBs are fabricated in four steps, as illustrated in Fig. 2: (A) formation of a monomeric bilayer on a solid substrate, (B) photolithographic polymerization by UV light, (C) removal of the nonreacted monomers, and (D) refilling the lipid-free regions with new lipid bilayers. In this configuration, polymeric bilayers act both as a barrier for the lateral diffusion of membrane-associated molecules and as a stabilizing framework for embedded SPBs.

Table 1 Chronological summary of patterning methods

Patterning methods	Year[a]	Type[b]	References
Patterning by scratching membranes with tweezers	1995	1	[80]
Bilayer on patterned substrate of metal and polymer	1997	2	[20, 34]
Bilayer on microcontact-printed SAM	1998	2	[36, 37]
Spatially addressable arrays by micropipette	1999	1,2	[29]
Pattern formation by a scanning probe microscopy tip	2000	1	[30–32]
Patterning by microcontact-printed proteins	2000	2	[38]
Patterning by microcontact-printed bilayers	2000	1	[24]
Patterning by microfluidics	2000	1	[26–28]
Patterning by polymerized lipid bilayer	2001	2,3	[40]
Lipid self-spreading on microstructure	2001	2	[81]
Membrane protein microarray by inkjet printing	2002	1	[22]
Patterning by parylene lift-off	2003	2	[82]
Patterning by deep UV light decomposition of lipids	2004	3	[39]
Patterning by hydrogel stamping	2005	1	[25]
Patterning by enzyme lithography using lipases	2005	1	[83]
Micropatterned corrugation of substrate	2006	2	[84]
Patterning by air bubble collapse	2007	1	[33]

[a] The year corresponds to the time of first publication in major scientific journals. It may differ from the time the technique was actually developed or introduced in scientific meetings.

[b] Types of the patterning methods: (1) spatially controlled deposition or removal of lipid membranes; (2) deposition of lipid membranes on prepatterned substrates; (3) photolithographic modification of lipid membranes.

Polymerization of lipidic molecules in lyotropic, self-assembled aggregations (lamellar, cubic, inverted hexagonal, etc.) has been studied extensively in the last several decades (see Fig. 3 for general structures) [2, 18]. In particular, stabilization of lipid vesicles (liposomes) by polymerization of lipids has been studied in conjunction with the potential application for encapsulation of medicinal materials (drug delivery) [46]. Lipid molecules having various moieties (e.g., dienoyl, sorbyl, diacetylene) were synthesized and polymerized *in situ* within the bilayers. Upon polymerization, the bilayers became significantly less soluble in organic solvents or detergent solutions [47–49]. In addition, a decrease in the lateral diffusion constant and the permeation coefficient of the bilayers was observed [50, 51]. More

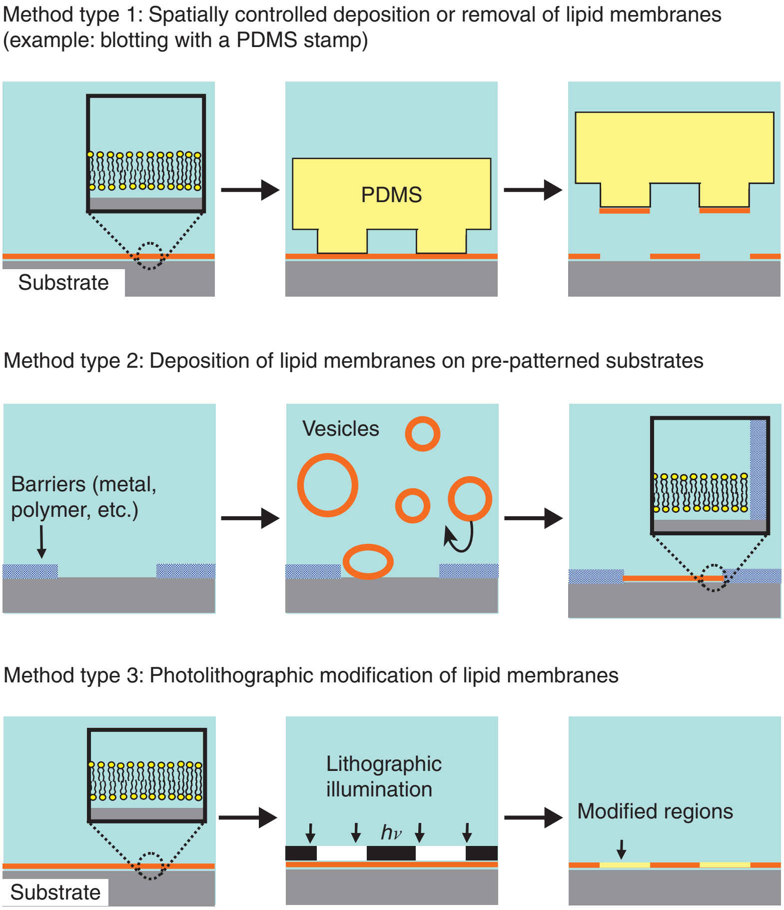

Figure 1 Schematic illustration of pattering methodologies.

recently, polymerization of SPBs on planar substrates or capillaries has been reported [19, 52–54]. For the present study, a diacetylene phospholipid, 1,2-bis(10,12-tricosadiynoyl)-*sn*-glycero-3-phosphocholine (DiynePC), has been used (Fig. 3). The choice of the diacetylene group for polymerization of bilayers was based on the following two properties: (i) diacetylene molecules can be polymerized efficiently in an ordered state (i.e., topochemical or solid-state polymerization) [55] and (ii) polydiacetylenes form long conjugation of ene−yne backbones that absorb UV/visible light strongly, and certain types of polydiacetylenes show a marked fluorescence (Fig. 4). These properties facilitate the characterization of the polymers both spectroscopically and microscopically. Figure 5 shows fluorescence

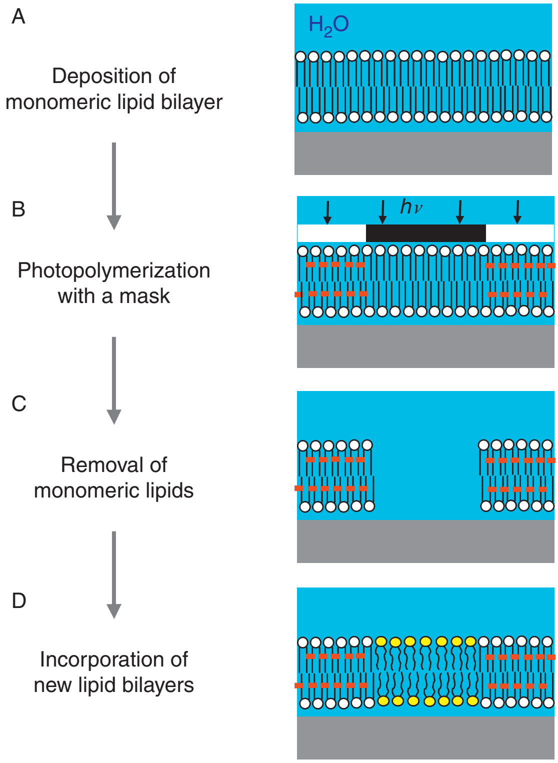

Figure 2 Schematic of the pattering method.

micrographs of a patterned bilayer. In Fig 5A, the polymerized bilayer is observed due to the fluorescence from a conjugated polymer backbone. Lipid bilayers of egg-PC containing 1 mol% of TR-PE were incorporated selectively into the square-shaped areas (corrals) where monomers had been protected with the mask during the lithographic UV exposure and selectively removed with a detergent solution (0.1 M sodium dodecylsulfate, SDS; Fig. 5B). The bilayers are continuous and fluid within the areas surrounded by the polymeric bilayers (corrals) as demonstrated by the formation of a concentration gradient of negatively charged TR-PE upon application of an electric field (Fig. 5C and D).

Compared with other approaches, micropatterning of SPBs by lithographic polymerization of lipid bilayers is unique in that polymeric and fluid bilayers are integrated as a continuous membrane. This feature gives various unique advantages and possibilities to the micropatterned model membrane, as discussed in the following sections.

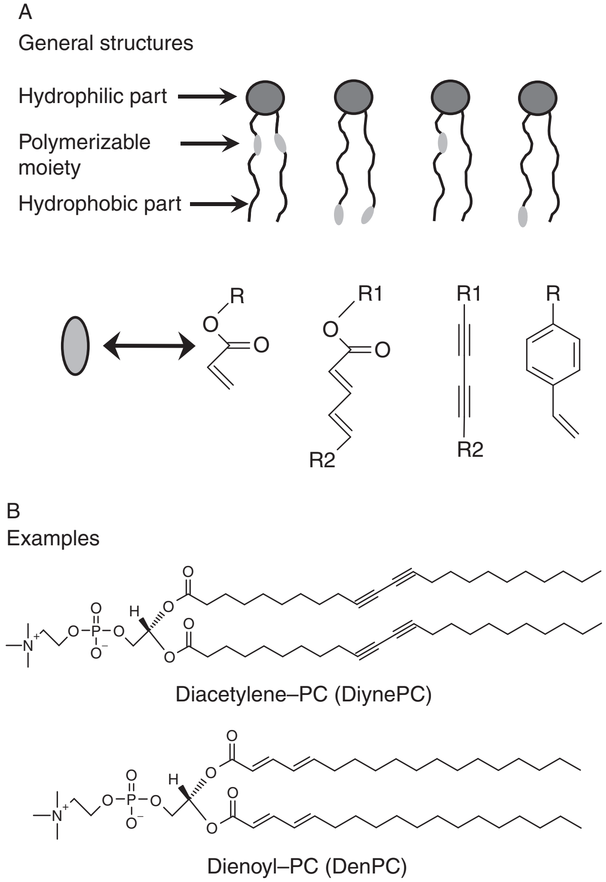

Figure 3 The general structures of polymerizable lipids and some examples (DiynePC and DenPC).

2. LITHOGRAPHIC POLYMERIZATION OF LIPID BILAYERS

The first step for generating micropatterned model membranes is the formation of polymeric bilayers in a structurally and spatially controlled manner. A typical procedure for this step is as follows. Two leaflets of DiynePC monolayers (monomer) were deposited onto solid substrates from the air/water interface, successively by the Langmuir–Blodgett (LB) and Langmuir–Schaefer (LS) methods. We did not use the vesicle fusion method for the deposition of DiynePC because of its high-phase transition temperature. Thus, formed bilayers underwent a photolithographic

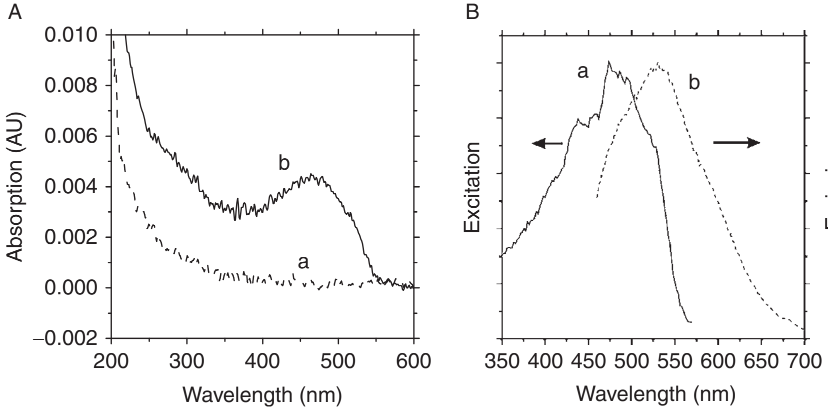

Figure 4 Absorption and fluorescence spectra of a polymeric DiynePC bilayer on quartz substrate. (A) Absorption spectrum before (a) and after the polymerization (b). (B) Fluorescence excitation/emission spectra: The excitation spectrum (solid line) was obtained by measuring the emission at 600 nm. The emission spectrum (dashed line) was obtained by the excitation at 430 nm. (Reprinted with permission from Ref. [43], Copyright: 2002 American Chemical Society.)

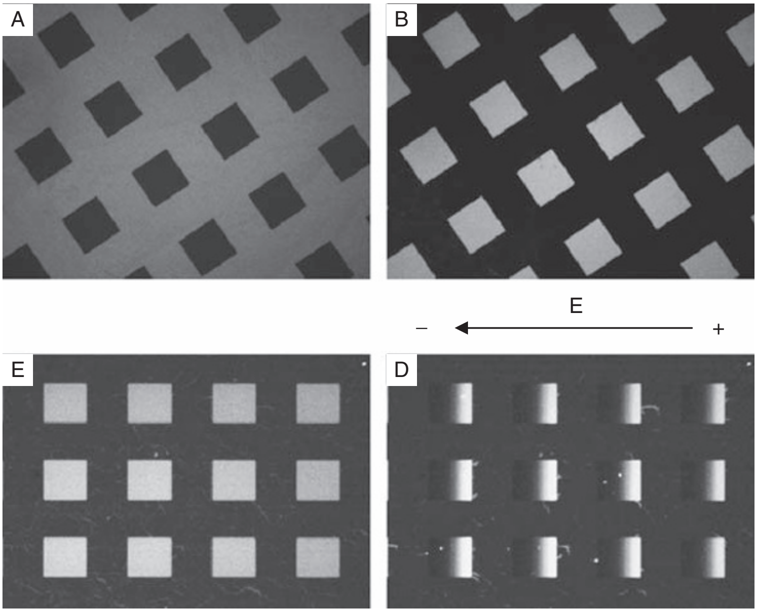

Figure 5 Fluorescence micrographs of a patterned bilayer on a glass substrate. (A) Fluorescence from polymerized DiynePC bilayers (UV irradiation dose: 4.4 J/cm^2). (B) Fluorescence from TR-PE doped egg-PC bilayers incorporated in the wells between polymerized bilayers (corrals). (C, D) Induction of the TR-PE concentration gradient by the application of an electric field. The size of corrals was 50 μm.

polymerization by placing a contact lithography mask on the bilayer surface during the photopolymerization. After the UV irradiation, nonreacted monomers were removed selectively by immersing the sample in a detergent solution (0.1 M SDS) for 30 min (25 °C). Figure 6 shows the *in situ* AFM images of a patterned polymeric bilayer. The grid-shaped area in Fig. 6A is the polymeric bilayer (UV irradiation: 5.0 J/cm^2), whereas the square-shaped areas are voids formed after removing monomers by SDS. Figure 6B is a magnified view of the boundary region marked in (A). The boundaries of the polymeric bilayers were rather uneven, presumably due to the limited resolution of the currently applied photolithography setup. The height step between the polymer film and corral was 5.1 nm, as shown in the line cross-section, which agrees favorably to a bilayer thickness [44, 56].

As described above, diacetylene polymerizes only in an ordered state (i.e., topochemical or solid-state polymerization) [55]. The efficiency of polymerization depends very sensitively on the factors that affect the molecular packing, such as the structure of molecules, substrate materials, and the way molecules are deposited onto the substrate [57–59]. For investigating the effect of molecular structures, we compared the photopolymerization behaviors of a diacetylene-containing single-chain amphiphile (monoalkylphosphate) and a phospholipid (DiynePC) [43]. Monoalkylphosphate showed a markedly higher reactivity compared with

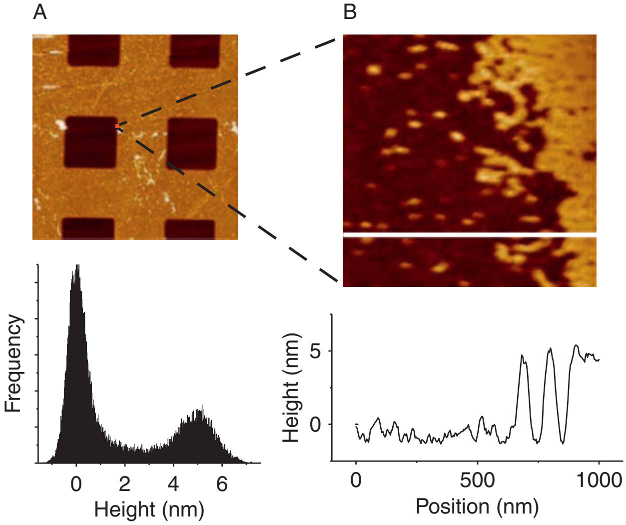

Figure 6 AFM image (80 × 80 μm^2) of a patterned polymeric bilayer after the SDS treatment (A). The image in (B) is a magnification (1 × 1 μm^2) of the boundary of polymeric bilayer marked. A histogram of height distribution and a line profile measured along the line are given in the lower row.

the phospholipid, resulting in a longer conjugation of the ene–yne backbones due to its favorable molecular packing in the bilayer. However at the same time, it developed large domain structures with defects and made the polymerized film mechanically less stable. The phospholipid (DiynePC), on the other hand, showed a high stability of polymerized bilayers. The higher stability of polymerized DiynePC bilayers should be, at least in part, due to the fact that each molecule has two polymerizable groups and the formed polymeric chains are cross-linked. The packing difficulties of the phospholipid also seem to prevent the formation of sharp domain boundaries. Photopolymerization of diacetylene amphiphiles in SPB also showed strong dependency on the underlying substrates. For example, the presence of a thin polymer layer on the substrate surface could alter the polymerization process of the bilayers significantly, as shown in Fig. 7.

Another important factor that influences the polymerization is the method for depositing monomeric lipid molecules onto the substrate. We discovered that the homogeneity of polymerized bilayers from DiynePC was very sensitively influenced by the film deposition temperature and alternatively by the annealing/quenching protocols [56]. Whereas DiynePC bilayers (monomer) deposited at a temperature below the triple-point temperature of DiynePC monolayers (~20 °C) formed homogeneous polymeric bilayers, those deposited at a temperature higher than the triple-point temperature showed a markedly increased number of line defects (Fig. 8). (Below the triple-point temperature, a direct transition from a gaseous state to a liquid condensed state occurs, whereas a coexistence plateau between the liquid expanded and liquid condensed phases is

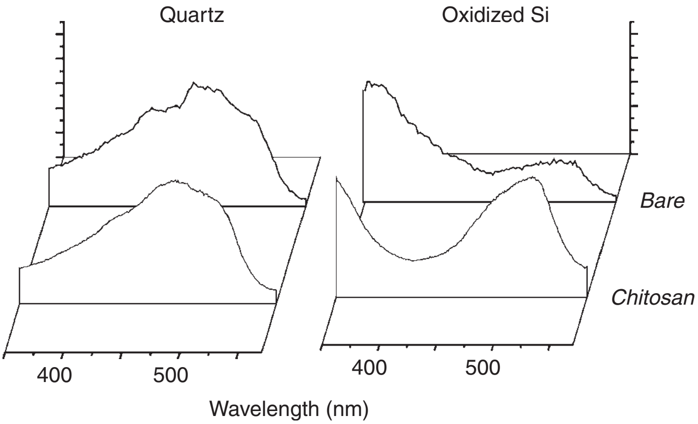

Figure 7 Fluorescence excitation spectra of polymerized DiynePC bilayers were compared on quartz and oxidized silicon substrates, which were modified with a thin layer of chitosan. The emission was measured at 600 nm. (Reprinted with permission from Ref., [43], Copyright: 2002 American Chemical Society.)

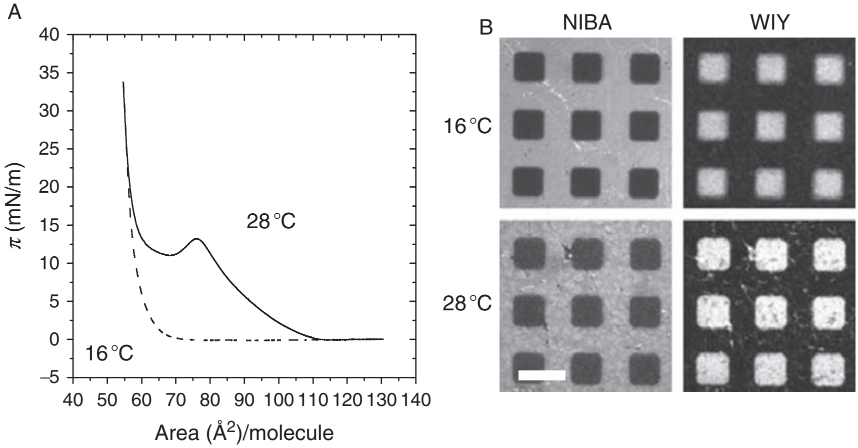

Figure 8 (A) π-A isotherms of DiynePC Langmuir monolayers at 16 and 28 °C. (B) Fluorescence micrographs of polymeric DiynePC bilayers prepared by the LB/LS method at 16 and 28 °C, followed by SDS treatment and backfilling with egg-PC. The polymeric bilayers were observed by the NIBA filter set (left side), whereas the backfilled fluid membranes were selectively observed by the WIY filter set (right side). The scale bar corresponds to 20 μm. (Reprinted with permission from Ref. [56]. Copyright: 2007 American Chemical Society.)

observed above this temperature [60].) The differences were attributed to the domain structures in the monolayer on water surface. Since the progress of polymerization as detected by the polymer-backbone conjugation (UV/visible absorption spectra) and the residual film thickness (AFM and ellipsometry) were unaffected by the film deposition temperatures, the domain size, rather than the molecular packing in each domain, were postulated to play a critical role. Changes in the spontaneous curvature and film area are the plausible source of destabilization and detachment of the films upon polymerization. These results highlight the importance of controlling the domain structures of polymerized bilayers for generating homogeneous polymeric bilayers.

3. INCORPORATION OF FLUID LIPID BILAYERS

In the present micropatterning methodology, the lipid-free regions that were generated by photolithographic polymerization of bilayers and removal of nonreacted monomers should be subsequently filled with lipid membranes. These membranes retain the physicochemical features of the biological membrane, such as lateral mobility of membrane components (fluidity), and are intended to be used as a model system of the biological membrane. Incorporation of SPBs into the voids has been typically achieved by the adsorption and subsequent reorganization of phospholipid vesicles on the substrate (vesicle fusion) [5, 10, 61–64]. Vesicle fusion is a self-assembly process widely used for the preparation of SPBs. However, successful preparation of SPBs via vesicle fusion also poses significant technological challenges for many types of substrate (such as hydrophilic polymers and self-assembled thiol monolayers) and lipid (such as negatively charged phospholipids), because it is not always possible for vesicles to overcome an energetic barrier of rupturing on the surface (Fig. 9) [61].

In the present micropatterned model membrane, polymeric scaffolds and incorporated fluid membranes have the same bilayer structure. This fact gives a unique advantage for incorporating fluid lipid bilayers. We have recently reported that incorporation of SPBs by the vesicle fusion method was significantly accelerated by the presence of preformed polymeric bilayers [65]. Total internal reflection fluorescence microscopy (TIR-FM) observations revealed that vesicle fusion started at the boundary of the

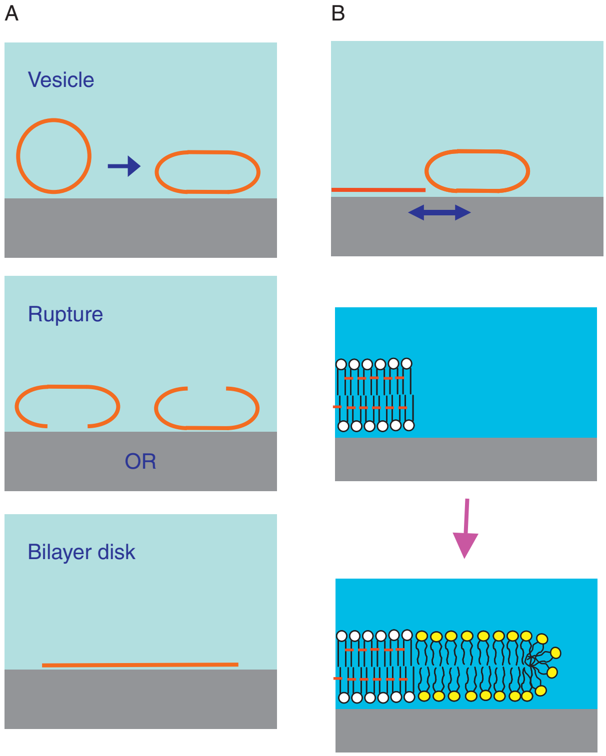

Figure 9 Schematic drawing of vesicle fusion processes occurring on the substrate surface with (A) and without the presence of polymeric a bilayer edge.

polymeric bilayers and propagated into the central part of the lipid-free regions. Figure 10 shows a vesicle fusion process on a patterned DiynePC bilayer substrate (20 μm stripe). For visualizing the vesicle fusion event more clearly, very low concentration of the labeled vesicle suspension (egg-PC/TR-PE, 30 mol%; 0.1 μM total lipid concentration) was first applied to the patterned DiynePC substrate and subsequently diluted with nonlabeled vesicles. Labeled vesicles are visible as bright dots, even though fluorescence from TR-PE is quenched to a large extent (Fig. 10B). The vesicles adsorbed preferentially on the glass surface between the patterned DiynePC bilayers. Unlabeled egg-PC vesicles were subsequently added with a much higher concentration (100 μM). Figure 10C shows the TIR-FM observation 5 min after the addition of the unlabeled vesicles. The fluorescence intensity of individual dots increased significantly by mixing of labeled and unlabeled bilayers. A closer inspection reveals that there are continuous fluorescent domains arising near the boundaries of DiynePC bilayers, which are most likely SPB patches. The fluorescent domains expanded from the boundaries toward the central regions of the stripes as shown in Fig. 10D and E, and finally formed a continuous bilayer within these areas (Fig. 10F).

The kinetics of vesicle fusion in the presence of preformed polymeric DiynePC bilayers was studied by QCM-D. Micropatterned polymeric bilayers with different stripe widths (10–200 μm) were generated in order to investigate the effect of the number of boundaries per unit area on the vesicle fusion process. Since the stripe width was approximately the same for the polymerized bilayers and lipid-free regions, the area available for the incorporation of new lipid bilayers was roughly half of the original silica-coated sensor, regardless of the width of the stripes. Figure 11 shows the measured responses in Δf and ΔD (fifth harmonics: 25 MHz) obtained for the application of 140 μM egg-PC vesicles containing 1 mol% TR-PE on the substrates with 3 stripe widths (10 μm, 50 μm, and 200 μm). The obtained QCM-D response on the SiO_2 substrate showed a characteristic two-phase process, similar to previous reports [10, 63]. In the first phase, Δf decreased and ΔD increased due to the adsorption of vesicles with trapped water (inside and between vesicles). In the second phase, the adsorbed vesicles ruptured and formed SPB, releasing trapped water as indicated by the increase of Δf and decrease of ΔD. On homogeneously polymerized DiynePC bilayer, on the other hand, Δf and ΔD did not change upon vesicle introduction. Vesicles apparently did not adsorb on the DiynePC bilayer surface. For the patterned substrates, the QCM-D profiles revealed smaller humps of Δf and ΔD compared with the case of SiO_2, indicating that the amount of vesicles accumulated before SPB formation was smaller. This tendency was more prominent on substrates with a higher density of boundaries. No hump of Δf was observed for the sample with 10-μm stripes, suggesting a rapid transformation of adsorbed vesicles into SPB. Regardless of the stripe width of patterned DiynePC bilayer stripes, the

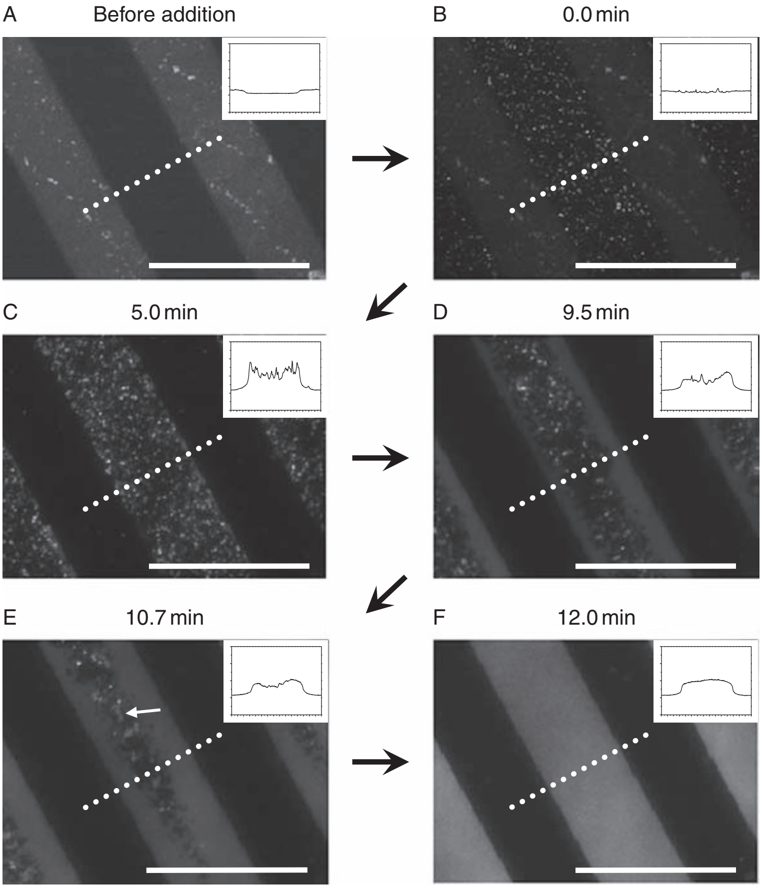

Figure 10 TIR-FM images of the vesicle fusion process on a glass substrate with patterned DiynePC bilayer. Application of vesicle suspensions was conducted in two steps. A dilute suspension of egg-PC vesicles (0.1 μM) containing 30 mol% TR-DHPE was first added and incubated for 5 min. Subsequently, unlabeled egg-PC vesicles were added at a much higher concentration (100 μM). Formation of SPBs was visualized with the increased fluorescence intensity (dequenching) due to the mixing of labeled and unlabeled bilayers. (A) Image obtained before the addition of labeled vesicles. The bright stripes are patterned DiynePC bilayers. (B) Image obtained after the addition of egg-PC vesicles containing 30 mol% TR-DHPE. Vesicles adsorbed preferentially on the glass surface. (C–F) Images obtained after the addition of unlabeled vesicles: SPBs were formed preferentially at the boundaries of DiynePC bilayer and expanded toward the central region of lipid-free stripes (D, E) and fused some independent domains (marked by an arrow in (E), finally covering the glass surface completely (F). The inset in each image is an intensity profile measured along the dotted line. The scale bars correspond to 40 μm. The elapsed time after the introduction of unlabeled vesicles is given at the top of each image. (Reprinted with permission from Ref. [65]. Copyright: 2006 Biophysical Society.)

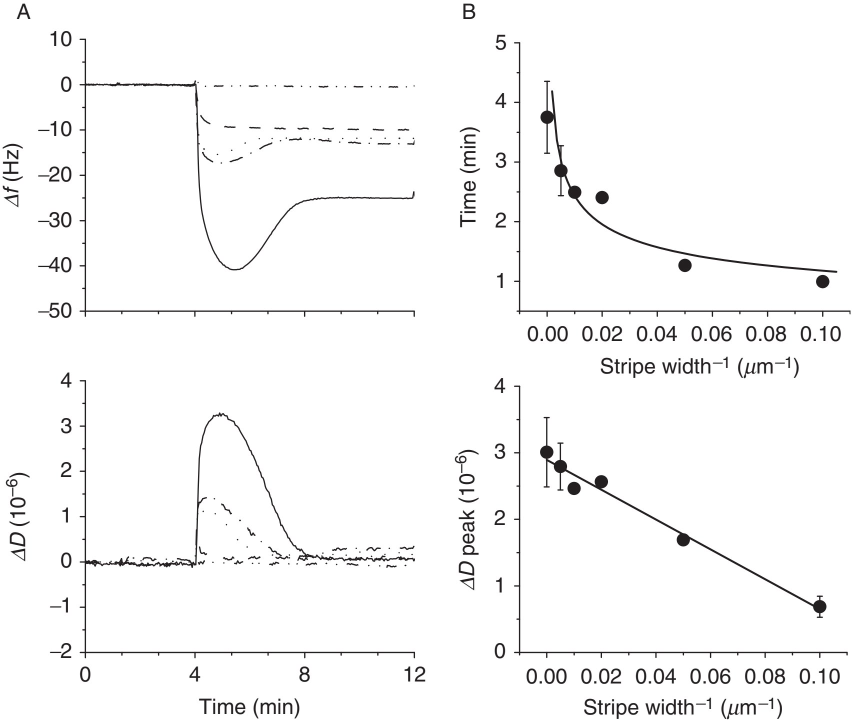

Figure 11 (A) QCM-D measurements of the vesicle fusion process on SiO_2 substrates with patterned DiynePC bilayers: Δf and ΔD were plotted during the fusion of egg-PC vesicles (140 μM) containing 1 mol% TR-DHPE on SiO_2 (no DiynePC bilayer: solid line), homogeneously polymerized DiynePC bilayer (dash-double dotted line), and patterned DiynePC bilayers. The patterned DiynePC bilayers had stripe widths of 10 μm (dashed line), 50 μm (dotted line), and 200 μm (dash-single dotted line). (B) Plot of vesicle fusion duration and maximum ΔD values versus inverse of stripe widths (the results of SiO_2 substrate were also incorporated): (A) Duration of vesicle fusion plotted versus the inverse of stripe widths. A line is given just to guide the eyes. (B) Maximum ΔD values plotted versus the inverse of stripe widths. The ΔD values were normalized, considering different areas of exposed SiO_2 for patterned substrates.) (Reprinted with permission from Ref. [65]. Copyright: 2006 Biophysical Society.)

final Δf was approximately half of that obtained on homogenous SiO_2 and the dissipation was near zero, corroborating the formation of SPBs in the previously lipid-free regions. We plotted the duration of vesicle fusion and the normalized maximum ΔD value as a function of the inverse of stripe widths (density of bilayer boundaries). Figure 11B (upper row) shows the duration of vesicle fusion, which was defined as the point where Δf values became constant after the formation of SPBs. The time needed for vesicle fusion decreased by the presence of preformed DiynePC bilayers. The reduction was significant also for large stripe widths (>50 μm), and rather leveled off for smaller stripe widths (20 μm and 10 μm). On the other hand, the maximum ΔD values, which represent the amount of vesicles accumulated temporarily on the substrate surface before transforming into SPBs, decreased linearly with the inverse of stripe widths (Fig. 11B; lower row). (These values were normalized considering the area occupied by the newly incorporated SPBs.) These results suggest clearly that vesicle fusion was accelerated in the presence of preformed polymeric bilayer domains, reducing the amount of transiently adsorbed vesicles.

Facilitated incorporation of fluid SPBs by preformed DiynePC bilayers has the following implications. First, accelerated vesicle fusion indicates that it is energetically favorable to incorporate guest SPBs into the matrix of DiynePC bilayers. In order to obtain an energetic gain, these two types of bilayers should be forming a continuous hybrid membrane, sealing the edges of DiynePC and fluid lipid bilayers. The formation of such hybrid membranes is the most important feature of the present micropatterning strategy, because the polymeric bilayers can act both as barriers for the lateral diffusion of membrane-associated molecules and as a scaffold to stabilize incorporated fluid bilayer membranes. The enhanced vesicle fusion by the presence of preformed polymeric bilayer scaffold also suggests the possibility that a wider variety of lipid membranes, including native cellular membranes, may be incorporated into micropatterned bilayers due to the catalytic effect of preformed bilayer edges.

4. CONTROLLING THE RATIOS OF POLYMERIZED AND FLUID LIPID BILAYERS

One of the unique features of the present micropatterning strategy is the fact that the area fraction of polymeric bilayers can be regulated by changing the UV irradiation dose applied for photopolymerization. This feature gives a possibility to generate composite membranes of polymeric and fluid lipid bilayers, where two types of lipid membranes are mixed as nanometer-sized domains. Figure 12A shows the amount of polymeric bilayers estimated by the ellipsometry for varied UV doses. The average thickness increased as a function of the applied UV irradiation dose, reaching a plateau between 4.0 and 5.5 J/cm^2, and slightly decreasing above 6.0 J/cm^2. Since the thickness of individual bilayer domains should be constant, a higher thickness indicates a higher coverage by polymeric bilayers. From the AFM observations, we suppose that the increase of polymer coverage was due to the increase in the number of polymeric bilayer domains without significant changes in their sizes. For estimating the amount of incorporated fluid bilayers within the matrix of partially polymerized DiynePC bilayers, we prepared composite membranes of

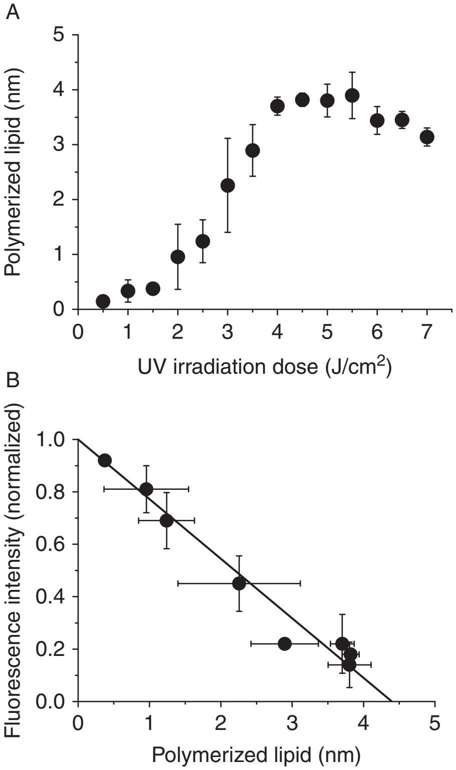

Figure 12 (A) The amount of polymerized DiynePC that remained on substrate after the SDS treatment was measured by the ellipsometry and plotted versus UV irradiation dose. The thickness represents an average value of polymeric bilayers and voids. (B) The fluorescence intensity of TR-PE arising from incorporated lipid bilayers was plotted versus the amount of polymerized DiynePC measured by the ellipsometry.

polymeric DiynePC and fluid bilayers (egg-PC containing 1 mol% TR-PE) and measured fluorescence arising from the fluid bilayer fractions. The fluorescence intensity was plotted versus the amount of polymerized DiynePC bilayers determined by the ellipsometry (Fig. 12B). The amount of incorporated lipids decreased linearly with the amount of preformed polymeric bilayers. This result is a clear indication that polymeric and fluid bilayers are forming a single layer of composite membrane. Interestingly, the fluorescence intensity from TR-PE was not zero for samples with the maximum polymer coverage. It may suggest that polymeric bilayers do not completely cover the surface even for the maximum coverage reached in the present experimental conditions. An alternative possibility is that there are some adsorbed lipid materials on the polymer surfaces. However, based on the QCM-D results, we do not suppose that this factor has a major contribution to the observed fluorescence (data not shown). By extrapolating the linear relation to the *x*-axis, the theoretical thickness for complete bilayer coverage could be estimated to be 4.4 nm.

Polymeric bilayer domains can act as an obstacle for the lateral diffusion of membrane-associated molecules. We determined the degree of obstruction as a function of the fraction of polymeric bilayers. The lateral diffusion coefficients of lipids (TR-PE) were measured by using the fluorescence recovery after photobleaching (FRAP) method. In the case of egg-PC/TR-PE bilayers on a glass substrate (no polymer), the average diffusion coefficient was determined to be 1.6 ± 0.4 $\mu m^2/s$. This value agrees well with the results in the previous reports [66–70]. The results of partially polymerized DiynePC bilayers are compiled in Fig. 13. The diffusion coefficients were normalized to the obstacle-free diffusion (i.e., 1.6 $\mu m^2/s$) and expressed as relative diffusion coefficients, $D^\star$. The area fractions of polymeric bilayers *c*, on the other hand, were derived by dividing the film thickness from ellipsometric measurements with the theoretical thickness corresponding to the full coverage (i.e., 4.4 nm). The diffusion coefficients decreased monotonically as a function of the area fraction, and were found to be nearly zero for a higher *c* (above ca. 0.7). The decrease was linear at low obstacle area fractions below 0.4. The effective obstruction observed in this regime should be ascribed to the small size of polymeric bilayer domains. We observed that a finite lateral diffusion remained for the area fraction between 0.4 and 0.7, and did not find a clear threshold at which the diffusion coefficient became zero. The increased coverage of the substrate surface with the polymeric bilayer domains, as indicated by the domain fraction in the AFM images, has most likely acted as an effective obstacle for the long-distance diffusion of lipid molecules [44]. For a sufficient UV-irradiation dose, the lateral diffusion of lipid molecules was completely hindered by the polymer domains.

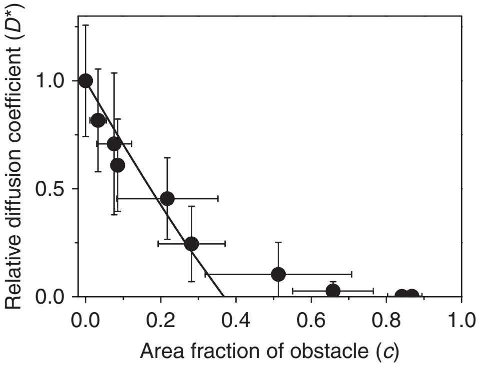

Figure 13 Relative diffusion coefficients of TR-PE in the composite membranes were plotted as a function of the area fraction of polymeric bilayers (obstacles) obtained from the ellipsometry and fluorescence microscopy.

These results suggest that one could modulate the lateral mobility of membrane-associated molecules by purposefully designing the geometry and degree of polymerization. In this way, one should be able to construct arrays of lipid bilayers that are not completely isolated but partially connected. A simplified conceptual illustration is given in Fig. 14. Figure 14A schematically depicts the procedure for generating a patterned bilayer film with spatially defined polymerization profiles. Either by using a contact mask with varied transmission profiles or by conducting successive exposure with multiple protection patterns, one can modulate the UV dose,

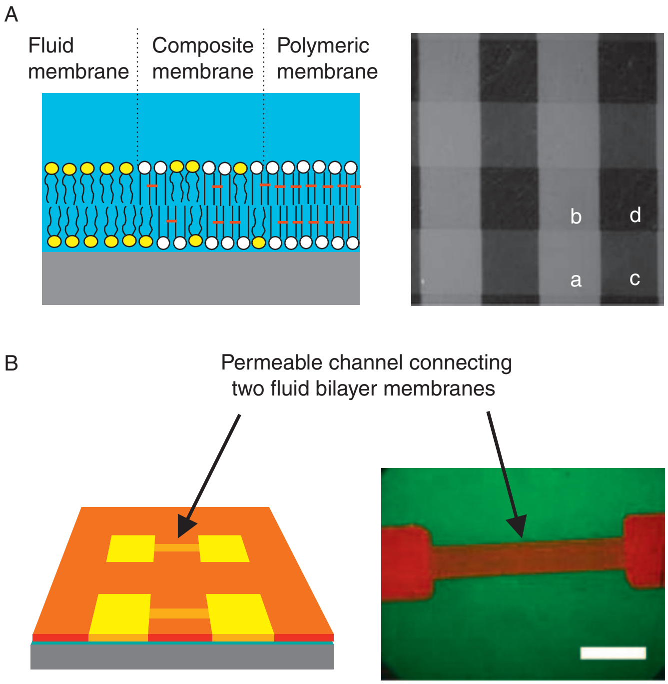

Figure 14 (A) Schematic drawing of SPB composed of fully fluid, fully polymerized, and composite membranes (left) and an example of a patterned hybrid SPB with spatially varied degree of polymerization (right). The applied UV dose for polymerization was varied with four steps (a = 0, b = 2, c = 3, d = 5 J/cm^2) and fluid bilayers (egg-PC containing 1 mol% TR-PE) were incorporated after removing monomers. Fluorescence from fluid bilayers was observed. (B) A membrane channel of permeable membrane domain consisting of polymerized DiynePC and fluid bilayers connects two fluid lipid bilayer membranes: Schematic illustration (left) and an experimental demonstration (right). The channel connecting two square areas has been created by polymerizing DiynePC with 40% of UV light dose compared with the surrounding area. Fluorescence image of polymerized DiynePC (green) and TR-PE (red) were superimposed. The scale bar corresponds to 50 μm. (Partially reproduced with permission from Ref. [45]. Copyright: 2004 American Chemical Society.)

and therefore the progress of UV polymerization. After removing monomers by a detergent solution, one obtains three distinctive regions: (i) a lipid-free area, (ii) an area partially covered by the polymer, and (iii) an area completely covered by the polymer. Lipid-free areas are subsequently refilled with fluid lipid bilayers. The areas partially covered by polymer can also incorporate fluid bilayer with partial lateral mobility of membrane-associated molecules, whereas long-range diffusion is completely suppressed in sufficiently polymerized bilayers. Figure 14B is an example of the configuration where patches of fluid lipid bilayers are connected by a membrane channel. In the channel region, the polymerization process is optimized such that the formed polymerized bilayers allow penetration of fluid lipid bilayers and lateral diffusion of membrane-associated molecules. In the current example, the monomeric DiynePC bilayer in the channel was irradiated with 40% of UV light compared with the surrounding area upon polymerization, whereas the square-shaped areas were completely protected. As a result of this controlled UV photopolymerization, the channel connects two fluid membrane domains with a reduced lateral mobility of molecules. It should be basically possible to impose molecular-size-dependent obstruction by optimizing the shape and area fraction of polymeric bilayer domains [71].

5. INCORPORATION OF BIOLOGICAL MEMBRANES INTO MICROPATTERNED BILAYERS

An important step for the development of micropatterned model membranes is the incorporation of membrane-associated proteins in their functional form. However, native biological membranes contain various lipids and proteins, and their incorporation into model membrane systems via vesicle fusion is generally very difficult. As an alternative approach, we studied the incorporation of biological membrane fractions into micropatterned polymeric bilayer scaffold together with a detergent, 1,2-dihexanoyl-*sn*-glycero-3-phosphocholine (DHPC). A preliminary study by using QCM-D suggested that incorporation of phospholipid bilayers by vesicle fusion was significantly accelerated in the presence of DHPC. TIR-FM observation demonstrated that homogeneous and fluid bilayers could be incorporated in the corrals surrounded by polymerized bilayers (Fig. 15). For the incorporation of biological membranes, we used sarcoplasmic reticulum (SR) membrane vesicles prepared from rabbit skeletal muscle as a model system [72]. SR membrane vesicles could not be incorporated into the corrals if they were directly adsorbed onto the surface (Fig. 16A). On the other hand, they could be homogeneously incorporated into the corrals in the presence of DHPC (Fig. 16B). The concentration of DHPC

Figure 15 Fluorescence microscopy observation of membrane incorporation from POPC/DHPC/TR-PE ($q = 0.1$: [POPC] = 1 mM, [DHPC] = 10 mM, [TR-PE] = 0.01 mM). (A) DiynePC bilayers observed in the presence of POPC/DHPC/TR-PE in the solution; (B) POPC/DHPC/TR-PE membranes incorporated in the corrals of DiynePC bilayers shown in (A) (TIR-FM observation); (C) POPC/DHPC/TR-PE membranes that remain in the corrals after rinsing with a buffer solution (TIR-FM observation). The size of corrals is 20 μm.

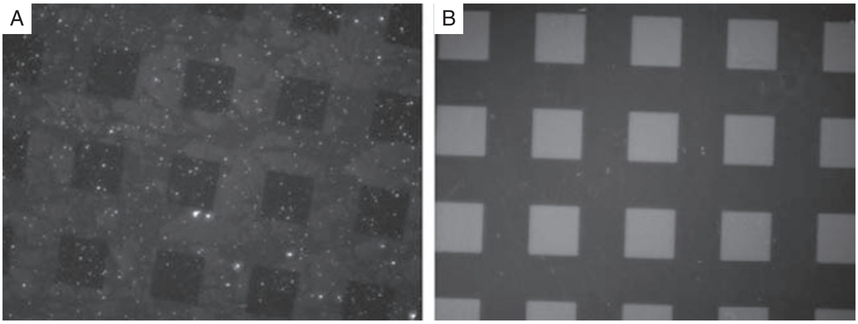

Figure 16 Incorporation of SR membranes into the corrals surrounded by polymeric bilayers using POPC/DHPC mixtures: (A) application of SR membranes; (B) SR membranes incorporated with DHPC (1% (w/v) = ca. 22 mM). The patterned membrane was observed after rinsing the solution (removing DHPC). (In all samples, membranes contained a fluorescence dye, 3,3′-dioctadecyloxacarbocyanine perchlorate.)

(1% (w/v) = ca. 22 mM) was higher than its critical micelle concentration (cmc) of 11 mM [73]. Therefore, SR membranes should be partially solubilized by DHPC. This result suggests that a purposeful use of detergents significantly improves the incorporation of membranes obtained from biological samples.

A more pragmatic approach for immobilizing membrane proteins in micropatterned bilayers is to attach them onto fluid bilayer domains by using fusogenic lipid compositions. For example, we have recently reported on a methodology for immobilizing cytochrome P450 enzymes that play critical roles in the oxidation of xenobiotics, including drugs and environmental pollutants [74–76]. We could attach microsomes containing P450 and detect the enzymatic activity on the substrate by using micropatterned membranes composed of a matrix of polymeric DiynePC bilayer and incorporated fluid bilayers composed of 1-palmitoyl-2-oleoyl-*sn*-glycero-3-phosphocholine (POPC), 1-palmitoyl-2-oleoyl-*sn*-glycero-3-phospho-L-serine (POPS), and 1-palmitoyl-2-oleoyl-*sn*-glycero-3-phosphoethanolamine (POPE). The bilayers of POPC/POPS/POPE had a significantly heightened adsorption of microsomes compared with the surrounding DiynePC bilayer. Phospholipids having a phosphatidylethanolamine (PE) polar group are known to induce membrane fusion due to their strong tendency to form inverted structures [77]. Therefore, one of the driving forces for the preferential adsorption of microsomes should be the fusion between the preformed planar bilayer and the microsomal membranes. From the microscopic features and the amount of adsorbed P450, we infer that microsomes are adsorbed with their vesicular structures retained on the surface of POPC/POPS/POPE. The enzymatic activity was significantly higher on lipid bilayer substrates compared with direct adsorption on glass. Furthermore, competitive assay experiments between two substrates demonstrated the feasibility of bioassays based on immobilized P450s. The polymeric bilayer played multiple roles in this configuration, that is, stabilization of incorporated bilayers, suppression of nonspecific binding to the surface, and patterning of P450s. Although the structure of immobilized membranes was not yet well-defined as in the case of pure lipid bilayers, this result represents an important step toward the high-throughput screening of P450 activities.

6. CONCLUSIONS AND OUTLOOK

Since the pioneering work by the group of S.G. Boxer, many approaches have been invented for micropatterning SPBs. The methods could be classified into the following three categories: (i) spatially controlled deposition or removal of lipid membranes, (ii) deposition of lipid membranes on prepatterned substrates, and (iii) photolithographic modification of lipid membranes. The present approach can belong to both the second and third categories. Compared with other approaches, micropatterning of SPBs by polymerized lipid bilayers is unique in that polymeric and fluid bilayers are integrated as a continuous membrane. This architecture gives various unique features to the model membrane. We observed accelerated transformation of vesicles into SPBs due to the presence of preformed polymeric bilayers, suggesting that edges of polymeric bilayers acted as a catalyst for the transformation [65]. This observation suggests that preformed polymeric bilayers could also facilitate the incorporation of membranes derived from biological samples. It should also be noted that polymeric bilayer matrices are a useful tool for studying the incorporation of various components derived from cellular membranes, because they are resistant toward nonspecific adsorption and provide a framework with a defined thickness. Since polymeric bilayers of DiynePC have a defined thickness of ca. 4.4 nm and a relatively low roughness of the surface, this bilayer scaffold can be used as a reference system for analyzing the thickness and structures of incorporated membranes. For example, it should be possible to study the structures of adsorbed membranes in detail by using SPR and surface plasmon fluorescence spectroscopy (SPR-SPFS) [12, 64].

We have also demonstrated that the composition of polymerized and fluid bilayers could be controlled by changing the applied UV dose for polymerization. By changing the compositions, the lateral diffusion of membrane-associated molecules could be regulated. Such obstructed lateral diffusion is commonly observed in cellular membranes, and in fact nonrandom distribution of membrane components and confinement of them in microdomains are regarded as a prerequisite for numerous vital functions such as signal transduction and trafficking [78, 79]. Therefore, micropatterned model membranes with modulated lateral mobility should be able to reproduce more precisely the situations in cellular membranes, such as interactions between membrane proteins and signal transduction through cell membranes in an artificial platform.

Based on these unique features, micropatterned membranes composed of polymeric and fluid bilayers provide a versatile platform for constructing complex model systems of the biological membranes with a well-defined architecture. For example, the fact that polymeric and fluid bilayers have an imprinted pattern in the membrane allows the membrane to be independent of the substrate and one could possibly construct a patterned bilayer separated from the substrate by a thin layer of soft polymeric cushion. Such polymer layers have been used as a spacer in order to accommodate membrane proteins in solid-supported bilayers in a functionally active form. It should be also possible to covalently attach the polymerized bilayer to the underlying polymer cushion by using a chemically reactive head group. The polymeric lipid bilayer might contribute to the mechanical stabilization of the membrane system, similar to the conjunctions between cytoskeleton and membrane proteins.

ACKNOWLEDGMENTS

The development of micropatterned model membranes based on polymerized lipid bilayers was initiated at the Max-Planck-Institute for Polymer Research (Mainz, Germany) in 1998, and has been continued at AIST since 2002. The author thanks many colleagues and collaborators for supporting and contributing to this project, including Wolfgang Knoll, Andreas Offenhäusser, Tobias Baumgart, Ulrich Jonas (Max-Planck-Institute for Polymer Research), Holger Schönherr, Curtis W. Frank (Stanford University), Takashi Okazaki, Shigeki Kimura, Takehiko Inaba, Saori Mori, Takahisa Taguchi, Noboru Yumoto, Yoshiro Tatsu, Keiko Tawa, Kazuyuki Kiyosue, Junji Nishii (AIST), Yoshihiro Ueda, and Hiromasa

Imaishi (Kobe University). This work was financially supported in part by the Promotion Budget for Science and Technology (AIST Upbringing of Talent in Nanobiotechnology Course) from the Ministry of Education, Science, Culture and Sports (MEXT), Grant-in-Aid for Scientific research from Japan Society for the Promotion of Science, Mitsubishi Chemical Corporation Fund, and Sekisui Chemical Grant Program.

REFERENCES

[1] I. Langmuir, The constitution and fundamental properties of solids and liquids. II. Liquids, J. Am. Chem. Soc. 39 (1917) 1848–1906.

[2] H. Ringsdorf, B. Schlarb, J. Venzmer, Molecular architecture and function of polymeric-oriented systems: Models for the study of organization, surface recognition, and dynamics of biomembranes, Angew. Chem., Int. Ed. 27 (1988) 113–158.

[3] D. Chapman, Biomembranes and new hemocompatible materials, Langmuir 9 (1993) 39–45.

[4] M. Edidin, Lipids on the frontier: A century of cell-membrane bilayers, Nat. Rev. Mol. Cell Biol. 4 (2003) 414–418.

[5] A.A. Brian, H.M. McConnell, Allogenic stimulation of cytotoxic T cells by supported planar membranes, Proc. Natl. Acad. Sci. USA 81 (1984) 6159–6163.

[6] L.K. Tamm, H.M. McConnell, Supported phospholipid bilayers, Biophys. J. 47 (1985) 105–113.

[7] E. Sackmann, Supported membranes: Scientific and practical applications, Science (Washington) 271 (1996) 43–48.

[8] B.W. Koenig, S. Krueger, W.J. Orts, C.F. Majkrzak, N.F. Berk, J.V. Silverton, K. Gawrisch, Neutron reflectivity and atomic force microscopy studies of a lipid bilayer in water adsorbed to the surface of a silicon single crystal, Langmuir 12 (1996) 1343–1350.

[9] E. Kalb, S. Frey, L.K. Tamm, Formation of supported planar bilayers by fusion of vesicles to supported phospholipid monolayers, Biochim. Biophys. Acta 1103 (1992) 307–316.

[10] C.A. Keller, B. Kasemo, Surface specific kinetics of lipid vesicle adsorption measured with a quartz crystal microbalance, Biophys. J. 75 (1998) 1397–1402.

[11] R. Richter, A. Mukhopadhyay, A. Brisson, Pathways of lipid vesicle deposition on solid surfaces: A combined QCM-D and AFM study, Biophys. J. 85 (2003) 3035–3047.

[12] K. Tawa, K. Morigaki, Substrate-supported phospholipid membranes studied by surface plasmon resonance and surface plasmon fluorescence spectroscopy, Biophys. J. 89 (2005) 2750–2758.

[13] B.A. Cornell, V.L.B. Braach-Maksvytis, L.G. King, P.D.J. Osman, B. Raguse, L. Wieczorek, R.J. Pace, A biosensor that uses ion-channel switches, Nature (London) 387 (1997) 580–583.

[14] A. Plant, Supported hybrid bilayer membranes as rugged cell membrane mimics, Langmuir 15 (1999) 5128–5135.

[15] J. Spinke, J. Yang, H. Wolf, M. Liley, H. Ringsdorf, W. Knoll, Polymer-supported bilayer on a solid substrate, Biophys. J. 63 (1992) 1667–1671.

[16] S.M. Schiller, R. Naumann, K. Lovejoy, H. Kunz, W. Knoll, Archaea analogue thiolipids for tethered bilayer lipid membranes on ultrasmooth gold surfaces, Angew. Chem., Int. Ed. 42 (2003) 208–211.

[17] V. Atanasov, N. Knorr, R.S. Duran, S. Ingebrandt, A. Offenhäusser, W. Knoll, I. Köper, Membrane on a chip: A functional tethered lipid bilayer membrane on silicon oxide surfaces, Biophys. J. 89 (2005) 1780–1788.

[18] A. Mueller, D.F. O'Brien, Supramolecular materials via polymerization of mesophases of hydrated amphiphiles, Chem. Rev. 102 (2002) 727–757.

[19] E.E. Ross, B. Bondurant, T. Spratt, J.C. Conboy, D.F. O'Brien, S.S. Saavedra, Formation of self-assembled, air-stable lipid bilayer membranes on solid supports, Langmuir 17 (2001) 2305–2307.

[20] J.T. Groves, N. Ulman, S.G. Boxer, Micropatterning fluid lipid bilayers on solid supports, Science (Washington) 275 (1997) 651–653.

[21] J.T. Groves, S.G. Boxer, Micropattern formation in supported lipid membranes, Acc. Chem. Res. 35 (2002) 149–157.

[22] Y. Fang, A.G. Frutos, J. Lahiri, Membrane protein microarrays, J. Am. Chem. Soc. 124 (2002) 2394–2395.

[23] J.T. Groves, S.G. Boxer, H.M. McConnell, Electric field-induced reorganization of two-component supported bilayer membranes, Proc. Natl. Acad. Sci. USA 94 (1997) 13390–13395.

[24] J.S. Hovis, S.G. Boxer, Patterning barriers to lateral diffusion in supported lipid bilayer membranes by blotting and stamping, Langmuir 16 (2000) 894–897.

[25] S. Majd, M. Mayer, Hydrogel stamping of arrays of supported lipid bilayers with various lipid compositions for the screening of drug-membrane and protein-membrane interactions, Angew. Chem., Int. Ed. 44 (2005) 6697–6700.

[26] L. Kam, S.G. Boxer, Formation of supported lipid bilayer composition arrays by controlled mixing and surface capture, J. Am. Chem. Soc. 122 (2000) 12901–12902.

[27] S. Künneke, A. Janshoff, Visualization of molecular recognition events on microstructured lipid-membrane compartments by in situ scanning force microscopy, Angew. Chem., Int. Ed. 41 (2002) 314–316.

[28] T. Yang, S. Jung, H. Mao, P.S. Cremer, Fabrication of phospholipid bilayer-coated microchannels for on-chip im, Anal. Chem. 73 (2001) 165–169.

[29] P.S. Cremer, T. Yang, Creating spacially addressed arrays of planar supported fluid phospholipid membranes, J. Am. Chem. Soc. 121 (1999) 8130–8131.

[30] J.W. Carlson, T. Bayburt, S.G. Sligar, Nanopatterning phospholipid bilayers, Langmuir 16 (2000) 3927–3931.

[31] B.L. Jackson, J.T. Groves, Scanning probe lithography on fluid lipid membranes, J. Am. Chem. Soc. 126 (2004) 13878–13879.

[32] S. Lenhert, P. Sun, Y. Wang, H. Fuchs, C.A. Mirkin, Massively parallel dip-pen nanolithography of heterogeneous supported phospholipid multilayer patterns, Small 3 (2007) 71–75.

[33] M.D. Mager, N.A. Melosh, Lipid bilayer deposition and patterning via air bubble collapse, Langmuir 23 (2007) 9369–9377.

[34] G. Wiegand, T. Jaworek, G. Wegner, E. Sackmann, Heterogeneous surfaces of structured hairy-rod polymer films: Preparation and methods of functionalization, Langmuir 13 (1997) 3563–3569.

[35] J.T. Groves, N. Ulman, P.S. Cremer, S.G. Boxer, Substrate–membrane interactions: Mechanisms for imposing patterns on a fluid bilayer membrane, Langmuir 14 (1998) 3347–3350.

[36] S. Heyse, O.P. Ernst, Z. Dienes, K.P. Hofmann, H. Vogel, Incorporation of rhodopsin in laterally structured supported membrane: Observation of transducin activation with spatially and time-resolved surface plasmon resonance, Biochemistry 37 (1998) 507–522.

[37] A.T.A. Jenkins, N. Boden, R.J. Bushby, S.D. Evans, P.F. Knowles, R.E. Miles, S.D. Ogier, H. Schönherr, G.J. Vancso, Microcontact printing of lipophilic self-assembled monolayers for the attachment of biomimetic lipid bilayers to surfaces, J. Am. Chem. Soc. 121 (1999) 5274–5280.

[38] L.A. Kung, L. Kam, J.S. Hovis, S.G. Boxer, Patterning hybrid surfaces of proteins and supported lipid bilayers, Langmuir 16 (2000) 6773–6776.

[39] C.K. Yee, M.L. Amweg, A.N. Parikh, Membrane photolithography: Direct micropatterning and manipulation of fluid phospholipid membranes in the aqueous phase using deep-UV light, Adv. Mater. 16 (2004) 1184–1189.

[40] K. Morigaki, T. Baumgart, A. Offenhäusser, W. Knoll, Patterning solid-supported lipid bilayer membranes by lithographic polymerization of a diacetylene lipid, Angew. Chem., Int. Ed. 40 (2001) 172–174.

[41] K.D. Mossman, G. Campi, J.T. Groves, M.L. Dustin, Altered TCR signaling from geometrically repatterned immunological synapses, Science 310 (2005) 1191–1193.

[42] M. Wu, D. Holowka, H.G. Craighead, B. Baird, Visualization of plasma membrane compartmentalization with patterned lipid bilayers, Proc. Natl. Acad. Sci. USA 101 (2004) 13798–13803.

[43] K. Morigaki, T. Baumgart, U. Jonas, A. Offenhäusser, W. Knoll, Photopolymerization of diacetylene lipid bilayers and its application to the construction of micropatterned biomimetic membranes, Langmuir 18 (2002) 4082–4089.

[44] K. Morigaki, H. Schönherr, C.W. Frank, W. Knoll, Photolithographic polymerization of diacetylene-containing phospholipid bilayers studied by multimode atomic force microscopy, Langmuir 19 (2003) 6994–7002.

[45] K. Morigaki, K. Kiyosue, T. Taguchi, Micropatterned composite membranes of polymerized and fluid lipid bilayers, Langmuir 20 (2004) 7729–7735.

[46] F.J. Freeman, D. Chapman, Polymerizable liposomes: Applications in biology and medicine, in: G. Gregoriadis (Ed.), Liposomes as Drug Carriers, John Wiley & Sons, New York, 1988, pp. 821–839.

[47] D.S. Johnston, L.R. McLean, M.A. Whittam, A.D. Clark, D. Chapman, Spectra and physical properties of liposomes and monolayers of polymerizable phospholipids containing diacetylene groups in one or both acyl chains, Biochemistry 22 (1983) 3194–3202.

[48] S. Takeoka, T. Ohgushi, E. Tsuchida, Destruction and reconstruction of polyphospholipid vesicles with size memory, Macromolecules 28 (1995) 7660–7666.

[49] T.M. Sisson, H.G. Lamparski, S. Köchens, A. Elayadi, D.F. O'Brien, Cross-linking polymerizations in two-dimensional assemblies, Macromolecules 29 (1996) 8321–8329.

[50] E. Sackmann, P. Eggl, C. Fahn, H. Bader, H. Ringsdorf, M. Schollmeier, Compound membranes of linearly polymerized and cross-linked macrolipids with phospholipids: Preparation, microstructure and applications, Ber. Bunsen-Ges. Phys. Chem. 89 (1985) 1198–1208.

[51] S. Kölchens, H. Lamparski, D.F. O'Brien, Gelation of two-dimensional assemblies, Macromolecules 26 (1993) 398–400.

[52] E.E. Ross, L.J. Rozanski, T. Spratt, S. Liu, D.F. O'Brien, S.S. Saavedra, Planar supported lipid bilayer polymers formed by vesicle fusion. 1. Influence of diene monomer structure and polymerization method on film properties, Langmuir 19 (2003) 1752–1765.

[53] E.E. Ross, T. Spratt, S. Liu, L.J. Rozanski, D.F. O'Brien, S.S. Saavedra, Planar supported lipid bilayer polymers formed by vesicle fusion. 2. Adsorption of bovine serum albumin, Langmuir 19 (2003) 1766–1774.

[54] E.E. Ross, E. Mansfield, Y. Huang, C.A. Aspinwall, *In situ* fabrication of three-dimensional chemical patterns in fused silica separation capillaries with polymerized phospholipids, J. Am. Chem. Soc. 127 (2005) 16756–16757.

[55] D. Bloor, R.R. Chance (Eds.), Polydiacetylenes: Synthesis, Structure and Electronic Properties, Martinus Nijhoff Publishers, Dordrecht/Boston/Lancaster, 1985.

[56] K. Morigaki, H. Schönherr, T. Okazaki, Polymerization of diacetylene phospholipid bilayers on solid substrate: Influence of the film deposition temperature, Langmuir 23 (2007) 12254–12260.

[57] K. Kuriyama, H. Kikuchi, T. Kajiyama, Solid-state polymerization behaviors of crystalline diacetylene monolayers on hydrophilic surfaces, Langmuir 12 (1996) 2283–2288.

[58] K. Kuriyama, H. Kikuchi, T. Kajiyama, Molecular packings: Photopolymerization behavior relationship of diacetylene Langmuir-Blodgett films, Langmuir 12 (1996) 6468–6472.

[59] D.W. Britt, U.G. Hofmann, D. Mobius, S.W. Hell, Influence of substrate properties on the topochemical polymerization of diacetylene monolayers, Langmuir 17 (2001) 3757–3765.

[60] L. Bourdieu, D. Chatenay, J. Daillant, D. Luzet, Polymerization of a diacetylenic phospholipid monolayer at the air-water interface, J. Phys. II(4) (1994) 37–58.

[61] P. Nollert, H. Kiefer, F. Jähnig, Lipid vesicle adsorption versus formation of planar bilayers on solid surfaces, Biophys. J. 69 (1995) 1447–1455.

[62] J.M. Johnson, T. Ha, S. Chu, S.G. Boxer, Early steps of supported bilayer formation probed by single vesicle fluorescence assays, Biophys. J. 83 (2002) 3371–3379.

[63] R.P. Richter, R. Berat, A.R. Brisson, Formation of solid-supported lipid bilayers: An integrated view, Langmuir 22 (2006) 3497–3505.

[64] K. Morigaki, K. Tawa, Vesicle fusion studied by surface plasmon resonance and surface plasmon fluorescence spectroscopy, Biophys. J. 91 (2006) 1380–1387.

[65] T. Okazaki, K. Morigaki, T. Taguchi, Phospholipid vesicle fusion on micropatterned polymeric bilayer substrates, Biophys. J. 91 (2006) 1757–1766.

[66] P.Y. Chan, M.B. Lawrence, M.L. Dustin, L.M. Ferguson, D.E. Golan, T.A. Springer, Influence of receptor lateral mobility on adhesion strengthening between membranes containing LFA-3 and CD2, J. Cell Biol. 115 (1991) 245–255.

[67] M. Stelzle, R. Miehlich, E. Sackmann, Two-dimensional microelectrophoresis in supported lipid bilayers, Biophys. J. 63 (1992) 1346–1354.

[68] M.L. Wagner, L.K. Tamm, Tethered polymer-supported planar lipid bilayers for reconstruction of integral membrane proteins: Silane-polyethyleneglycol-lipid as a cushion and covalent linker, Biophys. J. 79 (2000) 1400–1414.

[69] M.A. Deverall, E. Gindl, E.K. Sinner, H. Besir, J. Ruehe, M.J. Saxton, C.A. Naumann, Membrane lateral mobility obstructed by polymer-tethered lipids studied at the single molecule level, Biophys. J. 88 (2005) 1875–1886.

[70] M. Merzlyakov, E. Li, K. Hristova, Directed assembly of surface-supported bilayers with transmembrane helices, Langmuir 22 (2006) 1247–1253.

[71] M.J. Saxton, Lateral diffusion in an archipelago: Dependence on tracer size, Biophys. J. 64 (1993) 1053–1062.

[72] N. Yamaguchi, M. Kasai, Identification of 30 kDa calsequestrin-binding protein, which regulates calcium release from sarcoplasmic reticulum of rabbit skeletal muscle, Biochem. J. 335 (1998) 541–547.

[73] P. Martínez-Landeira, J.L. López-Fontán, J.M. Ruso, G. Prieto, F. Sarmiento, Surface behaviour of C5, C6, C7 and C8 lecithins at the aqueous solution/air interface, Colloids Surf. A 216 (2003) 91–96.

[74] P. Anzenbacher, E. Anzenbacherova, Cytochromes P450 and metabolism of xenobiotics, Cell. Mol. Life Sci. 58 (2001) 737–747.

[75] K.R. Korzekwa, J.P. Jones, Predicting the cytochrome P450 mediated metabolism of xenobiotics, Pharmacogenetics 3 (1993) 1–18.

[76] Y. Ueda, K. Morigaki, Y. Tatsu, N. Yumoto, H. Imaishi, Immobilization and activity assay of cytochrome P450 on patterned lipid membranes, Biochem. Biophys. Res. Commun. 355 (2007) 926–931.

[77] H. Ellens, D.P. Siegel, D. Alford, P.L. Yeagle, L. Boni, L.J. Lis, P.J. Quinn, J. Bentz, Membrane-fusion and inverted phases, Biochemistry 28 (1989) 3692–3703.

[78] K. Simons, E. Ikonen, Functional rafts in cell membranes, Nature 387 (1997) 569–572.

[79] A. Kusumi, Y. Sako, Cell surface organization by the membranes skeleton, Curr. Opin. Cell Biol. 8 (1996) 566–574.
[80] J.T. Groves, S.G. Boxer, Electric field-induced concentration gradients in planar supported bilayers, Biophys. J. 69 (1995) 1972–1975.
[81] J. Nissen, K. Jacobs, J.O. Rädler, Interface dynamics of lipid membrane spreading on solid surfaces, Phys. Rev. Lett. 86 (2001) 1904–1907.
[82] R.N. Orth, J. Kameoka, W.R. Zipfel, B. Ilic, W.W. Webb, T.G. Clark, H.G. Craighead, Creating biological membranes on the micron scale: Forming patterned lipid bilayers using a polymer lift-off technique, Biophys. J. 85 (2003) 3066–3073.
[83] P. Moraille, A. Badia, Spatially directed protein adsorption by using a novel, nanoscale surface template, Angew. Chem., Int. Ed. 41 (2002) 4303–4306.
[84] T.Y. Yoon, C. Jeong, S.W. Lee, J.H. Kim, M.C. Choi, S.J. Kim, M.W. Kim, S.D. Lee, Topographic control of lipid-raft reconstitution in model membranes, Nat. Mat. 5 (2006) 281–285.

CHAPTER SIX

SALT-INDUCED MORPHOLOGICAL TRANSITIONS IN NONEQUIMOLAR CATANIONIC SYSTEMS: SPONTANEOUS FORMATION OF BLASTULAE AGGREGATES

Nina Vlachy,* Didier Touraud, *and* Werner Kunz

Contents

* Corresponding author. Tel.: +49 941 943 42 47; Fax: +49 941 943 45 32;
E-mail address: nina.vlachy@chemie.uni-regensburg.de

Institute of Physical and Theoretical Chemistry, University of Regensburg, D-93040 Regensburg, Germany

Advances in Planar Lipid Bilayers and Liposomes, Volume 9
ISSN 1554-4516, DOI: 10.1016/S1554-4516(09)09006-1

Abstract

The transition of catanionic micelles to vesicles upon the addition of salt was explored. The catanionic surfactant solution comprised sodium dodecylsulfate (SDS) and dodecyltrimethylammonium bromide (DTAB) with an excess of SDS. The change in aggregate size can be accommodated by the increase of counterion binding and consequent dehydration of the surfactant headgroups. A new type of intermediate structure was found: a symmetrically shaped spherical superstructure, which we named blastulae vesicle. In contrast to known raspberry-like or egg-carton structures, we believe that charge fluctuations within the bilayers are responsible for this spontaneous superaggregation to occur in the presence of only a small amount of sodium chloride. A possible mechanism for the observed pattern formation is proposed.

1. INTRODUCTION

1.1. Self-Assembly of Amphiphilic Molecules

Surfactants are molecules with an amphiphilic character that makes them particularly favorable to reside at interfaces. Their chemical structure (similar to phospholipids) consists of two parts, one which is soluble in water (the hydrophilic part) and the other which is insoluble in water (the hydrophobic part). The degree of the hydrophobic chain branching, the position of the polar head group, and the length of the chain are parameters that affect the physicochemical properties of the surfactant [1, 2].

When surfactants are dissolved in water, the hydrophobic group disrupts the hydrogen-bonded structure of water and therefore increases the free energy of the system. The distortion of the water structure can be decreased (and the free energy reduced) by the aggregation of surface-active molecules into clusters (micelles) with their hydrophobic groups directed toward the interior of the cluster and their hydrophilic groups directed toward the water. The process of surfactant clustering or micellization is primarily an entropy-driven process [1, 3]. However, the surfactant molecules transferred from the bulk solution to the micelle may experience some loss of freedom from being confined to the micelle. In addition, they may experience an electrostatic repulsion from other similarly charged surfactant molecules in the case of surfactants with ionic head groups. These forces increase the free energy of the system and oppose micellization. Hence, micelle formation depends on the force balance between the factors favoring micellization (van der Waals and hydrophobic forces) and those opposing it (kinetic energy of the molecules and electrostatic repulsion).

Beside micelles, surfactants can self-assemble in dilute aqueous solutions into a variety of other microstructures, including vesicles, bicontinuous phases, and bilayers. In recent years, there has been an increasing interest in unilamellar vesicles, which are composed of a curved bilayer that separates an inner aqueous compartment from the outer aqueous environment. This is mainly because of their wide application in biology and medicine as model cell membranes, as well as their strong potential as drug carriers and other encapsulating agents of industrial relevance [4].

The first form of a primitive cell probably was a vesicle (from lat. vesicula = blister) [5–7], a simple biological membrane composed of lipids, which separated the substance inside from the outside. If the membrane is composed of aphospholipid and cholesterol bilayer, such a vesicle is called a liposome. In 1965, Alec Bangham discovered that phospholipids, when introduced into an aqueous environment, spontaneously form liposomes. The major force driving the formation of lipid bilayers is the hydrophobic interaction between the tails and their repulsion by water. From a biological view, vesicles are appropriate compartments in which cellular processes can occur apart from cytoplasm. Accordingly, vesicles are natural containers for storage and transport inside of a cellular system. For this reason, these type of molecular aggregate is of big scientific interest [8–22]. By varying the lipid compounds the characteristics of biological membranes (and also vesicles) can be selectively controlled to fulfill different tasks [23, 24]. Due to the fact that vesicles are closed biological membranes, it is imaginable to use the coherences of biochemistry to develop best biocompatible vehicles containing pharmacological active agents. But applicable and marketable vesicle-building surfactants must have certain properties that are adapted to their convenience.

1.2. Spontaneous Formation of Vesicles

It is known for a long time that phospholipids and double-chain surfactants can form vesicles [25]. In many cases, however, the formation of vesicles requires the input of some form of energy, for example, sonication, injection, or extrusion [26–31]. However, vesicles have been found to form spontaneously in some aqueous surfactant systems, including solutions containing (i) mixtures of lecithin and lysolecithin [32], (ii) mixtures of long- and short-chain lecithins [33], (iii) mixtures of AOT and choline chloride [34], (iv) dialkyldimethylammonium hydroxide surfactants [25, 35–38], (v) cationic siloxane surfactants [39], and (vi) mixtures of cationic and anionic surfactants [40–44]. These spontaneously forming vesicles offer advantages over the more traditional phospholipid vesicles in being easier to generate and more stable, thus making them more attractive as encapsulating agents in diverse practical applications, including the controlled delivery of drugs, active substances in cosmetics, and functional food ingredients such as enzymes [45, 46]. A similar phenomenon can be observed with mixtures of cationic and anionic surfactants (here called catanionics). These systems display a wide variety of phase behavior and structures such as micelles, vesicles, discs, and folded bilayers can be observed [41, 47, 48]. Recently, new self-assembled structures, such as onion phases and icosahedra were found in "true" catanionic solutions with no other ions than the surfactant molecules [49, 50]. Spontaneously formed vesicles are of interest, especially in catanionic systems, since they can be tailored at will by varying the anionic/cationic surfactant ratio, the size of the chain length, or the nature of the polar heads [51].

Two major theoretical approaches have been pursued in the modeling of surfactant self-assembly: the curvature–elasticity approach and the molecular approach. The curvature–elasticity approach describes the vesicle bilayer as a continuous membrane characterized by the spontaneous curvature and the elastic bending modulus [52]. In this approach, the formation of finite-sized vesicles thus depends on the interplay between these two quantities [53, 54]. The theory provides an elegant, simple way to describe the formation of vesicles. However, because this approach is based on a curvature expansion of the free energy of a membrane it breaks down for small vesicles for which the curvature is quite pronounced.

The molecular approach was pioneered by Israelachvili *et al.* [55–57], who developed a geometric packing argument that allows one to predict the shape of self-assembling microstructures, including spheroidal, cylindrical, or discoidal micelles, vesicles, and bilayers. Which aggregates form is determined primarily by geometric packing of amphiphiles, hydrocarbon chain stiffness, and the hydrophilic–hydrophobic balance? For dilute solutions in which interactions between aggregates are not important, the necessary (geometric) conditions for formation of an aggregate can be described by a surfactant packing parameter $P = v/(l_{\max}a)$ [55–57], where v is the volume per hydrocarbon chain, or the hydrophobic region of the surfactant, a is the actual headgroup area in the film, and $l_{\max}$ is an optimal hydrocarbon chain length related to about 90% of the maximum extended length. The optimal stability of the different aggregates occurs as follows: (i) spherical micelles $P \leq 1/3$; (ii) globular or cylindrical micelles $1/3 < P \leq 1/2$; (iii) vesicles or bilayers $1/2 < P \leq 1$.

Low packing parameters (around 1/3) are found for single-chain surfactants with a strongly polar head group. An increase in the packing parameter can be obtained by adding a second chain, therefore doubling the hydrocarbon volume. To reach this value, double-chain surfactants [36, 38, 58–61], two surfactants of opposite charge [41, 51, 62, 63], or the association of a surfactant and a cosurfactant [64–70] can be used. In the latter two cases, a pseudo-double-chain surfactant is obtained by either an ion-pair formation between the anionic and cationic surfactant or due to an association of the two different molecules via hydrogen bounds.

1.3. Catanionic Surfactant Mixtures

The main thermodynamic driving force for the association of a cationic and an anionic surfactant mixture is the release of counterions from the aggregate surfaces. This results in a large entropy increase. Since the two surfactants are single chained, the resulting catanionic surfactant can be considered as a pseudo-double-chain surfactant, in the sense that the two chains are not covalently bound to the same headgroup. For these systems a nonmonotonic change in P is observed, with a pronounced maximum as the mixing ratio is varied [1, 3]. Due to the strong electrostatic interaction between the oppositely charged headgroups catanionic mixtures exhibit CMC values much lower than those of the surfactants involved. The CMC is directly correlated to the cleaning efficiency of surfactants, pointing to yet another advantage of such systems.

Mixtures of anionic and cationic surfactants exhibit rich microstructure phase behavior in aqueous solutions. Aggregate structures such as spherical and rod-like micelles, vesicles, lamellar phases, and precipitates have all been observed depending on the concentration and the ratio of the surfactants in solutions [43, 51, 71–75]. A zone of precipitation is observed around equimolarity. However, when one of the surfactants is present in a small excess, the cationic–anionic surfactant bilayers usually spontaneously form closed vesicles.

Yuet and Blankschtein [76] presented a detailed molecular thermodynamic theory to describe the formation of catanionic vesicles as follows:

(i) The distribution of surfactant molecules between the two vesicle leaflets plays an essential role in minimizing the vesiculation free energies of finite-sized vesicles.
(ii) The composition of mixed cationic/anionic vesicles is mainly determined by three factors: the transfer free energy of the surfactant tails, the electrostatic interactions between the charged surfactant heads, and the entropic penalty associated with the localization of the surfactant molecules upon aggregation.
(iii) The entropy associated with mixing finite-sized vesicles can be an important mechanism of stabilizing vesicles in solution. The present molecular thermodynamic theory also has the ability to cover the entire range of vesicle sizes (or curvatures), thus enabling a description of small, energetically stabilized, vesicles.

The free energy of vesiculation, g_{ves}, can be viewed as composed of the following five contributions: (i) the transfer free energy, g_{tr}, (ii) the packing free energy, g_{pack}, (iii) the interfacial free energy, g_{σ}, (iv) the steric free energy, g_{steric}, and (v) the electrostatic free energy, g_{elec}. These five free-energy contributions account for the essential features that differentiate a surfactant molecule in the vesicle and in the monomeric state. The transfer free energy, g_{tr}, reflects the so-called hydrophobic effect [77], which constitutes the major driving force for surfactant self-assembly in water. Indeed, the transfer free energy is the only favorable free-energy contribution to molecular aggregation, with the other four free-energy contributions working against this process. The hydrophobic region in a vesicle is different from bulk hydrocarbon. In a vesicle, the surfactant tails are anchored at one end on either the outer or inner interfaces, which restricts the number of conformations that each surfactant tail can adopt while still maintaining a uniform liquid hydrocarbon density in the vesicle hydrophobic region. This subtle difference between a bulk hydrocarbon phase and the hydrophobic region in a vesicle is captured by the packing free energy, g_{pack}. In addition, free-energy penalties are imposed, upon aggregation, by the creation of the outer and inner hydrocarbon/water interfaces, captured in g_{σ}, and by the steric repulsions andelectrostatic interactions between the surfactant heads, captured in g_{steric} and g_{elec}, respectively.

A distinction is made in the literature between two types of catanionic systems: (i) the "simple mixtures" of cationic and anionic surfactants or catanionic surfactant systems with excess salt, both surfactants still behold their own counterions; (ii) the "true catanionics" (ion pair amphiphiles) consist of surfactant systems where the original counterions have been removed and replaced by hydroxide and hydronium ions. The combination of the counterions at equimolarity thus forms water molecules. Each surfactant stands as counterion for the surfactant of opposite charge. The present work will focus on the first type of catanionic systems (with counterions).

1.4. Application of Catanionic Vesicles in Cosmetic and Drug Delivery

Vesicles from catanionic systems are easily prepared. There is an expectation that they might also be used in cosmetics and pharmacy as vehicles for controlled delivery of drugs [78–80]. Active molecules can thus be encapsulated in the bilayer membrane if they are lipophilic or in the core of the vesicle if they are hydrophilic. Encapsulation is useful to protect actives in preventing any undesired reaction. Vesicles can thus be used as vectors to deliver drugs to a specific place, without being destroyed. The pharmaceutical applications continuously increase and vesicles are used more and more in the dermatology for prevention, protection and therapy.

The first encapsulation experiments on catanionic systems were performed by Hargreaves and Deamer [19] on the cetyltrimethylammonium bromide/sodium dodecylsulfate system. They successfully entrapped glucose. However, the system was limited to high temperatures (>47 °C). Ten years later, Kaler *et al.* [41] proceeded with similar experiments using vesicles formed from cetyltrimethylammonium tosylate and sodium dodecylbenzenesulfonate (CTAT/SDBS) mixtures. A more comprehensive study of the entrapment ability was made by Tondre and Caillet [78] on the CTAT/SDBS and by Kondo *et al.* [44] on the didodecyltrimethylammonium bromide/sodium dodecylsulfate (DDAB/SDS) system. The surfactant concentration as well as the ratio of the two participating surfactant have proved to have a big effect on the entrapment efficiency.

Another problem is the release of the entrapped active ingredient. In most cases a nonionic surfactant is used (i.e., Triton X-100) [44]. A more elegant solution for targeted drug delivery is designing vesicles that become unstable at an easily tuned pH value. It is known that, for example, tumors and inflamed tissues exhibit a decreased extracellular pH [81–85]. For this reason a large number of groups have focused their attention on the preparation of pH-sensitive liposomes [86–96] as possible drug carrier systems.

In addition to their entrapment abilities, vesicles serve also as models for membranes of biological cells [9, 20, 21] and as templates [79, 80, 97–101] for the synthesis of nanoparticles, extraction of rare earth metal ions [102], and as gene delivery systems [103].

1.5. The Present Study

One advantage of catanionic vesicles as compared with more robust genuinely double-chain surfactants is their greater sensitivity to parameters such as temperature [104] or the presence of salts [40] used to induce transitions from vesicles to micelles or to precipitation. Of particular interest is the direct transition from micelles to vesicles. Such a phenomenon offers in principle an easy way of encapsulating active agents by dissolving them in the micellar phase prior to vesicle formation. Micelle-to-vesicle transition was already observed when diluting a micellar solution with water [51, 105, 106], changing the anionic/cationic surfactant ratio [107–109], increasing temperature [110], or upon the addition of organic additives [111] and salt [112–114].

The effect of ionic strength on catanionic systems was previously studied experimentally by Brasher *et al.* [40]. Their results show that the addition of monovalent salt changes the phase behavior and aggregate properties of mixed surfactant solutions. Theoretically the effect of salt on the catanionics was described by Yuet and Blankschtein [76]. However, due to the constrictions of the model (smeared surface charges and point-sized ions), they could not reveal the specificity of different ions.

In this chapter we explore salt-mediated transition of micelles to vesicles in a well-studied system [40, 43, 115]. We are concerned with the influence of salts on a catanionic system composed of SDS and dodecyltrimethylammonium bromide (DTAB) in aqueous solution, with an excess of anionic surfactant. Increasing amounts of sodium chloride was successively added to a solution of mixed SDS/DTAB micelles. The micellar system was first characterized by rheometric measurements and cryo-TEM. We report on the particular morphologies that arise during the salt-induced micelle-to-vesicle transition. The formation of irregular convex–concave patterns and a secondary self-assembly of vesicle-like structures upon the addition of sodium chloride is presented. In order to study this transition in detail, the concentration of salt in the system was increased in small increments and the effect was studied using dynamic light scattering (DLS), cryo- and freeze-fracture transmission electron microscopy. Two different microscopy techniques were used in order to exclude the artifacts that might arise during the preparation of samples. FF-TEM provides a direct visualization of the three-dimensional structure of particles. The fracture follows the path of least resistance, and in colloidal dispersions, the fracture surface propagates along the interface of two phases. This makes FF-TEM ideal to study membrane surfaces. To observe whether the vesicles are closed and if the membranes are intact cryo-TEM was employed. Furthermore, cryo-TEM is very appropriate to study micellar solutions.

2. EXPERIMENTAL PROCEDURES

2.1. Materials

SDS (purity: 99%) and sodium chloride were purchased from Merck, Germany. The cationic surfactant used was 99% DTAB, purchased from Aldrich, Germany. All chemicals mentioned above were used as received without further purification. Millipore water was used as solvent in all cases.

2.2. Sample Preparation

Surfactant stock solutions were prepared by dissolving weighed amounts of dried substances in Millipore water. The solutions were then left for 24 h to equilibrate at 25 °C. The catanionic solutions were prepared by mixing the surfactant stock solutions to obtain a fixed anionic/cationic surfactant mass ratio of 70/30 (this corresponds to a molar ratio of about 2.5:1). The total surfactant concentration was kept at 1 wt.% at all times. Salts were added to the micellar solution at increasing concentrations. The solutions were then stirred and left to equilibrate for a week at 25 °C before making measurements.

2.3. Dynamic Light Scattering Measurements

Particle size analysis was performed using a Zetasizer 3000 PCS (Malvern Instruments Ltd., England), equipped with a 5 mW helium neon laser with a wavelength output of 633 nm. The scattering angle was 90° and the intensity autocorrelation functions were analyzed using the CONTIN software. All measurements were performed at 25 °C.

2.4. Rheology

Rheological experiments were performed on a Brookfield DV – III+ rate controlled rheometer. A cone-and-plate geometry of 48 mm diameter and with a 0.8° cone angle was used (spindle model CP-40).

2.5. Cryo-Transmission Electron Microscopy (cryo-TEM)

Specimens for cryo-TEM were prepared by placing a small drop (ca. 4 μl) of the sample on a holey carbon grid. Immediately after blotting with filter film to obtain a thin liquid film over the grid, the sample is plunged into liquid ethane (at its melting temperature). The vitrified film is then transferred under liquid nitrogen to the electron microscope. The grid was examined with a Zeiss EM922 EF transmission electron microscope (Zeiss NTS mbH, Oberkochen, Germany). Examinations were carried out at temperatures around 90 K. The TEM was operated at an acceleration voltage of 200 kV. Zero-loss filtered images ($DE = 0$ eV) were taken under reduced dose conditions (100–1000 e/nm^2). Images were registered digitally by a bottom-mounted CCD camera system (Ultrascan 1000, Gatan, Munich, Germany) combined and processed with a digital imaging processing system (Digital Micrograph 3.9 for GMS 1.4, Gatan, Munich, Germany).

2.6. Freeze-Fracture Electron Microscopy

Samples used for cryo-fracture were cryoprotected by 30% glycerol and frozen in liquid N_2. Freeze-fracture was performed in a Balzers (Balzers, Switzerland) apparatus at −150 °C under a vacuum of 10^{-6} Torr. Metallic replicas were obtained by Pt and carbon shadowing of fracture surfaces. The replica were examined and photographed with a Philips CM 12 transmission electron microscope.

3. RESULTS

3.1. Characterization of SDS/DTAB Micellar Solution

The system under study is a well-known mixture of cationic and anionic single-chain surfactants. The total surfactant concentration (1 wt.%; ≈33 mM) and the anionic/cationic molar ratio (2.5:1) remained constant throughout all the experiments. The initial sample was colorless and isotropic, corresponding to the micellar region of the phase diagram (Fig. 1).

DLS measurements confirm a micellar solution indicating a hydrodynamic radius (R_H) of 10 nm and a relatively high polydispersity index (0.27). Figure 2 (left) shows a cryo-TEM image of our reference solution (without

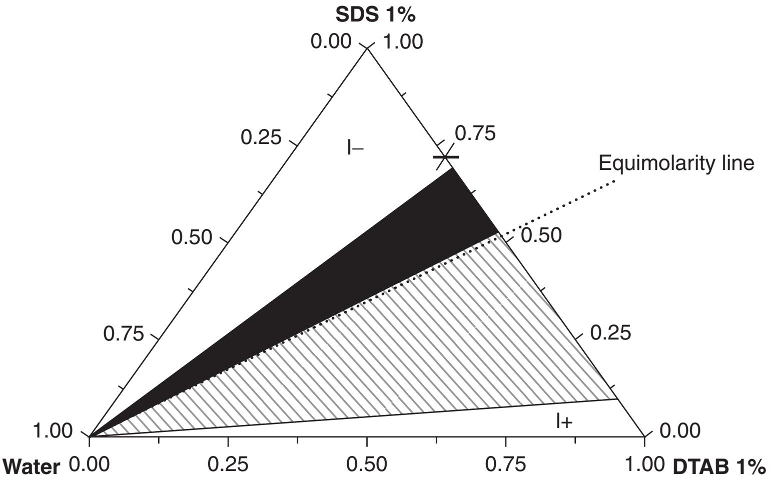

Figure 1 Schematic ternary phase diagram of the SDS/DTAB system at 25 °C (the black cross shows the starting point (reference sample), to which sodium chloride was added).

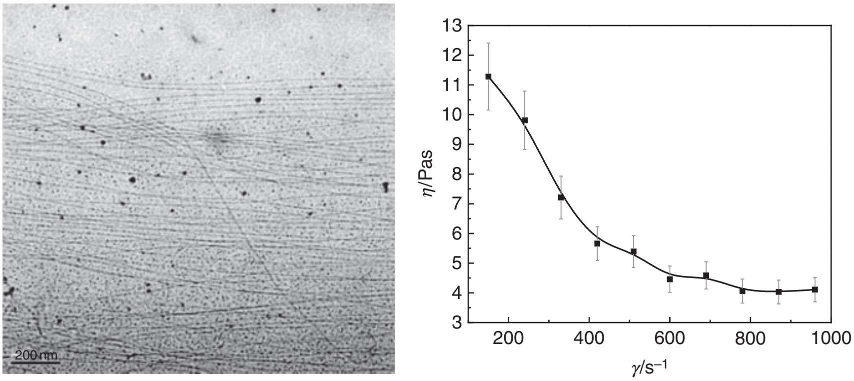

Figure 2 *Left*: cryo-TEM image of a SDS/DTAB aqueous solution at the molar ratio of 2.5:1 and a total surfactant concentration of 1 wt.%; *right*: viscosity of the same sample as a function of shear rate. Reprinted with permission of ACS, 2007, from Renoncourt *et al.* [149].

added salt), exhibiting very long rod- or ribbon-like micelles, in equilibrium with spherical micelles (hence explaining the high polydispersity). Long rod-like micelles have already been observed by SANS measurements in systems similar to ours [116]. Results from rheometry experiments show that the viscosity decreases with applied strain rate (Fig. 2 (right)), therefore exhibiting properties of non-Newtonian shear-thinning fluids. This kind of behavior is common for solutions containing large nonspherical molecules in a solvent with smaller molecules. It is generally supposed that the large molecular chains tumble at random and affect large volumes of fluid under low shear, but that they gradually align themselves in the direction of increasing shear and produce less resistance. This behavior confirms the presence of rod-like micelles. No enthalpy change could be detected by differential scanning calorimetry so that no information could be deduced about possible phase transitions occurring in the system between 10 and 80 °C [117–119]. Probably, the amount of surfactant was too low for such a detection with our equipment.

3.2. Salt-Induced Micelle-to-Vesicle Transition

Upon the addition of sodium chloride, the solutions exhibited a transition from a colorless to a blue solution, the blue color being typical of the presence of large objects. Samples with different salt concentrations were analyzed by DLS. The addition of chloride salts causes an increase in average particle size and a certain turbidity of the solution (Fig. 3). DLS indicated a significant increase in the mean hydrodynamic radius (R_H) of the micelles from 10 to ca. 70 nm. It can be expected that the salt screens the electrostatic interactions, which leads to smaller headgroups and therefore a higher packing parameter.

Freeze-fracture and cryo-TEM confirm the formation of lamellar sheets in the sample (Fig. 4). However, by carefully observing the cryo-TEM

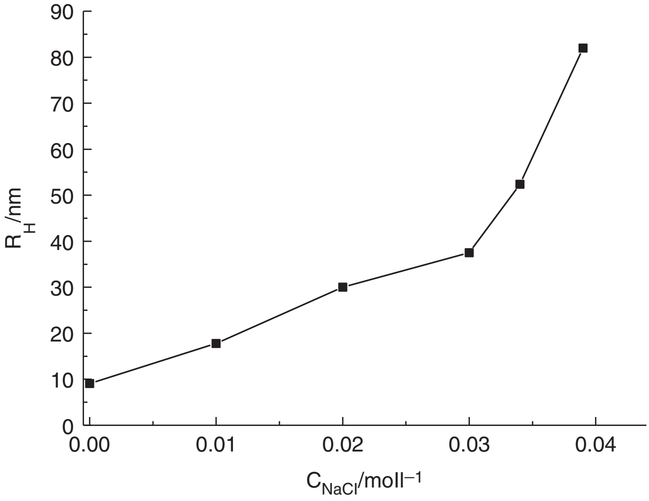

Figure 3 Increase in the mean hydrodynamic radius of catanionic aggregates upon the addition of sodium chloride.

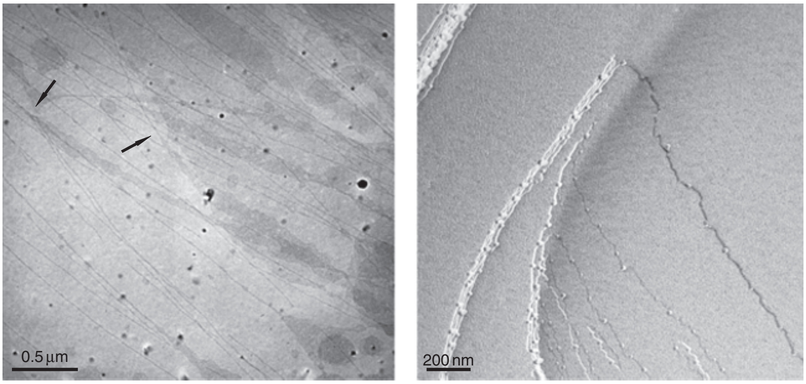

Figure 4 Cryo-TEM (left) and FF-TEM (right) photographs representing the formation of multilamellar sheets upon the addition of 10 mM NaCl. The arrows show regions where we can observe the unraveling of ribbon-like micelles into lamellar sheets. The molarity in the case of FF-TEM experiments corresponds to the concentration of the solutions prior to cryoprotecting.

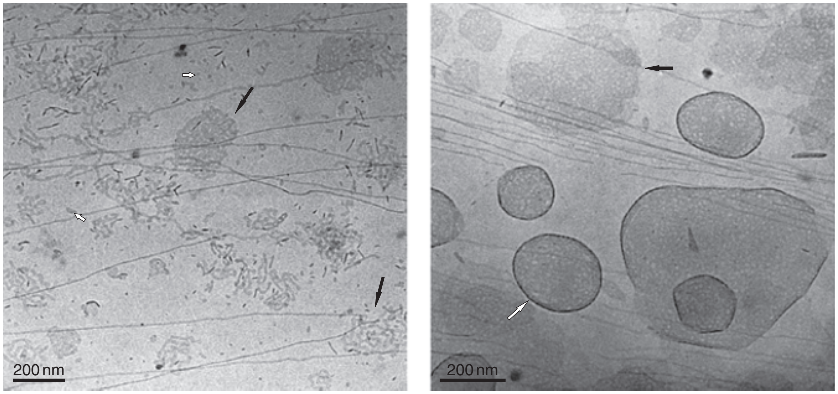

Figure 5 Cryo-TEM photographs representing the breaking up of ribbon-like micelles and consequent clustering of the pieces. Clusters of elongated aggregates are indicated by black (left), whereas individual aggregates are designated by white arrows. The image on the right shows clusters of smaller aggregates (black arrows) and vesicles with perforated surfaces (white arrows). Reprinted with permission of Elsevier, 2008, from Vlachy *et al.* [150].

images one can see that at lowest concentration of added salt (10 mM) the long rod-like micelles present in the starting solution start to break up and cluster together, see Fig. 5 (left). Other images from the same solution show that these clusters seem to form small pieces of lamellae, which eventually close to form round vesicles. The curving of membranes is represented by the presence of darker, stiff-looking edges, due to the higher electron density in these points. Figure 5 (right) shows some curved pieces of lamellar sheets as well as some complete vesicles. The vesicles represented in cryo-TEM appear to be perforated; such perforated vesicles have previously been observed in various surfactant systems [120–124]. Surprisingly, FF-TEM images do not confirm such perforations.

The addition of salt produces dramatic effects detected by freeze fracture. At 20 mM of NaCl, large spherical, highly undulated aggregates are observed. As mentioned previously, FF-TEM exploits the property that surfaces fractures along the area of least resistance. In the case of vesicles this is within the bilayer. Therefore, only three-dimensional objects can be observed. The size range of the particles is from 150 to 500 nm, see Fig. 6 (left). This apparent polydispersity is most likely due to the characterization technique used; the measured size of the object depends on the region where the samples are fractured. Some of the aggregates are fractured close to the middle; Fig. 6 (right) shows a ring of vesicles. Since the aggregates pictures in Fig. 6 are observed in high amounts, they most likely represent the same object, fractured in different places (close to the "poles" of the blastulae vesicles, as opposed to the middle of the vesicle). The images suggest that the inside of these particles are hollow and filled with the same solvent as the surrounding (water). Due to the similarities in appearance we named the observed structure blastulae, taking the name from biological origin; the blastulae are an early stage of embryonic development consisting of a spherical layer of cells surrounding a fluid-filled cavity. On the basis of the present pictures we cannot say whether the blastula vesicle is an aggregate consisting of one individual membrane or a cluster of

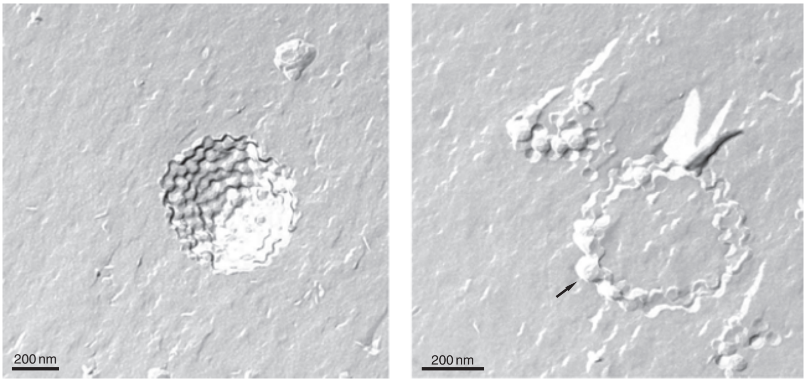

Figure 6 FF-TEM photographs representing the formation of blastulae-like clusters upon the addition of 20 mM NaCl cut near the surface (left); cut through the middle (right), clearly representing the solvent filled cavity. The arrow shows an individual vesicle with its own membrane. Reprinted with permission of Elsevier, 2008, from Vlachy *et al.* [150].

elongated micelles as observed in cryo-TEM. Both possibilities will be explored further in the text. However, it is interesting to note that some unilamellar individual vesicles are also present. Interestingly, the average diameter of the vesicles (ca. 60 nm) is of the same size as the bulges forming the blastulae structure. This might speak for the possibility that the blastula is actually a cluster of individual small vesicles. These, however, are not deformed in a way that it is usually observed in aggregates. A mechanism for this type of clustering will be discussed later, pointing to the similarity with specific site (or ligand–receptor) binding. It should be noted that similar aggregates have been observed in another context [125, 126] and will also be discussed later.

As more salt is added to the system the clusters begin to disaggregate. At sodium chloride concentrations of 30 mM only individual unilamellar vesicles are observed as can be seen in Fig. 7.

Finally, at NaCl concentrations of 40–45 mM, a loose and unstructured, randomly packed aggregation of vesicles is observed, see Fig. 8. These aggregates are not spherically symmetrical and the individual vesicles forming the aggregates are deformed.

In summary, two features are new in this system: (i) the appearance of blastulae structures, and (ii) the series of different structures that are induced by salt addition only, without any further additives.

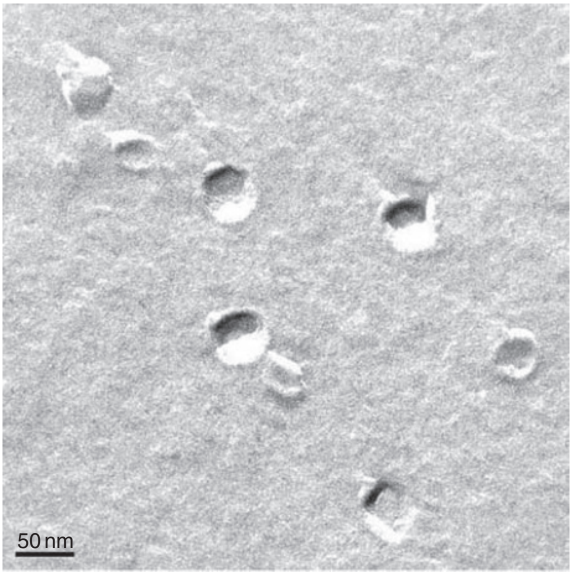

Figure 7 FF-TEM image of individual unilamellar vesicles upon the addition of 30 mM NaCl. The bar represents 100 nm.

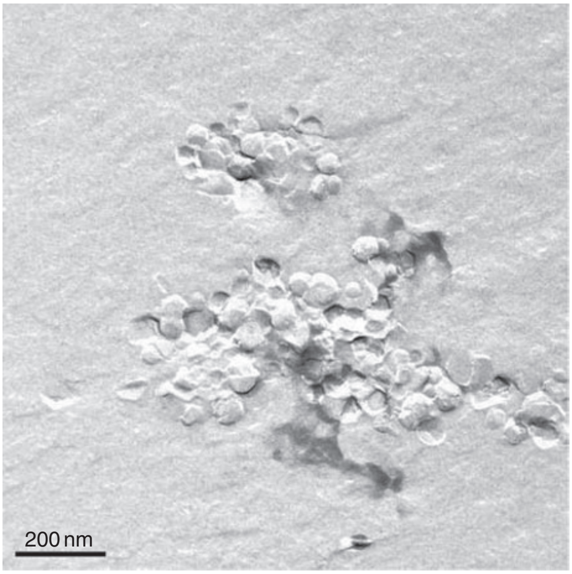

Figure 8 FF-TEM photograph representing the aggregation of vesicles upon the addition of 45 mM NaCl to the reference SDS/DTAB micellar solution. The bar represents 200 nm.

4. DISCUSSION

4.1. Models of the Micelle-to-Vesicle Transition

In the following we propose a possible mechanism for the observed pattern formation. The different steps are represented in Fig. 9.

4.1.1. Lamellar model

It is well known that as an electrolyte is added to a mixed micellar solution the effective surface area of the surfactant headgroups becomes smaller. This effect is mainly due to counterion concentration and screening as well as consequent dehydration of the neutralized heads. This effect favors a lamellar packing (step a → b′). The formation of large multilamellar sheets is energetically unfavorable, so these start curving and consequently forming large spherical objects. A theoretical model has been suggested by Safran *et al.* [54], showing that in cases of mixed surfactants vesicles are more stable than lamellar structures. This is due to the formation of surfactant bilayers, where the two monolayers consist of different surfactant concentrations, which results in equal and opposite monolayer spontaneous curvatures. This model is in accordance with our result, where the large spherical aggregates

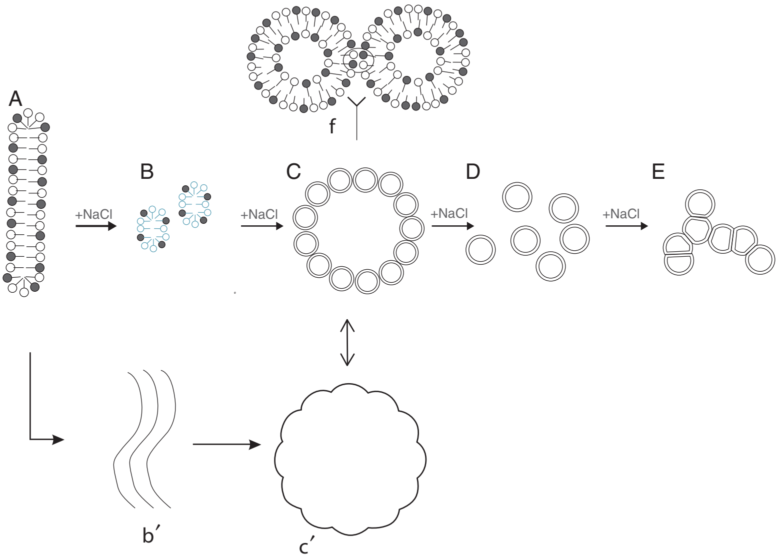

Figure 9 Schematic representation of the observed structures that form through increasing salt concentration: From the starting micellar solution, which exhibits rod-like micelles (A) two possibilities are presented: In the ''clustering model,'' the rod-like micelles (A) start breaking up into smaller pieces (B), which start clustering together to form spherical aggregates. In the ''lamellar model,'' multilamellar sheets are formed upon addition of salt (b′). These start closing to form undulated giant vesicles(c′). At higher ionic strength, the formation of blastulae clusters (C) is observed, where the outer layer is composed of individual vesicles, which enclose a fluid-filled cavity. The vesicles interact through oppositely charged headgroups of surfactants belonging to different vesicles (f; the open and filled circles represent headgroups of opposite charges). As salt concentration is further increased, the attraction is screened and the vesicles segregate (D). Still higher concentrations of salt in the system produce a nonspecific interaction, where van der Waals forces dominate, causing the vesicles to loosely aggregate while deforming (E).

are shown to form from micelles via lamellar sheets. The main factor governing the packing arrangement in these phases is the degree of hydration of the polar headgroup.

As the polar headgroups are dehydrated even more by the addition of salt, the packing parameter increases and the formation of individual vesicles is favored. In the present catanionic system the outer layer of the vesicles is composed of positively and negatively charged groups with the latter being in excess. A redistribution of charges may then take place in the highly flexible vesicle membranes leading to local patches of positive and negative charges. The locally positive charges of one vesicle can interact favorably with the negative charges of another vesicle and vice versa (Fig. 9, stage f). In other words, the vesicles can attract each other due to the +, − interactions among the headgroups of surfactants belonging to different vesicles.

This is somewhat similar to charge fluctuations in polarizable objects leading to van der Waals interactions. But the difference is that here the ion charge distribution of the headgroups fluctuates, and not the electron distribution. The local Coulomb attraction may be strong enough to overcome the overall repulsive force of equally charged vesicles acting at larger distances. Since vesicles are spontaneously formed from lamellar sheets, they are, at this starting point, in close enough contact for this to happen. In this case only localized parts of the membrane (patches) are interacting, similarly to specific site binding.

As the ion strength in the solution is increased the blastulae vesicles disaggregate. We suppose this is due to the fact that the interactions between the oppositely charged headgroups of neighboring vesicles are weaker than those within a vesicle (one must consider the additional strong van der Waals forces between the hydrophobic surfactant tails). Therefore, as more salt is added and the charges on the vesicles are screened, the ‘‘bonds’’ between the vesicles are broken. The cluster begins to disaggregate due to the net negative charge of the individual vesicles, resulting in the formation of individual unilamellar vesicles.

At still higher ionic strength the electrostatic repulsions are screened and the effect of van der Waals forces becomes significant. A loose and unstructured, randomly packed aggregation of vesicles is observed. A similar behavior (flocculation of vesicles) was observed upon the addition of NaCl to the micellar solution of dodecylbenzene sulfonic acid [127].

4.1.2. Clustering model

In this model, the ribbon-like micelles start breaking up into smaller cylindrical aggregates (corresponding to step a → b). These could be small vesicles, which grow until retaining a radius at which they are most stable (small vesicles are thermodynamically unfavorable due to high curvature). Again these aggregates start clustering together despite an overall net negative charge. Steps c → e remain the same as in the lamellar model.

4.2. Blastulae Vesicles

Microscopy images clearly show that the blastulae clusters are spherical and hollow. Figure 6 (right) shows the fluid-filled cavity and the astounding symmetry of the aggregate. The interesting phenomenon is that in this cluster the vesicles are not deformed in a way that is usually observed in aggregates. Aggregation of vesicles without accompanying deformation of membrane had until now been observed only in systems to which specific ligands and receptors were added. In such case no deformations occur when vesicles are brought together by a specific site-binding (ligand–receptor) interaction. This is because not the whole vesicle surface is involved in the interaction, but only a discrete number of contact points on each surface.

This kind of self-assembly of vesicles driven by ligand–receptor coupling was reported by Chiruvolu *et al.* and Walker *et al.* [128–130].

It is interesting to translate this concept to blastulae formation by proposing a fluctuation of the electron density in the membrane as was described above. Such a formation of localized partitions of opposite charge has been previously reported by Aranda-Espinoza *et al.* [131]. A spontaneous partitioning of positively charged mixed bilayer vesicles in the presence of negatively charged particles resulting in an electrostatic repulsion between oppositely charged particles was observed. In our case the effect is reversed, electrostatic attraction of vesicles of equal net charge are found. Recently, the asymmetry of charge in lipid bilayers induced by monovalent salts was reported. According to Gurtovenko [132], the difference in the headgroup orientation on both sides of the bilayer, coupled with salt-induced orientation of water dipoles, leads to an asymmetry in the charge density profiles and electrostatic potentials of the bilayer. In this report lipid vesicles with only one type of molecules are present. In our case, where two oppositely charged surfactants are present, the salt-induced asymmetry may be the reason for the patches of the single-charged surfactants of opposite sign. Finally, the overall shape of the blastulae formed by the "attached" vesicles can be explained by the preferential local aggregate curvature determined by geometrical constraints, obeying the same rules as the formation of vesicles from surfactants. It should be noted that the attraction of overall equally charged objects is discussed from time to time in literature [133]. The present findings and the model proposed here may help to understand such phenomena.

As far as coexistence of vesicles and micelles are concerned, intermediate structures have been reported in the literature: open vesicles, mesh phases, or even patches and discs [71, 124, 134]. However, to our knowledge such symmetrically shaped hollow structures as the blastulae vesicles have never been observed before in catanionic systems. One of the possible explanations is that blastulae are the diluted counterpart of the "oyster phase," which has been observed for other charged bilayers in the absence of salt [135].

The rationale in the sequence of observed shapes (as schematically represented in Fig. 9), when spontaneous curvature is varied via composition, is given by a general mechanism: a cocrystallization occurs, followed by a segregation of excess material. The amount of nonstoichiometric component distributes between the lattice and the edges and thus controls the shape of the crystallized colloids [136].

4.3. The Occurrence of Convex–Concave Patterns in Biological Systems

Experimentally, the occurrence of convex–concave deformations of high regularity, similar to our blastulae, was first observed in a study of lipid extracts from bacterial membranes [137, 138]. The egg carton pattern is mostly found in complex lipid mixtures of biological origin such as *Streptomyces hygroscopicus* and brain sphingomyelin [139]. Later on, this kind of curved patterns has also been observed in a few examples with a more simple composition such as in vesicles of DMPC mixed with a polymerized amphiphile with butadiene groups [140], *N*-nervonoyl sphingosylphosphorylcholine [141] both in their gel state and in systems containing the lipid complex soybean lecithin and poly(diallyldimethylammonium chloride) [142]. However, the repeating convex–concave patterns in these so-called "egg carton" structures are found on flat sheets and the objects are multilamellar vesicles with diameters largely exceeding the diameters of the bulges. By contrast, FF-TEM images of the present catanionic system show that the building blocks forming the blastulae aggregate are of the same average diameter as the individual vesicles present (ca. 60 nm) in solution. The origin of convex–concave bilayer deformation is believed to result from constraints imposed by limiting hydration of the headgroup and a frustration arising from the spontaneous curvature of the bilayers [143]. This effect had already been discussed by Gebhardt *et al.* [144]. Undulation and the formation of so-called egg carton structure had been extensively studied theoretically. A "hat and saddle" model was proposed by Helfrich [145] to explain the existence of corrugated membranes of biological origin. Fournier has shown that anisotropic inclusions can induce spontaneous bending in flat lipid membranes, which attract each other to form an egg carton structure [146, 147]. A model calculation based on bilayer bending elasticity yielding disordered egg carton textures was proposed by Goetz and Helfrich [148]. However, all these calculations are not appropriate to explain the peculiar vesicle patterns experimentally observed in present work.

4.4. Raspberry Vesicles

For the same reason the blastulae are different from the so-called raspberry vesicles. The term "raspberry vesicles" was used previously to describe convex–concave vesicles obtained after the induction of osmotic shock on giant unilamellar vesicles in different phospholipid systems [125]. The "raspberry effect" is related to the deflating of the liposome due to the volume reduction, the consequence being the existence of an excess membrane. This excess membrane induces the formation of inverted "daughter vesicles." Similar observations have been reported by Ménager and Cabuil [126] for the osmotic shrinkage of liposomes filled with a ferrofluid and in the case of liposomes subjected to a gradient of glucose [144]. However, the evolution of these vesicles is different from the one observed in our case. The initial membrane undulation of giant vesicles seems to be a common step in all cases. In the aforementioned cases, the osmotic shrinkage of vesicles was shown to be reversible which is proof of a persistent membrane neck connection between the mother and daughter vesicles. At high enough osmotic strength the membrane ruptured. No vesicles with individual membranes were observed. This is not the case in our system, where the increase of ionic strength promotes the formation of individual membranes, resulting in a spherically symmetrical cluster of unilamellar vesicles, the blastulae. Higher ionic strength results in a separation of the vesicles.

4.5. Blastulae Vesicles: A General Trend in Catanionic Systems?

Finally, we would like to report that similar images have been found also in samples containing cesium chloride and in a system composed of sodium dodecylcarboxylate and DTAB in the presence of sodium chloride (cf. Fig. 10). Further experiments and theoretical insights are necessary in order to clarify the exact mechanism of formation of such structures and the reason for this intermediate structure to be found only in catanionic systems containing salt.

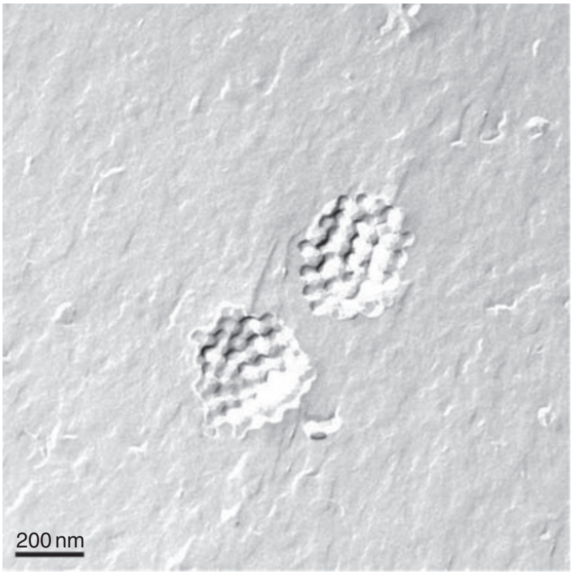

Figure 10 Blastulae vesicles in an SDS/DTAB system with the addition of 20 mM CsCl.

5. CONCLUSIONS

We have presented a way to make hollow regularly shaped structures by spontaneous secondary self-assembly of vesicles without additives except salt. These spherical, symmetrical aggregates of individual vesicles were never observed previously, even in systems with ligand–receptor binding. A mechanism of formation for this type of superstructures was proposed, showing the importance of charge fluctuation. Finally, such blastulae aggregates could be considered as an intermediate step in the formation of unilamellar vesicles from bilayers in nonequimolar catanionic systems.

REFERENCES

[1] K. Holmberg, B. Joensson, B. Kronberg, B. Lindman, Surfactants and Polymers in Aqueous Solutions, second ed., John Wiley & Sons, UK, 2003.
[2] M.J. Rosen, Surfactants and Interfacial Phenomena, second ed., John Wiley & Sons, New York, 1989.
[3] D.F. Evans, H. Wennerstroem, The Colloidal Domain, Wiley-VCH, New York, 1999.
[4] J.H. Fendler, Membrane Mimetic Chemistry, John Wiley & Sons, New York, 1982.
[5] D.W. Deamer, Role of amphiphilic compounds in the evolution of membrane structure on the early earth, Orig. Life Evol. Biosph. 17 (1986) 3–25.
[6] D.W. Deamer, J. Oro, Role of lipids in prebiotic structures, Biosystems 12 (1980) 167–175.
[7] J. Oro, S.L. Miller, A. Lazcano, The origin and early evolution of life on earth, Annu. Rev. Earth Planet. Sci. 18 (1990) 317–356.
[8] I.A. Chen, R.W. Roberts, J.W. Szostak, The emergence of competition between model protocells, Science 305 (2004) 1474–1476.
[9] I.A. Chen, J.W. Szostak, Membrane growth can generate a transmembrane ph gradient in fatty acid vesicles, Proc. Natl. Acad. Sci. USA 101 (2004) 7965–7970.
[10] P. Walde, M. Wessicken, U. Ralder, N. Berclaz, K. Conde-Frieboes, P.L. Luisi, Preparation and characterization of vesicles from mono-*n*-alkyl phosphates and phosphonates, J. Phys. Chem. B 101 (1997) 7390–7397.
[11] R. Bittman, L. Blau, Permeability behavior of liposomes prepared from fatty acids and fatty acid methyl esters, Biochim. Biophys. Acta 863 (1986) 115–120.
[12] R. Wick, P. Walde, P.L. Luisi, Self-Production of Supramolecular Structures. From Synthetic Structures to Models of Minimal Living Systems, Kluwer Academic Publishers, Dordrecht, 1994, Ch. Giant Vesicles, pp. 295–299.
[13] S. Bonaccio, C. Cescato, P. Walde, P.L. Luisi, Self-Production of Supramolecular Structures. From Synthetic Structures to Models of Minimal Living Systems, Kluwer Academic Publishers, Dordrecht, 1994, pp. 255–259.
[14] E.F. Marques, O. Regev, A. Khan, M. da Graça Miguel, B. Lindman, Vesicle formation and general phase behavior in the catanionic mixture sds-ddab-water the anionic-rich side, J. Phys. Chem. B 102 (1998) 6746–6758.
[15] S. Bonaccio, P. Walde, P.L. Luisi, Liposomes containing purine and pyrimidine bases: stable unilamellar liposomes from phosphatidyl nucleosides, J. Phys. Chem. 98 (1994) 6661–6663.

[16] H. Hoffmann, D. Greabner, U. Hornfeck, G. Platz, Novel vesicles from single-chain surfactants, J. Phys. Chem. B 103 (1999) 611–614.

[17] J.-H.S. Kuo, M.-S. Jan, C.-H. Chang, H.-W. Chiu, C.-T. Li, Cytotoxicity characterization of catanionic vesicles in raw 264.7 murine macrophage-like cells, Colloids Surf. B 41 (2005) 189–196.

[18] N. Berclaz, E. Bloechliger, M. Mueller, P. Luisi, Matrix effect of vesicle formation as investigated by cryotransmission electron microscopy, J. Phys. Chem. B 105 (2001) 1065–1071.

[19] W.R. Hargreaves, D.W. Deamer, Liposomes from ionic, single-chain amphiphiles, Biochemistry 17 (1978) 3759–3768.

[20] K. Morigaki, S. Dallavalle, P. Walde, S. Colonna, P.L. Luisi, Autopoietic self-reproduction of chiral fatty acid vesicles, J. Am. Chem. Soc. 119 (1997) 292–301.

[21] I. Chen, J.W. Szostak, A kinetic study of the growth of fatty acid vesicles, Biophys. J. 82 (2004) 988–998.

[22] A. Goto, A. Suzuki, H. Yoshioka, R. Goto, T. Imae, K. Yamazaki, P.Walde, Perspectives in Supramolecular Chemistry, Vol. 6, JohnWiley & Sons, Ltd, Chichester, 2000, (Ch. Dynamic Aspects of Fatty Acid Vesicles: pH-induced Vesicle-Micelle Transition and Dilution-induced Formation of Giant Vesicles), pp. 261–270.

[23] A.L. Lehninger, D.L. Nelson, M.M. Cox, Principles of Biochemistry, Worth Publishing, New York, 1993.

[24] F. Kamp, J.A. Hamilton, Movement of fatty acids, fatty acid analogs, and bile acids across phospholipid bilayers, Biochemistry 32 (1993) 11074–11085.

[25] J.E. Brady, D.F. Evans, B. Kachar, B.W. Ninham, Spontaneous vesicles, J. Am. Chem. Soc. 106 (1984) 4279–4280.

[26] J. Engberts, D. Hoekstra, Vesicle-forming synthetic amphiphiles, Biochim. Biopphys. Acta 1241 (1995) 323–340.

[27] A.M. Carmona-Ribeiro, Synthetic amphiphile vesicles, Chem. Soc. Rev. 21 (1992) 207–214.

[28] E. Feitosa, W. Brown, Fragment and vesicle structures in sonicated dispersions of dioctadecyldimethylammonium bromide, Langmuir 13 (1997) 4810–4816.

[29] M. Andersson, L. Hammarström, K. Edwards, Effect of bilayer phase transitions on vesicle structure and its influence on the kinetics of viologen reduction, J. Phys. Chem. 99 (1995) 14531–14538.

[30] E. Feitosa, G. Barreleiro, P.C.A. Olofsson, Phase transition in dioctadecyldimethylammonium bromide and chloride vesicles prepared by different methods, Chem. Phys. Lipids 105 (2000) 201–213.

[31] P. Saveyn, J. Cocquyt, P. Bomans, P. Frederik, M. De Cuyper, P. Van der Meeren, A ph dependent coil-to-sheet transition in a periodic artificial protein adsorbed at the air-water interface, Langmuir 23 (2007) 4775–4778.

[32] H. Hauser, Spontaneous vesiculation of uncharged phospholipid dispersions consisting of lecithin and lysolecithin, Chem. Phys. Lipid 43 (1987) 283–299.

[33] N.E. Gabriel, M.F. Roberts, Spontaneous formation of stable unilamellar vesicles, Biochemistry 23 (1984) 4011–4015.

[34] A.K. Murthy, E.W. Kaler, J.A. Zasadzinski, Spontaneous vesicles from aqueous solutions of aerosol ot and choline chloride compounds, J. Colloid. Interf. Sci. 145 (1991) 598–600.

[35] B.W. Ninham, D.F. Evans, The rideal lecture vesicles and molecular forces, Faraday Discuss, Chem. Soc. 81 (1986) 1–18.

[36] B. Ninham, D. Evans, G. Wei, The curious world of hydroxide surfactants. spontaneous vesicles and anomalous micelles, J. Phys. Chem. 87 (1983) 5020–5025.

[37] S. Hashimoto, J.K. Thomas, D.F. Evans, S. Mukherjee, B.W. Ninham, Unusual behavior of hydroxide surfactants, J. Colloid. Interf. Sci. 95 (1983) 594–596.

[38] Y. Talmon, D.F. Evans, B.W. Ninham, Science 221 (1983) 1047.
[39] Z. Lin, M. He, L.E. Scriven, H.T. Davis, Vesicle formation in electrolyte solutions of a new cationic siloxane surfactant, J. Phys. Chem. 97 (1993) 3571–3578.
[40] L.L. Brasher, K.L. Herrington, E. Kaler, Electrostatic effects on the phase behavior of aqueous cetyltrimethylammonium bromide and sodium octyl sulfate mixtures with added sodium bromide, Langmuir 11 (1995) 4267–4277.
[41] E.W. Kaler, A.K. Murthy, B.E. Rodriguez, J.A. Zasadzinski, Spontaneous vesicle formation in aqueous mixtures of single-tailed surfactants, Science 245 (1989) 1371–1374.
[42] E.W. Kaler, K.L. Herrington, A.K. Murthy, J.A.N. Zasadzinski, Phase behavior and structures of mixtures of anionic and cationic surfactants, J. Phys. Chem. 96 (1992) 6698–6707.
[43] K.L. Herrington, E.W. Kaler, D.D. Miller, J.A. Zasadzinski, S. Chiruvolu, Phase behavior of aqueous mixtures of dodecyltrimethylammonium bromide (dtab) and sodium dodecyl sulfate (sds), J. Phys. Chem. 97 (1993) 13792–13802.
[44] Y. Kondo, H. Uchiyama, N. Yoshino, K. Nishiyama, M. Abe, Spontaneous vesicle formation from aqueous solutions of didodecyldimethylammonium bromide and sodium dodecyl sulfate mixtures, Langmuir 11 (1995) 2380–2384.
[45] D.D. Lasic, Liposomes: From Physics to Applications, Elsevier Publishing Co., Amsterdam, 1993.
[46] G. Gregoriadis, Liposome Technology. Volume II: Entrapment of Drugs and Other Materials, second ed., CRC Press, Boca Raton, FL, 1988.
[47] H. Fukuda, K. Kawata, H. Okuda, Bilayer-forming ion pair amphiphiles from single-chain surfactants, J. Am. Chem. Soc. 112 (1990) 1635–1637.
[48] T. Zemb, M. Dubois, B. Demé, T. Gulik-Krzywicki, Self-assembly of flat nanodiscs in salt-free catanionic surfactant solutions, Science 283 (1999) 816–819.
[49] A. Song, S. Dong, X. Jia, J. Hao, W. Liu, T. Liu, An onion phase in salt-free zero-charged catanionic surfactant solutions, Angew. Chem. Int. Ed. Engl. 44 (2005) 4018–4020.
[50] M. Dubois, B. Demé, T. Gulik-Krzywicki, J.-C. Dedieu, C. Vautrin, S. Désert, E. Perez, T. Zemb, Self-assembly of regular hollow icosahedra in salt-free catanionic solutions, Nature 411 (2001) 672–676.
[51] M.T. Yatcilla, K.L. Herrington, L.L. Brasher, E.W. Kaler, S. Chiruvolu, J.A. Zasadzinski, Phase behavior of aqueous mixtures of cetyltrimethylammonium bromide (ctab) and sodium octyl sulfate (sos), J. Phys. Chem. 100 (1996) 5874–5879.
[52] W. Helfrich, Elastic properties of lipid bilayers theory and possible experiments, Z. Naturforsch. 28 (1973) 693–703.
[53] W. Helfrich, Helical bilayer structures due to spontaneous torsion of edges, J. Chem. Phys. 85 (1986) 1085–1087.
[54] S.A. Safran, P. Pincus, D. Andelman, Theory of spontaneous vesicle formation in surfactant mixtures, Science 248 (1990) 354–356.
[55] J.N. Israelachvili, D.J. Mitchell, B.W. Ninham, Theory of self-assembly of hydrocarbon amphiphiles into micelles and bilayers, J. Chem. Soc., Faraday Trans. 2(72) (1976) 1525–1568.
[56] J.N. Israelachvili, D.J. Mitchell, B.W. Ninham, Theory of self-assembly of lipid bilayers and vesicles, Biochem. Biophys. Acta 470 (1977) 185–201.
[57] D.J. Mitchell, B.W. Ninham, Micelles, vesicles and microemulsions, J. Chem. Soc., Faraday Trans. 2(77) (1981) 601–629.
[58] E.F. Marques, O. Regev, A. Khan, B. Lindman, Self-organization of double-chained and pseudodouble-chained surfactants: counterion and geometry effects, Adv. Coll. Interf. Sci. 100 (2003) 83–102, and references therein.

[59] M. Dubois, T. Zemb, Phase behavior and scattering of double-chain surfactants in diluted aqueous solutions, Langmuir 7 (1991) 1352–1360.

[60] D. Miller, J. Bellare, T. Kaniko, D. Evans, Control of aggregate structure with mixed counterions in an ionic double-chained surfactant, Langmuir 4 (1988) 1363–1367.

[61] M. Viseu, M. Velazquez, C. Campos, I. Garcia-Mateos, S. Costa, Structural transitions in a bicationic amphiphile system studied by light-scattering, conductivity, and surface tension measurements, Langmuir 16 (2000) 4882–4889.

[62] B.A. Coldren, H. Warriner, R. van Zanten, J.A. Zasadzinski, Lamellar gels and spontaneous vesicles in catanionic surfactant mixtures, Langmuir 22 (2006) 2465–2473.

[63] A. Shioi, T.A. Hatton, Model for formation and growth of vesicles in mixed anionic/cationic (sos/ctab) surfactant systems, Langmuir 18 (2002) 7341–7348.

[64] M. Bergmeier, H. Hoffmann, F. Witte, S. Zouraub, Vesicles from single-chain hydrocarbon surfactants and perfluoro cosurfactants, J. Colloid. Interf. Sci. 203 (1998) 1–15.

[65] M. Bergmeier, H. Hoffmann, C. Thunig, Preparation and properties of ionically charged lamellar phases that are produced without shearing, J. Phys. Chem. B 101 (1997) 5767–5771.

[66] J. Hao, H. Hoffmann, K. Horbaschek, A novel, cationic/anionic surfactant system from a zwitterionic alkyldimethylamine oxide and dihydroperfluorooctanoic acid, Langmuir 17 (2001) 4151–4160.

[67] M. Gradzielski, M. Bergmeier, M. Mueller, H. Hoffmann, Novel gel phase: A cubic phase of densely packed monodisperse unilamellar vesicles, J. Phys. Chem. B 101 (1997) 1719–1722.

[68] J. Huang, Y. Zhu, B. Zhu, R. Li, H. Fu, Spontaneous vesicle formation in aqueous mixtures of cationic surfactants and partially hydrolyzed polyacrylamide, J. Colloid. Interf. Sci. 236 (2001) 201–207.

[69] M. Gradzielski, M. Mueller, M. Bergmeier, H. Hoffmann, E. Hoinkis, Structural and macroscopic characterization of a gel phase of densely packed monodisperse unilamellar vesicles, J. Phys. Chem. B 103 (1999) 1416–1424.

[70] R. Oda, L. Bourdieu, Micelle to vesicle transition induced by cosurfactant: rheological study and direct observations, J. Phys. Chem. B 101 (1997) 5913–5916.

[71] E. Marques, A. Khan, M. Miguel, B. Lindman, Self-assembly in mixtures of a cationic and an anionic surfactant: the sodium dodecyl sulfate-didodecyldimethylammonium bromide-water system, J. Phys. Chem. 97 (1993) 4729–4736.

[72] S. Raghavan, G. Fritz, E. Kaler, Wormlike micelles formed by synergistic self-assembly in mixtures of anionic and cationic surfactants, Langmuir 18 (2002) 3797–3803.

[73] R. Koehler, S. Raghavan, E. Kaler, Microstructure and dynamics of wormlike micellar solutions formed by mixing cationic and anionic surfactants, J. Phys. Chem. B 104 (2000) 11035–11044.

[74] X. Li, H. Kunieda, Catanionic surfactants: microemulsion formation and solubilization, Curr. Opin. Colloid. Interf. Sci. 8 (2003) 327–336.

[75] M. Dubois, T. Zemb, Swelling limits for bilayer microstructures: the implosion of lamellar structure versus disordered lamellae, Curr. Opin. Colloid. Interf. Sci. 5 (2000) 27–37.

[76] P.K. Yuet, D. Blankschtein, Molecular-thermodynamic modeling of mixed cationic/anionic vesicles, Langmuir 12 (1996) 3802–3818.

[77] C. Tanford, The Hydrophobic Effect: Formation of Micelles and Biological Membranes, second ed., John Wiley & Sons, New York, 1980.

[78] C. Tondre, C. Caillet, Properties of the amphiphilic films in mixed cationic/anionic vesicles: a comprehensive view from a literature analysis, Adv. Colloid. Interf. Sci. 93 (2001) 115–134.

[79] T. Bramer, M. Paulsson, K. Edwards, K. Edsman, Catanionic drug–surfactant mixtures: phase behavior and sustained release from gels, Pharm. Res. 20 (2003) 1661–1667.

[80] H.P. Hentze, S.R. Raghavan, C.A. McKelvey, E.W. Kaler, Silica hollow spheres by templating of catanionic vesicles, Langmuir 19 (2003) 1069–1074.

[81] H. Kahler, W.V.B. Robertson, Hydrogen-ion concentration of normal liver and hepatic tumors, J. Natl. Cancer Inst. 3 (1943) 495–501.

[82] P.M. Gullino, F.H.F.H. Grantham, S.H. Smith, M. Haggerty, Modifications of the acid-base status of the internal milieu of tumors, J. Natl. Cancer Inst. 34 (1965) 857–869.

[83] K.A. Meyer, E.M. Kummerling, L. Altman, M. Koller, S.J. Hoffman, ph studies of malignant tissues in human beings, Cancer Res. 8 (1948) 513–518.

[84] J. Naeslund, K.E. Swenson, Investigations on the ph of the malignant tumors in mice and humans after the administration of glucose, Acta Obstet. Gynecol. Scand. 32 (1953) 359–367.

[85] M. Stubbs, P.M.J. McSheehy, J.R. Griffiths, C.L. Bashford, Causes and consequences of tumour acidity and implications for treatment, Mol. Med. Today 6 (2000) 15–19.

[86] M.C. De Oliveira, E. Fattal, C. Ropert, C. Malvy, P. Couvreur, Delivery of antisense oligonucleotides by means of ph-sensitive liposomes, J. Control. Release 48 (1997) 179–184.

[87] C.Y. Wang, L. Huang, Highly efficient dna delivery mediated by ph-sensitive immunoliposomes, Biochemistry 28 (1989) 9508–9514.

[88] C. Ropert, M. Lavignon, C. Dubernet, P. Couvreur, C. Malvy, Oligonucleotides encapsulated in ph sensitive liposomes are efficient toward friend retrovirus, Biochem. Biophys. Res. Commun. 183 (1992) 879–855.

[89] M.B. Yatvin, W. Kreutz, B.A. Horwitz, M. Shinitzky, ph-sensitive liposomes: possible clinical implications, Science 210 (1980) 1253–1255.

[90] X. Li, M. Schick, Theory of tunable ph-sensitive vesicles of anionic and cationic lipids or anionic and neutral lipids, Biophys. J. 80 (2001) 1703–1711.

[91] I.M. Hafez, S. Ansell, P.R. Cullis, Tunable ph-sensitive liposomes composed of mixtures of cationic and anionic lipids, Biophys. J. 79 (2000) 1438–1446.

[92] S. Simoes, J.N. Moreira, C. Fonseca, N. Duzgunes, M.C. Pedroso de Lima, Tunable ph-sensitive liposomes composed of mixtures of cationic and anionic lipids, Adv. Drug Deliv. Rev. 56 (2004) 947–965.

[93] S. Simoes, V. Slepushkin, N. Duzgunes, M.C. Pedroso de Lima, On the mechanisms of internalization and intracellular delivery mediated by ph-sensitive liposomes, Biochim. Biophys. Acta 1515 (2004) 23–37.

[94] J. Sudimack, W. Guo, W. Tjarks, R. Lee, A novel ph-sensitive liposome formulation containing oleyl alcohol, Biochim. Biophys. Acta 1564 (2002) 31–37.

[95] V. Torchilin, F. Zhou, L. Huang, ph-sensitive liposomes, J. Liposome Res. 3 (1993) 201–255.

[96] P. Venugopalan, S. Jain, S. Sankar, P. Singh, A. Rawat, S.P. Vyas, ph-sensitive liposomes: mechanism of triggered release to drug and gene delivery prospects, Pharmazie 57 (2002) 659–671.

[97] S. Mann, S. Burkett, S.A. Davis, C. Fowler, N. Mendelson, S. Sims, D. Walsh, N. Whilton, Sol-gel synthesis of organized matter, Chem. Mater. 9 (1997) 2300–2310.

[98] C. Goltner, M. Antonietti, Mesoporous materials by templating of liquid crystalline phases, Adv. Mat. 9 (1997) 431–436.

[99] R. Hoss, F. Voegtle, Templatsynthesen, Angew. Chem. 106 (1994) 389–398.

[100] C. McKelvey, E. Kaler, J. Zasadzinski, B. Coldren, H.-T. Jung, Templating hollow polymeric spheres from catanionic equilibrium vesicles: Synthesis and characterization, Langmuir 16 (2000) 8285–8290.

[101] M. Kepczynski, F. Ganachaud, P. Hemery, Silicone nanocapsules from catanionic vesicle templates, Adv. Mat. 16 (2004) 1861–1863.
[102] Z. Yuan, Z. Yin, S. Sun, J. Hao, Densely stacked multilamellar and oligovesicular vesicles, bilayer cylinders, and tubes joining with vesicles of a salt-free catanionic extractant and surfactant system, J. Phys. Chem. B 112 (2008) 1414–1419.
[103] A. Bonincontro, M. Falivene, C.L. Mesa, G. Risuleo, M.R. Pena, Dynamics of dna adsorption on and release from sds-ddab cat-anionic vesicles: a multitechnique study, Langmuir 24 (2008) 1973–1978.
[104] J.C. Amante, J.F. Scamehorn, J.H. Harwell, Precipitation of mixtures of anionic and cationic surfactants: II. Effect of surfactant structure, temperature, and ph, J. Colloid. Interf. Sci. 144 (1991) 243–253.
[105] A. Renoncourt, P. Bauduin, D. Touraud, W. Kunz, N. Azemar, C. Solans, Transition from mixed micelles to vesicles in a catanionic system of surfactants applied in cosmetics, Comunicaciones Presentadas a las Jornadas del Comite Espanol de la Detergencia 34 (2004) 273–282.
[106] N. Kamenka, M. El Amrani, J. Appell, M. Lindheimer, Mixed micelle-to-vesicle transition in aqueous nonionic phospholipid systems, J. Colloid. Interf. Sci. 143 (1991) 463–471.
[107] O. Soederman, K.L. Herrington, E.W. Kaler, D.D. Miller, Langmuir 13 (1997) 5531.
[108] A.J. O'Connor, T.A. Hatton, A. Bose, Dynamics of micelle-vesicle transitions in aqueous anionic/cationic surfactant mixtures, Langmuir 13 (1997) 6931–6940.
[109] N. Filipovic-Vincekovic, M. Bujan, I. Smit, L. Tusek-Bozic, I. Stefanic, Phase transitions from catanionic salt to mixed cationic/anionic vesicles, J. Colloid. Interf. Sci. 201 (1998) 59–70.
[110] H. Yin, Z. Zhou, J. Huang, R. Zheng, Y. Zhang, Temperature-induced micelle to vesicle transition in the sodium dodecylsulfate/dodecyltriethylammonium bromide system, Angew. Chem. Int. Ed. 42 (2003) 2188–2191.
[111] H. Yin, S. Lei, S. Zhu, J. Huang, J. Ye, Micelle-to-vesicle transition induced by organic additives in catanionic surfactant systems, Chem. Eur. J. 12 (2006) 2825–2835.
[112] L. Zhai, M. Zhao, D. Sun, J. Hao, L. Zhang, Salt-induced vesicle formation from single anionic surfactant sdbs and its mixture with lsb in aqueous aolution, J. Phys. Chem. B 109 (2005) 5627–5630.
[113] L. Zhai, G. Li, Z. Sun, Spontaneous vesicle formation in aqueous solution of zwitterionic and anionic surfactant mixture, Colloids Surf., A 190 (2001) 275–283.
[114] L. Hao, Y. Nan, H. Liu, Y. Hu, Salt effects on aqueous cationic/anionic surfactant two-phase regions, J. Dispersion Sci. Technol. 27 (2006) 271–276.
[115] A. Renoncourt, Ph.D. thesis, University of Regensburg, 2005.
[116] M. Bergstroem, J.S. Pedersen, Formation of tablet-shaped and ribbonlike micelles in mixtures of an anionic and a cationic surfactant, Langmuir 15 (1999) 2250–2253.
[117] C. Vautrin, M. Dubois, T. Zemb, S. Schmölzer, H. Hoffman, M.C. Gradzielski, Surfaces A: Physicochem. Eng. Aspects 2003, 217, Chain melting in swollen catanionic bilayers, Colloids Surf. A 217 (2003) 165–170.
[118] E.F. Marques, A. Khan, B. Lindman, A calorimetric study of the gel-to-liquid crystal transition in catanionic surfactant vesicles, Thermochim. Acta 394 (2002) 31–37.
[119] K. Tsuchiya, H. Nakanishi, H. Sakai, M. Abe, Temperature-dependent vesicle formation of aqueous solutions of mixed cationic and anionic surfactants, Langmuir 20 (2004) 2117–2122.
[120] H. Hoffmann, C.H. Thunig, U. Munkert, H.W. Meyer, W. Richter, From vesicles to the l3 (sponge) phase in alkyldimethylamine oxide/heptanol systems, Langmuir 8 (1992) 2629–2638.
[121] J. Gustafsson, G. Orädd, G. Lindblom, U. Olsson, M. Almgren, A defective swelling lamellar phase, Langmuir 13 (1997) 852–860.

[122] J. Gustafsson, G. Orädd, M. Nydén, P. Hansson, M. Almgren, Defective lamellar phases and micellar polymorphism in mixtures of glycerol monooleate and cetyltrimethylammonium bromide in aqueous solution, Langmuir 14 (1998) 4987–4996.

[123] M. Silvander, G. Karlsson, K. Edwards, Vesicle solubilization by alkyl sulfate surfactants: a cryo-tem study of the vesicle to micelle transition, J. Colloid. Interf. Sci. 179 (1996) 104–113.

[124] K. Edwards, J. Gustafsson, M. Almgren, G. Karlsson, Solubilization of lecithin vesicles by a cationic surfactant: Intermediate structures in the vesicle-micelle transition observed by cryo-transmission electron microscopy, J. Colloid. Interf. Sci. 161 (1993) 299–309.

[125] A.-L. Bernard, M.-A. Guedeau-Boudeville, L. Jullien, J.-M. di Meglio, Raspberry vesicles, Biochim. Biophys. Acta 1567 (2002) 1–5.

[126] C. Menager, V. Cabuil, Reversible shrinkage of giant magnetoliposomes under an osmotic stress, J. Phys. Chem. B 106 (2002) 7913–7918.

[127] J.B.F.N. Sein, A. Engberts, Micelle to lamellar aggregate transition of an anionic surfactant in dilute aqueous solution induced by alkali metal chloride and tetraalkylammonium chloride salts, Langmuir 11 (1995) 455–465.

[128] S. Chiruvolu, S.A. Walker, J. Israelachvili, F.J. Schmitt, D. Leckband, J.A. Zasadzinski, Higher order self-assembly of vesicles by site-specific binding, Science 264 (1994) 1753–1756.

[129] S.A. Walker, J.A. Zasadzinski, Electrostatic control of spontaneous vesicle aggregation, Langmuir 13 (1997) 5076–5081.

[130] S.A. Walker, M.T. Kennedy, J.A. Zasadzinski, Encapsulation of bilayer vesicles by self-assembly, Nature 387 (1997) 61–64.

[131] H. Aranda-Espinoza, Y. Chem, N. Dan, T.C. Lubensky, P. Nelson, L. Ramos, D.A. Weitz, Electrostatic repulsion of positively charged vesicles and negatively charged objects, Science 285 (1999) 394–397.

[132] A.A. Gurtovenko, Asymmetry of lipid bilayers induced by monovalent salt: Atomistic molecular-dynamics study, J. Chem. Phys. 122 (2005) 244902–1.

[133] B. Hribar, V. Vlachy, Evidence of electrostatic attraction between equally charged macroions induced by divalent counterions, J. Phys. Chem. B 101 (1997) 3457–3459.

[134] A. Walter, P.K. Vinson, A. Kaplun, Y. Talmon, Intermediate structures in the cholate-phosphatidylcholine vesicle-micelle transition, Biophys. J. 60 (1991) 1315–1325.

[135] B. Deme, M. Dubois, T. Gulik-Krzywicki, T. Zemb, Giant collective fluctuations of charged membranes at the lamellar-to-vesicle unbinding transition. 1. Characterization of a new lipid morphology by sans, saxs, and electron microscopy, Langmuir 18 (2002) 997–1004.

[136] M. Dubois, V. Lizunov, T.A. Meister, Gulik-Krzywicki, J.-M. Verbavatz, E. Perez, J. Zimmerberg, T. Zemb, Shape control through molecular segregation in giant surfactant aggregates, Proc. Natl. Acad. Sci. 101 (2004) 15082–15087.

[137] B. Sternberg, J. Gumpert, G. Reinhardt, K. Gawrisch, Electron microscopic and biophysical studies of liposome membrane structures to characterize similar features of the membranes of streptomyces hygroscopicus, Biochim. Biophys. Acta 898 (1987) 223–230.

[138] H.W. Meyer, W. Richter, J. Gumpert, Periodically curved bilayer structures observed in hyphal cells or stable l-form cells of a streptomyces strain, and in liposomes formed by the extracted lipids, Biochim. Biophys. Acta 1026 (1990) 171–178.

[139] H.W. Meyer, H. Bunjes, A.S. Ulrich, Morphological transitions of brain sphingomyelin are determined by the hydration protocol: ripples re-arrange in plane, and sponge-like networks disintegrate into small vesicles, Chem. Phys. Lipids 99 (1999) 111–123.

[140] E. Sackmann, T. Feder, Budding, fission and domain formation in mixed lipid vesicles induced by lateral phase separation and macromolecular condensation, Mol. Membr. Biol. 12 (1995) 21–28.

[141] V.S. Kulkarni, W.H. Anderson, R.E. Brown, Bilayer nanotubes and helical ribbons formed by hydrated galactosylceramides: acyl chain and headgroup effects, Biophys. J. 69 (1995) 1976–1986.

[142] M. Antonietti, A. Wenzel, A. Thünemann, The "egg-carton" phase: A new morphology of complexes of polyelectrolytes with natural lipid mixtures, Langmuir 12 (1996) 2111–2114.

[143] H.W. Meyer, K. Semmler, W. Rettig, W. Pohle, A.S. Ulrich, S. Grage, C. Selle, P. Quinn, Hydration of dmpc and dppc at 4c produces a novel subgel phase with convex–concave bilayer curvatures, J. Chem. Phys. Lipids 105 (2000) 149–166.

[144] C. Gebhardt, H. Gruler, E. Sackmann, On domain structure and local curvature in lipid bilayers and biological membranes, Z. Naturforsch. C Biosci. 32 (1977) 581–596.

[145] W. Helfrich, Hats and saddles in lipid membranes, Liq. Cryst. 5 (1989) 1647–1658.

[146] J.B. Fournier, Nontopological saddle-splay and curvature instabilities from anisotropic membrane inclusions, Phys. Rev. Lett. 76 (1996) 4436–4439.

[147] P.G. Dommersnes, J.B. Fournier, The many-body problem for anisotropic membrane inclusions and the self-assembly of "saddle" defects into an "egg carton", Biophys. J. 83 (2002) 2898–2905.

[148] R. Goetz, W. Helfrich, The egg carton: Theory of a periodic superstructure of some lipid membranes, J. Phys. II(6) (1996) 215–223.

[149] A. Renoncourt, N. Vlachy, P. Bauduin, M. Drechsler, D. Touraud, J.-M. Verbavatz, M. Dubois, W. Kunz, B.W. Ninham, Specific alkali cation effects in the transition from micelles to vesicles through salt addition, Langmuir 23 (2007) 2376–2381.

[150] N. Vlachy, A. Renoncourt, M. Drechsler, J.-M. Verbavatz, D. Touraud, W. Kunz, Blastulae aggregates: New intermediate structures in the micelle-to-vesicle transition of catanionic systems, J. Colloid. Interf. Sci. 320 (2008) 360–363.

CHAPTER SEVEN

TRANSFORMATION BETWEEN LIPOSOMES AND CUBIC PHASES OF BIOLOGICAL LIPID MEMBRANES INDUCED BY MODULATION OF ELECTROSTATIC INTERACTIONS

Masahito Yamazaki[1,2,*]

Contents

Abstract

Cubic phases of lipid membranes are nonbilayer membranes with connections in three-dimensional (3-D) space that have a cubic symmetry. Especially, one family of cubic (Q) phases such as Q^{224} (D surface), Q^{229} (P surface), and Q^{230} (G surface) phase, which has an infinite periodic minimal surface (IPMS) consisting of bicontinuous regions of water and hydrocarbon, have been observed in biological lipid membranes. Biomembranes having 3-D regular structures

---

* Corresponding author. Tel.:/Fax: +81 54 238 4741;
E-mail address: spmyama@ipc.shizuoka.ac.jp

[1] Integrated Bioscience Section, Graduate School of Science and Technology, Shizuoka University, 836 Oya, Suruga-ku, Shizuoka 422-8529, Japan
[2] Department of Physics, Faculty of Science, Shizuoka University, Shizuoka 422-8529, Japan

Advances in Planar Lipid Bilayers and Liposomes, Volume 9
ISSN 1554-4516, DOI: 10.1016/S1554-4516(09)09007-3

similar to cubic phases have been observed in various cells by transmission electron microscopy. It is very important to elucidate the mechanisms involved in the phase transitions between the bilayer liquid-crystalline (L_α) phase and Q phases and also to identify the factors which control these phase transitions. So far, effects of temperature, water content, and pressure on the stability of the Q phases and phase transitions between the L_α and the Q phases have been investigated. However, changes of these conditions are too severe for most cells to survive. Therefore, from a physiological point of view, it is important to find milder conditions inducing these phase transitions. Recently, we found for the first time that electrostatic interaction due to surface charges of lipid membranes is an important factor to control the stability of Q phases and to induce phase transitions between the L_α and Q phases. In lipid membranes of monoolein (MO) and negatively charged lipids such as dioleoylphosphatidic acid (DOPA) mixture, as electrostatic interactions in the membrane interface increased as a result of either an increase in the surface charge density of the membrane or a decrease in salt concentration, the most stable phase of these lipid membranes changed as follows: $Q^{224} \Rightarrow Q^{229} \Rightarrow L_\alpha$. The surface charges in MO membrane due to the adsorbed charged peptides had the same effect as the charged lipids; as the peptide concentration increased (and thereby the surface charge density of the MO membrane due to the bound peptide increased), the most stable phase of the MO membrane changed as follows: $Q^{224} \Rightarrow Q^{229} \Rightarrow L_\alpha$. Changes of the electrostatic interaction due to the surface charges in aqueous solution are mild for cells, and this interaction can also be controlled by ions, pH, and peptides. Low concentrations of Ca^{2+} induced an irreversible transformation of bilayer membranes of dioleoylphosphatidyl-glycerol (DOPG)/MO to cubic phases, and pH changes induced the reversible phase transitions between L_α and cubic phases in dioleoylphosphatidylserine (DOPS)/MO membranes. Positively charged peptides induced a Q^{229} to Q^{230} phase transition in DOPA/MO membranes. On the basis of these results, we have proposed that in cells transformations between the Q phases and the bilayer membranes would occur by the modulation of the electrostatic interactions due to the surface charges.

1. INTRODUCTION

Biomembranes and lipid membranes usually form planar bilayer membranes in the liquid-crystalline (L_α) phase. However, it is well known that under some conditions lipid membranes form nonbilayer membranes such as hexagonal II (H_{II}) phase (Fig. 1A), interdigitated gel ($L_\beta I$) phase (Fig. 1B), and cubic (Q) phases (Fig. 2). The Q phases of lipid membranes are nonbilayer membranes with connections in three-dimensional (3-D) space which have a cubic symmetry. One family of the Q phases, which includes Q^{224} phase (Schwartz' D surface, or diamond surface) (Fig. 2A), Q^{229} phase (P surface) (Fig. 2C) and Q^{230} phase (G surface or gyroid

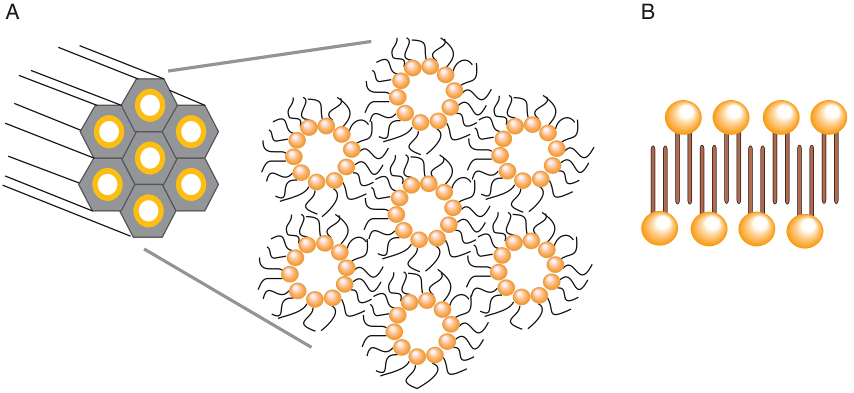

Figure 1 Structures of (A) hexagonal II (H_{II}) phase and (B) interdigitated gel ($L_{\beta}I$) phase.

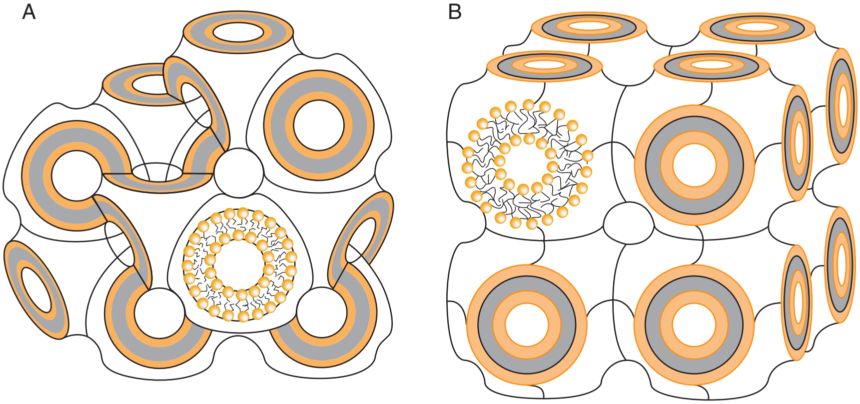

Figure 2 Structures of (A) Q^{224} phase (Schwartz' D surface, or diamond surface) and (B) Q^{229} phase (P surface).

surface), has an infinite periodic minimal surface (IPMS) (or triply periodic minimal surface) consisting of bicontinuous regions of water and hydrocarbon [1, 2]. The minimal surface has zero mean curvature ($H = (C_1 + C_2)/2 = 0$, where C_1 and C_2 are the principal curvatures, that is, the maximum and the minimum of the normal curvatures at a point in the surface) and negative Gaussian curvature ($K = -C_1 \cdot C_2 = -C_1^2 < 0$) at all points [2, 3]. Figure 3 shows three kinds of example of the minimal surface; (A) catenoid, (B) helicoid, and (C) Scherk. It is well known that the Bonnet transformation from helicoid to catenoid occurs without changing the Gaussian curvature, zero mean curvature, and length and angles defined at corresponding points [3]. In the Q phase membranes, the minimal surface is

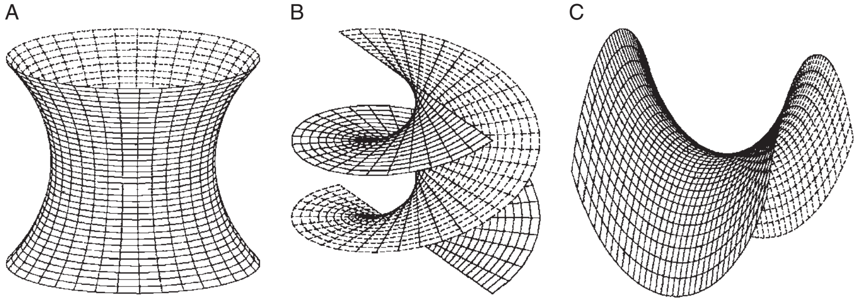

Figure 3 Example of the minimal surface: (A) catenoid, (B) helicoid, and (C) Scherk.

located at the bilayer midsurface, which is the interface of two monolayer membranes. Figure 4 shows the images of the minimal surfaces of Schwarz' D surface and Schwarz' P surface drawn by the Surface Evolver program. In the Q^{224} phase (D surface), four water channels meet at tetrahedral angle (109.5°) in the node of the D surface in a rhombic dodecahedron (Fig. 4C) and also two interwoven tetrahedral networks of rodlike water channels are arranged on a double-diamond lattice. In the Q^{229} phase (P surface), six water channels meet at orthogonal angle (90°) in the center of the cubical unit cell (Fig. 4D). The Q phases and their structures have been identified using small-angle X-ray scattering (SAXS) (Table 1) [1, 4–7]. The Q^{224} phase, the Q^{229} phase, and the Q^{230} phase are a primitive Q phase of space group *Pn*3*m*, a body-centered Q phase of space group *Im*3*m*, and a body-centered cubic phase of space group *Ia*3*d*, respectively. Freeze-fracture electron microscopy and NMR spectroscopy also have provided valuable information for determination of the phase and structure of the Q phases [8]. These Q phases have a different topology from spheres (Table 1). The topology of a surface is defined by the genus per unit cell, g (i.e., the number of handles or holes attached to a spherical surface), and Euler characteristics, χ (i.e., in the case of a polyhedron, the number of vertex + the number of face − the number of edge) [2, 3]. The relationship between χ and g is $\chi = 2(1 - g)$. According to the Gauss–Bonnet theorem, the topology (i.e., the Euler characteristics or the genus) is related to average value of Gaussian curvature of the membrane over a unit cell, $\langle K \rangle$, as follows [2, 3]:

$$\langle K \rangle = \frac{2\pi\chi}{A} = \frac{4\pi(1-g)}{A}$$

where A is the total surface area of the minimal surface per unit cell. Thereby, the transformation between the Q phases and a sphere (or a plane) requires some kinds of rupture and fusion of surfaces to change the topology.

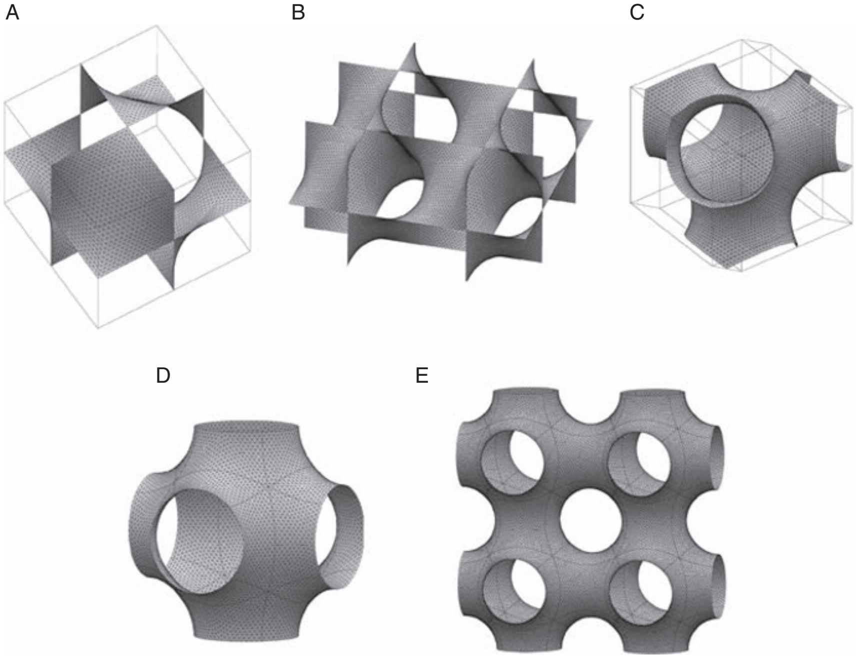

Figure 4 The images of Schwartz' D surface (corresponding to the Q^{224} phase) (A–C) and Schwarz' P surface (corresponding to the Q^{229} phase) (D, E) drawn by the Surface Evolver program developed by Dr. Ken Brakke. (A) a cubical unit cell of the D surface, (B) four cubical unit cells of the D surface, (C) the D surface in a rhombic dodecahedron, (D) a cubical unit cell of the P surface, and (E) four cubical unit cells of the P surface.

So far extensive studies on structures and phase stability of the H_{II} phase and the $L_{\beta}I$ phase have been conducted (e.g., [9–15]), but direct information on existence of biomembranes in the H_{II} phase or those in the $L_{\beta}I$ phase in cells has not been reported yet. In contrast, 3-D regular structures of biomembranes similar to the Q phases have been observed in various cells using transmission electron microscopy (TEM). Some of them were identified as cubic membranes using the direct template correlative (DTC) matching method based on pattern and symmetry recognition between the TEM micrographs and theoretical computer-generated projections of IPMSs [2, 16, 17]; for example, Q phase membranes are formed in prolamellar bodies (PLBs) of various plants [18–20], organized smooth endoplasmic reticulum (OSER) [17, 21], and mitochondrial inner membrane in starved amoeba (*Chaos carolinensis*) [22, 23]. It is considered that several kinds of environmental changes may induce the transformation between these Q membranes and bilayer membranes [6, 17].

Table 1 Three kinds of IPMS cubic phases of biological lipid membranes

Cubic phase	Schwartz surface	Space group	The ratio of reciprocal spacing of SAXS reflections	Cubic aspect	χ
Q^{224}	D (Diamond)	*Pn3m*	$\surd 2:\surd 3:\surd 4:\surd 6:\surd 8:\surd 9:\surd 10:\surd 11:\surd 12:\surd 14$	#4	−16
Q^{229}	P	*Im3m*	$\surd 2:\surd 4:\surd 6:\surd 8:\surd 10:\surd 12:\surd 14:\surd 16:\surd 18:\surd 20$	#8	−4
Q^{230}	G (Gyroid)	*Ia3d*	$\surd 6:\surd 8:\surd 14:\surd 16:\surd 20:\surd 22:\surd 24$	#12	−8

In membrane fusion and vesicle fission, topological changes of biomembranes (or lipid membranes) occur, and thereby, to reveal their molecular mechanisms the elucidation of the mechanism of any kinds of topological changes of lipid membranes is valuable [24, 25]. The physical properties of the Q phases may play an important role in a control of functions of membrane proteins and ultrastructural organizations inside cells [6, 26]. Recently, it was elegantly shown that the Q phases are also very useful for crystallization of membrane proteins [27–29].

Therefore, it is very important to elucidate the mechanism for the stability of the Q phases of biomembranes, especially; the mechanisms involved in the phase transitions between the Q and the L_α phases and also to identify the effective factors which control these phase transitions. Several factors have been reported to affect the stability of the Q phases. Among them, temperature and water content have been vigorously investigated (Table 2). In most cases, increasing temperature or decreasing water content induces transitions from the L_α to the Q phases. For example, at low water contents, phosphatidylcholine (PC) membranes form the Q phases [8]. In didodecyl phosphatidylethanolamine (DDPE) membrane, as temperature increases, the most stable phase of this membrane changed in high-temperature range (100−140 °C) as follows: $L_\alpha \Rightarrow Q^{229} \Rightarrow Q^{224} \Rightarrow H_{II}$ [30]. In *N*-methylated dioleoylphosphatidylethanolamine, as temperature increases, an L_α to Q phase transition occurs at 62 °C [31]. In membranes of 2:1 fatty acid/PC mixture, as water content is decreased, the most stable phase of these lipid membranes changed in temperature range (35−49 °C) as follows, $L_\alpha \Rightarrow Q^{229} \Rightarrow Q^{224} \Rightarrow Q^{230}$ [32]. In didodecyl alkyl *β*-D-glucopyranosyl-*rac*-glycerol membrane, as water content is decreased, the most stable phase of these lipid membranes changed in temperature range (50−70 °C) as follows: $Q^{224} \Rightarrow Q^{230}$ [33]. Several theoretical investigations on the effects of water contents and temperature have been published (e.g., [34–41]).

Table 2 Temperature or water content-induced phase transitions between IMPS cubic phases and those between the Q phases and the L_α phase

Lipid membrane	Water content (wt%)	Temperature range (°C)	Phase	Reference
Didodecyl-PE (DDPE)	≥50%	80–140	$L_\alpha \Rightarrow Q^{229} \Rightarrow Q^{224} \Rightarrow H_{II}$ as temperature increases	[30]
N-methylated DOPE	Excess	Phase transition temperature: 62	$L_\alpha \Rightarrow Q^{229}$ as temperature increases	[31]
Fatty acid/PC (2:1)	40–50%	35–49	$Q^{229} \Rightarrow Q^{224} \Rightarrow Q^{230}$ as water content decrease	[32]
Didodecyl alkyl β-D-glucopyranosyl-*rac*-glycerol	<30–40% Q^{230}	50–70	$Q^{224} \Rightarrow Q^{230}$ as water content decrease	[33]
Monoolein (MO)	<30% Q^{230}, L_α	<80	$Q^{224} \Rightarrow Q^{230} \Rightarrow L_\alpha$ as water content decrease	[4,34]

Recently, investigations on kinetics of the interconversion between the Q phases and the phase transition between the Q and the L_α phase have been started [42, 43].

However, these conditions are too severe for most cells to survive. Especially, homoiotherms such as mammalian and birds live at constant temperature, and thereby it is difficult for them to survive at higher temperature than normal one. Water contents in most animals and plants range from 60% to 80% (w/w), and thereby it is difficult for them to survive under the dry conditions whose water contents are less than 60%. Therefore, from a physiological point of view, it is necessary to find milder conditions for the formation of the Q phases and the phase transition between the Q phases and the L_α phase. About 10 years ago, I proposed a hypothesis that electrostatic interactions due to surface charges might induce phase transitions between the Q and the L_α phase, because the electrostatic interaction due to the surface charges is mild and biomembranes of most cells contain negatively charged lipids (such as phosphatidylserine (PS), phosphatidic acid (PA), and phosphatidylglycerol (PG)) whose content is about 20 mol% among total lipids (Interestingly, most biological cells do not contain positively charged lipids, indicating that during the evolution of life the negatively charged lipids were selected for biomembranes.). Thereby, cells used this electrostatic interaction to control the structures and the interactions of proteins. For example, myristoylated alanine-rich C kinase substrate (MARCKS) and src ($pp60^{src}$) can be bound with lipid membranes using both the electrostatic attractive interaction between the negatively charged lipid membranes and the positively charged domain of these proteins and the hydrophobic interaction due to the covalently linked fatty acid [44, 45]. Our groups started a project to check the validity of my hypothesis on the effect of the electrostatic interactions due to surface charges on the stability of the Q phases of biological lipid membranes. As a result, fortunately, we found for the first time that electrostatic interactions due to surface charges is an important factor to control the stability of the Q phases and to induce phase transitions between the L_α and the Q phases [46, 47]. Next, we developed a different approach which examines the effect of electrostatic interactions on the stability of the Q phases. To increase the surface charge density of the MO membrane, a charged peptide which can bind with the electrically neutral membrane interface was used instead of the negatively charged lipids [48]. As the peptide concentration increased, the most stable phase of the MO membrane changed as follows: $Q^{224} \Rightarrow Q^{229} \Rightarrow L_\alpha$. Moreover, other kinds of positively charged peptides induced a Q^{229} to Q^{230} phase transition [49]. Further, we found that change of Ca^{2+} and H^+ concentration induced phase transition from L_α to the Q phases [50, 51].

2. EFFECTS OF SURFACE CHARGES DUE TO CHARGED LIPIDS ON THE STABILITY OF THE Q PHASES

To reveal the effects of electrostatic interactions on the stability of the Q phases of biological membranes, at first we incorporated negatively charged lipids into electrically neutral lipid membranes in the Q phases, and investigated the effects of surface charges of the lipid membranes on the stability of the Q phases. As the host membrane in the Q phase, 1-monooleoyl-*rac*-glycerol (monoolein; MO) (Fig. 5A) membrane was used, because MO is one of the important biological lipids, which has a basic structure of glycerophospholipids, and the Q phases of the MO membrane have been extensively studied so far. It is well known that the MO membrane in excess water is in the Q^{224} phase, and at low water contents it is in the Q^{230} phase [4, 34]. As the first example, we describe the effect of a negatively charged lipid, dioleoylphosphatidic acid (DOPA) (Fig. 5B) on phases and structures of the MO membranes [47].

We investigated effects of DOPA concentration (mol%) in DOPA/MO membranes on their structures in 10 mM PIPES buffer (pH 7.0) under excess water condition at 20 °C using SAXS. Addition of small amounts of DOPA into the MO membrane changed its structure greatly. The SAXS pattern of 0.3%-DOPA/99.7%-MO membrane is similar to that of 100% MO membrane (Fig. 6A, C), which corresponds to the Q^{224} phase. On the other hand, the SAXS pattern of 2.0%-DOPA/98%-MO membrane shows a different kind of pattern (Fig. 6B, C), which corresponds to the Q^{229} phase. Figure 6D shows that dependence of the lattice constant (here, we

A

1-Monooleoyl-*rac*-glycerol (MO)

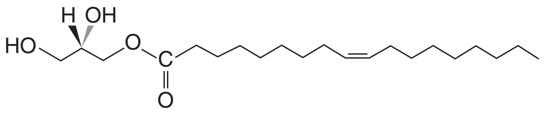

B

1, 2-Dioleoyl-*sn*-Glycero-3-Phosphate (DOPA)

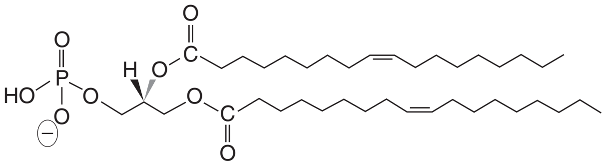

Figure 5 Structure of (A) MO and (B) DOPA.

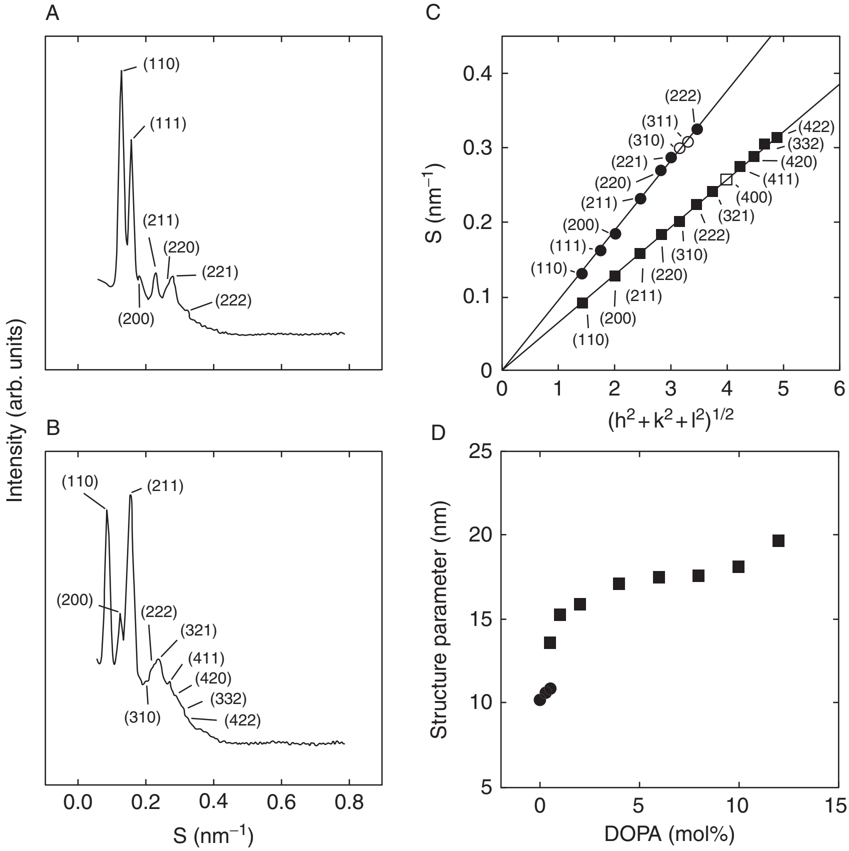

Figure 6 (A) A SAXS profile of 0.3%-DOPA/99.7%-MO membrane in excess 10 mM PIPES buffer (pH 7.0) at 20 °C. Several peaks had spacings in the ratio of √2:√3:√4:√6:√8:√9:√10:√11:√12, indexed as (1 1 0), (1 1 1), (2 0 0), (2 1 1), (2 2 0), (2 2 1), (3 1 0), (3 1 1), and (2 2 2) reflections. This corresponds to a primitive Q phase of space group *Pn*3*m* (Q^{224}) (cubic aspect #4). (B) A SAXS profile of 2.0%-DOPA/98%-MO membrane in excess 10 mM PIPES buffer (pH 7.0) at 20 °C. Several peaks had spacings in the ratio of √2:√4:√6:√8:√10:√12:√14:√16:√18:√20:√22:√24, indexed as (1 1 0), (2 0 0), (2 1 1), (2 2 0), (3 1 0), (2 2 2), (3 2 1), (4 0 0), (4 1 1), (4 2 0), (3 3 2), and (4 2 2) reflections on a body-centered Q phase of space group *Im*3*m* (Q^{229}) (cubic aspect #8). (C) Indexing of the SAXS data of the (A) (●) and (B) (■). The open symbols (○, □) show reflections which, although allowed by the space group, were not clearly observed due to weak intensities. The reciprocal spacing, *S*, of the cubic phase is connected with the lattice constant, *a*, by $S\ (h, k, l) = (1/a)\ (h^2 + k^2 + l^2)^{1/2}$, where *h, k*, and *l* are Miller indices. The lattice constant (structure parameter), *a*, of the Q phase can be determined by the gradient of the plot in (C). The lattice constant of (A) the 0.3%-DOPA/99.7%-MO and (B) 2.0%-DOPA/98%-MO membranes were 10.7 and 15.7 nm, respectively. (D) The structure parameter, that is, the lattice constant *a* of the Q phases of DOPA/MO membranes containing various concentrations of DOPA (mol%) in 10 mM PIPES buffer (pH 7.0) under excess water condition at 20 °C determined by SAXS. (●) denotes the Q^{224} phase and (■) denotes the Q^{229} phase. These figures are reprinted from Ref. [47] with permission from the American Biophysical Society.

call it the structure parameter to use this word for different kinds of phases) and kind of cubic phase on DOPA concentration in DOPA/MO membranes. Less than 0.5% DOPA, DOPA/MO membranes are in the Q^{224} phase. At 0.5% DOPA, a phase transition from the Q^{224} to the Q^{229} phase occurs, and above 0.5% DOPA, DOPA/MO membranes are in the Q^{229} phase. At 0.5% DOPA, both the Q^{224} and the Q^{229} phases coexist, and the lattice constant for the Q^{224} and the Q^{229} phase are 10.9 and 13.6 nm, respectively. Thereby, the ratio of the lattice constant (Q^{229}/Q^{224}) was 1.25, which is close to the theoretical value (1.28) determined by the analysis of the coexisting cubic phases based on the Bonnet transformation from the P to the D surface [34, 52]. The lattice constant of the membranes gradually increased with an increase in DOPA concentrations. Above 12% DOPA, peaks in SAXS pattern are broad, and thereby it was difficult to analyze it. Similar results were obtained in the effect of a negatively charged fatty acid, oleic acid (OA) on the structure and the phase of OA/MO membrane at neutral pH [46].

To elucidate the effects of high concentrations of DOPA in the DOPA/MO membranes, we investigated structures of DOPA/MO membranes at high lipid concentrations (30 wt% lipids, i.e., 70 wt% water) in 10 mM PIPES buffer (pH 7.0). At and above 25% DOPA, a new set of SAXS peaks appeared with a large spacing (11.3 ± 0.5 nm) in the ratio of 1:2:3 (Fig. 7A), which is consistent with an L_α phase. Figure 7B shows a detailed

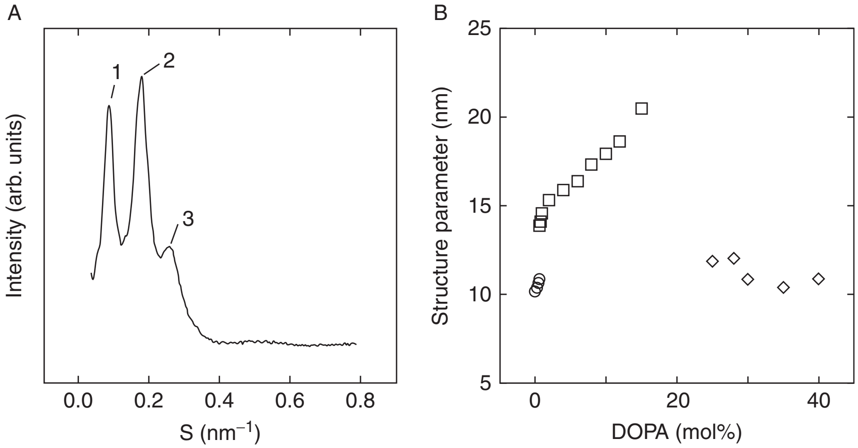

Figure 7 (A) A SAXS profile of 40%-DOPA/60%-MO membrane in 10 mM PIPES buffer (pH 7.0) at 30 wt% lipid condition at 20 °C. The spacing of L_α phase is 11.4 nm. (B) The structure parameter of DOPA/MO membranes containing various concentrations of DOPA (mol%) in 10 mM PIPES buffer (pH 7.0) at 30 wt% lipid condition at 20 °C determined by SAXS. (○), (□), and (◇) denote the Q^{224} phase, the Q^{229} phase, and the L_α phase, respectively. These figures are reprinted from Ref. [47] with permission from the American Biophysical Society.

dependence of the spacing and the structure of DOPA/MO membrane on DOPA concentration (mol%). SAXS patterns of the DOPA/MO membranes containing less than 13% DOPA under this condition are almost the same as those in excess water. At 0.6% DOPA, a phase transition from the Q^{224} to the Q^{229} phase occurs, and both the phases coexist, where the ratio of the lattice constant (Q^{229}/Q^{224}) is 1.27. The lattice constant of the DOPA/MO membrane in the Q^{229} phase gradually increases from 14.6 to 20.5 nm with an increase in DOPA concentration from 1.0% to 15%. At 16–24% DOPA, it was difficult to specify the phase. At and above 25% DOPA ($\leq$40%), the spacing (i.e., the structure parameter) of the L_α phase is almost constant. The condition of these membranes in the L_α phase is not in excess water, because the intermembrane distance of the DOPA/MO-multilamellar vesicle (MLV) is very large due to the electrostatic repulsion between the membranes and also the water content is not enough (70 wt% water). Thereby, the spacing does not change as the DOPA concentration increases. On the other hand, we found that giant unilamellar vesicles (GUVs) of DOPA/MO membranes containing more than 25 mol% DOPA were formed under excess water conditions. This result indicates that these membranes are in the L_α phase under excess water conditions, supporting the above conclusion based on the SAXS experiments.

The important factors to determine the electrostatic interactions of biomembranes (or lipid membranes) in a buffer are the surface charge density of the membranes and the electrolyte concentration in the buffer such as Na^+ and Cl^-. As the surface charge density of the lipid membranes increases or as the electrolyte concentration in solution decreases, the electrostatic interactions in the solution increase [53]. Thereby, to reveal whether the electrostatic interactions play an important role in the DOPA-induced phase transition, it is necessary to investigate the dependence of NaCl concentration on structures of these membranes under excess water condition. For example, in the case of 10%-DOPA/90%-MO membrane in 10 mM PIPES buffer (pH 7.0), which is in the Q^{229} phase in the absence of NaCl (Fig. 6D), with an increase in NaCl concentration, at 60 mM NaCl, a phase transition from the Q^{229} to the Q^{224} phase occurs, and the lattice constant of the Q^{224} phase gradually decreases with an increase in NaCl concentration (Fig. 8A). At high NaCl concentrations ($\geq$1.5 M), the membrane is in the H_{II} phase. Next, we show the effect of NaCl on the structure of 30%-DOPA/70%-MO membrane, which is in the L_α phase in the absence of NaCl. At and above 0.50 M NaCl (less than 0.75 M NaCl), the SAXS patterns show that the membranes are in the Q^{224} phase and that the lattice constant of the Q^{224} phase gradually decreases with an increase in NaCl concentration (Fig. 8B). At high NaCl concentrations ($\geq$0.65 M), the membranes are in the H_{II} phase. These results indicate that as NaCl

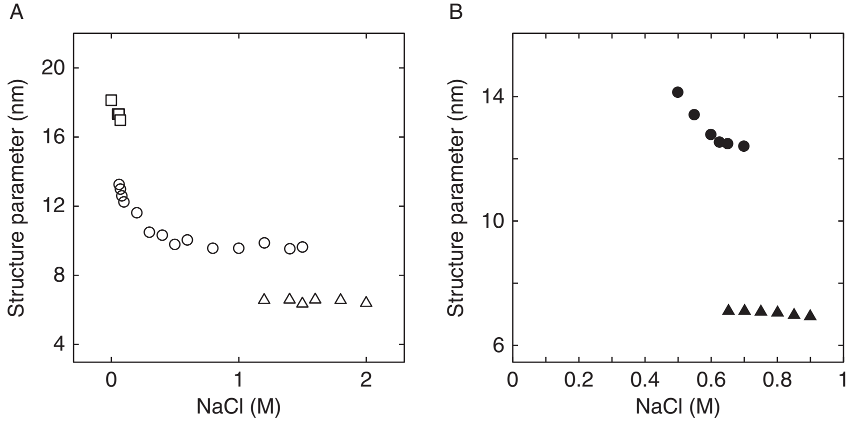

Figure 8 (A) The structural parameter (i.e., the lattice constant *a* of the Q phases and the basis vector length *d* of the H_{II} phase) of the 10%-DOPA/90%-MO membranes in 10 mM PIPES buffer (pH 7.0) containing various concentrations of NaCl (M) at 20 °C determined by SAXS. (□), (○), and (Δ) denote the Q^{229} phase, the Q^{224} phase, and the H_{II} phase, respectively. (B) The structural parameter of the 30%-DOPA/70%-MO membranes in 10 mM PIPES buffer (pH 7.0) containing various concentrations of NaCl (M) at 20 °C determined by SAXS. (●) and (▲) denote the Q^{224} phase and the H_{II} phase, respectively. These figures are reprinted from Ref. [47] with permission from the American Biophysical Society.

concentration increases, it becomes difficult to occur the DOPA-induced phase transitions and the phases of the DOPA/MO membranes returns to the original phase of the MO membrane; the Q^{229} phase changes into the Q^{224} phase, and the L_α phase transforms into the Q^{224} phase. The Poisson–Boltzmann theory shows that the increase in salt concentration induces the decrease in the electrostatic interactions due to the screening of the electrical potential [53]. Therefore, the effect of the salt concentration on the DOPA-induced phase transitions indicates that the main factor of these phase transitions is the electrostatic interactions due to the surface charges of DOPA/MO membranes. We conclude that as electrostatic interactions in the membrane interface increases as a result of either an increase in the surface charge density of the membrane or a decrease in salt concentration, the most stable phase of these lipid membranes changes as follows: $Q^{224} \Rightarrow Q^{229} \Rightarrow L_\alpha$ (Fig. 9).

After the publication of the paper [47] on the effect of DOPA on phase of MO membranes, other groups reported similar results that the MO membranes containing high concentrations of a negatively charged lipid such as dioleoylphosphatidylserine (DOPS) or dioleoylphosphatidylglycerol (DOPG) were in the L_α phase [54, 55], supporting our conclusion.

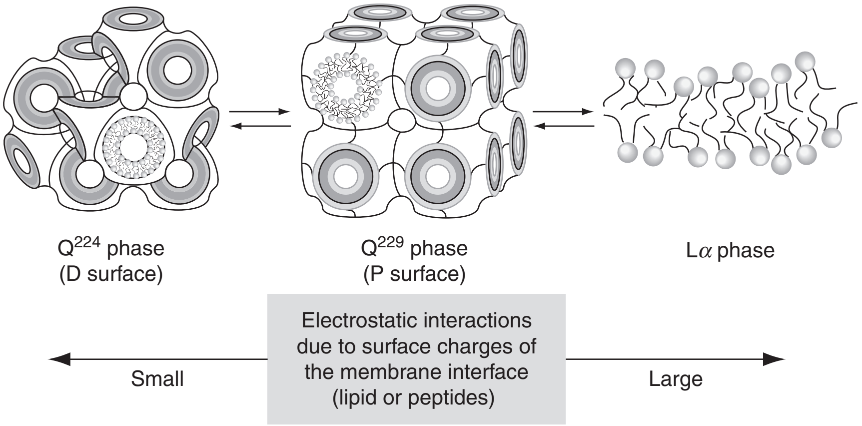

Figure 9 Effect of electrostatic interactions on phase stability of the Q phases and the L_α phase. The surface charge density of the lipid membrane can be controlled by the concentration of charged lipids in the membrane or by the amount of charged peptides partitioned into the membrane interface. As the electrostatic interactions increase (i.e., the surface charge density of the membrane increases, or the salt concentration in the bulk phase decreases), the most stable phase of the MO membrane changes; $Q^{224} \Rightarrow Q^{229} \Rightarrow L_\alpha$.

3. Effects of Surface Charges due to Adsorbed Charged Peptides on the Stability of the Q Phases

Next, we developed a different approach which examines the effect of electrostatic interactions on the stability of the Q phases. To increase the surface charge density of the MO membrane, a charged peptide which can bind with the electrically neutral membrane interface was used instead of the negatively charged lipids [48]. Recent biophysical studies indicate that the lipid membrane interface is composed of hydrophilic segments (so-called head group), hydrophobic acyl chains, and water molecules because of large thermal motions of the membranes such as undulation and protrusion [12, 53]. Peptides can be partitioned into the membrane interface or bound in the membrane interface. The thickness of the membrane interface of dioleoyl-PC (DOPC) membrane was 0.9–1.5 nm [56, 57], showing that an α-helix can be partitioned parallel to the bilayer plane into the membrane interface. As the *de novo* designed peptide which has positive charges and also can be partitioned into the lipid membrane interface composed of electrically neutral lipids such as PC, we designed and synthesized a peptide whose sequence is WLFLLKKK (peptide-1) [58]. The N-terminal region (WLFLL) is the site (or the segment) of the peptide partitioned into the membrane interface, since W and F have a high-interfacial hydrophobicity [59]. Since K is the positively charged amino acid Lysine, peptide-1 has three positive charges at its C-terminus and a positive charge at its N-terminus. We expected that the peptide-1 might give positive charges in the electrically neutral membrane interface by its binding to the interface (Fig. 10).

To confirm the validity of the design of peptide-1, we investigated the interaction of the peptide-1 with PC membranes in the L_α phase [58]. It is well recognized that the intermembrane distance between adjacent membranes inside a multilamellar vesicle (MLV) is a good measure for the intermembrane interaction [53, 60]. As shown in Fig. 11A, the spacing (d_l) of palmitoyloleoyl-PC (POPC)-MLV gradually increases from 6.3 to 8.8 nm with an increase in peptide-1 concentration (R, molar ratio of

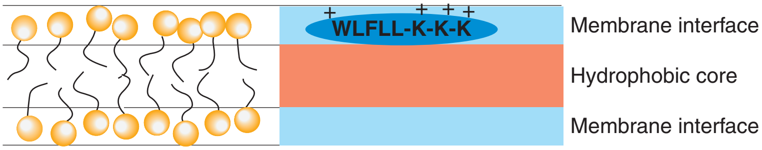

Figure 10 A schematic view of the membrane interface of MO membrane, and the partition of the peptide-1 into the membrane interface. The lipid membrane is consisted of two membrane interfaces and the hydrophobic core. The peptide-1 is located in the membrane interface.

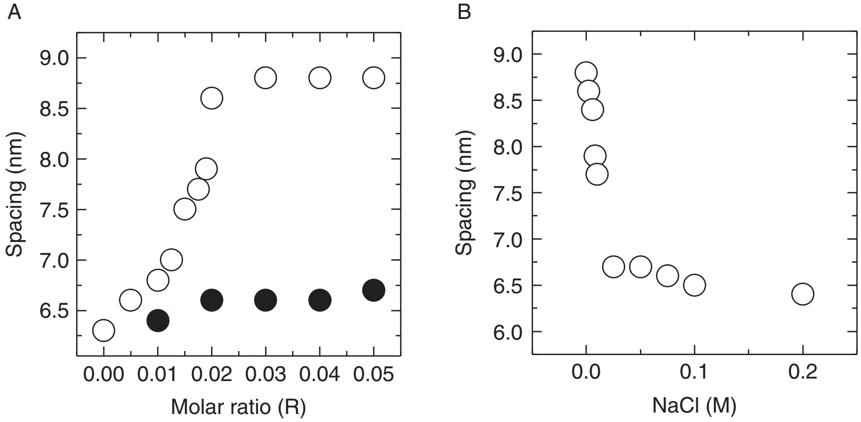

Figure 11 (A) Spacing of POPC-MLV in the presence of various concentrations of peptide-1 (○) and peptide-3K (●) in 10 mM PIPES buffer (pH 7.0) under excess water condition at 20 °C. R is the molar ratio of peptides to lipid (POPC). (B) Effect of NaCl concentration on the spacing of POPC/peptide-1 membrane ($R = 0.030$) in 10 mM PIPES buffer (pH 7.0) under excess water condition at 20 °C. These figures are reprinted from Ref. [58] with permission from the American Chemical Society.

peptides to lipid (POPC)). On the other hand, in the case of peptide-3K (LLKKK) which does not have the N-terminal segment (WLF), the spacing does not change. The spacing is determined by the summation of the intermembrane distance (d_f) and the membrane thickness (d_m), that is $d_l = d_f + d_m$. The values of d_f and d_m can be determined by the electron density profile of membranes obtained by the Fourier transformation of the SAXS data. However, in the presence of peptide-1 only two SAXS peaks were obtained, and thereby, it was difficult to obtain the electron density profile. In spite of this result, we can get qualitative information on the intermembrane distance (d_f) from Fig. 11A. The membrane thickness of the L_α phase membrane cannot change greatly. Thereby, the large increase in the spacing of POPC-MLV is due to the increase in the intermembrane distance. Figure 11B shows that the spacing of the POPC-MLV in the presence of peptide-1 ($R = 0.030$) decreases with an increase in NaCl concentration in solution. This result indicates that the increase in the intermembrane distance of POPC-MLV by peptide-1 is due to electrostatic repulsive interaction. On the basis of these results, we can reasonably conclude that the peptide-1 is partitioned into the membrane interface and gives positive charges to the PC membrane surface, resulting in the increase in the electrostatic repulsive interaction between the adjacent membranes in the MLV. On the other hand, we found that this peptide-1 induced shape changes of DOPC-GUVs. The addition of low concentration (e.g., 5 μM) of peptide-1 through a micropipet near a single DOPC-GUV induced several kinds of shape changes; for example, a discocyte was changed to two-spheres connected by a neck, and small vesicles were budded into the outside of the spherical GUV. The theoretical analysis on the results of the shape changes indicates that the peptide-1 binds with the membrane interface of the external monolayer of the GUV and increases the area of its membrane due to the partition itself and also the electrostatic repulsive interaction between the peptides partitioned into the membrane interface. These results indicate that the *de novo* designed peptide-1 can bind with the PC membrane interface and have large effect on its structure and property.

Next, we investigated effects of peptide-1 on phase stability of the MO membrane [48]. Little information is available regarding the structure of the membrane interface of the MO membrane. However, a recent molecular dynamics simulation shows that there is a great deal of undulation motion and peristaltic motion in the MO membranes [61]. This suggests that the membrane interface of the MO membrane is composed of hydrophilic segments, hydrophobic acyl chains, and water molecules, which is similar to that of the PC membranes. Therefore, we can expect that the peptide designed to be partitioned in the PC membrane interface can bind with the MO membrane interface. To verify this hypothesis, we investigated the effects of peptide-1 on the structures and the stability of the Q phase of MO membranes using SAXS. At high concentrations of peptide-1 (e.g., $R = 0.10$), a new set of SAXS peaks appeared with large spacing (ratio = 1:2:3), which is consistent with the L_α phase (Fig. 12A). Figure 12B shows the detail dependence of the structure and the phase of the MO/peptide-1 membrane at 30 wt% lipid on peptide-1 concentration. At $R < 0.0080$, MO membranes are in the Q^{224} phase. At $R \geq 0.0090$, MO membranes are in the Q^{229} phase. Thus, at $R = 0.0090$, a transition from the Q^{224} to the Q^{229} phase occurs. The lattice constant of the Q^{224} phase immediately before the phase transition ($R = 0.0080$) and that of the Q^{229} phase immediately after the phase transition ($R = 0.0090$) are 11.2 and 14.5 nm, respectively. Thereby, the lattice constant ratio (Q^{229}/Q^{224}) is 1.29, which is close to the theoretical value (1.28) determined by analysis of coexisting cubic phases based on the Bonnet transformation from the D to the P surface. The lattice constant of the MO/peptide-1 membrane in the Q^{229} phase gradually increases from 14.5 to 18.7 nm as peptide-1 concentration increases from $R = 0.0090$ to 0.030. At $R \geq 0.040$, the membranes are in with the L_α phase, and the spacing of the L_α phase decreases slightly as peptide-1 concentration increases from $R = 0.040$ to 0.12 (Fig. 12B). In contrast, peptide-3K does not change the phase of the MO membrane under the same conditions (Fig. 12B).

To confirm that these phase transitions are induced by the electrostatic interactions due to the surface charges of the adsorbed peptide-1 on the MO

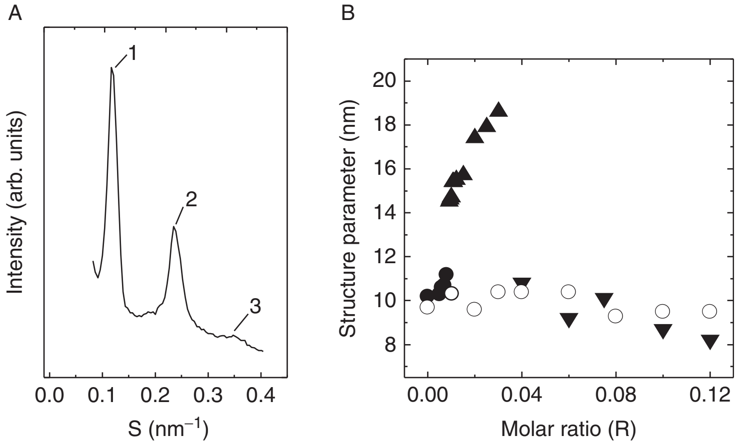

Figure 12 (A) SAXS pattern of MO/peptide-1 membranes ($R = 0.10$, R is the molar ratio of peptide-1 to MO) in 10 mM PIPES buffer (pH 7.0) at 30 wt% lipid concentration at 20 °C. (B) The structure parameter of MO/peptide-1 membranes in the presence of various concentrations of peptide-1 (●, ▲, ▼) and peptide-3K (○) in 10 mM PIPES buffer (pH 7.0) at 30 wt% lipid concentration at 20 °C determined by SAXS. R is the molar ratio of peptides to MO. (●) and (○) denote the Q^{224} phase, (▲) denotes the Q^{229} phase, and (▼) denotes the L_α phase. These figures are reprinted from Ref. [48] with permission from the American Chemical Society.

membrane, we investigated the effect of NaCl on the phase of the MO/peptide-1 membrane in excess water. The MO/peptide-1 membrane ($R = 0.030$) was in the Q^{229} phase in the absence of NaCl (Fig. 12B). With an increase in NaCl concentration, at 120 mM NaCl, a phase transition from the Q^{229} to the Q^{224} occurred (Fig. 13A). The lattice constant of the Q^{229} phase immediately before the phase transition (110 mM NaCl) and that of the Q^{224} phase immediately after the phase transition (120 mM NaCl) are 15.6 and 12.2 nm, respectively. Thereby, the lattice constant ratio (Q^{229}/Q^{224}) is 1.28. The lattice constant of the Q^{224} phase gradually decreases as NaCl concentration increases. Next, we investigated dependence of NaCl concentration on structures of the MO/peptide-1 membrane ($R = 0.080$), which is in the L_α phase (Fig. 12B) in the absence of NaCl. At a NaCl concentration of ≥ 0.4 M, the membranes are in the Q^{224} phase, and that the lattice constant of the Q^{224} phase gradually decreases as NaCl concentration increases (Fig. 13B).

On the basis of these results, we can reasonably consider a following scenario for the peptide-1 induced the Q to the L_α phase transition. Peptide-1 binds with the electrically neutral MO membrane interface due to the segment (WLFLL) with high-interfacial hydrophobicity, which increases the surface charge density of the MO membrane. As the peptide-1 concentration increases and thereby the surface charge density of the membrane consequently increases, electrostatic repulsive interaction between the positive charges increases. In contrast, in the MO/peptide-1

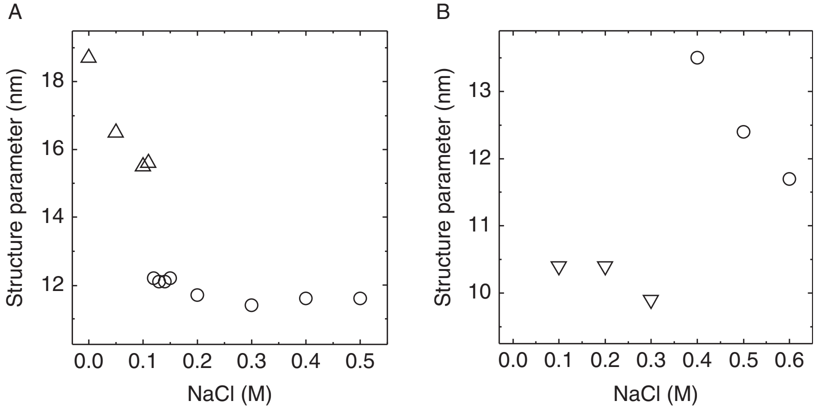

Figure 13 (A) The lattice constant of the Q phases of the MO/peptide-1 membranes ($R = 0.030$) in 10 mM PIPES buffer (pH 7.0) containing various concentrations of NaCl (M) in excess water at 20 °C determined by SAXS. (Δ) denotes the Q^{229} phase and (○) denotes the Q^{224} phase. (B) The structure parameter of the MO/peptide-1 membrane ($R = 0.080$) in 10 mM PIPES buffer (pH 7.0) containing various concentrations of NaCl (M) at 20 °C determined by SAXS. (Δ) Denotes the L_α phase and (○) denotes the Q^{224} phase. These figures are reprinted from Ref. [48] with permission from the American Chemical Society.

membrane, as the salt concentration in the bulk phase increases, the electrostatic repulsion decreases due to screening of the charges of the peptides. Therefore, we conclude that as the electrostatic interactions in the membrane interface increases as a result of either an increase in the surface charge density of the adsorbed peptide-1 on the MO membrane or a decrease in salt concentration, the most stable phase of these lipid membranes changes as follows: $Q^{224} \Rightarrow Q^{229} \Rightarrow L_\alpha$ (Fig. 9). These results clearly show that the origin of the surface charge is not important in the electrostatic interaction-controlled phase transitions between different Q phases and also between the Q phases and the L_α phase (Fig. 9). This was the first example demonstrating the peptide (or protein)-induced phase transition between the Q phases and bilayer membranes of biological lipid membranes.

4. MECHANISM OF THE ELECTROSTATIC INTERACTIONS-INDUCED PHASE TRANSITION BETWEEN THE Q PHASE AND THE L_α PHASE

To consider the mechanism of the electrostatic interaction-induced phase transitions, we investigated effects of the electrostatic interactions due to the surface charges on the spontaneous curvature of MO monolayer membrane. The spontaneous curvature of a single monolayer membrane, H_0, is defined as the curvature to minimize the curvature elastic energy of the monolayer, which is determined by physical properties of the monolayer by itself without the interaction of other monolayer [9–11] (Appendix). The absolute value of the spontaneous curvature, $|H_0|$, is determined as the reciprocal number of the radius of the spontaneous curvature (i.e., $|H_0| = 1/R_0$). To allow the MO monolayer in the H_{II} phase to express the spontaneous curvature, H_0, we added 16% tetradecane to the MO membranes (or DOPA/MO membranes) to relax the alkyl chain packing stress (Appendix).

First, we investigated the effect of the incorporation of DOPA in the MO membrane on its spontaneous curvature [47]. The basis vector length (i.e., the distance between the centers of neighboring cylinders in the H_{II} phase), d, of the DOPA/MO/tetradecane membrane in the H_{II} phase in 10 mM PIPES buffer (pH 7.0) gradually increases from 6.5 to 9.4 nm with an increase in DOPA concentration from 0 to 40 mol% (Fig. 14A). On the other hand, d of the same membrane in 10 mM PIPES buffer (pH 7.0) containing 1.0 M NaCl is almost the same with an increase in DOPA concentration (Fig. 14A). The basis vector length of the H_{II} phase, d, is expressed as a sum of the distance between the center of the cylinder and the neutral surface (or pivotal surface), R_{pp}, and the distance between the bilayer midsurface and the neutral surface, ξ, that is $d = 2\ (R_{pp} + \xi)$

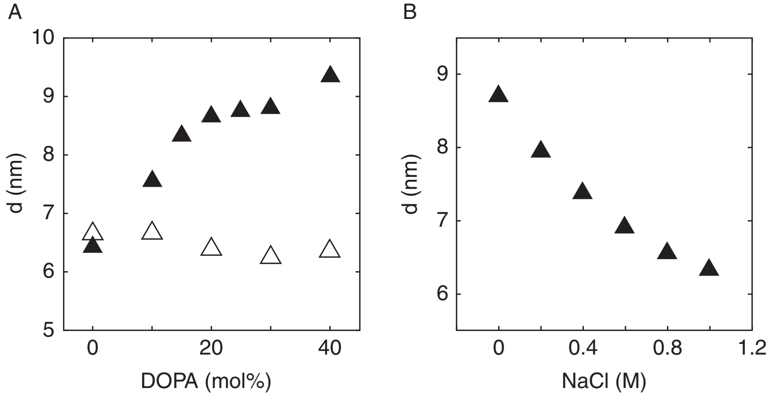

Figure 14 (A) The basis vector length, *d*, of H_{II} phases of DOPA/MO membrane containing 16 wt% tetradecane versus DOPA (mol%) concentration in 10 mM PIPES buffer (pH 7.0) under excess water condition at 20 °C determined by SAXS: (▲) in 0 M NaCl and (Δ) in 1.0 M NaCl. (B) The basis vector length, *d*, of H_{II} phases of the 30%-DOPA/ 70%-MO membrane containing 16 wt% tetradecane in 10 mM PIPES buffer (pH 7.0) versus NaCl concentration (M) in excess water condition at 20 °C determined by SAXS. These figures are reprinted from Ref. [47] with permission from the American Biophysical Society.

(Appendix; Fig. A3). The neutral surface is the appropriate surface to define the curvature of the membrane, because the area of this surface keeps constant as the monolayer is bent. These membranes have the spontaneous curvature, H_0, and thereby, $R_{pp} \approx R_0$. The increase in *d* of the DOPA/MO/tetradecane membrane induced by the increase in content of DOPA is attributed to the increase in R_{pp}, since the change in ξ is reasonably considered to be small ($\leq$0.5 nm). Thus, the result of Fig. 14A shows that R_0 of the DOPA/MO membranes increases with an increase in DOPA concentration. It was reported that $R_0 = 2.0$ nm for the MO membrane [62]. If we assume that ξ does not change appreciably, it turns out that R_0 of the DOPA/MO membranes increased from 2.0 to 3.4 nm as the DOPA concentration increases from 0 to 40 mol%. Thereby this data indicates that the increase in electrostatic interactions reduces $|H_0|$ of the monolayer. From this analysis and the result of Fig. 7B, we can indicate that as $|H_0|$ of the monolayer decreases, the most stable phase of the DOPA/MO membranes changes as follows: $Q^{224} \Rightarrow Q^{229} \Rightarrow L_\alpha$. Hence, the phase stability of these three phases is deeply correlated with the spontaneous curvature of the monolayer.

Figure 14B shows the effect of NaCl concentration on the spontaneous curvature of 30%-DOPA/70%-MO monolayer in 10 mM PIPES buffer (pH 7.0). In 0 M NaCl, the 30%-DOPA/70%-MO membrane without tetradecane was in the L_α phase (Fig. 7B), but the 30%-DOPA/ 70%-MO membrane containing 16 wt% tetradecane was in the H_{II} phase

(d = 8.7 nm). As shown in Fig. 14B, d of the 30%-DOPA/70%-MO/tetradecane membrane in excess water gradually decreases from 8.7 to 6.4 nm with an increase in NaCl concentration from 0 to 1.0 M. This result shows that R_0 of the 30%-DOPA/70%-MO monolayer decreases with an increase in NaCl concentration, indicating that with a decrease in the electrostatic interactions $|H_0|$ of the monolayer increases. Therefore, this result and the results of Fig. 13 support our hypothesis above mentioned; as $|H_0|$ of the monolayer increases, the most stable phase of these lipid membranes changed as follows: $L_\alpha \Rightarrow Q^{229} \Rightarrow Q^{224}$.

Second, to get information of the effect of peptide-1 concentration on its spontaneous curvature of the MO monolayer, we investigated the structure of MO/peptide-1 membrane containing 16 wt% tetradecane in excess water at 20 °C. In excess water at 20 °C, the basis vector length, d, of MO/peptide-1/tetradecane membrane in 10 mM PIPES buffer (pH 7.0) gradually increases from 6.7 to 9.0 nm as peptide-1 concentration increased from $R = 0$ to 0.15 (Fig. 15A–C). Figure 15D shows the effect of NaCl concentration on the structure of the MO/peptide-1 membrane ($R = 0.080$) containing 16 wt% tetradecane in 10 mM PIPES buffer (pH 7.0) in excess water. In 0 M NaCl, the MO/peptide-1 membrane ($R = 0.080$) without tetradecane is in the L_α phase, but the MO/peptide-1 membrane ($R = 0.080$) containing 16 wt% tetradecane is in the H_{II} phase ($d = 8.2$ nm). d of its monolayer gradually decreases from 8.2 to 6.7 nm as NaCl concentration increased from 0 to 1.0 M. These data show a strong correlation between the spontaneous curvature of the MO/peptide-1 monolayer and the phase stability of MO/peptide-1 membrane. As $|H_0|$of the MO/peptide-1 monolayer decreases, the most stable phase of these lipid membranes changed as follows: $Q^{224} \Rightarrow Q^{229} \Rightarrow L_\alpha$.

We consider the free energy difference between the Q phases and the L_α phase. Here we use the parallel surface model for the Q phases. In the parallel surface to the minimal midsurface, we consider only the curvature elastic energy for the estimation of the Q phase stability, because the parallel surface has optimal chain length and thereby there is no stretching energy of chains [40, 63]. The curvature elastic energy of the monolayer, f_{curv}, can be expressed as [40, 64]

$$f_{\text{curb}} = \int \{2\kappa_{\text{m}}(H^{\xi} - H_0)^2 + \bar{\kappa}_{\text{m}} K^{\xi}\}\, \mathrm{d}A^{\xi} \tag{1}$$

where κ_{m} is the elastic bending modulus (i.e., bending rigidity) of the monolayer, H^{ξ} the mean curvature at the neutral surface of the monolayer, K^{ξ} the Gaussian curvature at the neutral surface, $\bar{\kappa}_{\text{m}}$ the Gaussian curvature modulus (i.e., saddle-spray modulus) of the monolayer, and the integration extends over the monolayer's neutral surface, which is at a distance ξ from

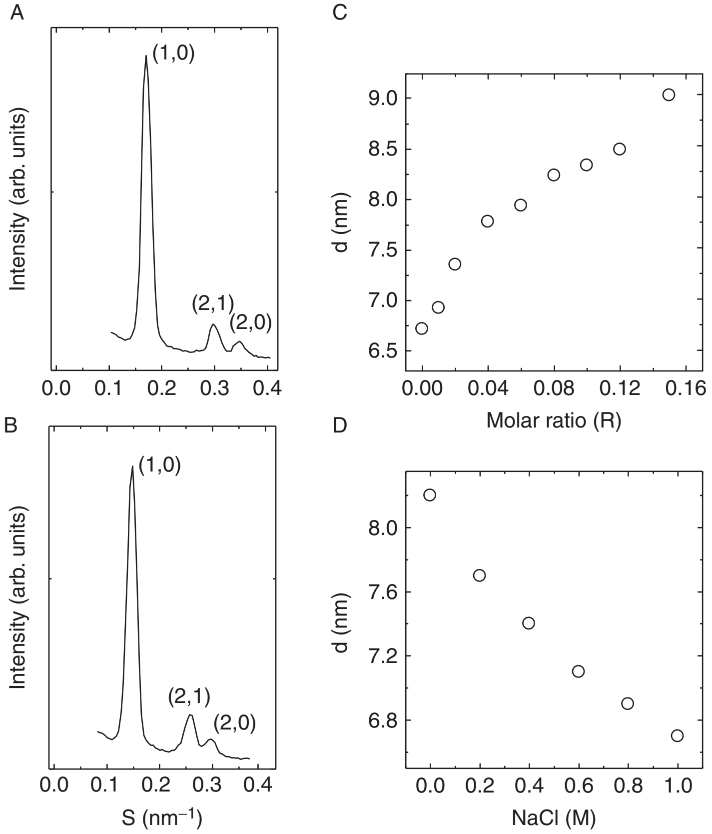

Figure 15 SAXS pattern of MO/peptide-1 membranes containing 16 wt% tetradecane in 10 mM PIPES buffer (pH 7.0) in excess water at 20 °C. (A) $R = 0$; pure MO membrane without peptide-1. (B) $R = 0.060$. (C) The basis vector length, d, of the H_{II} phases of MO membranes containing 16 wt% tetradecane versus peptide-1 concentration (R) in 10 mM PIPES buffer (pH 7.0) in excess water at 20 °C determined by SAXS. (D) Effect of NaCl concentration on d of H_{II} phases of MO/peptide-1 membrane ($R = 0.080$) containing 16 wt% tetradecane in 10 mM PIPES buffer (pH 7.0) in excess water at 20 °C determined by SAXS. These figures are reprinted from Ref. [48] with permission from the American Chemical Society.

the midsurface of the bilayer (i.e., the parallel surface). Note that we define negative curvature of the monolayer to be toward the water region (Fig. A1(A)) (opposite to Ref. [40]). The differential area element dA^{ξ}, the mean curvature H^{ξ}, and the Gaussian curvature K^{ξ} on the neutral surface (i.e., the parallel surface) can be expressed by the quantities (dA and K) on the midsurface [35, 40]:

$$\begin{aligned} \mathrm{d}A^{\xi} &= \mathrm{d}A(1+K\xi^2) \\ H^{\xi} &= \frac{K\xi}{1+K\xi^2} \\ K^{\xi} &= \frac{K}{1+K\xi^2} \end{aligned} \tag{2}$$

From Eq. (2), we reasonably conclude that the mean curvature at the neutral surface, H^{ξ}, has negative value since $K < 0$ at the minimal midsurface.

First, we consider the phase transition between the Q phases and the L_{α} phase qualitatively. From Eqs. (1) and (2), we can obtain the free energy of the bilayers in the Q phase, F_{cubic}, as follows [40]:

$$\begin{aligned} F_{\mathrm{cubic}} &= \int \{4\kappa_{\mathrm{m}}(H^{\xi}-H_0)^2(1+K\xi^2)+2\bar{\kappa}_{\mathrm{m}}K\}\mathrm{d}A \\ &= \{4\kappa_{\mathrm{m}}\langle H^{\xi}-H_0\rangle^2+2\bar{\kappa}_{\mathrm{m}}\langle K\rangle\}A \end{aligned} \tag{3}$$

where $\langle\ \rangle$ means the average value over the total area, and we used $1+K\xi^2 \approx 1$ since ξ is very small. Since $H = K = 0$ in the L_{α} phase, the free energy of the bilayer in the L_{α} phase, $F_{L_{\alpha}}$, can be expressed as

$$F_{L_{\alpha}} = 4\kappa_{\mathrm{m}}H_0^2A \tag{4}$$

Thereby, the difference between the free energy of two phases, ΔF, can be expressed as

$$\Delta F = F_{\mathrm{cubic}} - F_{L_{\alpha}} = \{4\kappa_{\mathrm{m}}(\langle H^{\xi}-H_0\rangle^2 - H_0^2)+2\bar{\kappa}_{\mathrm{m}}\langle K\rangle\}A \tag{5}$$

Equation (5) is almost the same equation in Ref. [47]. From the data of the elastic bending modulus of the bilayers of lipid membranes in the L_{α} phase [65], κ_{m} is of the order 3–15 $k_{\mathrm{B}}T$. In the case of the MO membrane, $\kappa_{\mathrm{m}} = 1.2 \times 10^{-20}\mathrm{J} = 3k_{\mathrm{B}}T > 0$ [62]. It is theoretically predicated that $\bar{\kappa}_{\mathrm{m}} < 0$ [66] and thereby, $\bar{\kappa}_{\mathrm{m}}\langle K\rangle > 0$. We can reasonably consider that $H_0 < H^{\xi} < 0$ for the Q phase membranes. If we assume that the electrostatic interactions do not change $\bar{\kappa}_{\mathrm{m}}$ and κ_{m} greatly, we can consider a following scenario. When H_0 of the monolayer has a large negative value (i.e., $|H_0|$ is large) (e.g., for the MO membrane), $\Delta F < 0$, indicating that the Q phase is stable. As the electrostatic interactions increase owing to the charged lipid or the bound charged peptide, $|H_0|$ of the membrane decreases, inducing the decrease in $|\Delta F|$. At the critical value of the electrostatic interactions,

$\Delta F = 0$, and thereby the Q to the L_α phase transition occurs. If the electrostatic interactions are larger than the critical value, $\Delta F > 0$ and thereby the L_α phase is stable. Hence, the decrease in $|H_0|$ with an increase in the electrostatic interactions induces the Q to the L_α phase transition in the DOPA/MO membrane [47] and in the MO/peptide-1 membrane [48].

Next, we consider the phase transition between the Q phases and the L_α phase more quantitatively. From Eqs. (1) and (2), we can obtain the free energy of the bilayers in the Q phase, F_{cubic} and that in the L_α phase, F_{L_α}, as follows [40]:

$$\begin{aligned} F_{\mathrm{cubic}} &= \int \{4\kappa_{\mathrm{m}} H_0^2 + 2(\bar{\kappa}_{\mathrm{m}} - 4\kappa_{\mathrm{m}} H_0 \xi + 2\kappa_{\mathrm{m}} H_0^2 \xi^2) K + 4\kappa_{\mathrm{m}} K^2 \xi^2\} \mathrm{d}A \\ &= \int \{4\kappa_{\mathrm{m}} H_0^2 + \bar{\kappa}_{\mathrm{bil}} K + 4\kappa_{\mathrm{m}} K^2 \xi^2\} \mathrm{d}A \end{aligned} \tag{6}$$

where $\bar{\kappa}_{\mathrm{bil}}$ is the Gaussian curvature modulus of the bilayer:

$$\bar{\kappa}_{\mathrm{bil}} = 2(\bar{\kappa}_{\mathrm{m}} - 4\kappa_{\mathrm{m}} H_0 \xi + 2\kappa_{\mathrm{m}} H_0^2 \xi^2) \tag{7}$$

Since ξ is very small, we can reasonably approximate Eqs. (6) and (7) as follows:

$$\begin{aligned} F_{\mathrm{cubic}} &= \int \{4\kappa_{\mathrm{m}} H_0^2 + \bar{\kappa}_{\mathrm{bil}} K\} \mathrm{d}A \\ &= 4\kappa_{\mathrm{m}} H_0^2 A + \bar{\kappa}_{\mathrm{bil}} \langle K \rangle A \end{aligned} \tag{8}$$

$$\bar{\kappa}_{\mathrm{bil}} = 2(\bar{\kappa}_{\mathrm{m}} - 4\kappa_{\mathrm{m}} H_0 \xi) \tag{9}$$

In Eq. (8), $\langle K \rangle$ is the surface average value of the Gaussian curvature. The Gaussian curvature modulus of the bilayer expressed in Eq. (9) is the same as that derived using another approach [37]. Note that $\bar{\kappa}_{\mathrm{bil}} > 2\bar{\kappa}_m$, since $H_0 < 0$ and $\kappa_{\mathrm{m}} > 0$. Using Eq. (4), the difference between the free energy of two phases, ΔF, can be obtained as

$$\Delta F = F_{\mathrm{cubic}} - F_{L_\alpha} = \bar{\kappa}_{\mathrm{bil}} \langle K \rangle A \tag{10}$$

Equation (10) shows that ΔF is determined by the value of $\bar{\kappa}_{\mathrm{bil}}$, since $\langle K \rangle A = 2\pi n \chi < 0$ (where n is the ratio of the total area to the area of the unit cell of the Q phase); if $\bar{\kappa}_{\mathrm{bil}} > 0$ the Q phase is more stable, if $\bar{\kappa}_{\mathrm{bil}} < 0$ the L_α phase is more stable, and the phase transition between the Q phase and the L_α phase occurs at $\bar{\kappa}_{\mathrm{bil}} = 0$ [40, 41]. Equation (9) shows that $\bar{\kappa}_{\mathrm{bil}}$ greatly depends on the value of H_0 of the monolayer; when H_0 has a large negative value (i.e., $|H_0|$ is large), $\bar{\kappa}_{\mathrm{bil}} > 0$ since $\bar{\kappa}_{\mathrm{m}} < 0$, indicating that the Q phase is more stable. If we assume that the electrostatic interactions do not change $\bar{\kappa}_{\mathrm{m}}$ and κ_{m} greatly, we can consider a following scenario. As the electrostatic interactions increase owing to the charged lipid or the bound charged peptide, $|H_0|$ of the membrane decreases, inducing the decrease in $\bar{\kappa}_{\mathrm{bil}}$. At the critical value of the electrostatic interactions, $\bar{\kappa}_{\mathrm{bil}} = 0$, and thereby the Q to the L_α phase transition occurs. Above the critical value of the electrostatic interactions, $\bar{\kappa}_{\mathrm{bil}} < 0$ and thereby the L_α phase is more stable. Hence, the decrease in $\bar{\kappa}_{\mathrm{bil}}$ due to the decrease in $|H_0|$ with an increase in the electrostatic interactions is one of the main factors for the Q to the L_α phase transition in the DOPA/MO membrane and in the MO/peptide-1 membrane. However, for further analysis, the quantitative analysis on the effect of the electrostatic interactions on $\bar{\kappa}_{\mathrm{m}}$ and κ, and also the quantitative estimation on the electrostatic interaction energy between neighboring membranes in each phase are necessary.

5. EFFECTS OF Ca^{2+} AND PH ON THE PHASE TRANSITION BETWEEN THE L_α PHASE AND THE Q PHASES

The results described in the Sections 2 and 3 clearly show that the electrostatic interactions in the membrane interface increases as a result of either an increase in the surface charge density on the MO membrane (due to negatively charged lipids or the adsorbed peptide) or a decrease in salt concentration, the most stable phase of these lipid membranes changes as follows: $Q^{224} \Rightarrow Q^{229} \Rightarrow L_\alpha$ (Fig. 9). As described in Section 1, the electrostatic interaction is very mild one, and thereby there is high possibility that phase transitions (or transformation) between the L_α phase and the Q phases are induced in various cells by these electrostatic interactions. When these phase transitions would be induced in cells by negatively charged lipids or by charged peptides/proteins, it might take a lot of time, because after a signal arrives in a cell these negatively lipids or charged peptides/proteins must be produced and then transported to a target membrane. However, in some cases cells may require rapid interconversion between the bilayer and the Q membranes. It is therefore important to identify the factors to induce the rapid interconversion between these structures. On the other hand, in cells, rapid changes in the concentrations of Ca^{2+} and H^+ (i.e., pH change) are widely used to implement a variety of physiological functions and changes in protein structures [67]. In this section, I describe the effect of Ca^{2+} and H^+ (i.e., pH change) on the phase transition (or the transformation) between the L_α phase and the Q phases.

First, we investigated the effect of Ca^{2+} on the DOPG/MO membranes [50]. The effect of DOPG on the phase stability of MO membranes in

10 mM excess PIPES buffer (pH 7.0) at 20 °C was almost the same as that of DOPA as follows. At very low concentrations of DOPG ($\leq$0.55% DOPG), the DOPG/MO membranes are in the Q^{224} phase, at low DOPG concentrations (0.55% $\leq$ DOPG $\leq$ 16%) they are in the Q^{229} phase, and at high DOPG concentrations (25% $\leq$ DOPG $\leq$ 40%) they are in the L_α phase. This result indicated that as the surface charge density of the membrane increased (i.e., as the DOPG concentration increases), the most stable phase changed as follows: $Q^{224} \Rightarrow Q^{229} \Rightarrow L_\alpha$. In contrast, in the presence of 1.0 M NaCl, no phase transitions occur; that is, all the membranes are in the Q^{224} phase, indicating that electrostatic interactions due to the surface charge induced these phase transitions.

The effect of DOPG concentration on the spontaneous curvature of MO monolayer was also similar to that of DOPA as follows. The basis vector length, *d*, of the DOPG/MO monolayer containing 16 wt% tetradecane in 10 mM PIPES buffer (pH 7.0) at 20 °C increased rapidly from 7.0 to 15.6 nm with increasing the DOPG concentration from 0 to 30%. In contrast, in the presence of 1.0 M NaCl, a slight increase in the *d* value from 7.0 to 8.0 nm was observed with increasing the DOPG concentration from 0% to 30%. Thereby, the increase in *d* of the DOPG/MO/tetradecane membranes in 10 mM PIPES buffer is mainly due to the electrostatic repulsive interaction between the negative charges of the membrane. The slight increase is thus due to the increase in the content of DOPG, which has a small packing parameter compared with that of MO in the membrane. Therefore, there is a strong correlation between the spontaneous curvature of the DOPG/MO monolayer and the phase stability of DOPG/MO membrane, which is the same as that observed in the DOPA/MO membranes.

Next, we investigated the effects of Ca^{2+} concentration in the bulk on the structure and the phase of the preformed 30%-DOPG/70%-MO-MLV in excess PIPES buffer. Various concentrations of Ca^{2+} in 10 mM PIPES buffer (pH 7.0) were added to suspensions of the preformed 30%-DOPG/70%-MO-MLV, and then mixed thoroughly by a vortex mixer, and incubated at 25 °C. After a long incubation time (2–3 days), SAXS patterns corresponding to the Q phases were observed at and above 15 mM Ca^{2+}. Figure 16 shows a detailed dependence of the lattice constant and the phase of the 30%-DOPG/70%-MO membrane on the Ca^{2+} concentration. At very low concentrations of Ca^{2+} (<15 mM), it was difficult to determine the phase as the SAXS patterns displayed a broad peak. At low concentrations of Ca^{2+}(15 mM $\leq Ca^{2+} \leq$ 25 mM), the membranes are clearly in the Q^{229} phase. At and above 28 mM Ca^{2+}, they are in the Q^{224} phase. The lattice constant of the Q^{224} phase immediately before the phase transition (25 mM Ca^{2+}) and that of the Q^{229} phase immediately after the phase transition (28 mM Ca^{2+}) are 15.9 and 12.2 nm, respectively. Thereby, the lattice constant ratio (Q^{229}/Q^{224}) is 1.30, which is close to the theoretical value (1.28) determined by the analysis of coexisting cubic phases based on

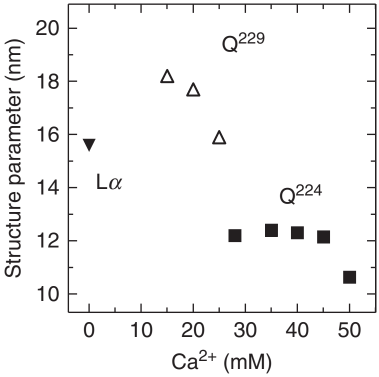

Figure 16 The structural parameter of the 30%-DOPG/70%-MO membranes in 10 mM PIPES buffer (pH 7.0) containing various concentrations of Ca^{2+} (mM) at 20 °C determined by SAXS. (■) and (Δ) denote the Q^{224} and the Q^{229} phase, respectively. This figure is reprinted from Ref. [50] with permission from the American Chemical Society.

the Bonnet transformation. In contrast, in the interaction of Na^+ with the 30%-DOPG/70%-MO membrane, the Q^{224} phase was induced only at very high concentrations of NaCl ($\geq$0.7 M), quite similar to its effect on the 30%-DOPA/70%-MO membrane (Fig. 8B).

Figure 17 shows the effect of the Ca^{2+} on the spontaneous curvature of the 30%-DOPG/70%-MO monolayer. Without Ca^{2+}, the 30%-DOPG/70%-MO membrane containing 16 wt% tetradecane in excess PIPES buffer is in the H_{II} phase ($d = 15.6$ nm). By increasing Ca^{2+} concentration from 0 to 50 mM, d of the 30%-DOPG/70%-MO monolayer gradually decreases from 15.6 to 10.2 nm. This result indicates that the increase in the Ca^{2+} concentration greatly decreases the electrostatic interactions as a result of a decrease in the surface charge density due to the binding of Ca^{2+} to the membrane, and thereby, $|H_0|$ of the membrane increases. The data in Figs. 16 and 17 also support the above hypothesis, i.e., as $|H_0|$ of the monolayer membrane increases, the most stable phase changes from the L_α phase to the Q phase.

We also investigated the reversibility of the Ca^{2+}-induced the L_α to the Q phase transition. After 30%-DOPG/70%-MO-MLV transformed into the Q^{224} phase in the presence of 50 mM Ca^{2+}, the suspension was diluted 10 times with 50 mM EDTA in PIPES buffer to decrease Ca^{2+} concentration in the buffer. After 1 h incubation at 25 °C, the membrane transformed into the Q^{229} phase with lattice constant 17.1 nm, and no alternation in this phase structure was observed during 24 h of incubation. This result indicates that the Ca^{2+}-induced the L_α to the Q phase transition is irreversible (Fig. 18). At present, we consider the reason of this irreversibility as follows. During the L_α to the Q phase transition, the addition of Ca^{2+} induces a

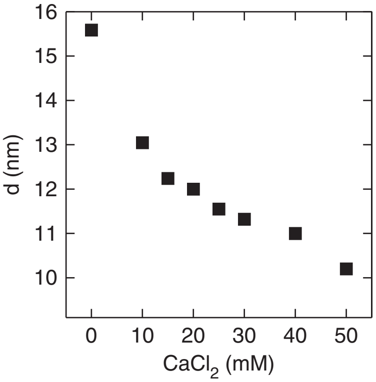

Figure 17 The effect of the Ca^{2+} concentration on the basis vector length, *d*, of the H_{II} phases of the 30%-DOPG/70%-MO membrane containing 16 wt% tetradecane in excess PIPES buffer at 20 °C determined by SAXS. This figure is reprinted from Ref. [50] with permission from the American Chemical Society.

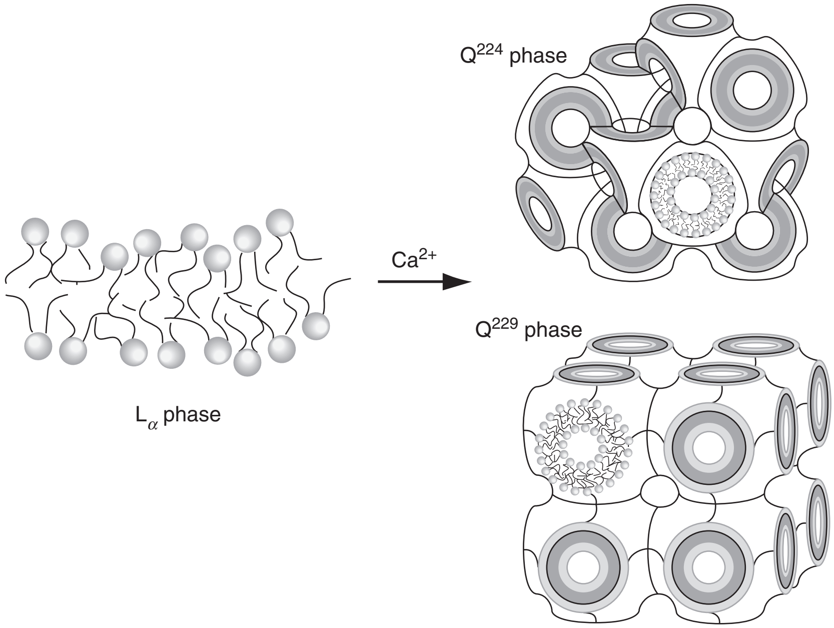

Figure 18 A scheme of the irreversible Ca^{2+}-induced phase transition from the L_α phase to the Q phases (the Q^{224} and the Q^{229} phase).

phase separation of DOPG-rich domains in the DOPG/MO membrane and then complex formation between DOPG-rich domains and Ca^{2+} in neighboring membranes, and thereby, the DOPG-rich membranes may segregate from the DOPG/MO-MLV, leaving the MO-rich membrane which is in the Q phase.

In cells, a decrease in pH from neutral to low pH is widely used for structural changes of biomembranes such as membrane fusion (e.g., fusion between influenza virus and endosome) and for changes of binding of proteins with ligands (or proteins) [67]. Thereby, we can expect that in cells a transformation between the Q phases and the bilayer membranes would occur by the decrease in pH. We examined a possibility of inducing a phase transition between the L_α and the Q phases through a change in pH.

For this purpose, we first investigated the effect of negatively charged DOPS concentration on the phase and structure of DOPS/MO membranes at 25 °C using SAXS under a physiological ion concentration (20 mM PIPES buffer (pH 7.0) containing 100 mM NaCl and 5% (w/v) PEG 6K (buffer A)) condition [51]. Figure 19 shows the dependence of the DOPS/MO membrane structure on DOPS concentration. At a concentration of $\leq$14% DOPS, the DOPS/MO membranes are in the Q^{224} phase, and the lattice constant increases with an increase in DOPS concentration. In contrast, at and above 16% DOPS they are in the L_α phase. Thereby, we can conclude that a phase transition from the Q^{224} to the L_α phase occurs at 16% DOPS under this condition. We also investigated the effect of NaCl on this phase transition. For example, the 20%-DOPS/80%-MO membranes are in the L_α phase at a NaCl concentration of $\leq$0.5 M, but are in the Q^{224} phase at higher NaCl concentrations (0.6–0.8 M). This result indicates that the electrostatic interactions due to the surface charges is a main factor in the DOPS-induced the Q^{224} to the L_α phase transition in the DOPS/MO membranes.

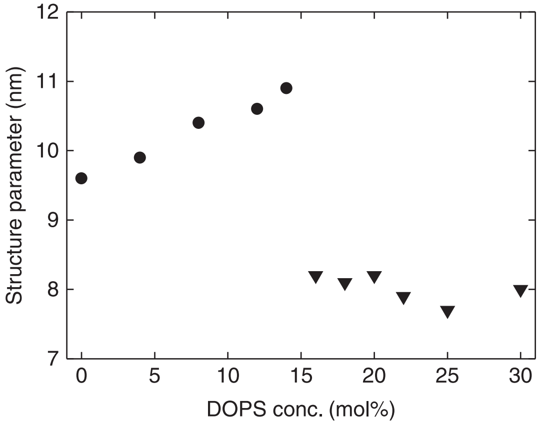

Figure 19 Dependence of the structure parameter and the phase of DOPS/MO membranes on DOPS concentrations (mol%) in buffer A at 25 °C, as determined by SAXS. (●) and (▼) denote the Q^{224} and L_α phases, respectively. This figure is reprinted from Ref. [51] with permission from the American Chemical Society.

Next, we investigated the pH effect on the structure and the phase of preformed 20%-DOPS/80%-MO-MLVs in excess buffer. At first, 20%-DOPS/80%-MO-MLVs were prepared in 10 mM ammonium acetate buffer (pH 6.7), which has a weak buffer activity. Various low-pH buffers were mixed with the MLV suspension, and the resultant suspension was incubated for 1 h before SAXS measurement. The phase and the structure of the membrane depended on pH greatly (Fig. 20A). From pH 6.9 to 3.3, the membranes are in the L_α phase. At and below pH 2.9, the membranes are in the Q^{224} phase, with the lattice constant decreasing sharply with decreasing pH. This result clearly shows that, with decreasing pH (i.e., increasing H^+ concentration), the L_α to the Q^{224} phase transition occurred at pH 2.9. In the similar experiment using 25%-DOPS/75%-MO-MLVs, we found a similar phase transition (Fig. 20B). From pH 7.0 to 2.8, the membranes are clearly in the L_α phase. At and below pH 2.7, they are in the Q^{224} phase, with the lattice constant decreasing greatly with decreasing pH. At pH 2.4, the H_{II} phase and the Q^{224} phase coexist. The critical pH value for the onset of the L_α to Q^{224} phase transition of the preformed 25%-DOPS/75%-MO-MLV (pH 2.7) is lower than that of the 20%-DOPS/80%-MO-MLV (pH 2.9).

Further, we investigated the reversibility of the low pH-induced L_α to cubic phase transition. After the 20%-DOPS/80%-MO-MLV preformed at

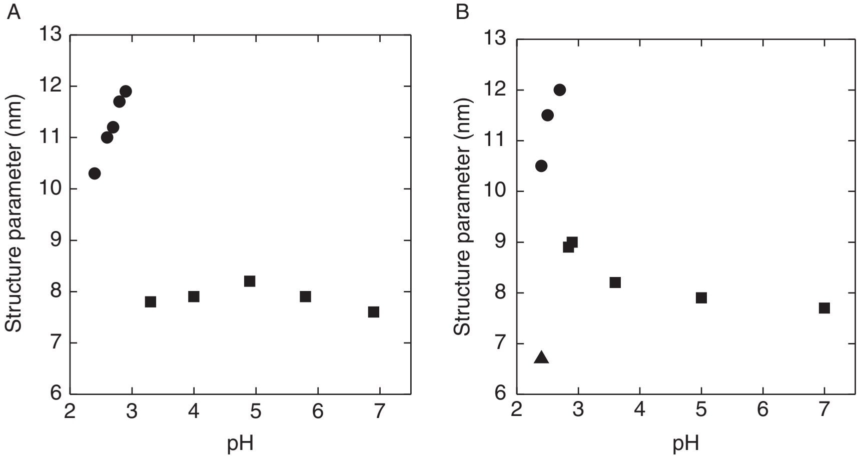

Figure 20 (A) pH dependence of the structure parameter and the phase of 20%-DOPS/80%-MO membranes in 20 mM buffer containing 100 mM NaCl and 5% (w/v) PEG 6K at 25 °C. (■) and (●) denote the L_α and Q^{224} phases, respectively. (B) pH dependence of the structure parameter and the phase of 25%-DOPS/75%-MO membranes in 20 mM buffer containing 100 mM NaCl and 5% (w/v) PEG 6K at 25 °C, determined by SAXS. (■), (●), and (▲) denote the L_α, Q^{224}, and H_{II} phases, respectively. These figures are reprinted from Ref. [51] with permission from the American Chemical Society.

neutral pH was transformed into the Q^{224} phase by addition of a low-pH buffer (final pH of 2.5), the suspension was diluted 10 times with 20 mM PIPES buffer (pH. 7.5) to give a final pH of 6.9. SAXS results indicate that, after 2 h incubation at 25 °C, the Q phase transformed into the L_α phase with a spacing of 8.3 nm. This data shows clearly that the low pH-induced transition from L_α to cubic phase is reversible. We also investigated the pH effect on the structure and the phase of preformed 20%-DOPS/80%-MO membrane in the Q^{224} phase, which were prepared by vortexing dry lipids in low pH buffer (less than pH 2.8). We obtained almost the same pH dependence as that of Fig. 20A; at and above pH 3.2, they were in the L_α phase (unpublished results). These data show clearly that the pH-induced phase transition between the L_α and the Q phases is reversible (Fig. 21).

We made a quantitative analysis on the critical pH of the phase transition from the L_α to the Q^{224} phase [51]. In the case of 20%-DOPS/80%-MO-MLV, the L_α to the Q^{224} phase transition occurred at pH 2.9. If we consider that only the surface charge density of the membrane determines the phase transition, the L_α to Q^{224} phase transition in the 20%-DOPS/80%-MO membrane would occur when the membrane has the same charge density of the 14%-DOPS/86%-MO membrane (Fig. 19). In this case, at pH 2.9, the degree of the dissociation of the carboxylic group of the DOPS in the membrane is 0.7. Thereby, from the experimental result, the apparent pK of the PS carboxylic group in the 20%DOPS/80%MO membrane was estimated to be pH 2.5. On the other hand, we obtained the apparent pK of the PS carboxylic group in the membrane theoretically. H^+ concentration near the membrane interface increases due to the electric field of the negatively charged membrane, which increases the apparent pK from the intrinsic pK by 1.2 (i.e., $\Delta pK = pK^{app} - pK^{int} = 1.2$). We estimated the shift of the pK due to the higher dielectric constant of the 20%DOPS/80%MO membrane interface than that of 100% DOPS membrane using the concept of Born energy. The apparent pK of the PS carboxylic group in the membrane

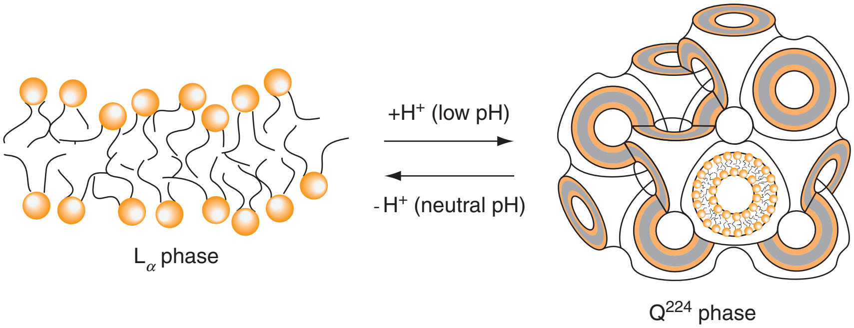

Figure 21 A scheme of the reversible low pH (or H^+)-induced phase transition between the L_α phase and the Q phase (the Q^{224} phase).

theoretically estimated was pH 2.1–2.9, which agreed well with the experimental value. The details of this analysis are described in ref. [51].

The above results suggest a possibility of the transformation of large unilamellar vesicles (LUVs) of lipid membranes into the Q phase by low pH, and thereby, we investigated a possibility of low pH-induced transformation of DOPS/MO-LUVs into the Q phase membranes [51]. For this purpose, a low pH buffer was mixed thoroughly with a 20%-DOPS/80%-MO-LUV suspension in ammonium acetate buffer (pH 6.9), and pH of the resultant suspension became 2.5. After 1 h incubation at 25 °C, the SAXS pattern of the membranes revealed a Q^{224} phase structure with a lattice constant of 11.2 nm. Next, other pH buffers were mixed thoroughly with the 20%-DOPS/80%-MO-LUV suspension. In a suspension with a final pH of 2.3, the Q^{224} phase was identified after 1 h incubation at 25 °C, but in a suspension with a final of pH 2.8 or 3.5, the Q^{224} phase was not formed even after 19 h incubation at 25 °C. These results clearly show that low pH ($\leq$2.5) rapidly induces a complete transformation of the 20%-DOPS/ 80%-MOLUVs into a cubic structure (the Q^{224} phase) (Fig. 22), within less than 1 h. This rate of the transformation is much larger than that of the Ca^{2+}-induced transformation of 30%DOPG/70%MO-LUVs into the Q phase membranes, which required 2–3 days. Further investigation on the detailed process and the mechanism of the low pH-induced transformation of LUVs into the Q phase is necessary.

This is the first result of a reversible pH-induced transition between L_α and cubic phases in biomembranes. Moreover, the rate of the phase transition is large (the transition completed within 1 h). Further, we found that DOPS/MO-LUVs were transformed into cubic phase membranes at low pH. In cells, changes in pH between neutral and low pH are widely used in various physiological functions, and therefore, we believe that pH-induced interconversion between the Q and the L_α phases would also occur in cells.

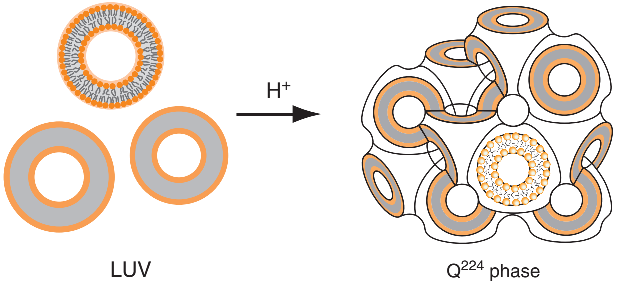

Figure 22 A scheme of the transformation from LUVs to the Q phase (the Q^{224} phase). This figure is reprinted from Ref. [51] with permission from the American Chemical Society.

6. EFFECTS OF CHARGED PEPTIDES AND OSMOTIC STRESS ON THE STABILITY OF THE Q PHASES OF THE CHARGED LIPID MEMBRANES

As described in the Section 1, cells use the electrostatic interactions between the negatively charges lipid membranes and positively charged peptides and proteins (e.g., [44, 45]). We consider that basic peptides, LLKKK (i.e., peptide-3K), LLKK (i.e., peptide-2K), and poly(L-lysine) (i.e., poly K) with molecular weight of 1K–4K can be used as simple model peptides for the positively charged proteins. In this section, we describe the effect of these model basic peptides on the phase stability of 10%-DOPA/90%-MO, which is in the Q^{229} phase at neutral pH in excess water (Fig. 7B) [49].

We added various concentrations of peptide-3K solution into this pre-formed membrane in the Q^{229} phase, and investigated the structures of these membranes using SAXS after 24 h incubation. At low concentrations of peptide-3K, the 10%-DOPA/90%-MO membranes are still in the Q^{229} phase (e.g., at 3.0 mM peptide-3K; Fig. 23A). In contrast, the SAXS pattern of 10%-DOPA/90%-MO membrane in the presence of 8.0 mM peptide-3K shows a different kind of pattern (Fig. 23C), which corresponds to the Q^{230} phase. Figure 23E shows a detailed dependence of the structure of 10%-DOPA/90%-MO membranes on peptide-3K concentration. It indicates that a phase transition from the Q^{229} to the Q^{230} phase occurs at 3.4 mM peptide-3K, where the two phases coexist, and the lattice constant for the Q^{229} and the Q^{230} phase are 12.8 and 16.0 nm, respectively (Fig. 23B, E). Thereby, the ratio of their lattice constant (Q^{230}/Q^{229}) is 1.25, which is almost the same as the theoretical value (1.23) determined by the analysis of the coexisting Q phases based on the Bonnet transformation from the G to the P surface. This also supports that the Q^{229} to the Q^{230} phase transition occurred at 3.4 mM peptide-3K (Fig. 24). As a control experiment, we investigated effects of peptide-3K on 100%-MO membranes in 10 mM PIPES buffer (pH 7.0) in excess water at 20 °C. The phase and its lattice constant did not change up to 10 mM peptide-3K. Poly (L-lysine) also induced the Q^{230} phase the 10%-DOPA/90%-MO membrane at and above 16 mM (Fig. 24), but LLKK (i.e., peptide-2K) could not induce the Q^{230} phase.

To consider the mechanism of these effects, we investigated effects of peptide-3K and poly(L-lysine) on 25%-DOPA/75%-MO-MLV, which is in the L_α phase under the same condition. At 30 wt% lipid condition, the spacing of 25%-DOPA/75%-MO-MLV was 11.3 nm, and thereby, in excess water, its spacing should be larger than 11.3 nm. In excess water, the presence of low concentrations of peptide-3K changed greatly the

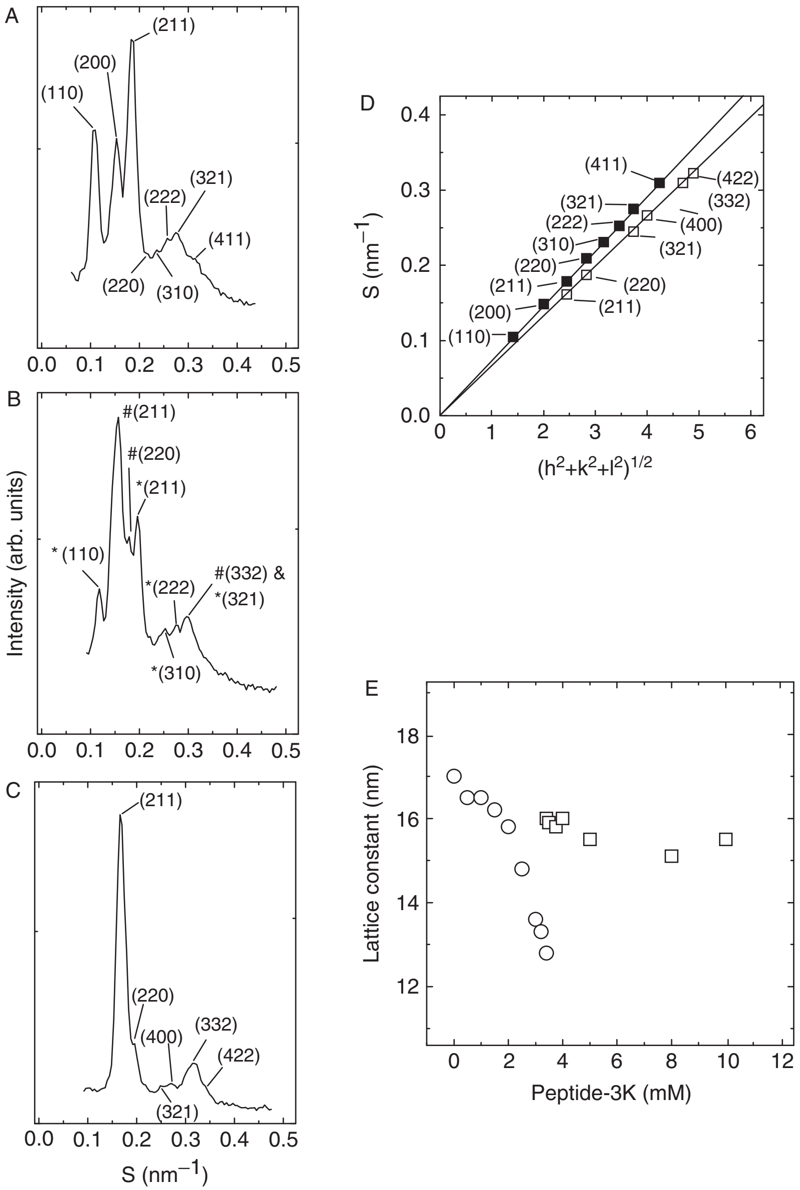

Figure 23 X-ray diffraction profiles of 10%-DOPA/90%-MO membrane in excess water in 10 mM PIPES buffer (pH 7.0) at 20 °C. (A) at 3.0 mM, (B) at 3.4 mM, and (C) at 8.0 mM peptide-3K. (A) Several peaks had spacings in the ratio of √2:√4:√6:√8:√10:√12:√14:√16:√18:√20:√22, which were indexed as (1 1 0), (2 0 0), (2 1 1), (2 2 0), (3 1 0), (2 2 2), (3 2 1), (4 0 0), (4 1 1), (4 2 0), and (3 3 2) reflections, indicating that the membrane was in the Q^{229} phase. (C) Several peaks had spacings in the ratio of √6:√8:√14:√16:√20:√22:√24, indexed as (2 1 1), (2 2 0), (3 2 1), (4 0 0), (4 2 0), (3 3 2),

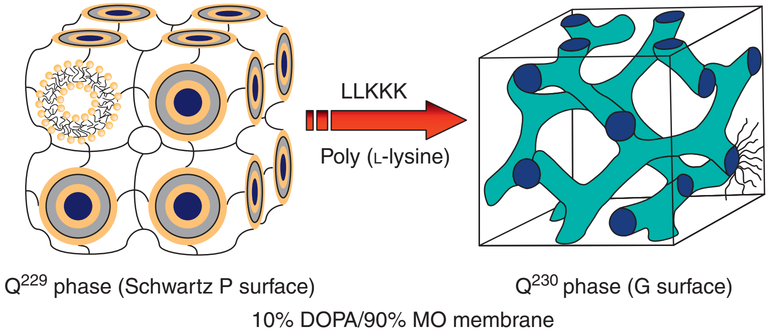

Figure 24 A schematic drawing of the Q^{229} to Q^{230} phase transition induced by peptide-3K and also poly(L-lysine) in 10%-DOPA/90%-MO membrane in excess water at neutral pH. This figure is reprinted from Ref. [49] with permission from the American Chemical Society.

SAXS pattern of 25%-DOPA/75%-MO membrane. For example, in the presence of 10 mM peptide-3K in excess water, a set of sharp SAXS peaks appeared with a small spacing ($d_1 = 5.2$ nm) in the ratio of 1:2:3, indicating that this membrane was in the L_α phase. Figure 25A shows a detailed dependence of the spacing of the 25%-DOPA/75%-MO membranes on peptide-3K concentration. At high concentrations of peptide-3K ($\geq$8 mM), the membranes are in the L_α phase, and the spacings are almost constant (5.2 ± 0.1 nm). At low concentrations of peptide-3K (<8 mM), we could not specify a phase due to complicated SAXS patterns, probably because it was very difficult to attain equilibrium condition. Low concentrations of poly(L-lysine) also changed greatly the structure of 25%-DOPA/75%-MO membrane (Fig. 25B). At high concentrations of poly(L-lysine) ($\geq$4 mM), the membranes are in the L_α phase, and the spacings are almost constant (5.5 ± 0.1 nm).

For a control experiment for the effect of peptide-3K and poly(L-lysine), we investigated effects of osmotic stress, using poly(ethylene glycol) with average molecular weight of 7500 (PEG-6K), on the structure and the phase of 10% DOPA/90% MO membrane. Preferential exclusion of

---

and (4 2 2) reflections on a body-centered cubic phase of space group $Ia3d$ (Q^{230}) (cubic aspect #12). (B) shows the coexistence of both the phases. In (B), * peaks are due to the Q^{229} phase, and # peaks are due to the Q^{230} phase. (D) Indexing of SAXS data of 10%-DOPA/90%-MO membrane in 10 mM PIPES buffer (pH 7.0) in excess water at 20 °C. (■) (A) (at 3.0 mM peptide-3K) and (□) (C) (at 8.0 mM peptide-3K) (E) The lattice constant of cubic phases of 10%-DOPA/90%-MO membranes in the presence of various concentrations of peptide-3K in 10 mM PIPES buffer (pH 7.0) in excess water at 20 °C determined by SAXS. (○) denotes the Q^{229} phase, and (□) denotes the Q^{230} phase. These figures are reprinted from Ref. [49] with permission from the American Chemical Society.

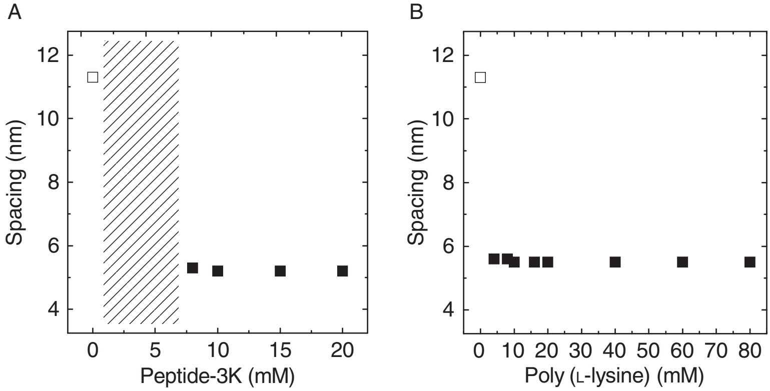

Figure 25 Spacing of 25%-DOPA/75%-MO membranes in the presence of various concentrations of (A) peptide-3K and (B) poly(L-lysine) in 10 mM PIPES buffer (pH 7.0) in excess water at 20 °C determined by SAXS. Shading by slant lines indicates the nonequilibrium area. These figures are reprinted from Ref. [49] with permission from the American Chemical Society.

high-molecular weight water-soluble polymers such as PEG-6K from the inside of membrane systems (i.e., membranes + water) induced a difference of chemical potential of water between inside and outside the membrane system (i.e., osmotic stress) [68, 69, 36]. At equilibrium, chemical potential of water inside the membrane system decreases to be equal to that outside the membrane system (i.e., bulk phase). Figure 26 shows the PEG-6K concentration dependence of the structure and the phase of 10% DOPA/ 90% MO membrane. At low PEG-6K concentrations, the lattice constant of the Q^{229} phase decreases with an increase in PEG concentration. At the intermediate concentration of PEG-6K (i.e., from 10% to 15%(w/v)), the membranes are in the Q^{224} phase. At 10%(w/v) PEG-6K, both the Q^{224} and Q^{229} phases coexists, and the lattice constant for the Q^{224} and Q^{229} phase are 12.0 and 15.3 nm, respectively. Thereby, the ratio of the lattice constant (Q^{229}/Q^{224}) is 1.28, which is the same as the theoretical value (1.28) determined by the analysis of the coexisting cubic phases based on the Bonnet transformation from the P to the D surface. Therefore, at 10%PEG-6K, a transition from Q^{229} to Q^{224} phase occurred. At high concentration of PEG-6K ($\geq$15%(w/v)), the membranes are in the Q^{230} phase. The ratio of the lattice constant of Q^{230} phase (16.8 nm) at 15%(w/v) PEG-6K to that of Q^{224} phase (10.4 nm) at 14%(w/v) PEG-6K is 1.62, which is close to the theoretical value (1.58) determined by the analysis of the coexisting cubic phases based on the Bonnet transformation from the G to the P surface. Thereby, at 15%(w/v) PEG-6K, a phase transition from Q^{224} to Q^{230} phase occurs. At higher concentrations of PEG-6K, the lattice constant of the Q^{230} phase greatly decreases from 16.8 to 11.1 nm as the

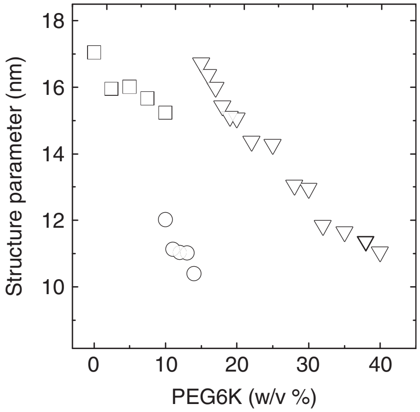

Figure 26 The structural parameter (i.e., the lattice constant of cubic phases) of 10%-DOPA/90%-MO membranes in 10 mM PIPES buffer (pH 7.0) under excess water condition containing various concentrations of PEG-6K at 20 °C determined by SAXS. (□), (○), and (▽) denote the Q^{229}, Q^{224}, and Q^{230} phase, respectively. This figure is reprinted from Ref. [49] with permission from the American Chemical Society.

PEG-6K concentration increases from 15% to 40% (w/v). These data clearly show that with an increase in PEG-6K concentration, that is, with an increase in osmotic stress, the most stable phase of the 10%-DOPA/90%-MO membranes changes as follows: Q^{229} (P surface) $\Rightarrow$ Q^{224} (D) $\Rightarrow$ Q^{230}(G). With an increase in osmotic stress, the water content in the unit cells of the Q phases decreases, in order to decrease the chemical potential of water inside the lipid membranes-water system (i.e., the Q phase membrane). Several theoretical studies have shown that, as water contents decreases, the phase should change in the sequence $Q^{229} \Rightarrow Q^{224} \Rightarrow Q^{230}$, that is P ⇒ D ⇒ G, due to the curvature elastic energy of these Q phase membranes [37, 40]. Thereby, the results of 10%-DOPA/ 90%-MO membranes agree with the prediction of these theories. As far as we know, so far, only one experimental system of lipid membranes showing validity of this theory has been reported; membranes of the 2:1 fatty acid/PC mixture, whose phase changed in the sequence $Q^{229} \Rightarrow Q^{224} \Rightarrow Q^{230}$ with a decrease in water content [32]. Therefore, the experimental system of 10%-DOPA/ 90%-MO membranes is the second one.

It is evident that the peptide-3K-induced the Q^{229} to the Q^{230} phase transition cannot be explained by the decrease in the electrostatic interactions in DOPA/MO membranes. Moreover, the effect of peptide-3K and poly(L-lysine) cannot be explained by that of osmotic stress; the lattice constant of Q^{230} phase does not depend on the peptide-3K and poly (L-lysine) concentration, but in the case of osmotic stress, it decreased greatly with an increase in PEG-6K concentration (Fig. 26). What is the main effect of peptide-3K and poly(L-lysine) on DOPA/MO membranes?

First, we consider the structure of 25%-DOPA/75%-MO-MLV in the presence of low concentrations of peptide-3K and poly(L-lysine). These membranes are in the L_α phase, whose spacings are nearly constant (5.2 ± 0.1 nm) irrespective of peptide-3K concentration from 8 to 20 mM, which indicates that the intermembrane distance in the MLV is very small and a kind of complex is formed. This strongly suggests that the adjacent membranes in the MLV are in close contact with each other, which is the same situation as in the interaction of epigallocatechin gallate (EGCg) (one of tea catechins) with PC membranes [70]. These results indicate that peptide-3K and two adjacent 25%-DOPA/75%-MO membranes form an electrostatically stabilized complex, where each peptide-3K molecule can interact with two neighboring membranes due to the electrostatic attraction between positively charged peptides and negatively charged DOPA/MO membranes, and thereby, the water content in the intermembrane region of the MLV must be low. We can consider a same scenario for the interaction of poly(L-lysine) with 25%-DOPA/75%-MO-MLV.

Second, we consider the structure of 10%-DOPA/90%-MO membranes in the presence of high concentrations of peptide-3K. These membranes are in the Q^{230} phase, whose lattice constants are almost the same (15.4 nm) irrespective of peptide-3K concentration. In this case, each peptide-3K molecule exists in the water cylinder of the Q^{230} phase (Fig. 24), and interacts with DOPA/MO membrane at two opposing sides of the water cylinder. The formation of this kind of structure decreases the water contents in the water cylinder of the Q phase. As described in the previous section, when the osmotic stress is large, that is, the water content in the water cylinder inside the Q phase is low, the Q^{230} phase is most stable. Thereby, we can consider the mechanism for the peptide 3K-induced Q^{229} to Q^{230} phase transition as follows. The electrostatic attraction between positively charged peptide-3K and the negatively charged 10%DOPA/90% MO membrane at two opposing sides of the water cylinder inside the Q^{229} phase induces the decrease in water content in the water cylinder. At critical intensity of the electrostatic attraction, the Q^{229} to Q^{230} phase transition occurs. We can consider a same scenario for the interaction of poly(L-lysine) with 10%-DOPA/90%-MO-MLV.

7. CONCLUSION

In this review, I clearly showed that as the electrostatic interactions in the membrane interface increase as a result of either an increase in the surface charge density due to negatively charged lipids or adsorbed positively charged peptides on the MO membrane or a decrease in salt concentration in solution, the most stable phase of these lipid membranes changes as follows: $Q^{224} \Rightarrow Q^{229} \Rightarrow L_\alpha$. I also described several methods to modulate the electrostatic interactions, which induce the phase transitions (or the transformation) between the Q phases and the liposomes (MLVs and LUVs) whose membranes are in the L_α phase, and also the phase transitions between different Q phases (Table 3). All the materials used in these studies such as negatively charged lipids, MO, charged peptides, Ca^{2+}, and low pH are extensively used in all the biological cells. As I described in the Section 1, the electrostatic interactions due to the surface charges are very mild, and thereby, we conclude that the electrostatic interaction is the most biologically important parameter to control the stability of the Q phases of biological lipid membranes or biomembranes, compared with temperature, water content, and pressure. On the basis of these results, we have proposed that in cells transformations between the Q phases and the bilayer membranes would occur by the modulation of the electrostatic interactions due to the surface charges.

We experimentally demonstrated these phenomena using simple model systems, but I believe that the basic principles of the stability of the Q phases we found in these studies can be applied to various membrane systems in cells and other various synthetic lipid (or detergent) systems, and also to various materials such as polymers which form the Q phases.

Further investigation is necessary in near future to elucidate the detail process (i.e., the kinetics) and the mechanism of these electrostatic interaction-induced phase transitions (or transformation) between the Q phases and the L_α phase.

APPENDIX: SPONTANEOUS CURVATURE OF MONOLAYER MEMBRANES

The spontaneous (or intrinsic) curvature of a single monolayer membrane, H_0, is a useful parameter characterizing nonbilayer membranes, and its absolute value is expressed as $|H_0| = 1/R_0$, where R_0 is the radius of the spontaneous curvature [9–11]. The spontaneous curvature of a single monolayer is defined as its radius of curvature to minimize the curvature elastic energy of the monolayer. Inverted curved structures such as the H_{II} phase, where the spontaneous curvature of the monolayer is toward the water region, have large negative H_0 values. On the other hand, normal structures such as micelles, where the spontaneous curvature of the monolayer is toward the alkyl chain region, have large positive H_0 values (Fig. A1). The spontaneous curvature of the monolayer is determined by physical properties of the monolayer by itself without the interaction of other monolayer [9–11]. Thereby, it is a kind of an ideal curvature of the monolayer. In most cases, it is difficult for lipid membranes to have the

Table 3 Electrostatic interaction (EI)-induced phase transitions between IMPS cubic phases and those between the Q phases and the L_α phase

Lipid membrane	Water content (wt%)	Temperature (°C)	Phase	Reference
OA/MO	Excess	20	$Q^{224} \Rightarrow Q^{229}$ as EI[a] increases	[46]
			$Q^{229} \Rightarrow Q^{224} \Rightarrow H_{II}$ as pH decrease	
DOPA/MO	Excess	20	$Q^{224} \Rightarrow Q^{229} \Rightarrow L_\alpha$ as EI increases	[47]
			$Q \Rightarrow L_\alpha$ as EI increases	[54]
DOPS/MO	Excess	20	$Q^{224} \Rightarrow Q^{229} \Rightarrow L_\alpha$ as EI increases	[53]
		25	$Q^{224} \Rightarrow L_\alpha$ (5% PEG6K) as EI increases	[51]
DOPG/MO	Excess	20	$Q \Rightarrow L_\alpha$ as EI increases	[54]
			$Q^{224} \Rightarrow Q^{229} \Rightarrow L_\alpha$ as EI increases	[50]
MO/peptide-1	Excess	20	$Q^{224} \Rightarrow Q^{229} \Rightarrow L_\alpha$ as EI increases	[48]
DOPG/MO	Excess	20	$L_\alpha \Rightarrow Q^{229}$ (or Q^{224}) as Ca^{2+} conc. Increases	[50]
			LUVs $\Rightarrow Q^{229}$ (or Q^{224}) as Ca^{2+} conc. increases	
DOPS/MO	Excess	25	$L_\alpha \Rightarrow Q^{224}$ ($\Rightarrow H_{II}$) as pH decreases	[51]
			$Q^{224} \Rightarrow L_\alpha$ as pH increases	
			LUVs $\Rightarrow Q^{224}$ as pH decreases	
10%DOPA/90%MO	Excess	20	$Q^{229} \Rightarrow Q^{230}$ as basic peptides conc. increases	[49]
			$Q^{229} \Rightarrow Q^{224} \Rightarrow Q^{230}$ as PEG6K conc. increases	

[a] EI is the abbreviation of the electrostatic interaction due to surface charges.

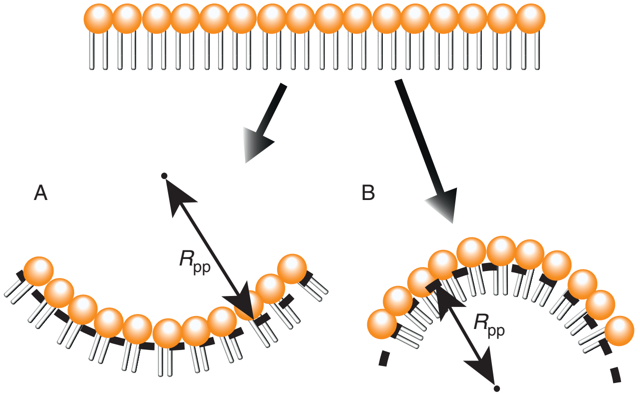

Figure A1 The spontaneous curvature of a single monolayer is defined as its radius of curvature to minimize the curvature elastic energy of the monolayer. (A) The spontaneous curvature of the monolayer which bends toward the water region is defined to have negative curvature (i.e., negative H_0 value). (B) The spontaneous curvature of the monolayer which bends toward the acyl chain region is defined to have curvature (i.e., positive H_0 value). Long-dashed line represents neutral surface (or pivotal surface) of monolayers.

spontaneous curvature, because the interaction between two monolayers in the bilayers also plays an important role in the determination of the curvature of the monolayer. The determinant of the spontaneous curvature of the single monolayer membrane is a packing parameter, V/Al, where V is the volume of the entire lipid molecule, A the area of the lipid headgroup at the lipid–water interface, and l its length as follows [11]:

$$|H_0| = \frac{1}{R_0} = \frac{(1-c)/l}{cV/Al - 1 - \sqrt{(cV/Al)^2 - 2cV/Al + c}} \qquad \text{(A1)}$$

where c is constant: $\pi/(2\sqrt{3}) < c < 2\pi/(3\sqrt{3})$. $|H_0|$ decreases as V/Al decreases. Values of these parameters (V, A, l) depend not only on the molecular structure of lipids but also on external conditions such as temperature and solvents (including salts), because these external conditions largely change optimal values of these parameters (V, A, l) [11, 12]. Therefore, the spontaneous curvature of the monolayer depends on both the molecular structure of the constituent lipids and various external conditions, which has been verified by experiments [11, 12]. For example, the decrease in $|H_0|$ induced by the increase in the electrostatic interaction (Figs. 14 and 15) indicates the decrease in the averaged value of V/Al, which is caused by the increase in the averaged value of A due to the electrostatic repulsion between the surface charges of the monolayer membrane.

There is a useful method to get information of the spontaneous curvature of the lipid monolayer. To allow the lipid monolayer in the H_{II} phase under excess water condition to express the spontaneous curvature, the addition of alkanes such as decane and tetradecane to the membranes is required, because they fill the interstitial region of the H_{II} phase and relax the alkyl chain packing stress (Fig. A2) [9, 10, 68, 71]. Under this condition, the curvature of the monolayer in the H_{II} phase is very close to the spontaneous curvature. The basis vector length of the H_{II} phase (i.e., the distance between the centers of neighboring cylinder), d, is expressed as a sum of the distance between the center of the cylinder and the neutral surface (or pivotal surface), R_{pp}, and the distance between the bilayer midsurface and the neutral surface, ξ, that is $d = 2\ (R_{pp} + \xi)$ (Fig. A3) [10, 68]. The neutral surface is the appropriate surface to define the curvature of the membrane, because the area of this surface keeps constant as the monolayer is bent. Experimentally, it is determined as the surface whose area does not change while water content varies, and is located at the acyl chain region near the polar–apolar interface [68, 72].

We investigated effect of concentration of tetradecane in the membrane on structure of the MO membrane in excess water condition at 20 °C in 10 mM PIPES buffer (pH 7.0) [47]. Above 8%(w/w) tetradecane, the MO membranes were in the H_{II} phase. Thereby, to get information of the effects of the electrostatic interactions due to the surface charges on the spontaneous curvature of MO membrane, we investigated the structure of MO membrane containing 16 wt% tetradecane in excess water condition at 20 °C under various conditions (in the presence of DOPA, peptide-1, NaCl). These membranes have the spontaneous curvature, H_0, and thereby, $R_{pp} \approx R_0$. The large increase in d of the DOPA/MO/tetradecane

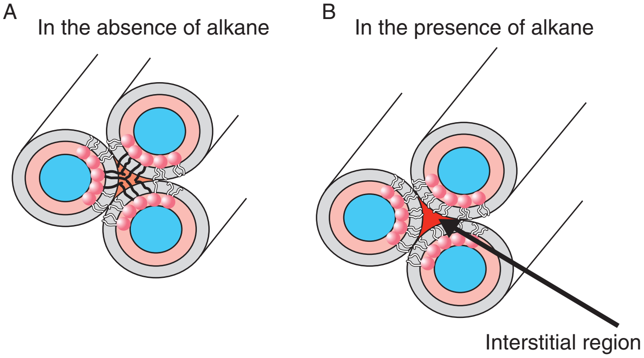

Figure A2 (A) In the H_{II} phase, acyl chains should fill the interstitial region, and as a result, they extend or deform and also the curvature is changed (i.e., the acyl chain packing stress). (B) In the presence of alkanes such as decane and tetradecane, the alkane molecules fill the interstitial region of the H_{II} phase and relax the acyl chain packing stress.

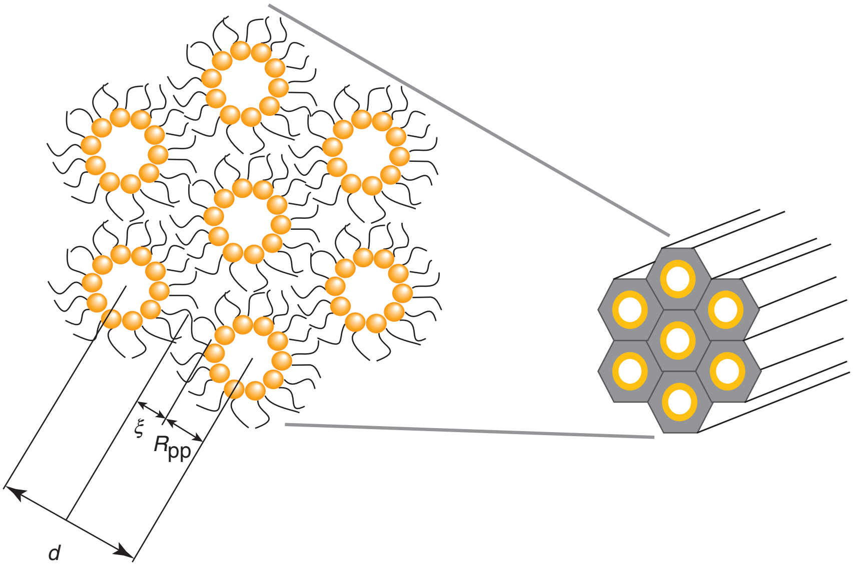

Figure A3 The basis vector length of the H_{II} phase (i.e., the distance between the centers of neighboring cylinder), d, is expressed as a sum of the distance between the center of the cylinder and the neutral surface (or pivotal surface), R_{pp}, and the distance between the bilayer midsurface and the neutral surface, ξ, that is $d = 2(R_{pp} + \xi)$.

membrane induced by the increase in content of DOPA is attributed to the increase in R_{pp}, since the change in ξ assumes to be small.

ACKNOWLEDGMENTS

This work was supported in part by a Grant-in-Aid for General Scientific Research (B) (No. 17310071) and also a Grant-in-Aid for Scientific Research in Priority Areas (Soft Matter Physics) (No. 19031011) from the Ministry of Education, Culture, Sports Science, and Technology (MEXT) of Japan to M. Yamazaki. We thank Dr. Makito Ohichi for drawing of Figs. 3 and 4. We thank Dr. Ken Brakke at Department of Mathematics, Susquehanna University, USA, for the Surface Evolver Program.

REFERENCES

[1] J.M. Seddon, R.H. Templer, Polymorphism of lipid-water systems, in: R. Lipowsky, E. Sackmann (Eds.), Structure and Dynamics of Membranes, Elsevier Science B. V., Amsterdam, 1995, pp. 97–160.
[2] S. Hyde, S. Andersson, K. Larsson, Z. Blum, T. Landh, B.W. Ninham, The Language of Shape, Elsevier Science B.V., Amsterdam, 1997.
[3] S. Kobayashi, Differential Geometry of Curves and Surfaces, Shokabo, Tokyo, 1995.

[4] W. Longley, T.J. McIntosh, A bicontinuous tetrahedral structure in a liquid-crystalline lipid, Nature 303 (1983) 612–615. K. Larsson, Two cubic phases in monoolein-water system, Nature 304 (1983) 664.

[5] P. Mariani, V. Luzzati, H. Delacroix, Cubic phases of lipid-containing systems—Structure analysis and biological implications, J. Mol. Biol. 204 (1988) 165–189.

[6] V. Luzzati, Biological significance of lipid polymorphism: The cubic phases, Curr. Opin. Struct. Biol. 7 (1997) 661–668.

[7] V. Luzzati, H. Delacroix, A. Gulik, T. Gulik-Kryzwicki, P. Mariani, R. Vargas, The cubic phases of lipids, in: R. Epand (Ed.), Lipid Polymorphism and Membrane Properties, Academic Press, San Diego, 1997, pp. 3–24.

[8] G. Lindblom, L. Rilfors, Cubic phases and isotropic structures formed by membrane lipids—possible biological relevance, Biochim. Biophys. Acta 988 (1989) 221–256.

[9] S.M. Gruner, Intrinsic curvature hypothesis for biomembrane lipid composition: A role for nonbilayer lipids, Proc. Natl. Acad. Sci. USA 82 (1985) 3665–3669.

[10] S.M. Gruner, Stability of lyotropic phases with curved interfaces, J. Phys. Chem. 93 (1989) 7562–7570.

[11] D. Marsh, Intrinsic curvature in normal and inverted lipid structures in membranes, Biophys. J. 70 (1996) 2248–2255.

[12] K. Kinoshita, S.J. Li, M. Yamazaki, The mechanism of the stabilization of the hexagonal II (H_{II}) phase in phosphatidylethanolamine membranes in the presence of low concentrations of dimethylsulfoxide, Eur. Biophys. J. 30 (2001) 207–220.

[13] C. Huang, T.J. McIntosh, Probing the ethanol-induced chain interdigitations in gel-state bilayers of mixed-chain phosphatidylcholines, Biophys. J. 72 (1997) 2702–2709.

[14] M. Yamazaki, M. Miyazu, T. Asano, A. Yuba, N. Kume, Direct evidence of induction of interdigitated gel structure in large unilamellar vesicles of dipalmitoylphosphatidylcholine by ethanol: Studies by excimer method and high-resolution electron cryomicroscopy, Biophys. J. 66 (1994) 729–733.

[15] S. Furuike, V.G. Levadny, S.J. Li, M. Yamazaki, Low pH induces an interdigitated gel to bilayer gel phase transition in dihexadecylphosphatidylcholine membrane, Biophys. J. 77 (1999) 2015–2023.

[16] T. Landh, From entangled membranes to eclectic morphologies: Cubic membranes as subcellular space organizers, FEBS Lett. 369 (1995) 13–17.

[17] Z.A. Almsherqi, S.D. Kohlwein, Y. Deng, Cubic membranes: A legend beyond the Flatland of cell membrane organization, J. Cell. Biol. 173 (2006) 839–844.

[18] S. Murakami, N. Yamada, M. Nagano, M. Osumi, Three-dimensional structure of prolamellar body in squash etioplasts, Protoplasma 128 (1985) 147–156.

[19] I. Lindstedt, C. Liljenberg, On the periodic minimal surface structure of the plant prolamellar body, Physiol. Plant. 80 (1990) 1–4.

[20] W.P. Williams, E. Selstam, T. Brain, X-ray diffraction studies of the structural organization of prolamellar bodies isolated from *Zea mays*, FEBS Lett. 422 (1998) 252–254.

[21] E.L. Snapp, R.S. Hegde, M. Francolini, F. Lombardo, S. Colombo, E. Pedrazzini, N. Borgese, J. Lippincott-Schwartz, Formation of stacked ER cisternae by low affinity protein interactions, J. Cell Biol. 163 (2003) 257–269.

[22] Y. Deng, M. Marko, K.F. Buttle, A. Leith, M. Mieczkowski, C.A. Mannella, Cubic membrane structure in amoeba (*Chaos carolinensis*) mitochondria determined by electron microscopy tomography, J. Struct. Biol. 127 (1999) 231–239.

[23] Y. Deng, S.D. Kohlwein, C.A. Mannella, Fasting induces cyanide-resistant respiration and oxidative stress in the amoeba *Chaos carolinensis*: Implications for the cubic structural transition in mitochondrial membranes, Protoplasma 219 (2002) 160–167.

[24] A. Colotto, I. Martin, J.M. Ruysschaert, A. Sen, S.W. Hui, R.P. Epand, Structural Study of the interaction between the SIV fusion peptide and model membranes, Biochemistry 35 (1996) 980–989.

[25] A. Colotto, R.P. Epand, Structural Study of the relationship between the rate of membrane fusion and the ability of the fusion peptide of influenza virus to perturb bilayers, Biochemistry 36 (1997) 7644–7651.

[26] B. de Kruijff, Lipids beyond the bilayer, Nature 386 (1997) 129–130.

[27] E.M. Landau, J.P. Rosenbusch, Lipidic cubic phases: A novel concept for the crystallization of membrane proteins, Proc. Natl. Acad. Sci. USA 93 (1996) 14532–14535.

[28] E. Pebay-Peyroula, G. Rummel, J.P. Rosenbusch, E.M. Landau, X-ray structure of bacteriorhodopsin at 2.5 Angstroms from microcrystals grown in lipidic cubic phases, Science 277 (1997) 1676–1681.

[29] M. Kolbe, H. Besir, L.O. Essen, D. Oesterhalt, Structure of the light-driven chloride pump halorhodopsin at 1.8 Å resolution, Science 288 (2000) 1390–1396.

[30] J.M. Seddon, J.L. Hogan, N.A. Warrender, E.P. Peyroula, Structural studies of phospholipid cubic phases, Prog. Colloid Poly. Sci. 81 (1990) 189–197.

[31] D.P. Siegel, J.L. Banschbach, Lamellar/inverted cubic phase transition in N-methylated dioleoylphosphatidylethanolamine, Biochemistry 29 (1990) 5975–5981.

[32] R.H. Templer, J.M. Seddon, N.A. Warrender, A. Syrykh, Z. Huang, Inverse bicontinuous Cubic phases in 2:1 fatty acid/phosphatidylcholine mixtures. The effects of chain length, hydration, and temperature, J. Phys. Chem. 102 (1998) 7251–7261.

[33] D.C. Turner, Z.G. Wang, S.M. Gruner, D.A. Mannock, R.N. McElhaney, Structural study of the inverted cubic phases of di-dodecyl alkyl-β-D-glucopyranosyl-*rac*-glycerol, J. Phys. II (France) 2 (1992) 2039–2063.

[34] S.T. Hyde, S. Andersson, B. Ericsson, K. Larsson, A cubic structure consisting of a lipid bilayer forming an infinite periodic minimum surface of the gyroid type in the glycerolmonooleat-water system, Z. Kristallogr. 168 (1984) 213–219.

[35] S.T. Hyde, Microstructure of bicontinuous surfactant aggregates, J. Phys. Chem. 93 (1989) 1458–1464.

[36] H. Chung, M. Caffrey, The curvature elastic energy function of the lipid-water cubic mesophase, Nature 368 (1994) 224–226.

[37] R.H. Templer, J.M. Seddon, N.A. Warrender, Measuring the elastic parameters for inverse bicontinuous cubic phase, Biophys. Chem. 49 (1994) 1–12.

[38] R.H. Templer, D.C. Turner, P. Harper, J.M. Seddon, Corrections to some models of the curvature elastic energy of inverse bicontinuous cubic phase, J. Phys. II France 5 (1995) 1053–1065.

[39] U.S. Schwarz, G. Gompper, Stability of inverse bicontinuous cubic phases in lipid-water mixtures, Phys. Rev. Lett. 85 (2000) 1472–1475.

[40] U.S. Schwarz, G. Gompper, Bending frustration of lipid-water mesophases based on cubic minimal surfaces, Langmuir 17 (2001) 2084–2096.

[41] D.P. Siegel, M.M. Kozlov, The Gaussian curvature elastic modulus of N-monomethylated dioleoylphosphatidylethanolamine; relevance to membrane fusion and lipid phase behavior, Biophys. J. 87 (2004) 366–374.

[42] V. Cherezov, D.P. Siegel, W. Shaw, S.W. Burgess, M. Caffrey, The kinetics of non-lamellar phase formation in DOPE-Me: Relevance to biomembrane fusion, J. Memb. Biol. 195 (2003) 165–182.

[43] A.M. Squires, R.H. Templer, J.M. Seddon, J. Woenkhaus, R. Winter, T. Narayanan, S. Finet, Kinetics and mechanism of interconversion of inverse bicontinuous cubic mesophase, Phys. Rev. E 72 (2005) 011502.

[44] C.T. Sigal, W. Zhou, C.A. Buser, S. McLaughlin, M.D. Resh, Amino-terminal basic residues of Src mediate membrane binding through electrostatic interaction with acidic phospholipids, Proc. Natl. Acad. Sci. USA 91 (1994) 12253–12257.

[45] C.A. Buser, C.T. Sigal, M.D. Resh, S. McLaughlin, Membrane binding of myristylated peptides corresponding to the NH2 terminus of Src, Biochemsitry 33 (1994) 13093–13101.

[46] Y. Aota-Nakano, S.J. Li, M. Yamazaki, Effects of electrostatic interaction on the phase stability and structures of cubic phases of monoolein/oleic acid mixture membranes, Biochim. Biophys. Acta 1461 (1999) 96–102.

[47] S.J. Li, Y. Yamashita, M. Yamazaki, Effect of electrostatic interactions on phase stability of cubic phases of membranes of monoolein/dioleoylphosphatidic acid mixture, Biophys. J. 81 (2001) 983–993.

[48] S.M. Masum, S.J. Li, Y. Tamba, Y. Yamashita, T. Tanaka, M. Yamazaki, Effect of de novo designed peptides interacting with the lipid-membrane interface on the stability of the cubic phases of the monoolein membrane, Langmuir 19 (2003) 4745–4753.

[49] S.M. Masum, S.J. Li, T.S. Awad, M. Yamazaki, Effect of positively charged short peptides on stability of cubic phases of monoolein/dioleoylphosphatidic acid mixtures, Langmuir 21 (2005) 5290–5297.

[50] T.S. Awad, Y. Okamoto, S.M. Masum, M. Yamazaki, Formation of cubic phases from large unilamellar vesicles of dioleoylphosphatidylglycerol/monoolein membranes induced by low concentrations of Ca^{2+}, Langmuir 21 (2005) 11556–11561.

[51] Y. Okamoto, S.M. Masum, H. Miyazawa, M. Yamazaki, Low pH-induced transformation of bilayer membrane into bicontinuous cubic phase in dioleoyl-phosphatidylserine/monoolein membranes, Langmuir 24 (2008) 3400–3406.

[52] B. Tenchov, R. Koynova, G. Rapp, Accerated formation of cubic phases in phosphatidylethanolamine dispersions, Biophys. J. 75 (1998) 853–866.

[53] J. Israerachvili, Intermolecular and Surface Forces second ed., Academic Press, 1992.

[54] V. Cherezov, J. Clogston, Y. Misquitta, W. Abdel-Gawad, M. Caffrey, Membrane protein crystallization in meso: Lipid type-tailoring of the cubic phase, Biophys. J. 83 (2002) 3393–3407.

[55] V. Chupin, J.A. Killian, J.B. de Kruijff, Effect of phospholipids and a transmembrane peptides on the stability of the cubic phase of monoolein: Implication for protein crystallization from a cubic phase, Biophys. J. 84 (2003) 2373–2381.

[56] M.C. Wiener, S.H. White, Structure of a fluid dioleoylphosphatidylcholine bilayer determined by joint refinement of X-ray and neutron diffraction data, III, Complete Struct. Biophys. J. 61 (1992) 434–447.

[57] J.F. Nagle, S. Tristram-Nagle, Structure of lipid bilayers, Biochim. Biophys. Acta 1469 (2000) 159–195.

[58] Y. Yamashita, S.M. Masum, T. Tanaka, M. Yamazaki, Shape changes of giant unilamellar vesicles of phosphatidylcholine induced by a *de novo* designed peptide interacting with membrane interface, Langmuir 18 (2002) 9638–9641.

[59] W.C. Wimley, S.H. White, Experimentally determined hydrophobicity scale for proteins at membrane interface, Nat. Struct. Biol. 3 (1996) 842–848.

[60] K. Kinoshita, S. Furuike, M. Yamazaki, Intermembrane distance in multilamellar vesicles of phosphatidylcholine depends on the interaction free energy between solvents and the hydrophilic segments of the membrane surface, Biophys. Chem. 74 (1998) 237–249.

[61] S.J. Marrink, A.E. Mark, Effect of undulations on surface tension in simulated bilayers, J. Phys. Chem. B 105 (2001) 6122–6127.

[62] H. Vacklin, B.J. Khoo, K.H. Maden, J.M. Seddon, R.H. Templer, The bending elasticity of 1-monoolein upon relief of packing stress, Langmuir 16 (2000) 4741–4748.

[63] D.M. Anderson, S.M. Gruner, S. Leibler, Geometrical aspects of the frustration in the cubic phases of lyotropic liquid crystals, Proc. Natl. Acad. Sci. USA 85 (1988) 5364–5368.

[64] W. Helfrich, Elastic properties of lipid bilayers: Theory and possible experiments, Z. Naturforsch. C 28 (1973) 693–703.

[65] U. Seifert, R. Lipowsky, Morphology of vesicles, in: R. Lipowsky, E. Sackmann (Eds.), Structure and Dynamics of Membranes, Elsevier Science B.V., Amsterdam, 1995, pp. 403–463.
[66] A. Ben-Shaul, Molecular theory of chain packing, elasticity and lipid-protein interaction in lipid bilayers, in: R. Lipowsky, E. Sackmann (Eds.), Structure and Dynamics of Membranes, Elsevier Science B. V., Amsterdam, 1995, pp. 359–401.
[67] B. Alberts, A. Johnson, J. Lewis, M. Raff, K. Roberts, P. Walter, Molecular Biology of the Cell, fourth ed., Garland Science, New York, 2002.
[68] R.P. Rand, N.L. Fuller, S.M. Gruner, V.A. Parsegian, Membrane curvature, lipid segregation, and structural transitions for phospholipids under dual-solvent stress, Biochemistry 29 (1990) 76–87.
[69] T. Ito, M. Yamazaki, S. Ohnishi, Poly (ethylene glycol)-induced shrinkage of Sephadex gel: A model system for quantitative analysis of osmoelastic coupling, Biophys. J. 56 (1989) 707–711.
[70] Y. Tamba, S. Ohba, M. Kubota, H. Yoshioka, H. Yoshioka, M. Yamazaki, Single GUV method reveals interaction of tea catechin (−)-epigallocatechin gallate with lipid membranes, Biophys. J. 92 (2007) 3178–3194.
[71] Z. Chen, R.P. Rand, Comparative study of the effects of several n-alkanes on phospholipid hexagonal phases, Biophys. J. 74 (1998) 944–952.
[72] R.P. Rand, N.L. Fuller, Structural dimensions and their changes in a reentrant hexagonal-lamellar transition of phospholipids, Biophys. J. 66 (1994) 2127–2138.

CHAPTER EIGHT

THE IMPACT OF ASTROCYTES IN THE CLEARANCE OF NEUROTRANSMITTERS BY UPTAKE AND INACTIVATION

Katja Perdan, Metoda Lipnik-Štangelj, *and* Mojca Kržan*

Contents

---

* Corresponding author. Tel.: +386 1 543 7349; Fax: +386 1 543 7331;
E-mail address: mojca.limpel@mf.uni-lj.si

Department of Pharmacology and Experimental Toxicology, Faculty of Medicine, University of Ljubljana, Korytkova 2, Si-1000 Ljubljana, Slovenia

Advances in Planar Lipid Bilayers and Liposomes, Volume 9
ISSN 1554-4516, DOI: 10.1016/S1554-4516(09)09008-5

Abstract

Astrocytes, which are no longer considered as passive supportive cells of central nervous system, actively participate in brain communication as well as take care for proper microenvironment, because they take up the excess of extracellular potassium ions and neurotransmitters.

Neurotransmitter transporters are key elements in terminating synaptic activity of distinct neurotransmitters. They use energy stored in the electrochemical gradient of either sodium ions or protons across neuronal or glial cell membrane for uphill transport of neurotransmitters from extracellular to intracellular site. Sodium-coupled neurotransmitter transporters belong to two distinct families of transporters of solute carrier proteins (SLC): SLC 1 which represents glutamate transporters and SLC6 to which the other neurotransmitter transporters belong.

Apart from neurotransmitter transporters, there is another family in the SLC transporter super family that participates in movement of some monoamines across membranes, a SLC22 family. They act in a sodium- and chloride-independent manner.

Because of direct involvement of transporters in the availability of neurotransmitters, they represent a site of action of many present and future drugs.

In the present review we would like to address the importance of neurotransmitter transporters on astrocytes in the regulation of synaptic signaling.

1. ASTROCYTES

Astrocytes, which were first described and named neuroglia (neuronal glue) by German pathologist Rudolf Virchow [1], were recognized and classified as a distinct cell type at the beginning of 20th century [2, 3]. Other types of glial cells include oligodendrocytes, Schwann cells, and microglia.

Most glial cells are like neurons of ectodermal origin, but are not excitable, and do not form synaptic contacts with other cells. However, astrocytes possess numerous gap junctions [4], which allow signaling among themselves, in particular via propagation of calcium waves [5]. It is now recognized that astrocytes do not play just a passive supportive role, but are capable of releasing neuroactive compounds like neurotransmitters, cytokines, and growth factors in response to neurotransmitters or other signaling molecules, making them active partners in central nervous system (CNS) communications. Their star-shaped form with many processes enables them to envelope synapses made by neurons. Perisynaptic astrocytes are not just gap fillers, but equipotent members of so-called tripartite synapse, consisting of presynaptic and postsynaptic neuronal cells and perisynaptic astrocytes [6].

Astrocytes have a unique characteristic—they are able to change their morphology and function throughout life in response to changes in the brain microenvironment. In the developmental phase, astrocytes elongate and as radial glia form fibers that guide neurons toward their targets during their migration. In addition, they synthesize and release high levels of certain neurotrophic factors such as nerve growth factor (NGF) [7], brain-derived neurotrophic factor (BDNF) [8], and neurotrophin-3 (NT-3) [9]. Later on, radial glia retracts the long processes and transform into protoplasmatic astrocytes. As the brain matures, trophic support offered by astrocytes is no longer needed, so the levels of neurotrophic factors drop to very low or even undetectable levels [10]. The main function of astrocytes in the normal adulthood is the protection of neurons. Astrocytes thus buffer extracellular ion levels and take up different neurotransmitters as well as exogenous compounds.

Various forms of brain injury to the adult brain, like viral infections [11, 12], mechanical trauma [13], degenerative disorders [14, 15], and certain neurotoxins [16–20] transform resting astrocytes to reactive ones, which participate in the healing process of the brain, but also form a glial scar after excessive neuron loss. The scar is frequently an impediment to neuronal outgrowth after the lesion, but may also be involved in the healing process, since astrocytes in addition to microglia, participate in the clearance of posttraumatic debris.

1.1. Structure

Astrocytes are star-shaped process-bearing cells which constitute 25–50% of the cellular volume of most human brain regions. In the adult mammalian brain they are present in two major forms, *fibrous* which are predominantly located in the white matter, and *protoplasmatic* which exist mainly in the gray matter of the brain. Protoplasmatic astrocytes are spheroid in shape, contain clumped chromatin, and have many highly branched processes. Fibrous astrocytes have characteristic oval-shaped nucleus, evenly dispersed chromatin, and less pronounced processes. Astrocytes are classically identified histologically as many of these cells express the intermediate filament glial fibrillary acidic protein (GFAP) (Fig. 1).

1.2. Metabolic Support

The human brain constitutes only 2% of the body weight, yet the energy-consuming processes that ensure proper brain function account for approximately 25% of total body glucose utilization. Because glucose is a polar molecule it cannot cross the cell membrane by itself, but requires a special carrier protein. Glucose thus enters brain by facilitated diffusion via different glucose transporters (GLUT1–5), all members of solute carrier protein (SLC) 2 family.

Glucose enters the brain through glucose transporter GLUT1, weighing 55 kDa and located on endothelial cells of the blood–brain barrier. Uptake of glucose into astrocytes is mediated via 45 kDa glucose transporter

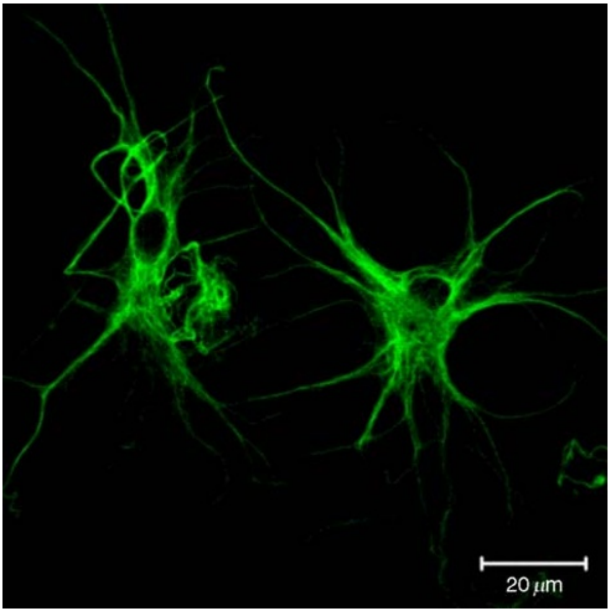

Figure 1 Astrocytes in primary culture prepared from neonatal rat cortex stained with GFAP (1:1000). Scale bar: 20 μm. Image was obtained with confocal microscopy at Carl Zeiss Reference Center for Confocal Microscopy at LN-MCP, Institute of Pathophysiology, Ljubljana, Slovenia.

GLUT1, whereas glucose transporter GLUT3 mediates glucose transport into neurons, and GLUT5 into microglial cells. The utilization of glucose by astrocytes is significantly higher than utilization of glucose by neurons. The contribution of astrocytes to glucose utilization during activation is even more striking, since the glucose uptake in astrocytes is significantly increased in the presence of increased concentrations of extracellular glutamate. The released glutamate is taken up into astrocytes together with two to three Na^+ ions and one glucose molecule. Simultaneously two molecules of ATP are produced through glycolysis and two lactate molecules are released and consumed by neurons.

Astrocytes represent a major glycogen storage site within CNS and thus provide neurons with glucose. Regardless the fact that astrocytes' glycogen stores are relatively small, if they are compared with glycogen stores in skeletal muscle (10-fold more abundant) and liver (100-fold more abundant), glycogen represents the only energy reserve source within CNS. Astrocyte glycogen stores are made directly from molecules of glucose taken up by perivascular astrocytes from brain blood vessels. Glycogen supply is sufficient to cover energy loss due to normal brain activity [21]. In addition to glycogen, taken up glucose is incorporated also in other macromolecules such as proteins (glycoproteins) and lipids (glycolipids).

1.3. Blood–Brain Barrier

For a long time it was thought that astrocyte do form the blood–brain barrier, which prevents the entry of cells and regulates the transport of nutrients and exogenous substances from the blood to the brain parenchyma. Indeed astrocytes constitute the blood–brain barrier in lower animal species; however, in higher species astrocytes do not play a substantial role in the function of blood–brain barrier. In fact, tight junctions and basal lamina of the endothelial cells are responsible for maintaining the barrier [22, 23].

1.4. Regulation of Ion Concentration in Extracellular Space

Astrocyte cell membranes express multiple ion channels like K^+, Na^+, Cl^-, HCO_3^-, and Ca^{2+} ion channels. When neurons are active, they release potassium ions into extracellular space. Increased extracellular potassium level can induce epileptic seizures, so the excess of extracellular potassium must be removed. The potassium ions released during neuronal activity are afterward soaked into astrocytes through astrocyte gap junction by a process known as "spatial buffering" [24].

1.5. Vasomodulation

Astrocytes may be directly and indirectly involved in the regulation of blood flow in CNS. After intense neuronal activity a spilt over glutamate activates adjacent astrocytes by binding to metabotropic glutamate receptors, which in turn release mediators (like epoxyeicosatrienoic acid and prostanglandins), which dilate local arterioles and increase blood flow and oxygen supply for the active brain areas [25, 26]. In addition, the activation of Ca^{2+}-activated K^+ channels in astrocyte endfeet and the efflux of K^+ have also been suggested to modify vascular tone by hyperpolarization and relaxation of smooth muscle cells in CNS blood vessels [25].

1.6. Transmitter Uptake and Release

During neurotransmission, high concentrations of neurotransmitters and ions are released into synaptic cleft. To prevent further involvement of the released neurotransmitters with synaptic activity, which might result in the inducing of epileptic activity or excitotoxic nerve injury (caused by, e.g., increased levels of glutamate), the excess of neurotransmitters and potassium should be rapidly removed from synaptic cleft. The concentration of neurotransmitters suddenly drops because of diffusion into extracellular fluid, reuptake of the released neurotransmitters into presynaptic neurons, enzymatic degradation, and the transport into perisynaptically localized astrocytes, in which enzymatic degradation of taken up neurotransmitters can also occur [27].

2. NEUROTRANSMITTERS

Neurotransmitters are signaling molecules, which are synthesized in presynaptic neurons, packed into synaptic vesicles, and released into synaptic cleft upon depolarization of presynaptic neuron. The classical neurotransmitters are small molecules like acetylcholine, biogenic amines (nordrenaline, dopamine, serotonin, and histamine), glutamate, and γ-amino butyric acid (GABA). Certain neuropeptides, for example, enkephalins, endorphins, neurotensin, substance P, somatostatin, and even gases like nitric oxide and carbon monoxide belong to neurotransmitters. Released neurotransmitters communicate with postsynaptic neuron and other target cells by binding to specific cell surface receptors. In order to terminate the neuronal signal in time, neurotransmitters must be afterward removed quickly from synaptic cleft either by the reuptake into the presynaptic neuron, uptake into other perisynaptic cells like astrocytes, or degradation by specific enzymes. The only exception to this rule represents acetylcholine, which is first metabolized to acetate and choline. The latter is further taken up by presynaptic neuron as well as astrocytes via choline transporters [28].

3. TRANSPORTERS

Astrocytes are known to express transporters for different neurotransmitters. Transporters are membrane proteins and their primary function is to facilitate the flux of molecules in and out of cells. The primary function of transporters is to carry the nutrients and endogenous substances such as sugars, amino acids, nucleotides, and vitamins across cell membranes and different body barriers and to protect the body from toxic actions of different compounds. However, the transporters do not specifically carry over just the physiologically occurring molecules, but they can also take up exogenous compounds that are structurally similar to endogenous substrates, e.g., different drugs and neurotoxins. Consequently these transporters play a significant role in determining the availability, therapeutic efficacy, and pharmacokinetics of certain drugs.

Transporters can be classified in a number of different manners: according to the way of traffic into influx and efflux transporters; according to the process they mediate into secretory transporters versus absorptive transporters; according to location into intracellular vesicular transporters that are responsible for sequestering transmitters from the cytoplasm into synaptic vesicles and plasma membrane transporters that are responsible for sequestering the released neurotransmitters from extracellular to intracellular compartment. The vesicular transporters are localized in synaptic vesicles and include: vesicular monoamine transporter (VMAT), vesicular glutamate transporter (VGLUT), and vesicular inhibitory amino acid transporter (VGAT). The cell membrane transporters can mediate either facilitated transport or active energy-dependent transport. Facilitated transport allows molecules to move across the cell membrane down their electrochemical gradients. Therefore, this process does not require any chemical energy. On a contrary, active transporters that carry molecules across cell membrane against their electrochemical gradient, therefore, need coupling to the hydrolysis of adenosine triphosphate (ATP) as an energy source. In primary active transport active transporters move the molecules across cell membranes against their electrical and chemical gradient and need concomitant hydrolysis of ATP for energy support. In the secondary active transport, transporters use the ion (most often sodium or proton) gradients across cell membrane produced by primary active transporters and carry substrates against an electrochemical difference.

Another classification distinguishes ATP-binding cassette (ABC) transporters versus SLC. ABC transporters require coupling with hydrolysis of ATP to transport substrates across the cell membrane. Multidrug resistance protein (MDR), multidrug resistance associated protein (MRP), and breast cancer resistance protein (BCRP) belong to this group, which are mostly involved in the efflux of different compounds.

SLC transporters utilize electrochemical potential difference like transmembrane sodium and proton potential difference and do not posses ATP-binding sites. There are two major classes of neurotransmitter transporters present in cell membranes of neurons and glia belonging to SLC family: the high affinity glutamate transporters (SLC1 gene family) and SLC6 gene transporter family, which includes dopamine transporter (DAT), serotonin transporter (SERT), noradrenaline transporter (NET), glycine transporter (GLYT), and GABA transporter (GAT), which were all found to be expressed on astrocyte cell membranes. They depend on sodium and chloride ions for their function [29]. A schematic structure transporter belonging to SLC6 gene family is shown in Fig. 2. Biogenic amines can be transported in neurons and astrocytes also by three members of SLC22 family, namely organic cation transporters (OCTs), that mediate a Na^+- and Cl^--independent low-affinity and high-capacity transport [30].

Rapid reuptake of the released neurotransmitters is essential because it limits the duration of synaptic communication as well as diffusion to other synaptic sites and enables recycling and reuse of unmetabolized neurotransmitters, and thereby reducing requirements for *de novo* neurotransmitter synthesis. Neuronal transporters, present in the vicinity of synapse are

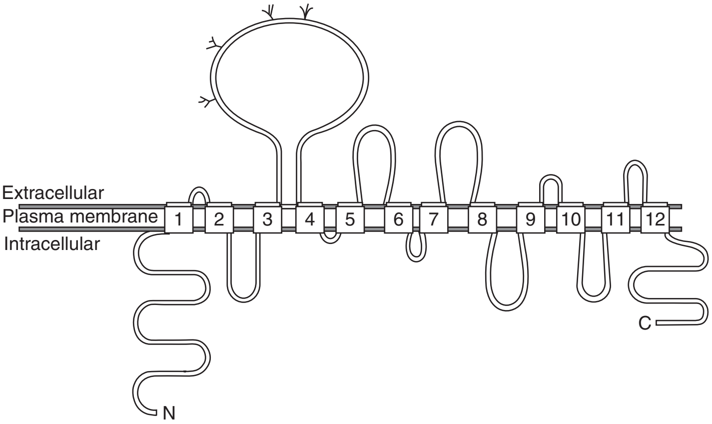

Figure 2 Schematic representation of a transporter for biogenic amines (family SLC 6). It is a protein with 12 hydrophobic transmembrane domains (TM) joined by alternating extracellular and intracellular loops and N- and C-terminal residues, both located in intracellular space. On the extracellular loop between TM3 and TM4 there are several *N*-glycosylation sites present.

essential for rapid termination of the signal in neuronal-effector organ transmission, whereas nonneuronal transporters and transporters located on neuronal axons are more important for limiting the spread of the signal and for clearance of catecholamines from the bloodstream and extracellular space (Fig. 3). The activity of transporters for biogenic amines is not constant, but depends on several factors. Protein kinase C activation [31] and transporter protein phosphorylation [32] can lead to reduced capacity of transporters for biogenic amines on cell membrane. Activity of transporters can be altered due to presence of substrates (neurotransmitter) and activation of presynaptic receptors and second messengers. Because of these the role of transporters is not just the removal of neurotransmitters, but they take an active part in synaptic communication.

The characteristics of classical neurotransmitters uptake and inactivation within astrocytes will be discussed in the continuation of the paper.

3.1. Glutamate Uptake

Glutamate is a major excitatory neurotransmitter and plays critical roles in fundamental processes in the brain, for example, learning and memory [33]. It has also been implicated as a potent neurotoxin. To ensure a high signal-to-noise ratio during synaptic transmission and to prevent neuronal damage that might occur as a result of excessive activation of glutamate receptors, the extracellular glutamate concentration is tightly controlled

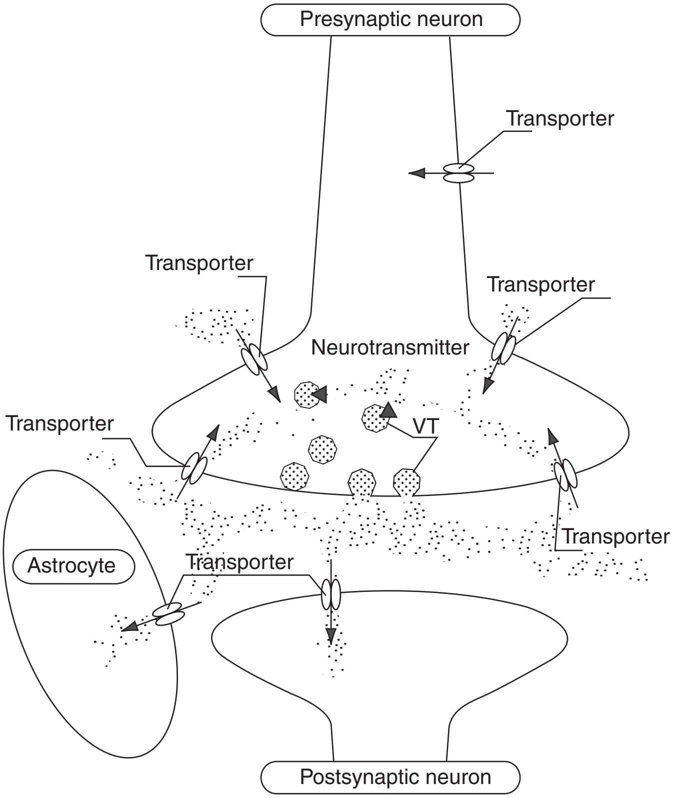

Figure 3 Schematic localization of transporters in neuronal and glial cells. Transporters are located on pre- and postsynaptic neuronal cell membranes, on neuronal dendrites and on astrocytes. In presynaptic neuron neurotransmitter molecules are packed into vesicles by the action of vesicular transporter (VT).

by glutamate transporters in the plasma membrane of neurons and the surrounding glial cells. Studies of glutamate transporters, using the genetic knockout strategy, indicate that glial, but not neuronal, glutamate transporters play critical roles in maintaining the extracellular glutamate concentrations, and are thereby essential for both normal synaptic transmission and protection of neurons against glutamate excitotoxicity [34].

Glutamate transporters belong to two families: plasma membrane transporters in neurons and glial cells that remove the neurotransmitter glutamate from the synapse using preexisting ionic gradients as a source of energy [35, 36] and intracellular vesicular transporters. Thus far, five Na^+-dependent excitatory amino acid transporters (EAATs 1–5), which belong to plasma membrane transporters [37, 38], and three vesicular glutamate transporters (VGLUTs 1–3) have been identified. Examination of EAATs and

VGLUTs in brain preparations and by heterologous expression of the various cloned subtypes shows these two transporter families differ in many of their functional properties including substrate specificity and ion requirements [39].

3.1.1. EAATs

The EAATs structure reveals a bowl-shaped trimer, with a solvent-accessible extracellular basin extending halfway across the membrane. Each EAAT monomer is composed of eight transmembrane helices (TM1-TM8) and two highly conserved helical hairpins (HP1 and HP2) forming a lumen for binding and permeation of the substrate and Na^+ ions. Each substrate-binding site is cradled by the two helical hairpins reaching from the opposite sides of the membrane. The functional importance of HP1 and HP2 [40] is supported by biochemical experiments on bacterial [37] and mammalian transporters [41–45]. In a recent crystallographic and thermodynamic study of EAATs [46], HP2 was proposed to serve as the extracellular gate that adopts an open conformation exposing the substrate binding site to the extracellular solution.

EAATs transport their substrates against the concentration gradient by coupling to cotransport of three Na^+ and one H^+, and countertransport of one K^+ ion [47–49]. Hence, glutamate transport by EAAT is an electrogenic process resulting in a net translocation of two positive charges to the intracellular side during each transport cycle. In addition to this coupled flux, Na^+ and substrate transport by EAAT also activates a thermodynamically uncoupled flux of Cl^- from the extracellular side to the cytoplasmic site [50]. The uncoupled Cl^- conductance plays an important physiological role by hyperpolarizing the membrane and dissipating the electrical potential generated during the substrate transport [51]. There is, however, conflicting evidence with regard to the Cl^- permeation pathway through EAAT. Some studies suggest that individual monomers might provide the pathway for Cl^- [36, 52], whereas others indicate that Cl^- permeates through a pore formed at the centre of the trimeric structure of EAAT [53, 54]. Recent S65V mutation experiment 1 in EAAT [51] indicates that Na^+-driven substrate transport by EAAT induces conformational changes of monomers regulating Cl^- permeation and that the uncoupled Cl^- permeation pathway is different from the substrate transport pathway. However, the problem of the exact permeation pathway of Cl^- is still unresolved.

The taken up glutamate within astrocytes is converted into inactive glutamine, which is released from astrocytes via transporter system N-1, and afterward taken into neurons, where it is recycled into glutamate and reused as a neurotransmitter.

3.1.2. VGLUTs

Astrocytes exhibit excitability based on variations of their intracellular Ca^{2+} concentrations, which leads to glutamate release that, in turn, can signal to adjacent neurons. This glutamate-mediated astrocyte–neuron signaling occurs at physiological intracellular Ca^{2+} levels in astrocytes and includes modulation of synaptic transmission. The mechanism underlying Ca^{2+}-dependent glutamate release from astrocytes is most likely exocytosis [55], because astrocytes express the protein components of the soluble *N*-ethyl maleimide-sensitive fusion protein attachment protein receptors complex, including synaptobrevin 2, syntaxin and synaptosome-associated protein of 23 kDa [56]. Astrocytes also express vesicular glutamate transporters (VGLUTs) that are critical for vesicle refilling. It was found in cultured and freshly isolated astrocytes that the presence of brain-specific Na^+-dependent inorganic phosphate cotransporter and differentiation-associated Na^+-dependent inorganic phosphate cotransporter that have recently been identified as VGLUTs 1 and 2. Indirect immunocytochemistry showed a punctate pattern of VGLUT immunoreactivity throughout the entire cell body and processes, whereas pharmacological inhibition of VGLUTs abolished mechanically and agonist-evoked Ca^{2+}-dependent glutamate release from astrocytes. Taken together, these data indicate that VGLUTs play a functional role in exocytotic glutamate release from astrocytes [57].

3.2. GABA Uptake

GABA is synthesized in neurons from L-glutamic acid and packed into synaptic vesicles by a specific vesicular GABA transporter (VGAT) [58]. Depolarization of presynaptic neuron induces the release of GABA, which freely diffuses across the synaptic cleft to interact with appropriate receptors on target cells. Free synaptic GABA is taken back to presynaptic neurons and glial cells.

There are at least three different GABA transporters (GAT1, GAT2, and GAT3) found in the brain tissue, which are located on neurons and glia [59, 60]. Transporters GAT1, which are triggered by a novel antiepileptic drug tiagabine, are located mostly on neurons, while transporters GAT2 and GAT3 are present on other brain cells including glia. GABA uptake in membrane vesicles derived from astroglial cells was found to be Na^+- and Cl^--dependent, electrogenic and sensitive to β-alanine. To carry one GABA molecule across the cell membrane two Na^+ and one Cl^- molecules are needed for cotransport [61].

GAT1–3 share the structure common to all transporters belonging to SLC6 transporter family. The protein is an α-helix with 12 transmembrane domains, connected with hydrophilic loops with amino and carboxyl intracellular termini [62].

GAT transporters have a prominent role in the pathogenesis of epilepsy, since their expression is significantly different in epileptic (temporal lobe epilepsy) than in healthy hippocampus [63]. The immunoreactivity for GAT1 is significantly reduced, whereas the expression of GAT3 is increased in hippocamus exhibiting Amonn horn sclerosis in comparison with healthy human hippocampus. The GAT3 localization was greater in astrocytes next to remaining functional neurons in sclerotic hippocampus.

GABA can be broken down within astrocytes into succinic semialdehyde, due to presence of GABA degrading enzyme GABA-transaminase. Glutamine formed from GABA in astrocytes can be transferred to GABAergic neurons and subsequently converted to GABA [64].

3.3. Glycine Uptake

Neurotransmitter glycine has a double role in human CNS. It acts as an inhibitory neurotransmitter as well as a coagonist of glutamate when activating NMDA (*N*-methyl-D-aspartate) receptors for glutamate. In order to activate glutamate NMDA receptors, it is necessary that glutamate and glycine bind at the same time.

Glycine is synthesized from amino acid serine in a presynaptic neuron and stored into synaptic vesicles by the same vesicular transporter as GABA (VGAT). Upon depolarization, glycine is released into synaptic cleft from where it is transported either to astrocytes via transporter GLYT1 or to presynaptic neuron via transporter GLYT2. Two Na^+ and one Cl^- are cotransported along with a molecule of glycine via GLYT1, whereas GLYT2 has a transport stoihiometry of three Na^+, one Cl^- ion, and one glycine molecule [65], thus the driving force is much higher into neurons than into astrocytes. GLYT1 eliminates glycine from synaptic cleft and terminates synaptic signaling, whereas GLYT2 enhances the reuse of previously released glycine [66]. The transport occurring through GLYT1 is bidirectional, glycine can be released from astrocytes into extracellular space [67] using the reverse transport. There are three different isoforms of GLYT, which do not differ in kinetic properties (K_m and V_{max} for glycin), but have different pharmacological profile (sensitivity to different ligands) and different distribution throughout brain areas [68]. GLYT1 transporters are located also in brain regions without glycine neurotransmission. There role might be involvement in the modulation of glycine-stimulated activity of glutamate NMDA receptors.

The taken up glycine can be either released from astrocytes or metabolically degraded.

3.4. Noradrenaline Uptake

Synthesized noradrenline is packed into the synaptic vesicles of noradrenergic neurons via VMAT2. The released noradrenaline diffuses in the synaptic cleft and activates its receptors. The synaptic action of noradrenaline is terminated by its uptake either into presynaptic neuron [69] or to perisynaptic astrocytes [70] using specific NET.

NET belongs to SLC family (SLC 6) with a typical 12 hydrophobic domain structure. There are three extracellular *N*-glycosylation sites, and one serine–threonine intracellular phosphorylation site. NET is found on neuronal cells in different brain regions as well as in astrocytes in primary cultures [70, 71]. The uptake of noradrenaline via NET is Na^+ dependent and can be blocked by inhibiting Na^+K^+-ATPase [70]. Uptake of triatiated noradrenaline showed regional differences. Astrocyte cultures derived from hippocampus take up greater amounts of [^{3}H]-noradrenaline than astrocyte cultures from corpus striatum and cerebral cortex [72]. Reuptake of noradrenaline increases in parallel with noradrenaline release. The phosphorylation of NET protein may play a role determining the rate of noradrenaline uptake. The Na^+-dependant component of the uptake is inhibited by tricyclic antidepressant drugs desipramine and amitriptyline with IC_{50} values in nmol range. Noradrenaline can be taken up in a Na^+-independent manner by a low-affinity, high-capacity transport, which is not inhibited by tricylic antidepressants but sensitive to the inhibition with *O*-methylated metabolites of catecholamines and corticosterone [73, 74] named also uptake$_2$ occurring via organic cationic transporter 3.

The noradrenaline degrading enzymes (monoamino oxidase and catechol-*O*-methyl transferase) are located intracellularly in many different cell types including astrocytes [74]. Enzymatic degradation transforms noradrenaline to inactive metabolites.

3.5. Serotonin Uptake

Serotonin released into synaptic cleft can be inactivated by several different mechanisms including diffusion away from synapse, metabolic degradation by enzyme MAO or taking up by specific serotonin transporter (SERT) either into presynaptic neurons or into glial cells. The reuptake of serotonin mediated by SERT represents the most important mechanism of serotonin inactivation within CNS.

Human SERT is 630 amino acid residues long protein, organized in 12 transmembrane domains joined with alternating extracellular and intracellular loops, and intracellular N- and C-terminal residue. On the extracellular site there are two putative *N*-glycosylation sites and eight serine–threonine phosphoralation sites. mRNA for SERT is located only in raphe nuclei, whereas SERT protein is located diffusely in brain along with the projections of serotonergic nerve fibers. SERT protein is not localized mainly in the synaptic site, but mostly perisynaptically. That is consistent with the idea that the majority of the brain serotonin is released by volume and not synaptic transmission [75]. In addition to neuronal site, SERT was found to be localized also in astrocyte cell membranes *in vitro* [76] and *in vivo* [77], where is able to transfer serotonin bidirectionally in Na^+- and antidepressant drugs-sensitive manner [78] but with a K_m value approximately 10 times greater than found in adult brain synaptosomes [76].

Due to the presence of monoamine oxidase within astrocytes taken up serotonin can be enzymatically degraded to 5-hydroxyindoleacetic acid (5-HIAA) [79].

3.6. Dopamine Uptake

The importance of dopamine in neuropharmacological respect lies in its involvement in many disorders of brain function, such as Parkinson's disease, schizophrenia and attention deficit disorder as well as drug dependence and endocrine disorders.

The synthesis of dopamine follows the same path as that of noradrenaline, namely the conversion of tyrosine to dihydroxy-phenylalanine, followed by decarboxilation to dopamine. Dopaminergic neurons lack β-hydroxylase, therefore the process stops at this stage and dopamine is packed into synaptic vesicles through VMAT2. After being released, dopamine exhibits its intra- and extrasynaptic effects [80] and is later removed via dopamine transporter (DAT), the neuronal presynaptic plasmalemmal protein (member of SLC 6 family of transporters) that is responsible for the reuptake of released dopamine [81]. DAT and VMAT2 are critical regulators of dopamine disposition within the brain. Following uptake into presynaptic neurons, dopamine is either recycled and packed into synaptic vesicles or metabolized by MAO and COMT. Numerous abused substances and drugs in clinical use have important pharmacological interactions with DAT. These compounds fall into two categories: those that block dopamine transport (e.g., cocaine, methylphenidate) and those that serve as substrates for transport (e.g., dopamine, amphetamine and 3, 4-methylenedioxymethamphetamine (ecstasy)).

The rat [82], bovine [83], and human [84] neuronal DAT have been cloned. Besides neurons, astrocytes also contain DAT and $uptake_2$ (OCT3) transporters. Due to the close apposition of astrocytes to synaptic cleft, glial and neuronal transport systems are well positioned to remove monoamine neurotransmitters released from the presynaptic neuron. Since key enzymes, MAO and COMT, are also present in astrocytes, glial uptake systems are likely to play an important role in regulating extracellular dopamine concentrations [71, 85]. Data suggest that astrocytes really do regulate extracellular dopamine concentrations, but to what extent and whether through NET and uptake$_2$ (OCT3) transport [86], or through DAT itself [87], remains to be resolved.

3.7. Histamine Uptake

Synthesis of histamine in histaminergic neurons occurs through the action of histidine decarboxylase on histidine. Later on, synthesized histamine is taken up into synaptic vesicles by the vesicular monoamine transporter 2 (VMAT2) [88] and released into the synaptic cleft upon depolarization stimuli. The released neurotransmitter histamine is metabolized by the enzyme histamine *N*-methyltransferase (HNMT) producing telemethylhistamine [89, 90], which can occur in astrocytes due to expression of HNMT within. In order to be enzymatically degraded or recycled, histamine must be transported either into the presynaptic neuron or into surrounding glial cells. Reports from Huszti's laboratory described histamine uptake by cultured glial cells prepared from embryonic chicks [91], neonatal rats [92–94], and adult rats [95], which was Na^+ dependent but not Cl^- dependent [95] and bidirectional [91–93]. Glial cells were also found to be involved in the continuous removal of neuronal histamine from the synaptic cleft in *in vivo* conditions [96]. Stuart and coworkers [97, 98] described a Na^+-dependent histamine uptake into arthropod photoreceptors, which use histamine as their neurotransmitter, as well as into surrounding glia. Interestingly, preferential uptake of histamine into the arthropod photoreceptor terminals occurred under constant light exposure, when the cells were depolarized, while in the dark histamine was taken up by glial cells. Recently, Yanai's group [99] reported a high and low affinity, Na^+-, Cl^--, and HCO_3^--dependent [^{3}H]-histamine transport into rat brain synaptosomes, but a specific histamine transporter has not been elucidated yet.

3.8. Organic Cation Transporters

The SLC22 family comprises OCTs, zwitterion/cation transporters (OCTNs), and organic anion transporters (OATs). These transporters contain 12 α-helical transmembrane domains (TMDs) and one large extracellular loop between TMDs 1 and 2. OCTs (OCT1–3) are involved in membrane transport of organic cations, which include many drugs and endogenous substances, including monoamine neurotransmitters. In addition to kidney and liver [100, 101], OCTs were also found in neuronal [102] and glial cells [28, 103] in humans and rodents. As for regional distribution in the CNS, OCT3 is highly expressed in hippocampus, cerebellum, and cerebral cortex [104], in the choroid plexus ependymal cells and circumventricular organs [105, 106]. Whether they actually play a functional role on glial cells, however, remains yet to be established.

All three OCTs translocate various organic cations in a bidirectional, Na^+- and Cl^--independent manner. The main function of OCT1 and OCT2 is efflux of exogenous compounds, whereas OCT3 is thought to have important functions in the brain, including in clearance of monoamine neurotransmitters. The affinity of OCT3 to transport noradrenaline, serotonin, dopamine and histamine is significantly lower than the affinity of SERT, NET, DAT, but the maximal uptake rate is significantly higher than the maximal rate of uptake by the corresponding high affinity transporters. OCT3 is alternatively called "extraneuronal monoamine transporter" because its functional properties match those of the corticosterone-sensitive catecholamine transport system originally characterized in nonneuronal cells, such as cardiac myocytes and smooth muscle cells (so called $uptake_2$). The distinguishing characteristics of $uptake_2$ are the ability to transport cateholamines in a Na^+- and Cl^--independent manner, interactions with a variety of organic cations, membrane potential driven transport, inhibition by steroids, and expression in a variety of tissues [104].

Thus OCTs, in particular OCT3, probably represent another firewall involved in the reuse of neurotransmitters. Moreover, mice with knockout gene for OCT3 show diminished intracellular levels of biogenic amines, particularly dopamine and histamine. OCT3-deficient mice are more prone to anxiety and stress than wild-type animals and show higher sensitivity to psychostimulants [107]. In circumstances, when blood levels of corticosterone are increased (e.g., chronic stress), the $uptake_2$ of monoamine neurotransmitters occurring via OCT3 might be lowered and this can contribute to elevated local monoamine concentrations [108].

4. DRUGS AFFECTING TRANSPORT FUNCTION

High- and low-affinity transporters for neurotransmitters regulate their spatial and temporal concentrations in extracellular space and thus regulate the activation of receptors, which is necessary for proper communication in CNS. Drugs that block these transporters increase levels of neurotransmitters in synaptic cleft and in the extracellular space, which results in a profound behavioral effect.

Table 1 shows a list of drugs acting on different transporters and their present and possible future therapeutic indications.

At the moment there are no drugs available in the market that would act as inhibitors of glutamate transport. But there are diseases (amyotrophic lateral sclerosis, epilepsy and hyperekplexia) that may be associated with a dysfunction of glutamate transport. Therefore, EAAT transporters might represent a useful experimental tool to study the involvement of glutamate transport in these diseases and the effect of excitotoxic nerve injury induced

Table 1 The connection of neurotransmitter transporters to pathogenesis of certain diseases and pharmacotherapy

Transporter	Disease	Drugs acting as	Reference
EAAT	*Amyotrophic lateral sclerosis?*	*Activity enhancers*	[109]
	Neurodegenerative disorders	*Inhibitors*	[60]
	Schizophrenia	*Typical and atypical antipsychotics?*	[110]
EAAT3	Epilepsy	*Carbamazepine?*	[111]
GAT1	Epilepsy	Tiagabine	[112]
GAT3	*Epilepsy*	*Other anticonvulsants*	[113]
		Levetiracetam?	[114]
GLYT1	*Schizophrenia, pain treatment, narcosis*	*GLYT1 inhibitors*	[115]
GLYT2	↑*general muscle tone*	*GLYT2 antagonists*	
NET	Depression	Reboxetine	[116]
	Panic disorders	Amoxetine	[117]
	Attention deficit hyperactivity disorder	Imipramine and other tricyclic antidepressants	[84]
	Drug dependence	Cocaine[a]	
SERT	Depression	Fluoxetine, Paroxetine Citalopram	[84]
	Drug dependence	Fluvoxamine	[117]
		Imipramine and other tricyclic antidepressants	
		Cocaine[a]	
DAT	Depression	Sertraline	[84]
	Drug dependence	Amphetamines[a]	[117]
	Euphoria	Cocaine[a]	

[a] Recreational drugs.

Words in italics indicate "possible future treatment." Words in roman indicate "already in use or effects already known."

by increased glutamate levels. Maybe a different strategy would be better—to increase the transport ability or to increase expression of functional glutamate transporters.

Tiagabine is a GAT 1 inhibitor and is clinically used as an effective antiepileptic drug. It increases GABA levels by blocking its reuptake and decreases neuronal excitability by binding to neuronal GABA receptors. Although selective for GAT1, tiagabine lacks cell type selectivity and is an equipotent inhibitor of neuronal and glial GAT1 [118].

Taking into consideration the "glutamate hypothesis" of schizophrenia, which states that the illness is associated with decreased activity of glutamate, especially acting through NMDA receptors, GLYT1 inhibitors might prove beneficial if taken together with other antipscychotic drugs [119].

Drugs inhibiting NET (tricyclic antidepressant drugs, reboxetine) and SERT (flouxetine, citalopram, paroxetine, etc.) in a more or less selective way have been used for a long time for treatment of depression, eating disorders, obsessive compulsive, and panic disorders. The exact mechanism of action has not been elucidated yet. Although they cause immediate inhibition of NET and/or SERT, it takes several weeks of continuous administration of antidepressant drugs to observe beneficial effects.

Cocaine inhibits DAT and euphoric effects are a consequence of increased dopaminergic stimulation of reward pathways. Unselective inhibition of DAT and NET is achieved by amphetamines. In fact, amphetamines block the reuptake and at the same time increase the efflux of monoamines from presynaptic neurons. By blocking VMAT amphetamines also prevent filling of synaptic vesicles with monoamines. All these effects eventually lead from transient increase to depletion of monoamines in the brain. Apart from their actions on transporters, they also act as partial agonists at adrenergic receptors.

Transporters can also represent a gate to neuron intracellular space for neurotoxic compounds, which structurally resemble neurotransmitters. MPTP, after being metabolized to MPP^+ by MAO-B in glia, enters the neuron through DAT and can cause severe neurotoxic damage.

5. CONCLUSION

In the past decades we have witnessed tremendous progress in the field of neurotransmission, and its inactivation patterns. Reuptake and uptake through neurotransmitter transporters into presynaptic neurons and glia, respectively, represent only one of the mechanisms of terminating neurotransmitter action. Amino acid neurotransmitters, glutamate, GABA, and glycine are predominantly inactivated by astrocytes. Glial cells represent an additional uptake and inactivation option for biogenic amine neurotransmitters. As the activity of transporters is not constant but is adapting to changes in the microenvironment, transporter functions represent a regulatory step in constant communication and signaling process within the brain. Drugs that block neurotransmitter transporter functions prolong transmitter's action and are nowadays used as therapeutics as well as recreational compounds and provide an excellent tool for further investigation of neurotransmitter transporters.

ACKNOWLEDGMENTS

This work was supported by the research grant P3-067 of Ministry of Higher Education, Science and Technology, Republic of Slovenia. We would like to acknowledge Carl Zeiss Reference Center for Confocal Microscopy at LN-MCP, Institute of Pathophysiology, Faculty of Medicine Ljubljana for sharing and helping with confocal microscopy.

REFERENCES

[1] R. Virchow, Über das granulierte Aussehen der Wandungen der Gehirnventrikel, Allg. Z. Psychiatr. 3 (1846) 242–255.

[2] E. Mugnaini, F. Walberg, Ultrastructure of neuroglia, Ergeb. Anat. Entwicklungsgesch. 37 (1964) 194–236.

[3] V. Garcia-Marin, P. Garcia-Lopez, M. Freire, Cajal's contributions to glia research, Trends Neurosci. 30 (2007) 479–487.

[4] C. Giaume, K.D. Mc Carthy, Control of gap-junctional communication in astrocytic networks, Trends. Neurosci. 19 (1996) 319–325.

[5] A. Verkhratsky, H. Kettenmann, Calcium signalling in glial cells, Trends. Neurosci. 19 (1996) 346–352.

[6] A. Araque, V. Parpura, R.P. Sanzgiri, P.G. Haydon, Tripartite synapses: Glia, the unacknowledged partner, Trends. Neurosci. 22 (1999) 208–215.

[7] M. Lipnik-Stangelj, Multiple role of histamine H1-receptor-PKC-MAPK signalling pathway in histamine-stimulated nerve growth factor synthesis and secretion, Biochem. Pharmacol. 72 (2006) 1375–1381.

[8] Š. Miklic, D.M. Jurič, M. Čarman-Kržan, Differences in the regulation of BDNF and NGF synthesis in cultured neonatal rat astrocytes, Int. J. Dev. Neurosci. 22 (2004) 119–130.

[9] G. Moretto, R.Y. Xu, D.G. Walker, S.U. Kim, Co-expression of mRNA for neurotrophic factors in human neurons and glial cells in culture, J. Neuropathol. Exp. Neurol. 53 (1994) 78–85.

[10] M. Krzan, V.W. Wu, J.P. Schwartz, Serotonin regulation of nerve growth factor synthesis in neonatal and adult astrocytes: Comparison to the beta-adrenergic agonist isoproterenol, J. Neurosci. Res. 64 (2001) 261–267.

[11] K.C. Ma, X.J. Nie, A. Höög, Y. Olsson, W.W. Zhang, Reactive astrocytes in viral infections of the human brain express endothelin-like immunoreactivity, J. Neurol. Sci. 126 (1994) 184–192.

[12] T. Wyss-Coray, E. Masliah, S.M. Toggas, E.M. Rockenstein, M.J. Brooker, H. S. Lee, L. Mucke, Dysregulation of signal transduction pathways as a potential mechanism of nervous system alterations in HIV-1 gp120 transgenic mice and humans with HIV-1 encephalitis, J. Clin. Invest. 97 (1996) 789–798.

[13] A.I. Faden, Experimental neurobiology of central nervous system trauma, Crit. Rev. Neurobiol. 7 (1993) 175–186.

[14] A. Delacourte, General and dramatic glial reaction in Alzheimer brains, Neurology. 40 (1990) 33–37.

[15] C.J. Pike, B.J. Cummings, C.W. Cotman, Early association of reactive astrocytes with senile plaques in Alzheimer's disease, Exp. Neurol. 132 (1995) 172–179.

[16] P. Rataboul, N. Faucon-Biguet, P. Vernier, F. Vitry, S. Boularand, A. Privat, J. Mallet, Identification of a human glial acidic fibrillary protein c DNA: A tool for the molecular analysis of reactive gliosis in the mammalian central nervous system, J. Neurosci. Res. 20 (1988) 165–175.

[17] J.F. Reinhard Jr, D.B. Miller, J.P. O'Callaghan, The neurotoxicant MPTP (1-methyl-4-phenyl-1,2,3, 6-tetrahydropyridine) increases glial fibrillary acidic protein and decreases dopamine levels of the mouse striatum: Evidence for glial response to injury, Neurosci. Lett. 95 (1988) 246–251.

[18] J.S. Schneider, F.J. Denaro, Astrocytic responses to the dopaminergic neurotoxin 1-methyl-4-phenyl-1,2,3,6-tetrahydropyridine (MPTP) in cat and mouse brain, J. Neuropathol. Exp. Neurol. 47 (1988) 452–458.

[19] M. Ogawa, I. Nagatsu, M. Yoshida, Astroglial cell alteration caused by neurotoxins: Immunohistochemical observations with antibodies to glial fibrillary acidic protein, laminin, and tyrosine hydroxylase, Exp. Neurol. 106 (1989) 187–196.

[20] J.G. Sheng, S. Shirabe, N. Nishiyama, J.P. Schwartz, Alterations in striatal glial fibrillary acidic protein expression in response to 6-hydroxydopamine-induced denervation, Exp. Brain. Res. 95 (1993) 450–456.

[21] P.J. Magistretti, L. Pellerin, Astrocytes Couple Synaptic Activity to Glucose Utilization in the Brain, News. Physiol. Sci. 14 (1999) 177–182.

[22] G.W. Goldstein, Endothelial cell-astrocyte interactions: A cellular model of the blood brain barrier, Ann. NY. Acad. Sci. 529 (1988) 31–39.

[23] T.J. Raub, S. Kuentzel, G.A. Sawada, Permeability of bovine brain microvessel endothelial cells *in vitro*. Barrier tightening by a factor released from astroglioma cells, Exp. Cell. Res. 199 (1992) 330–340.

[24] W. Walz, Role of astrocytes in the clearance of excess extracellular potassium, Neurochem. Int. 36 (2000) 291–300.

[25] G.R. Gordon, S.J. Mulligan, B.A. MacVicar, Astrocyte control of the cerebrovasculature, Glia. 55 (2007) 1214–1221.

[26] H. Hirase, A multi-photon window onto neuronal-glial-vascular communication, Trends. Neurosci. 28 (2005) 217–219.

[27] J.R. Cooper, F.E. Bloom, R.H. Roth, The biochemical basis of neuropharmacology, 18th Ed., Oxford University Press, New York, 2003.

[28] M. Inazu, H. Takeda, T. Matsumiya, Molecular and functional characterization of an Na^+-independent choline transporter in rat astrocytes, J. Neurochem. 94 (2005) 1427–1437.

[29] L. Iversen, Neurotransmitter transporters and their impact on the development of psychopharmacology, Br. J. Pharmacol. 147 (2006) S82–S88.

[30] H. Koepsell, K. Lips, C. Volk, Polyspecific organic cation transporters: Structure, function, physiological roles and biopharmaceutical implications, Phram. Res. 24 (2007) 1227–1251.

[31] R.D. Blakely, S. Ramamoorthy, S. Schroeter, Y. Qian, S. Apparsundaram, A. Galli, L.J. De Felice, Regulated phosphorylation and trafficking of antidepressant-sensitive serotonin transporter proteins, Biol. Psychiatry. 44 (1998) 169–178.

[32] R.D. Blakely, A.L. Bauman, Biogenic amine transporters: Regulation in flux, Curr. Opin. Neurobiol. 10 (2000) 328–336.

[33] R. Dingledine, K. Borges, D. Bowie, S.F. Traynelis, The glutamate receptor ion channels, Pharmacol. Rev. 51 (1999) 7–61.

[34] K. Tanaka, Role of glutamate transporters in brain development, Nippon Yakurigaku Zasshi. 130 (2007) 455–457.

[35] N.H. Chen, M.E. Reith, M.W. Quick, Synaptic uptake and beyond: The sodium- and chloride-dependent neurotransmitter transporter family SLC6, Pflugers Arch. 447 (2004) 519–531.

[36] C. Grewer, T. Rauen, Electrogenic glutamate transporters in the CNS: Molecular mechanism, pre-steady-state kinetics, and their impact on synaptic signaling, J. Membr. Biol. 203 (2005) 1–20.

[37] D.J. Slotboom, W.N. Konings, J.S. Lolkema, Structural features of the glutamate transporter family, Microbiol. Mol. Biol. Rev. 63 (1999) 293–307.

[38] Z. Huang, E. Tajkhorshid, Dynamics of the extracellular gate and ion-substrate coupling in the glutamate transporter, Biophys. J. 95 (2008) 2292–2300.

[39] Y. Shigeri, R.P. Seal, K. Shimamoto, Molecular pharmacology of glutamate transporters, EAATs and VGLUTs, Brain Res. Rev. 45 (2004) 250–265.

[40] D. Yernool, O. Boudker, Y. Jin, E. Gouaux, Structure of a glutamate transporter homologue from Pyrococcus horikoshii, Nature. 431 (2004) 752–753.

[41] M. Grunewald, B.I. Kanner, The accessibility of a novel reentrant loop of the glutamate transporter GLT-1 is restricted by is substrate, J. Biol. Chem. 275 (2000) 9684–9689.

[42] R.P. Seal, S.G. Amara, A reentrant loop domain in the glutamate carrier EAAT1 participates in substrate binding and translocation, Neuron. 21 (1998) 1487–1498.

[43] M.P. Borre, Kavanaugh, B.I. Kanner, Dynamic equilibrium between coupled and uncoupled modes of a neuronal glutamate transporter, J. Biol. Chem. 277 (2002) 13501–13507.

[44] B.H. Leighton, R.P. Seal, K. Shimamoto, S.G. Amara, A hydrophobic domain in glutamate transporters forms an extracellular helix associated with the permeation pathway for substrates, J. Biol. Chem. 277 (2002) 29847–29855.

[45] R.M. Ryan, R.J. Vandenberg, Distinct conformational states mediated the transport and anion channel properties of the glutamate transporter EAAT-1, J. Biol. Chem. 277 (2002) 13494–13500.

[46] O. Boudker, R.M. Ryan, D. Yernool, K. Shimamoto, E. Gouaux, Coupling substrate and ion binding to extracellular gate of a sodium-dependent aspartate transporter, Nature. 445 (2007) 387–393.

[47] G. Pines, B.I. Kanner, Counterflow of l-glutamate in plasma membrane vesicles and reconstituted preparations from rat brain, Biochemistry. 29 (1990) 11209–11214.

[48] M.P. Kavanaugh, A. Bendahan, N. Zerangue, Y. Zhang, B.I. Kanner, Mutation of an amino acid residue influencing potassium coupling in the glutamate transporter GLT-1 induces obligate exchange, J. Biol. Chem. 272 (1997) 1703–1707.

[49] L.M. Levy, O. Warr, D. Attwell, Stoichiometry of the glial glutamate transporter GLT-1 expressed inducibly in a Chinese hamster ovary cell line selected for low endogenous Na^+-dependent glutamate uptake, J.Neurosci. 18 (1998) 9620–9628.

[50] S. Eliasof, C.E. Jahr, Retinal glial cell glutamate transporter is coupled to an anionic conductance, Proc. Natl. Acad. Sci. USA. 93 (1996) 4153–4158.

[51] R.M. Ryan, J.A. Mindell, The uncoupled chloride conductance of a bacterial glutamate transporter homolog, Nat. Struct. Mol. Biol. 14 (2007) 365–371.

[52] R.M. Ryan, A.D. Mitrovic, R.J. Vandenberg, The chloride permeation pathway of a glutamate transporter and its proximity to the glutamate translocation pathway, J. Biol. Chem. 279 (2004) 20742–20751.

[53] S. Eskandari, M. Kreman, M.P. Kavanaugh, Pentameric assembly of a neuronal glutamate transporter, Proc. Natl. Acad. Sci. USA. 97 (2000) 8641–8646.

[54] D. Torres-Salazar, C. Fahlke, Intersubunit interactions in EAAT4 glutamate transporters, J. Neurosci. 26 (2006) 7513–7522.

[55] M. Kreft, M. Stenovec, M. Rupnik, S. Grilc, M. Krzan, M. Potokar, T. Pangrsic, P.G. Haydon, R. Zorec, Properties of $Ca^{(2+)}$-dependent exocytosis in cultured astrocytes, Glia 46 (2004) 437–445.

[56] Q. Zhang, T. Pangrsic, M. Kreft, M. Krzan, N. Li, J.Y. Su, M. Halassa, E. Van Bockstaele, R. Zorec, P.G. Haydon, Fusion-related release of glutamate from astrocytes, J. Biol. Chem. 279 (2004) 12724–12733.

[57] V. Montana, Y. Ni, V. Sunjara, X. Hua, V. Parpura, Vesicular glutamate transporter-dependent glutamate release from astrocytes, J. Neurosci. 24 (2004) 2633–2642.

[58] S.L. McIntire, R.J. Reimer, K. Schuske, R.H. Edwards, E.M. Jorgensen, Identification and characterization of the vesicular GABA transporter, Nature 389 (1997) 870–876.

[59] A. Minelli, N.C. Brecha, C. Karschin, S. DeBiasi, F. Conti, GAT-1, a high-affinity GABA plasma membrane transporter, is localized to neurons and astroglia in the cerebral cortex, J. Neurosci. 15 (1995) 7734–7746.

[60] J. Masson, C. Sagne, M. Hamon, S. Mestikawy, Neurotransmitter transporters in the central nervous system, Pharmacol. Rev. 51 (1999) 439–464.

[61] N.J. Mabjeesh, M. Frese, T. Rauen, G. Jeserich, B.I. Kanner, Neuronal and glial gamma-aminobutyric acid transporters are distinct proteins, FEBS Lett. 299 (1992) 99–102.

[62] J. Guastella, N. Nelson, H. Nelson, L. Czyzyk, S. Keynan, M.C. Miedel, N. Davidson, H.A. Lester, B.I. Kanner, Cloning and expression of a rat brain GABA transporter, Science 249 (1990) 1303–1306.

[63] T.S. Lee, L.P. Bjørnsen, C. Paz, J.H. Kim, S.S. Spencer, D.D. Spencer, T. Eid, N.C. de Lanerolle, GAT1 and GAT3 expression are differently localized in the human epileptogenic hippocampus, Acta Neuropathol. 111 (2006) 351–363.

[64] A. Schousboe, H.S. Waagepetersen, Glial modulation of GABAergic and glutamatergic neurotransmission, Curr. Top. Med. Chem. 6 (2006) 929–934.

[65] M.J. Roux, S. Suplisson, Neuronal and glial glycine transporters have different stoichiometries, Neuron. 25 (2000) 373–383.

[66] J. Gomeza, K. Ohno, S. Hülsmann, W. Armsen, V. Eulenburg, D.W. Richter, B. Laube, H. Betz, Deletion of the mouse glycine transporter 2 results in a hyperekplexia phenotype and postnatal lethality, Neuron 40 (2003) 797–806.

[67] C. Aragon, B. Lopez, Corcuera, Structure, function and regulation of glycine transporters, Eur. J. Pharmacol. 479 (2003) 249–262.

[68] K.M. Kim, S.F. Kingsmore, H. Han, T.L. Yang-Feng, N. Godinot, M.F. Seldin, M.G. Caron, B. Giros, Cloning of the human glycine transporter type 1: Molecular and pharmacological characterization of novel isoform variants and chromosomal localization of the gene in the human and mouse genomes, Mol. Pharmacol. 45 (1994) 608–617.

[69] J. Axelroad, L.G. Whitby, G.G. Hertting, Effect of psychotropic drugs on the uptake of ^{3}H-norepinephrine by tissues, Science 133 (1961) 383–384.

[70] H.K. Kimelberg, E.W. Pelton 2nd, High-affinity uptake of [^{3}H]-norepinephrine by primary astrocyte cultures and its inhibition by tricyclic antidepressants, J. Neurochem. 40 (1983) 1265–1270.

[71] M. Inazu, H. Takeda, T. Matsumiya, Functional expression of the norepinephrine transporter in cultured rat astrocytes, J. Neurochem. 84 (2003) 136–144.

[72] H.K. Kimelberg, D.M. Katz, Regional differences in 5-hydroxytryptamine and catecholamine uptake in primary astrocyte cultures, J. Neurochem. 47 (1986) 1647–1652.

[73] G. Eisenhofer, The role of neuronal and extraneuronal plasma membrane transporters in the inactivation of peripheral catecholamines, Pharmacol. Ther. 91 (2001) 35–62.

[74] E. Hansson, Enzyme activities of monoamine oxidase, catechol-O-methyltransferase and gamma-aminobutyric acid transaminase in primary astroglial cultures and adult rat brain from different brain regions, Neurochem. Res. 9 (1984) 45–57.

[75] E. Torres, S.G. Amara, Glutamate and monoamine transporters: New visions of form and function, Curr. Opin. Neurobiol. 17 (2007) 304–312.

[76] W.D. Hirst, G.W. Price, M. Rattray, G.P. Wilkin, Serotonin transporters in adult rat brain astrocytes revealed by [^{3}H]5-HT uptake into glial plasmalemmal vesicles, Neurochem. Int. 33 (1998) 11–22.

[77] N. Bal, G. Figuras, M.T. Vilaró, C. Suñol, F. Artigas, Antidepressant drugs inhibit a glial 5-hydroxytryptamine transporter in rat brain, Eur. J. Neurosci. 9 (1997) 1728–1738.

[78] M. Inazu, H. Takeda, H. Ikoshi, M. Sugisawa, Y. Uchida, T. Matsumiya, Pharmacological characterization and visualization of the glial serotonin transporter, Neurochem. Int. 39 (2001) 39–49.

[79] L.W. Fitzgerald, L. Kaplinsky, H.K. Kimelberg, Serotonin metabolism by monoamine oxidase in rat primary astrocyte cultures, J. Neurochem. 55 (1990) 2008–2014.

[80] S.J. Cragg, M.E. Rice, DAncing past the DAT at a DA synapse, Trends Neurosci. 27 (2004) 270–277.

[81] E.L. Riddle, A.E. Fleckenstein, G.R. Hanson, Role of monoamine transporters in mediating psychostimulant effects, AAPS J. 7 (2005) 847–851.

[82] B. Giros, S. el Mestikawy, L. Bertrand, M.G. Caron, Cloning and functional characterization of a cocaine-sensitive dopamine transporter, FEBS Lett. 295 (1991) 149–154.

[83] T.B. Usdin, E. Mezey, C. Chen, M.J. Brownstein, B.J. Hoffman, Cloning of the cocaine-sensitive bovine dopamine transporter, Proc. Natl. Acad. Sci. USA 88 (1991) 11168–11171.

[84] B. Giros, S. E4l Mestikawy, N. Godinot, K. Zheng, H. Han, T. Yang-Feng, M.G. Caron, Cloning, pharmacological characterization, and chromosome assignment of the human dopamine transporter, Mol. Pharmacol. 42 (1992) 383–390.

[85] M. Inazu, H. Takeda, T. Matsumiya, The role of glial monoamine transporters in the central nervous system, Nihon Shinkei Seishin Yakurigaku Zasshi. 2 (2003) 171–178.

[86] H. Takeda, M. Inazu, T. Matsumiya, Astroglial dopamine transport is mediated by norepinephrine transporter, Naunyn Schmiedeberg's Arch. Pharmacol. 366 (2002) 620–623.

[87] S. Karakaya, M. Kipp, C. Beyer, Oestrogen regulates the expression and function of dopamine transporters in astrocytes of the nigrostriatal system, J. Neuroendocrinol. 9 (2007) 682–690.

[88] A. Merickel, H. Edwards, Transport of histamine by vesicular monoamine transporter-2, Neuropharmacology. 34 (1995) 1543–1547.

[89] L.B. Hough, E.F. Domino, Tele-methylhistamine oxidation by type B monoamine oxidase, J. Pharmacol. Exp. Ther. 208 (1979) 422–428.

[90] G.D. Prell, J.P. Green, Measurement of histamine metabolites in brain and cerebrospinal fluid provides insights into histaminergic activity, Agents and Actions. 41 (1994) C5–C8.

[91] Z. Huszti, A. Rimanóczy, A. Juhasz, K. Magyar, Uptake, metabolism, and release of [^{3}H]-histamine by glial cells in primary cultures of chicken cerebral hemispheres, Glia 3 (1990) 159–168.

[92] Z. Huszti, Mechanism and function of histamine-sodium cotransport by astroglial cells, Agents Actions 41 (1994) C58–C59.

[93] Z. Huszti, Carrier-mediated high affinity uptake system for histamine in astroglial and cerebral endothelial cells, J. Neurosci. Res. 51 (1998) 551–558.

[94] Z. Huszti, Histamine uptake into non-neuronal brain cells, Inflamm. Res. 52 (Suppl. 1) (2003) S03–S06.

[95] M. Krzan, J.P. Schwartz, Histamine transport in neonatal and adult astrocytes, Inflamm. Res. 55(Suppl. 1) (2006) S36–S37.

[96] Z. Huszti, H. Prast, M.H. Tran, H. Fischer, A. Philippu, Glial cells participate in histamine inactivation *in vivo*, Naunyn Schmiedeberg's Arch. Pharmacol. 357 (1998) 49–53.

[97] A.E. Stuart, J.R. Morgan, H.E. Mekeel, E. Kempter, J.C. Callaway, Selective activity-dependent uptake of histamine into an arthropod photoreceptor, J. Neurosci. 16 (1996) 3178–3188.

[98] A.E. Stuart, K.A. Gebhardt, S.N. Vogel, O. Rodriguez, Does the neurotransmitter transporter underlie adaptation at a histaminergic photoreceptor synapse? Vis. Neurosci. 19 (2002) 307–319.

[99] E. Sakurai, E. Sakurai, L. Oreland, S. Nishiyama, M.Kato, T. Watanabe, K. Yanai, Evidence for the presence of histamine uptake into the synaptosomes of rat brain, Pharmacology. 78 (2006) 72–80.

[100] D. Gründemann, V. Gorboulev, S. Gambaryan, M. Veyhl, H. Koepsell, Drug excretion mediated by a new prototype polyspecific transporter, Nature (Lond.) 372 (1994) 549–552.

[101] N. Ishiguro, A. Saito, K. Yokoyama, M. Morikawa, T. Igarashi, I. Tamai, Transport of the dopamine D2 agonist pramipexole by rat organic cation transporters OCT1 and OCT2 in kidney, Drug. Metab. Dispos. 33 (2005) 495–499.

[102] A.E. Busch, U. Karbach, D. Miska, V. Gorboulev, A. Akhoundova, C. Volk, P. Arndt, J.C. Ulzheimer, M.S. Sonders, C. Baumann, F.L. Waldegger, H. Koepsell, Human neurons express the polyspecific cation transporter hOCT2, which translocates monoamine neurotransmitters, amantadine and memantine, Mol. Pharmacol. 54 (1998) 342–352.

[103] H. Russ, K. Staust, F. Martel, M. Gliese, E. Schomig, The extraneuronal transporter for monoamine transmitters exists in cells derived from human central nervous system glia, Eur. J. Neurosci. 8 (1996) 1256–1264.

[104] X. Wu, R. Kekuda, W. Huang, Y.J. Fei, F.H. Leibach, J. Chen, S.J. Conway, V. Ganapathy, Identity of the organic cation transporter OCT3 as the extraneuronal monoamine transporter (uptake$_2$) and evidence for the expression of the transporter in the brain, J. Biol. Chem. 273 (1998) 32776–32786.

[105] C. Haag, R. Berkels, D. Grundemann, A. Lazar, D. Taubert, E. Schömig, The localisation of the extraneuronal monoamine transporter (EMT) in rat brain, J. Neurochem. 88 (2004) 291–297.

[106] A. Amphoux, V. Vialou, E. Drescher, M. Bruss, C. Mannoury La Cour, C. Rochat, M.J. Millan, B. Giros, H. Bonisch, S. Gautron, Differential pharmacological in vitro properties of organic cation transporters and regional distribution in rat brain, Neuropharmacol. 50 (2006) 941–952.

[107] V. Vialou, L. Balasse, J. Callbert, J.M. Launay, B. Giros, S. Gautron, Altered aminergic neurotransmission in the brain of organic cation transporter 3-deficient mice, J. Neurochem. 10 (2008) 1–12.

[108] P.J. Gasser, C.A. Lowry, M. Orchink, Corticosterone sensitive monoamine transport in rat dorsomedial hypothalamus: Potential role for organic cation transporter 3 in stress-induced modulation of monoaminergic neurotransmission, J. Neurosci. 26 (2006) 8758–8766.

[109] D.E. Bergles, Neurotransmitter Ttransporters, in: Encyclopedia of Life Sciences, Nature Publishing Group and www.els.net, 2001.

[110] S. Colleoni, A.A. Jensen, E. Landucci, E. Fumagalli, P. Conti, A. Pinto, M. De Amici, D.E. Pellegrini-Giampietro, C. De Micheli, T. Mennini, M. Gobbi, Neuroprotective effects of the novel glutamate transporter inhibitor (-)-HIP-A which preferentially inhibits reverse transport (glutamate release) compared to glutamate reuptake, J. Pharmacol. Exp. Ther. 135251 (2008) 1–35.

[111] G. Lee, Y. Huang, J.M. Washington, N.W. Briggs, Z. Zuo, Carbamazepine enhances the activity of glutamate transporter type 3 via phosphatidylinositol 3-kinase, Epilepsy Res. 66 (2005) 145–153.

[112] K.K. Borowicz, Æ.M. Zadrozniak, C.J.J. Luszczki, C.S.J. Czuczwar, Interactions between tiagabine and conventional antiepileptic drugs in the rat model of complex partial seizures, J. Neural. Transm. 115 (2008) 661–667.

[113] N.O. Dalby, GABA-level increasing and anticonvulsant effects of three different GABA uptake inhibitors, Neuropharmacology 39 (2000) 2399–2407.

[114] Y. Ueda, T. Doi, K. Nagatomo, J. Tokumaru, M. Takaki, L.J. Willmore, Effect of levetiracetam on molecular regulation of hippocampal glutamate and GABA transporters in rats with chronic seizures induced by amygdalar $FeCl_3$ injection, Brain Res. 1151 (2007) 55–61.

[115] H. Betz, J. Gomeza, W. Armsen, P. Scholze, V. Eulenburg, Glycine transporters: Essential regulators of synaptic transmission, Mol. Determinants Synaptic Funct. 34 (2006) 55–58.

[116] J. Zhou, Norepinephrine transporter inhibitors and their therapeutic potential, Drugs Future 29 (2004) 1235–1244.

[117] L.D. Jayanthi, S. Ramamoorthy, Regulation of monoamine transporters: Influence of psychostimulants and therapeutic antidepressants, The AAPS J. 7 (2005) E728–E738.

[118] M.J. Brodie, Tiagabine pharmacology in profile, Epilepsia. 36(Suppl. 6) (1995) S7–S9.

[119] G. Tsai, H.Y. Lane, P. Yang, M.Y. Chong, N. Lange, Glycine transporter I inhibitor, N-methylglycine (sarcosine), added to antipsychotics for the treatment of schizophrenia, Biol. Psychiatry. 55 (2004) 452–456.

CHAPTER NINE

STABILITY OF THE INVERTED HEXAGONAL PHASE

Šárka Perutková,[1,*] Matej Daniel,[2] Gregor Dolinar,[3]
Michael Rappolt,[4] Veronika Kralj-Iglič,[5] *and* Aleš Iglič[1]

Contents

---

* Corresponding author. Tel.: +386 31 356 953; Fax: +386 1 4768 850;
E-mail address: sarka.perutkova@fe.uni-lj.si

[1] Laboratory of Biophysics, Faculty of Electrical Engineering, University of Ljubljana, Slovenia
[2] Laboratory of Biomechanics, Faculty of Mechanical Engineering, Czech Technical University in Prague, Czech Republic
[3] Laboratory of Mathematics, Faculty of Electrical Engineering, University of Ljubljana, Slovenia
[4] Institute of Biophysics and Nanosystems Research, Austrian Academy of Sciences c/o Sincrotrone Trieste, Italy
[5] Laboratory of Clinical Biophysics, Faculty of Medicine, University of Ljubljana, Slovenia

Advances in Planar Lipid Bilayers and Liposomes, Volume 9
ISSN 1554-4516, DOI: 10.1016/S1554-4516(09)09009-7

Abstract

The inverted hexagonal phase (H_{II}) belongs to the biologically most significant nonlamellar lipid phases in biomembranes. Hence the geometric properties and conditions of transition to the H_{II} phase are nowadays widely studied. In this chapter we offer a brief overview on the mechanics of the H_{II} lipid phase. In our derivation of the free energy of lipid monolayers, we assume that lipid molecules are in general anisotropic with respect to the axis perpendicular to the membrane plane. In our model the expression for the lipid monolayer free energy consists of two energy contributions: the bending energy which involves also a deviatoric term, and the interstitial energy which describes the deformation energy due to stretching of the phospholipid molecule chains. On the basis of the derived expression for the lipid monolayer free energy, we theoretically predict optimal geometry and physical conditions for the stability of the inverted hexagonal phase. Using the Monte Carlo simulated annealing method, we theoretically describe first steps in the L_α–H_{II} phase transition, which may contribute to a better understanding of different biologically important processes within biomembranes.

1. INTRODUCTION

One of the main components of biological membranes are phospholipids. They have amphiphatic character, that is, they comprise a polar headgroup as well as nonpolar hydrocarbon chains in one molecule. Such molecules in aqueous solution undergo a self-assembling process and form various structures. Biologically important lipid/water systems are known for their rich polymorphism [1]. Driving force of this process is predominantly the hydrophobic effect where the hydrophilic (polar) surfaces are in contact with aqueous solution while the hydrophobic (nonpolar) parts composed of hydrocarbon chains are hidden from water [2, 3]. The most common and biologically most relevant phase is the fluid lamellar lipid bilayer phase (L_α). The bilayer of lipid molecules represents the basic building block of the plasma membrane, which encloses the cell interior. Nevertheless, nonlamellar model membranes are subject of increasing interest [1, 4–6], due to their importance in living organisms and due to their promising technical applications such as in drug delivery [7, 8], gene transport and nanotechnology [9].

The curvature of different monolayer and bilayer lipid structures (Fig. 1) depends to a great extent on the intrinsic shape of the phospholipid molecules, which in turn depends on the temperature, degree of hydration, presence of specific enzymes, pH, etc. [10].

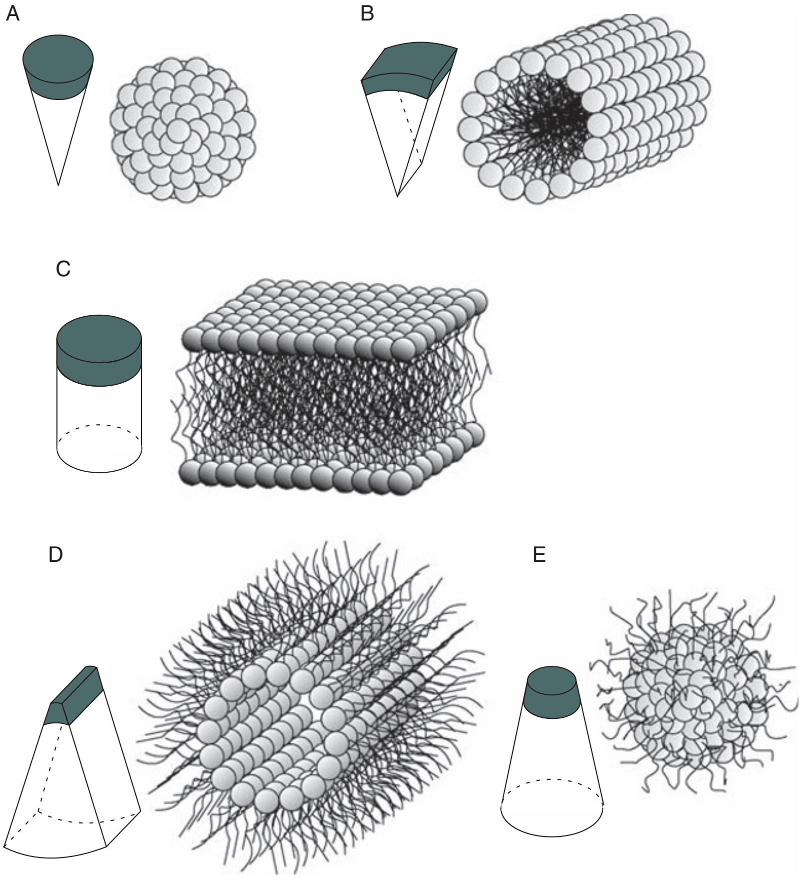

Figure 1 Schematically depicted polymorphism of phospholipid aggregates. Aggregated forms with appropriate shapes of phospholipid molecules: (A) spherical micelle, (B) cylinder, (C) bilayer, (D) inverted cylinder, and (E) inverted micelle.

Flat lipid bilayers are formed preferentially, when the lipid molecules have cylindrical shapes (Fig. 1C), whereas cylindrical monolayers are formed when the lipid molecules are wedge shaped (as depicted in Fig. 1B and D). Conical and inverted conical shapes of lipids favor spherical (Fig. 1A) and inverted spherical (Fig. 1E) micellar shapes, respectively (see also Ref. [11]).

1.1. Mathematical Description of Membrane Curvature

Biological membranes may be in the first approximation considered as curved and deformable smooth plates that are described by two principal radii (curvatures) at each point of the surface. Consider for the moment the phospholipid monolayer as a pure mathematical surface. At every point P on this surface one can find a vector normal to the surface and the corresponding normal plane which contains the normal vector (Fig. 2). There is an infinite number of such normal planes, but only two orthogonal normal planes contain curves of intersection with maximum and minimum curvature (see Fig. 2). These two curvatures are named the two principal curvatures of the surface at the given point P and are defined as [1]

$$C_1 = \frac{1}{r_1} \text{ and } C_2 = \frac{1}{r_2} \qquad (1)$$

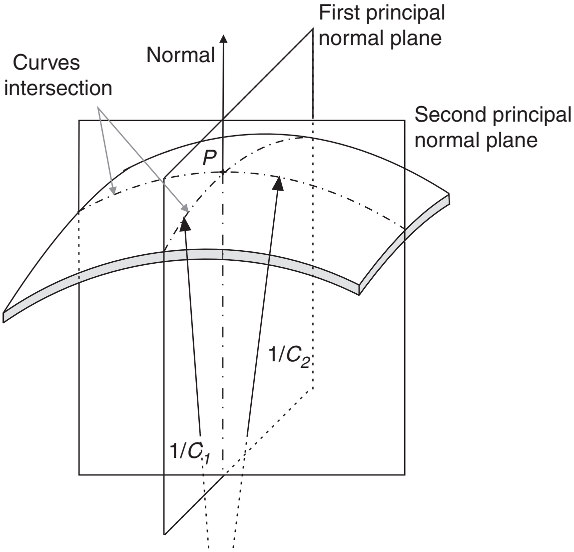

Figure 2 A schematic figure of the phospholipid monolayer. In the point P the normal surface is shown together with a pair of orthogonal principal planes that define the two principal curvatures C_1 and C_2.

For the sake of later computations, the principal curvatures are written in a tensor notation as a diagonalized curvature tensor:

$$\underset{\sim}{C} = \begin{bmatrix} C_1 & 0 \\ 0 & C_2 \end{bmatrix} \tag{2}$$

Within the theory of elasticity, the membrane curvature at a given point is usually described by the mean and the Gaussian curvature, that are invariants of the curvature tensor $\underset{\sim}{C}$ (Eq. (2)). The mean curvature H is related to the trace of the curvature tensor $\underset{\sim}{C}$ and the Gaussian curvature K is the determinant of $\underline{C}$ [1]:

$$H = \frac{C_1 + C_2}{2} \tag{3}$$

$$K = C_1 C_2 \tag{4}$$

For the lipid monolayer of finite thickness, the following convention was adopted [1]: when, for instance, the pivotal plane (molecular area in pivotal plane does not change upon bending deformation [12]) bends toward the chain region, we define the curvature positive ($C > 0$), whereas when the pivotal plane bends toward the water region the curvature is negative ($C < 0$) (Fig. 3). According to this convention the mean curvature H (Eq. (3)) can be positive or negative, that is, the monolayer can be regular or inverted. For positive values of K the planes are naturally convex or concave and bend round to form closed shells, micelles or inverted micelles, respectively. On the other hand, when K is negative the principal curvatures are of opposite sign, that is, the plane is saddle-like [1].

For planar and spherical surfaces the principal curvatures are equal while for saddle-like and cylindrical planes the principal curvatures are different. High anisotropy in the curvature (a large difference between the two

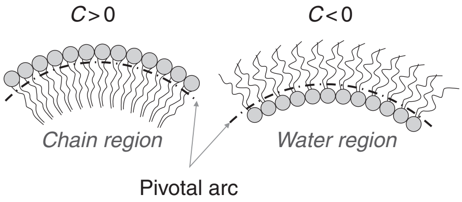

Figure 3 Sign convention of the curvature $C = C_1 \cos^2 \beta + C_2 \sin^2 \beta$ of the normal cut of the lipid monolayer. The curvature C is positive when the monolayer is bent toward the chain region and negative when the monolayer is bent toward the water region. The angle β describes the orientation of the normal plane with respect to the first principal normal plane.

principal curvatures) has been revealed in numerous membrane systems, for example, in phospholipid bilayer nanotubes [13–16], torocytic endovesicles of erythrocyte membranes [17, 18], phospholipid bilayer membrane pores [19, 20] and narrow necks of phospholipid bilayers connecting buds to the mother membrane [21]. To explain the stability of these structures instead of the Gaussian curvature another invariant is advantageous in description of membrane free (elastic) energy, namely the curvature deviator D [21]:

$$D = \frac{|\, C_1 - C_2 \,|}{2} \tag{5}$$

The invariants H, K, and D are connected through the relation:

$$H^2 = D^2 + K \tag{6}$$

1.2. Influence of Spontaneous Curvature on the Self-Assembling Process

Obviously the curvature of membranes depends on the intrinsic shape of the phospholipid molecules (see Fig. 1). Hence noncylindrically shaped phospholipids self-assemble in aqueous solutions in nonplanar structures. The tendency to curve the shape of the monolayer without any external torques and forces is called the spontaneous (intrinsic) curvature [10]. The definition of the principal intrinsic curvatures that define the intrinsic shape of the lipid molecules (see Fig. 4) is very similar to the description of membrane curvature. The principal intrinsic curvatures are defined as [22, 23]:

$$C_{1\mathrm{m}} = \frac{1}{r_{\mathrm{m}1}} \tag{7}$$

and

$$C_{2\mathrm{m}} = \frac{1}{r_{\mathrm{m}2}} \tag{8}$$

where $r_{\mathrm{m}1}$ and $r_{\mathrm{m}2}$ are the principal radii of a monolayer that would completely suit the shape of the molecule. Written in tensor notation:

$$\underline{C}_{\mathrm{m}} = \begin{bmatrix} C_{1\mathrm{m}} & 0 \\ 0 & C_{2\mathrm{m}} \end{bmatrix} \tag{9}$$

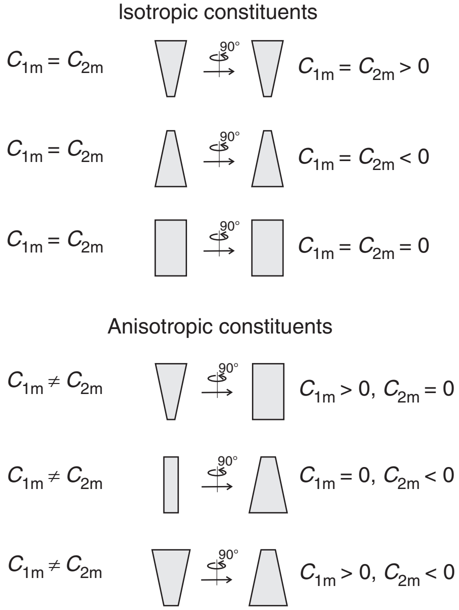

Figure 4 **Molecular sketches describing differences between isotropic and anisotropic phospholipid molecules and values of their principal intrinsic curvatures.**

where $\underline{C}_{\mathrm{m}}$ is defined as an intrinsic curvature tensor [21, 23].

Similar to the mean curvature H, we can define the mean intrinsic curvature H_{m}, which is now related to the molecular shape:

$$H_{\mathrm{m}} = \frac{C_{1\mathrm{m}} + C_{2\mathrm{m}}}{2} \tag{10}$$

and intrinsic curvature deviator of the molecule:

$$D_{\mathrm{m}} = \frac{\mid C_{1\mathrm{m}} - C_{2\mathrm{m}} \mid}{2} \tag{11}$$

If the intrinsic principal curvatures are different ($C_{1\mathrm{m}} \neq C_{2\mathrm{m}}$), the molecules are anisotropic. If the intrinsic curvatures are equal ($C_{1\mathrm{m}} = C_{2\mathrm{m}}$), the membrane constituents are isotropic (Fig. 4). Isotropic constituents with zero intrinsic curvatures ($C_{1\mathrm{m}} = C_{2\mathrm{m}} = 0$) will tend to form planar monolayers, while the constituents having inverted conical shape ($C_{1\mathrm{m}} = 0$, $C_{2\mathrm{m}} < 0$) will favor the formation of an inverted hexagonal structure [11] (see also Fig. 1). The intrinsic principal curvatures account for the geometrical shape of the lipid molecule and the local interactions of the molecule with its surroundings, including the hydration effects [24].

2. INVERTED HEXAGONAL PHASE

The inverted hexagonal phase (H_{II}) is one of the lipid mesophases that are important for many biological processes in nature. Understanding the mechanisms of their formation and stability, and their physical properties may help us to elucidate their biological functions.

2.1. Relevance of Nonlamellar Phases in Biological Systems

The bicontinuous cubic phase, inverse hexagonal phase, and inverse micellar cubic phase belong to the biologically most relevant nonlamellar mesophases. These mesophases resist excess of water and thus they are stable under certain conditions in biological systems [6, 25].

It is known that a wide range of phospholipids which occur in biological organisms may self-assemble into nonlamellar structures when they are extracted from cells and rehydrated in aqueous solution. However, despite the fact that many nonlamellar phases have been undoubtedly identified also in various biological systems [26], still little is understood concerning their function. The induction of nonplanar mesophases might play a role in the regulation of protein function, further, membrane fusion for instance in endo- and exocytosis is thought to be dependent on such highly curved lipid structures. It is also supposed that interbilayer tight junctions host nonbilayer structures. Direct evidence for the formation of the stable H_{II} phase was found in paracrystalline inclusions of the retina [27].

The nonlamellar structures of phospholipids are also common in some species of bacteria. It was suggested that the bilayers of bacteria are close to the transition from lamellar to nonlamellar structure [10]. Many different types of bacteria can enzymatically change the intrinsic curvature of phospholipids, consequently, they can prefer the nonlamellar phases [10].

2.2. Geometry of the Inverted Hexagonal Phase

The lipids in the inverted hexagonal phase are self-assembled in long tubes arranged in a hexagonal lattice. Figures 5 and 6 show the geometry of the H_{II} phase: two neighboring tubes with diameter *r* are located at the distance *a*. The phospholipid chains point outward from the cylinder surface defined as the pivotal plane while the headgroups form polar nanotubes filled with aqueous solution. Experiments revealed high anisotropy in the curvature (one principal curvature is equal to negative inverse value of radius of the tube and the second principal curvature is equal to zero) of tubes of the H_{II} phase.

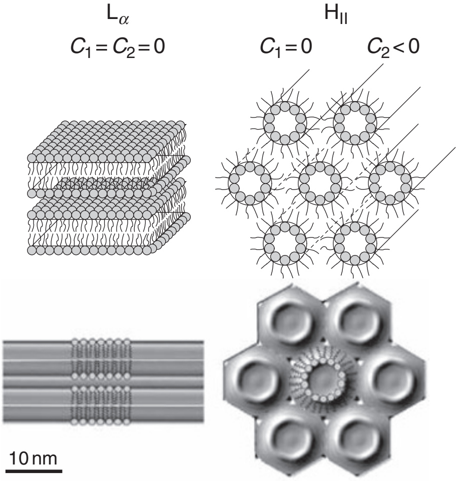

Figure 5 A scheme and a corresponding electron density map of the lamellar fluid (L_α) phase (left) and of the inverted hexagonal (H_{II}) phase (right). The configurations of the lipid molecules are indicated. In the L_α phase both principal curvatures are equal to zero, while in the H_{II} phase one of the principal curvatures is equal to zero and the other one is negative. The data for the electron density reconstructions are taken from Ref. [28]. The maps depict the POPE/water structures at the phase transition temperature of 74 °C (compare also Table 1). Adapted from Ref. [29].

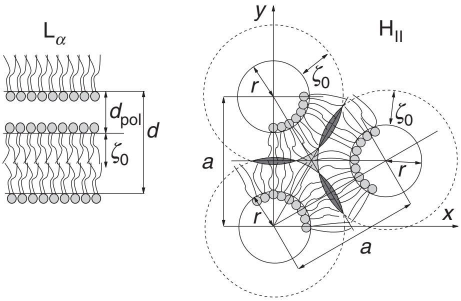

Figure 6 Geometry of the lamellar and inverted hexagonal phases. One bilayer and one neighboring monolayer are depicted for the lamellar phase. The lattice unit of lamellar phase (d-spacing) (d) and distance of polar region between the two bilayers (d_{pol}) are denoted. For the inverted hexagonal phase three cylinders of radius r at the distance a are depicted. ζ_0 denotes the equilibrium length of hydrocarbon chains. The H_{II} phase requires stretching or compressing of some of the hydrocarbon chains as shown schematically. Adapted from Ref. [29].

It can be seen in Fig. 6 that not all lipid tails in the hexagonal lattice have the same length. There are triangular regions (called voids) between neighboring tubes that are considerably energetically expensive, because the lipid chains in these regions need to stretch beyond the average length ζ_0. In theoretical studies of stability of inverted hexagonal phases, it is therefore necessary to take into account an energy term which accounts for the stretching of the hydrocarbon chains in the void regions [24, 30–32].

Some recent studies have shown that the cross sections of the tubes in the inverted hexagonal phase is not precisely circular but it is rather an intermediate between a circle and a hexagon [31, 33]. In our case we suppose, for sake of simplicity, that the cross section is circular.

2.3. Models of the Transition of the Lamellar to Inverted Hexagonal Phase

Transitions between different phospholipid phases and mechanisms that drive these transitions are of special interest. To interpret the experimental data and to contribute to a better understanding of underlying mechanisms, different models have been put forward [24, 28, 30, 34, 35].

The majority of models of the formation of the inverted hexagonal phase have in common the assumption that nucleation starts with a linearly localized lipid rearrangement. Based on freeze-fracture electron microscopy experiments, a deformation pair of intramembrane cylinders embedded in a tight junction was proposed [35], and also monolayer embedded lipid tubes forming via the coalescence of a "pearl string" of inverted micellar intermediates (IMIs) was suggested by Hui *et al.* [36]. In 1986 Siegel further elaborated this model of the L_α–H_{II} transition [30]. He proposed a three-step process with forming of intermediates driven by changes in temperature and lipid composition. The first step is formation of IMIs, which forms between two sufficiently close apposed bilayers. The IMI can diffuse within the plane of the membrane and form IMI coalescence representing the second step. Two possible ways of IMI coalescence were suggested. Two spherical micelles can fuse into a single rod shaped micelle and form rod micellar intermediates (RMIs) or they can separate within the coalescence intermediate and form line defects (LDs) [30].

Based on the temperature-dependent experimental results from differential scanning calorimetry and small-angle X-ray scattering, a similar view on L_α–H_{II} transition is given by Rappolt *et al.* [28, 34]. The hypothesis of the growth mechanism of the first few rods is connected with spontaneous creation of the line defect (water core) at the transition temperature. The first rod is created due to the spontaneous monolayer curvature, which induces the formation of new water cores. The pivotal plane arrangement corresponding to the first few steps of transition was proposed in Ref. [34] (see Figs. 7 and 8). The first cylinder of the H_{II} phase forms from the linearly localized lipid rearrangement between two bilayers. Thus, a system of one cylinder, two monolayers, and bulby closures on both sides of the cylinder originates. The bulby closures are created from neighboring disjunct layers as a consequence of reducing void apolar regions. The two outer monolayer leaflets follow the contours of the cylinder and the bulby closures. This configuration is the smallest unit to study the nucleation of the H_{II}–L_α transition (Fig. 7).

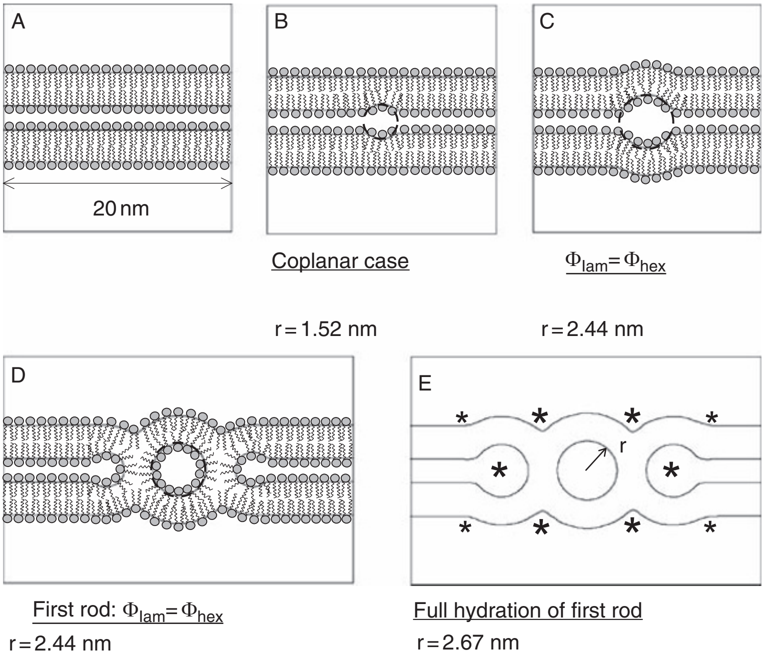

Figure 7 Intermediate steps in the formation of a cylinder between two bilayers. The structural schemes base on structural data of POPE recorded at the transition temperature $T = 74\ ^\circ\mathrm{C}$ [28]. Pivotal interfaces are outlined with full lines and for the ease of interpretation lipid molecules are superimposed in the first four panels. (A) The fluid lamellar phase can be decomposed into steric monolayer thickness (2.27 nm) and free water layer thickness per lipid molecule (0.27 nm). (B) Allowing for spontaneous splay of lipid molecules a line defect may form, which is integrated in the stack of bilayers in a coplanar fashion. (C) If one sets the water concentration per lipid in the line defect, Φ_{hex}, to be equal to the water concentration given in the fluid lamellar phase, Φ_{lam}, then the radius of the pivotal plane increases from $r = 1.52$ to 2.44 nm. (D) This panel shows the formation of a first rod under the condition of $\Phi_{lam} = \Phi_{hex}$. (E) Finally, full hydration of the first cylinder in between of two bilayers increases the pivotal plane radius to $r = 2.67$ nm. Loci for the formation of new cylinders are marked with stars. Sketches are adapted from Ref. [34].

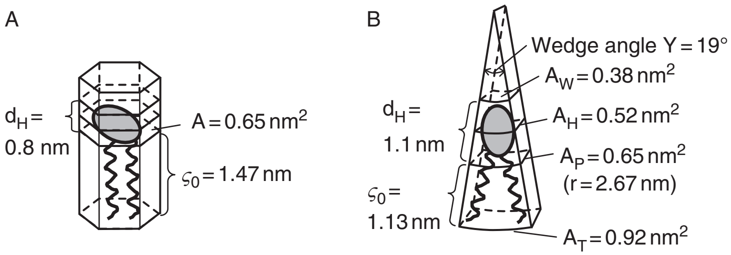

Figure 8 Simplest space filling molecular models for the fluid lamellar (A) and the inverse hexagonal phase (B). The models are derived from structural data of POPE at $T = 74$ °C, at which the L_α-phase coexists with the H_{II}-phase [28]. (A) The steric length of a lipid molecule of 2.27 nm can be divided into headgroup extension, d_H (0.8 nm), and hydrocarbon chain length, ζ_0 (1.47 nm). The area per lipid was determined to be 0.65 nm^2. (B) Simplest anisotropic molecular model for PE lipids in the inverted hexagonal phase. The different molecular areas are defined graphically, which are the lipid–water, the headgroup, the pivotal and terminal interface, respectively. Explicit values for the areas are given. Under the assumption that area per lipid at the headgroup position A_H is squared, it follows that about 19 lipid molecules are necessary for a full revolution in fully hydrated lipid cylinder (compare Fig. 7). Panel B is adapted from Ref. [34].

2.4. Models of Free Energy of the Inverted Hexagonal Phase

In general, solving the stability conditions for different lipid phases as well as conditions for the transition between lipid phases is a problem of defining the free energy of the system and its minimization. In the following a brief overview of theoretical models of L_α to H_{II} phase transition and the corresponding expression for the free energy of the system are described.

Kozlov *et al.* [24] studied the energy of the hexagonal phase in the H_{II}–L_α–H_{II} reentrant phase transition of dioleoylphosphatidylethanolamine (DOPE) upon changes in hydration and temperature. Combining osmotic stress and X-ray diffraction experiments, the spontaneous curvature (R_0^{-1}) and the monolayer bending constant (k_c) of the H_{II} phase were determined. Further, they considered a theoretical model describing the stability of hexagonal and lamellar lipid phases by minimization of the free energy consisting of elastic, hydration, interstitial, and van der Waals energies.

In the model of Kozlov and colleagues, the free energy of the hexagonal phase was approximated by the elastic energy of local bending deformation [37]:

$$F^{\mathrm{H}} = N_{\mathrm{l}}^{\mathrm{H}} \frac{1}{2} k_{\mathrm{c}} a_0 \left(\frac{1}{R} - \frac{1}{R_0} \right)^2 \tag{12}$$

where N_l^H is the number of lipid molecules, k_c is the bending elasticity of the lipid monolayer, a_0 is the area per lipid molecule, $1/R$ is the curvature of the pivotal plane of the lipid monolayer, and $1/R_0$ is the spontaneous curvature in fully hydrated (unstressed) state. For convenience, it was assumed that the free energy of fully hydrated hexagonal phase is 0 ($1/R = 1/R_0$) [24].

The free energy of the lamellar phase was assumed as follows:

$$\begin{aligned} F^L = {} & N_l^L \frac{1}{2} P_0 \lambda a_0 M \exp\left(-\frac{d_w}{\lambda}\right) \\ & - N_l^L a_0 \frac{A_H}{24\pi d_w^2} + N_l^L a_0 \frac{1}{2} k_c \frac{1}{R_0^2} - N_l^L g_i \end{aligned} \tag{13}$$

where N_l^L is the number of lipid molecules in the lamellar phase and d_w is the thickness of the water layer separating the bilayers. The first term is the energy of hydration repulsion between the bilayers (P_0 and λ are preexponential factor and characteristic length of the repulsion, respectively). The second term is the leading term in the energy of van der Waals interaction between the bilayers (A_H is the Hamaker constant [11]). The last two terms describe the difference between the free energies in the fully hydrated hexagonal and lamellar phases and give a constant contribution independent of the distance between the bilayers. The third term is the energy of "unbending" the lipid monolayer to flatness according to Eq. (12) and the last term represents the energy associated with voids in the hexagonal lattice. For simplicity $g_i > 0$ was referred as a curvature-independent part of the interstitial energy (curvature-dependent part is accounted for within the elastic energy of inverted hexagonal phase F^H (Eq. (12))) [24].

Kozlov *et al.* assumed that all parameters in Eqs. (12) and (13) except the intrinsic curvature $R_0{}^{-1}$ are independent on temperature. By assuming a negligible dependence of g_i on temperature and equating the free energies in the hexagonal and lamellar phases in excess water in the temperature for reentrant transition ($T_H = 10\ °C$) gives [24]

$$\begin{aligned} g_i = {} & \frac{1}{2} k_c a_0 \frac{1}{[R_0(T_H)]^2} + \frac{1}{2} P_0 a_0 \lambda \exp\left(-\frac{d_{w\,max}}{\lambda}\right) \\ & - \frac{a_0 A_H}{24\pi (d_{w\,max})^2} \end{aligned} \tag{14}$$

where N_l^L and N_l^H are taken to be equal and the free energy of the inverted hexagonal lipid phase is assumed to be $F^H = 0$ (i.e., $1/R = 1/R_0$), $d_{w\ max}$

represents the equilibrium spacing in the lamellar phase in the absence of osmotic stress and T_{H} is the temperature of the hexagonal–lamellar reentrant transition in excess water. g_{i} was computed by introducing the measured parameters into Eq. (14) and is a positive constant in this case.

In summary, Kozlov *et al.* have described a model of L_α–H_{II}–L_α reentrant transition. On the basis of experiments, they have derived structural parameters and all of the force constants defining the energetic terms of the H_{II} and L_α lipid phases. They found an expression of interstitial energy of the inverted hexagonal phase as a constant difference between H_{II} and L_α phases at the transition point.

Another study on the hexagonal phase was performed by Rand *et al.* [38]. In this work, two types of energy contributions to the free energy of the lipid monolayer were taken into account:

$$G_{\mathrm{H_{II}}} = \frac{1}{2} k_{\mathrm{c}} a_0 \left(\frac{1}{R} - \frac{1}{R_0} \right)^2 + \Pi V_{\mathrm{w}} \tag{15}$$

The first term in Eq. (15) introduces local bending energy and the second term is the osmotic energy, where k_{c} is the bending modulus, a_0 is the area per lipid molecule, R and R_0 are the actual local radii of the curvature and the intrinsic radius of curvature at the pivotal plane, respectively, Π is the difference in osmotic pressure between the outer bulk and inner confined solution, and V_{w} is the volume of water per lipid inside the cylinder [38]. Without consideration of the energy of interstices they made two approximations. The first approximation is that the water cylinders are perfectly circular in cross section (Fig. 9A). Second, the interstitial energy is proposed to be independent on the size of the hexagonal unit cell [38].

There exist two different approaches to express the interstitial (void) energy of the inverted hexagonal phase. In the first approach, rods of inverted hexagonal phase are assumed to be circular in cross section and the interstitial energy is assumed to be proportional to some imaginary surface of the voids between hexagonally packed cylinders [39] (Fig. 9A). In a second approach the interstitial energy was accounted in the terms of tilt and splay deformation of the phospholipid chains which have to fill the hexagonal unit cell while the cross section of neutral plane of lipid rods is assumed to be hexagonal [40] (Fig. 9B). Both approaches result in a proportionality constant by equating the free energies of the lamellar and inverted hexagonal phases at the transition temperature.

Malinin and Lentz [31] later improved the model of Rand *et al.* [38] (Eq. (15)), since the improved model included an energy cost due to voids (interstitial energy), see Fig. 9. To calculate the interstitial energy they assumed that the cross section of pivotal plane is intermediate between

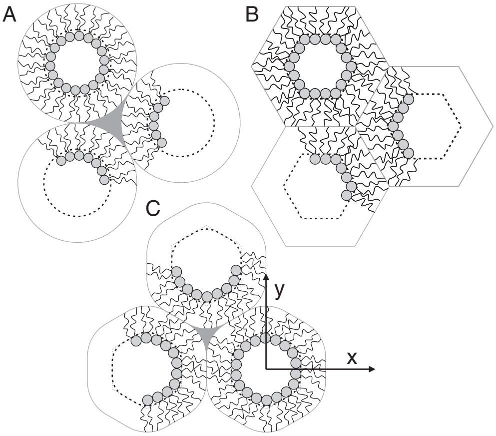

Figure 9 Schemes of different approaches to the expression of the free energy models of inverted hexagonal phase: (A) Circular cross section—Siegel [39] and Rand *et al.* [38], (B) hexagonal cross section—Hamm and Kozlov [40], (C) intermediate between circular and hexagonal cross section—Malinin and Lentz [31].

circular and hexagonal geometry (Fig. 9C), thus they parameterized the shape of the cross section:

$$y = \sqrt{d_{\mathrm{p}}^2 - x^2} + \delta_0 \left(1 - \frac{4x^2}{d_{\mathrm{p}}^2}\right)^2 \tag{16}$$

where x, y are coordinates of the pivotal plane, d_{p} is the distance from the axis of a rod to the pivotal plane in interaxial direction, and δ_0 is the maximal deviation from circular cylindrical geometry. Using Eq. (16) they computed the volumes of the water, voids, and the total unit cell volume. With assuming that the interstitial energy of inverted hexagonal phase is proportional to the volume of voids, the total free energy per lipid molecule is then derived as

$$g = \frac{A_0(K_{\mathrm{b}}/2)\int_{-d_{\mathrm{p}}/2}^{d_{\mathrm{p}}/2} [(1/R_{\mathrm{p}}) - (1/R_{\mathrm{p}_0})]^2 \sqrt{1 + y'^2}\,\mathrm{d}x}{\int_{-d_{\mathrm{p}}/2}^{d_{\mathrm{p}}/2} \sqrt{1 + y'^2}\,\mathrm{d}x} + K_{\mathrm{v}} V_{\mathrm{v}} + \Pi V_{\mathrm{w}} \tag{17}$$

where K_v is a proportionality coefficient representing the free energy of a unit of void volume, V_v and V_w are the volumes of the void and of the water, respectively and $dx\sqrt{1+y'^2}$ is the differential of the arclength [31].

The theoretical model of Malinin and Lentz included deviations from circularity in the inverted hexagonal phase cross section. The interstitial energy K_v (Eq. (17)) turned out to be constant, was derived from the volume of the voids in the hexagonal lattice.

In contrast to these models of interstitial energy g_i (Eq. (14)) and K_v in Eq. (17) we have expressed a relation for the interstitial energy dependent on stretching of the phospholipid chains on account to fill the voids directly. We also developed a new formalism to involve possible anisotropy of phospholipid shapes in our model calculations. In the following sections the new bottom up approach concerning the description of monolayer bending and packing frustration in the formation of the inverted hexagonal phase is outlined.

3. FREE ENERGY OF LIPID MONOLAYERS

It was shown in Ref. [24] that the free energy of the phospholipid monolayer in hexagonal phase may be expressed in terms of bending, interstitial, hydration, and van der Waals energy contribution. However, the contribution of the hydration energy in the excess water conditions is insignificant and also van der Waals energy only slightly contributes to the total free energy. Thus, we consider for the total free energy of the hexagonal phase two energy contributions: the energy of local bending and the interstitial energy (voids filling energy). Starting from a single molecule energy and applying the methods of statistical physics, the free energy of a lipid monolayer (bilayer) was derived [15, 21, 41, 42]. The local bending energy of laterally homogeneous monolayer (bilayer) [37, 43, 44] was recovered; however, an additional contribution due to average orientational ordering of lipid molecules, that is, the contribution of the deviatoric bending [45, 46] was included [15, 21, 42]. The average orientational ordering of anisotropic phospholipids lowers the free energy of the system; the effect is more pronounced for larger anisotropy of lipid molecules and stronger membrane curvature anisotropy [21].

3.1. Bending Energy of Lipid Monolayers

For better understanding we briefly repeat the derivation of the bending energy per lipid, which in general may be anisotropic [21]. This energy of a single lipid molecule depends on mismatch between curvature tensors $\underline{C}_m$ (Eq. (9)) and $\underline{C}$ (Eq. (2)). In general the curvature tensors $\underline{C}_m$ and $\underline{C}$ have different orientations, that is, they are rotated by an angle ω. To express their mismatch we introduce the mismatch tensor $\underline{M}$:

$$\underline{M} = \underline{R}\,\underline{C}_\mathrm{m}\underline{R}^{-1} - \underline{C} \tag{18}$$

where $\underline{R}$ is transformation matrix for rotation:

$$\underline{R} = \begin{bmatrix} \cos\omega & -\sin\omega \\ \sin\omega & \cos\omega \end{bmatrix} \tag{19}$$

The single molecule energy at a given point of the membrane should be a scalar quantity, hence it may be expressed by two invariants of the tensor $\underline{M}$, trace, and determinant:

$$w_\mathrm{b} = \frac{K_1}{2}\left(\mathrm{Tr}(\underline{M})\right)^2 + K_2\,\mathrm{Det}(\underline{M}) \tag{20}$$

where K_1 and K_2 are constants [21].
Eq. (20) can be rewritten as

$$\begin{aligned} w_\mathrm{b} = {} & (2K_1 + K_2)(H - H_\mathrm{m})^2 \\ & - K_2\left(D^2 - 2DD_\mathrm{m}\cos(2\omega) + D_\mathrm{m}^2\right) \end{aligned} \tag{21}$$

where H is the mean curvature of a membrane (Eq. (3)), H_m is the mean intrinsic (spontaneous) curvature of the molecule (Eq. (10)), and D and D_m are the curvature deviators of the membrane and the molecule (Eqs. (5) and (11)), respectively [21]. In the following we introduce the definitions:

$$2K_1 + K_2 = \frac{\xi}{2} \text{ and } K_2 = -\frac{\xi + \xi^*}{4} \tag{22}$$

Constants ξ and ξ^* describe the strength of intermolecular interactions. Using the definitions of ξ and ξ^*, Eq. (21) can be rewritten in the form

$$\begin{aligned} E(\omega) = {} & \frac{\xi}{2}(H - H_\mathrm{m})^2 \\ & + \frac{\xi + \xi^*}{4}\left(D^2 - 2DD_\mathrm{m}\cos(2\omega) + D_\mathrm{m}^2\right) \end{aligned} \tag{23}$$

For sake of simplicity we assume that $\xi = \xi^*$. This equality yields $K_1 = -K_2$. It is obvious that the energy expressed by Eq. (23) reaches its minimum when $\cos(2\omega) = 1$ and its maximum when $\cos(2\omega) = -1$. In the first case the systems of tensors $\underline{C}_\mathrm{m}$ and $\underline{C}$ are aligned ($\omega = 0$) or rotated by the angle $\omega = \pi$:

$$E_\mathrm{min} = \frac{\xi}{2}(H - H_\mathrm{m})^2 + \frac{\xi}{2}(D^2 + D_\mathrm{m}^2) - \xi D D_\mathrm{m} \tag{24}$$

while in the second case the systems are rotated by the angle $\omega = \pi/2$ or $\omega = 3\pi/2$:

$$E_\mathrm{max} = \frac{\xi}{2}(H - H_\mathrm{m})^2 + \frac{\xi}{2}(D^2 + D_\mathrm{m}^2) + \xi D D_\mathrm{m} \tag{25}$$

To derive the deviatoric bending energy of the whole monolayer, the membrane monolayer is divided into small patches that contain a sufficient large number of lipid molecules in order to apply the methods of statistical mechanics [21]. The principal curvatures C_1 and C_2 are taken to be constant over the patch and phospholipid molecules are considered to be equal and independent. Considering a simple two state model there are M equivalent molecules within the patch. Each molecule can exist in state of lower energy E_min or higher energy E_max. It means that N molecules are assumed to be in the state with E_max and consequently $(M - N)$ molecules in the state with E_min as shown in the next equation:

$$\frac{E_\mathrm{D}}{kT} = N\frac{E_\mathrm{max}}{kT} + (M - N)\frac{E_\mathrm{min}}{kT} \tag{26}$$

where E_D is the deviatoric bending energy of the membrane patch. The energy of the patch is divided by k (Boltzmann constant) and T (thermodynamic temperature). Introducing Eqs. (24) and (25) into Eq. (26) gives

$$\frac{E_\mathrm{D}}{kT} = M\frac{E_\mathrm{q}}{kT} - \left(\frac{M}{2} - N\right) d_\mathrm{eff} \tag{27}$$

where

$$\frac{E_\mathrm{q}}{kT} = \frac{\xi}{2kT}(H - H_\mathrm{m})^2 + \frac{\xi}{2kT}(D^2 + D_\mathrm{m}^2) \tag{28}$$

and

$$d_{\mathrm{eff}} = \frac{(2\xi)D_{\mathrm{m}}D}{kT} \tag{29}$$

d_{eff} is called the effective curvature deviator [21].

Another contribution to the bending energy is the direct interaction between molecules. At most the molecules interact with their nearest neighbors. It is assumed that if the actual shape of the membrane is in tune with the local curvature field, tails of the molecules move in average closer together and this leads to lowering energy. On the other side, if the molecules are oriented less favorable the average chain packing is less dense. This causes increasing of the energy. It is considered that this effect is proportional to d_{eff} (local effective curvature deviator). Direct interaction energy of N molecules that exhibit less favorable average packing is taken into account by the expression

$$\frac{E_{\mathrm{N}}}{kT} = \frac{\tilde{k}}{kT} N d_{\mathrm{eff}} \tag{30}$$

while the direct interaction energy of molecules that exhibit more favorable average packing (negative contribution) is described by

$$\frac{E_{M-N}}{kT} = -\frac{\tilde{k}}{kT}(M-N)d_{\mathrm{eff}} \tag{31}$$

where $\tilde{k}$ is the interaction constant [21].

The total energy caused by direct interaction is given by summation of Eqs. (30) and (31) divided by 2 as to avoid counting each molecule twice:

$$\frac{E_{\mathrm{i}}}{kT} = -\frac{\tilde{k}}{kT}\left(\frac{M}{2} - N\right)d_{\mathrm{eff}} \tag{32}$$

The total bending energy of the patch is thus

$$\frac{E^{\mathrm{p}}}{kT} = \frac{E_{\mathrm{D}}}{kT} + \frac{E_{\mathrm{i}}}{kT} \tag{33}$$

where E_{D}/kT is the contribution of the average mutual orientation of the local curvature tensor and intrinsic curvature tensor (deviatoric bending) and E_{i}/kT is the contribution of the direct interaction between the neighbor molecules.

We consider all the patches to have a constant area A^{p}, a constant number of molecules M and a constant temperature T of the system.

The phospholipid molecules within the system are treated as indistinguishable. We assumed that the system is in thermodynamical equilibrium and only two states are possible just like in the description of a two-orientation model of noninteracting magnetic dipoles in the external magnetic field [47]. In our model the external magnetic field is represented by curvature deviator D [21]. By analogy, N molecules are in state with maximal energy and $(M - N)$ molecules are in state with minimal energy. The number of possibilities is $M!/N!(M-N)!$ while the corresponding energy is E^{P}. N can be any number from 0 to M. The canonical partition function $Q^{\mathrm{P}}(M, T, D)$ of M molecule in the patch of the membrane is therefore

$$Q^{\mathrm{P}} = \sum_{N=0}^{M} \frac{M!}{N!(M-N)!} \exp\left(-\frac{E^{\mathrm{P}}}{kT}\right) \tag{34}$$

where k is the Boltzmann constant. Using Eqs. (27)–(34) gives

$$Q^{\mathrm{P}} = q^M \sum_{N=0}^{M} \frac{M!}{N!(M-N)!} \exp\left(d_{\mathrm{eff}}\left(1 + \frac{\tilde{k}}{kT}\right)\left(\frac{M}{2} - N\right)\right) \tag{35}$$

where by considering Eq. (28)

$$q = \exp\left(-\frac{E_{\mathrm{q}}}{kT}\right) \tag{36}$$

Using the binominal (Newton) formula in summation of the finite series in Eq. (35) yields

$$Q^{\mathrm{P}} = \left[2q \cosh\left(\frac{d_{\mathrm{eff}}\left(1 + (\tilde{k}/kT)\right)}{2}\right)\right]^M \tag{37}$$

The Helmholtz free energy of the patch is $F^{\mathrm{P}} = -kT \ln Q^{\mathrm{P}}$. Combining Eqs. (35)–(37) yields the free energy of the patch:

$$\begin{aligned} F^{\mathrm{P}} = {} & M\frac{\xi}{2}\left[(H - H_{\mathrm{m}})^2 + D^2 + D_{\mathrm{m}}^2\right] \\ & -kTM \ln\left[2\cosh\left(\frac{\left(1 + (\tilde{k}/kT)\right)\xi D_{\mathrm{m}} D}{kT}\right)\right] \end{aligned} \tag{38}$$

The bending energy of the monolayer is given by the summation of the contributions of the all patches of the monolayer, i.e. integration is performed over the whole area A:

$$F_\mathrm{b} = \int_A \frac{n_0\xi}{2}\left[(H - H_\mathrm{m})^2 + D^2 + D_\mathrm{m}^2\right] \mathrm{d}A \\ -n_0 kT \int_A \ln\left[2\cosh\left(\frac{\xi\left(1 + (\tilde{k}/kT)\right) D_\mathrm{m} D}{kT}\right)\right] \mathrm{d}A \tag{39}$$

where n_0 is the area density of the lipid molecules, ξ is the constant describing the strength of the interaction between a single lipid molecule and the surrounding membrane continuum, k is the Boltzmann constant, T is temperature, $\tilde{k}$ is the constant describing the direct interaction between lipid molecules [21], and $\mathrm{d}A$ is the area element of the lipid monolayer.

If we consider surfaces with small curvature deviators D or molecules with small D_m, we can substitute the term $\ln(\cosh(x))$ in Eq. (39) by the first term in Taylor expansion: $\ln(\cosh(x)) \cong \ln(1 + x^2/2) \cong x^2/2$. Thus, our general expression for monolayer bending energy transforms into Helfrich expression for local bending energy of lipid monolayer [37]:

$$w_\mathrm{b} = \frac{k_\mathrm{c}}{2}(2H - C_0)^2 + k_\mathrm{G} K \tag{40}$$

where w_b is the area density of the monolayer bending energy, while the constants k_c, k_G, and C_0 are defined as

$$k_\mathrm{c}/n_0 = \frac{\xi}{2} - \frac{(1 + \tilde{k}/kT)^2 \xi^2 D_\mathrm{m}^2}{4kT} \tag{41}$$

$$k_\mathrm{G}/n_0 = -\frac{\xi}{2} + \frac{(1 + \tilde{k}/kT)^2 \xi^2 D_\mathrm{m}^2}{2kT} \tag{42}$$

and

$$C_0 = H_\mathrm{m}\left[1 + \frac{[1 + (\tilde{k}/kT)]^2 \xi D_\mathrm{m}^2}{2kT}\right] \tag{43}$$

The constant C_0 represents spontaneous (intrinsic) curvature of the lipid monolayer.

In the simplest case, where only isotropic phospholipid molecules within the lipid monolayer are taken into account ($D_\mathrm{m} = 0$), the constants are defined as

$$k_\mathrm{c}/n_0 = \frac{\xi}{2} \tag{44}$$

$$k_\mathrm{G}/n_0 = -\frac{\xi}{2} \tag{45}$$

while the expression for the spontaneous (intrinsic) curvature is equal to the mean curvature of the lipid monolayer:

$$C_0 = H_\mathrm{m} \tag{46}$$

3.2. Interstitial Energy of the Inverted Hexagonal Phase

In this section we are interested in the derivation of a dependence for an energy contribution from "voids"—interstitial energy, which was already discussed in Section 2.2 [1, 24, 31]. The need of additional interstitial energy contribution in the H_II phase appears due to the special packing geometry of the inverted hexagonal phase (compare with Section 2).

In the lamellar phase L_α, the monolayers have a constant thickness and there are no voids in the mid-plane of the bilayer. On the other hand, in the inverted hexagonal phase, the distance between two adjacent monolayers varies over the monolayer surface. Some of the lipid tails have more space, while others are squeezed with respect to an average length ζ_0 (Fig. 6). To avoid water pockets, the hydrocarbon tails of lipid molecules have to stretch accordingly. The void-filling energy contribution due to lipid stretching can be expressed on the basis of Hooke's law [48]:

$$f_\mathrm{d} = \tau(\zeta - \zeta_0)^2 \tag{47}$$

where ζ is the actual length of the fatty acid chain and τ is the proportionality constant reflecting the stiffness of the chains (stretching modulus). We suppose that the area density of the contact energy is given as

$$\lambda_\mathrm{c} = \tau(\zeta - \zeta_0)^2 n_0 \tag{48}$$

where n_0 is the area density of phospholipid molecules ($n_0 = 1/a_0$). The total contact energy is given as

$$F_{\mathrm{i}} = \int_A \lambda_{\mathrm{c}} \, \mathrm{d}A \tag{49}$$

where we integrate over the whole area of lipid monolayer A. The Eq. (49) can be written in the form

$$F_{\mathrm{i}} = Y\tau n_0 \int_l (\zeta - \zeta_0)^2 \mathrm{d}l \tag{50}$$

where $\mathrm{d}l$ is the element of the length of the curve corresponding to phospholipid monolayer in the projection of hexagonal phase shown in Fig. 6 and Y is the length of the inverted hexagonal tube.

To estimate the actual length of hydrocarbon chain ζ, cylindrical coordinates are introduced. The length of hydrocarbon chains may be estimated from hexagonal geometry of the lattice. From the rectangular triangle depicted in Fig. 10 it follows:

$$\zeta = \frac{a}{2\cos\varphi} - r \tag{51}$$

Because of hexagonal symmetry, Eq. (51) is valid for the contact region of two adjacent lipid cylinders, that is, for 1/12 of the area of one lipid cylinder. The values of the angle φ are therefore defined in the range of

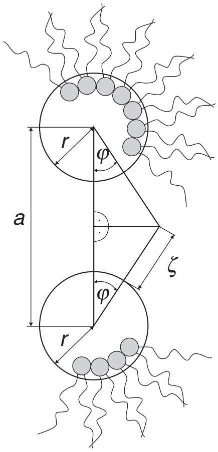

Figure 10 Scheme of two neighboring inverted lipid tubes in hexagonal lattice. The lipid tails have to stretch in order to fill voids in the hydrocarbon region. The symbol a denotes the $\mathrm{H_{II}}$ phase lattice constant and r denotes the radius of the pivotal plane of the $\mathrm{H_{II}}$ phase. The actual length of hydrocarbon tails (ζ) depends on the angle φ.

$$\varphi \in \left[0, \frac{\pi}{6}\right) \tag{52}$$

If $\varphi = 0$, the length of hydrocarbon chains ζ is equal to $(a/2) - r$. At the upper limit of the range of φ, the length of the hydrocarbon chain is equal to $(a/\sqrt{3}) - r$.

Considering the cylindrical transformation ($r\,\mathrm{d}\varphi = \mathrm{d}l$), the symmetry of the problem (12 identical segments) and the expression for the length of hydrocarbon chains (Eq. (51)), Eq. (50) can be written in the form

$$F_{\mathrm{i}} = Y\tau n_0 12r \int_0^{\pi/6} \left(\frac{a}{2\cos\varphi} - r - \zeta_0\right)^2 \mathrm{d}\varphi \tag{53}$$

After solving the integral in Eq. (53), the contact energy of one lipid cylinder (Eq. (53)) can be written as

$$F_{\mathrm{i}} = 12Y\tau n_0 r\left(\frac{a^2\sqrt{3}}{12} - a(r+\zeta_0)\ln\sqrt{3} + \frac{\pi}{6}(r+\zeta_0)^2\right) \tag{54}$$

3.3. Total Free Energy per Lipid Molecule

The total free energy per lipid molecule in inverted hexagonal phase can be computed as

$$f = \frac{E}{M} \tag{55}$$

where M is the total number of lipid molecules in the system with energy E. The total number of molecules can be calculated from the total area of membrane A and the area corresponding to one lipid molecule (a_0), that is, the area density of the lipid molecule (n_0):

$$M = \frac{A}{a_0} = n_0 A \tag{56}$$

The total area of one lipid cylinder in the inverted hexagonal phase is

$$A = 2\pi r Y \tag{57}$$

From summation of Eqs. (39) and (49) it follows that the free energy per lipid molecule in the H_{II} phase can be expressed as

$$\begin{aligned} F = \frac{F_b + F_i}{2\pi n_0 Y r} &= \frac{\xi}{2}\left[(H - H_m)^2 + D^2 + D_m^2\right] \\ &- kT \ln\left[2\cosh\left(\frac{\left(1 + (\tilde{k}/kT)\right)\xi D_m D}{kT}\right)\right] \\ &+ \frac{6}{\pi}\tau\left(\frac{a^2\sqrt{3}}{12} - a(r + \zeta_0)\ln\sqrt{3} + \frac{\pi}{6}(r + \zeta_0)^2\right) \end{aligned} \qquad (58)$$

Equations (1) and (3) yield for cylindrical geometry of the H_{II} phase $H = -1/2r$ and $D = |H|$. The first two terms in Eq. (58) represent the bending energy contribution and the third term is interstitial energy contribution to the free energy.

4. ESTIMATION OF MODEL CONSTANTS

In order to determine the free energy of different configurations of the lipid monolayers, the values of the model constants were estimated. The value of interaction constant ξ was estimated from monolayer bending constant $\xi = 2k_c a_0$, where for POPE $k_c = 11kT$ is the bending constant [49] and $a_0 = 0.65 \times 10^{-18}$ m^2 is the area per phospholipid molecule [28]. The reference (nonstretched) length of the phospholipid tails ζ_0 (Fig. 6) was taken to be 1.30 nm [28]. In calculation of the interstitial energy the lipid stretching modulus τ was taken to be in the range from $0.95kT\,\mathrm{nm}^{-2}$ to $95kT\,\mathrm{nm}^{-2}$ (see Ref. [48]). For the sake of simplicity it was taken that the molecules favor cylindrical geometry, that is $|H_m| = D_m$. The effect of the temperature was simulated by increasing the intrinsic curvatures $|H_m|$ and D_m with increasing temperature which is consistent with increased spreading of the phospholipid tails while the headgroup extensions in POPE remain relatively unchanged. The range of the intrinsic curvatures was taken to be from 0 to $0.4\,\mathrm{nm}^{-1}$, corresponding to curvature radii down to 1 nm. To study the effect of the deviatoric bending, also the hypothetical case where the molecules are isotropic ($D_m = 0$) was considered.

5. DETERMINATION OF EQUILIBRIUM CONFIGURATION OF PLANAR AND INVERTED CYLINDRICAL SYSTEMS

5.1. Numerical Solution

To show the importance of the interstitial energy, we compare three different geometries of lipid monolayers: planar, cylindrical, and spherical. The systems were described as surfaces with constant principal curvatures. In the planar system, $H = D = 0$, in the inverted spherical system $H = -1/r_s$ and $D = 0$, while in the inverted cylindrical system $H = -D = -1/2r$, where r is the radius of the cylinder and r_s is the radius of the sphere. The minimal value of the free energy of a unit patch of the lipid monolayer with respect to the mean curvature H was calculated by using Eq. (58) while the model constants are given in Section 4.

5.2. Results of Equilibrium Configurations of Planar and Inverted Cylindrical Systems

To explain the effect of individual contributions to the free energy, we first determine the equilibrium configuration obtained by minimization of the bending energy alone (first two terms in Eq. (58)). There are three different geometries compared in Fig. 11: planar (corresponding to lamellar L_α phase), spherical (corresponding to inverted micellar M_{II} phase), and cylindrical (corresponding to inverted hexagonal H_{II} phase), see also Fig. 1. Figure 11 shows the equilibrium bending energy per lipid molecule dependent on the mean intrinsic curvature H_m for anisotropic molecules, for which $|H_m| = D_m$ (panel A) and isotropic molecules, for which $D_m = 0$ (panel B). For small $|H_m| = D_m$, the bending energy increases with increasing $|H_m|$ in all three geometries (panel A). In the M_{II} and L_α phases, which are isotropic with respect to the curvature ($D = 0$), there is no orientational ordering of the molecules and the bending energy monotonously increases also for larger $|H_m| = D_m$. In the H_{II} phase, however, the nonzero values of both the intrinsic curvature deviator D_m and the curvature deviator D give rise to a negative energy contribution of the deviatoric bending. Therefore, the equilibrium free energy reaches a maximum upon an increase of D_m (which for this particular choice of molecules it is equal to $|H_m|$), but then decreases at a certain threshold, and such the H_{II} phase becomes energetically the most favorable. Summing up, for small $|H_m| = D_m$, the M_{II} phase has the lowest bending energy, while at larger $|H_m| = D_m$, the H_{II} phase becomes the most favorable due to the average orientational ordering of phospholipid molecules. The effect is stronger for higher values of $\tilde{k}$ describing the direct interaction between phospholipid tails (Fig. 11A).

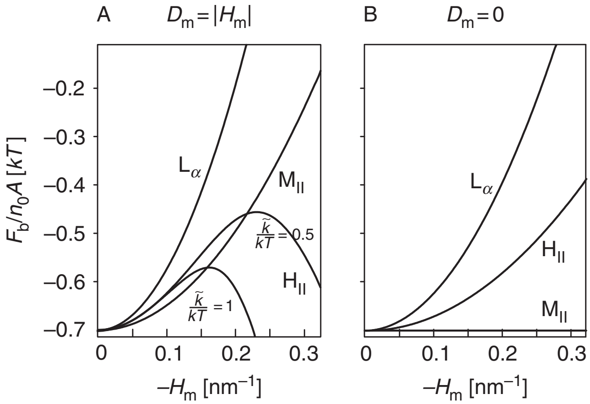

Figure 11 The equilibrium bending energy per lipid molecule F_b/n_0A in dependence on the intrinsic mean curvature H_m for the L_α, M_{II}, and H_{II} phases: (A) a system composed of anisotropic molecules ($D_m = |H_m|$) and (B) a system composed of isotropic molecules ($D_m = 0$). For the bending contribution, see Eq. (58). Adapted from Ref. [29].

Figure 11B shows that for isotropic molecules (having $D_m = 0$, i.e., $C_{1m} = C_{2m}$, see also Fig. 2), the M_{II} phase is always favored, that is, the calculated energy per lipid F_b/n_0A in the M_{II} phase is equal to the reference value and is the smallest comparing to the energy of the L_α and the H_{II} phase. We note that for isotropic molecules there can be no energy lowering due to the average orientational ordering of the molecules since all orientations of the lipid molecules are energetically equivalent.

The deviatoric bending of anisotropic molecules may thus alone explain the stability of the H_{II} phase at higher temperatures. At lower temperatures, the M_{II} phase is energetically favored except for $|H_m| = D_m = 0$, where the L_α phase is the stable phase. At small $|H_m| = D_m$, however, the equilibrium radii of the simulated M_{II} phase are so large that this case would correspond to flat membrane systems. For some intermediate $|H_m| = D_m$, the simulated M_{II} phase would consist of aggregated micelles of a given size, however such a configuration is actually not observed [50, 51].

To obtain a better agreement with experimental observations also in the intermediate range of $|H_m| = D_m$, we include the effect of void filling energy by using a simple model, where the void-filling energy is considered constant for a given geometry (see also Ref. [24]). Figure 12 shows the minimal free energy $F/n_0A = F_b/n_0A + F_i/n_0A$ in dependence on the intrinsic mean curvature H_m for the L_α, H_{II}, and M_{II} phases. Here F_i is the interstitial energy, n_0 is the area density of the lipid molecule, and A is the area of the whole monolayer (see Eqs. (39) and (54)). Since the energy contribution of voids is smaller in the system of close packed inverted

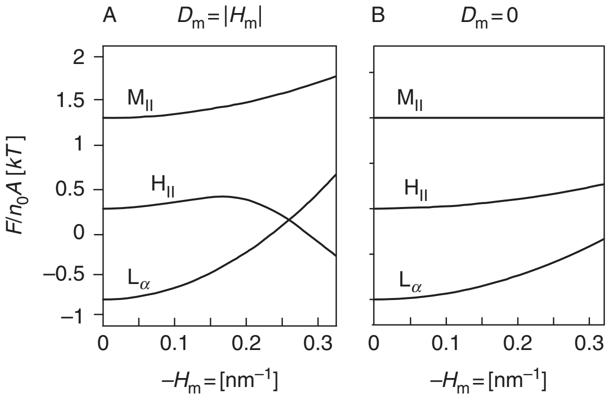

Figure 12 The equilibrium free energy per lipid molecule $F_b/n_0A + \chi$ consisting of the contribution of bending and of a constant for the void filling energy per lipid molecule in dependence on the intrinsic mean curvature $|H_m|$ for the L_α ($\chi = 0$), H_{II} ($\chi = 1kT$) and M_{II} ($\chi = 2kT$) phases: (A) $D_m = |H_m|$ and (B) $D_m = 0$, $\bar{k}/kT = 1$. Adapted from Ref. [29].

cylinders than in the system of close packed inverted spheres, the value of the void-filling energy per lipid molecule $F_i = \chi$ was taken to be lower for cylinders than for spheres. It was estimated from the results of Kozlov *et al.* [24] that χ should be of the order of kT [24], therefore we took for the H_{II} phase $\chi = 1kT$ and for the M_{II} phase $\chi = 2kT$.

In Fig. 12A and B the curves corresponding to the H_{II} and M_{II} phases in Fig. 11 are shifted up for different constants χ, respectively, and the overall picture is now more realistic. It can be seen in Fig. 12A and B that for small $D_m = |H_m|$ the L_α phase is energetically the most favorable, since it requires no void-filling energy. For anisotropic molecules (Fig. 12A) at a certain threshold $D_m = |H_m|$, the H_{II} phase becomes energetically the most favorable due to the average orientational ordering of the lipid molecules. In the isotropic case (Fig. 12B), all curves monotonously increase; however, the curve corresponding to the L_α phase increases faster and therefore it would eventually cross with the curve corresponding to the H_{II} phase. However, the value of H_m where the intersection would take place would be very high (out of range given in Fig. 12, where the maximal value 0.4 nm^{-1} already corresponds to a cylinder with a radius of only 1.25 nm).

In short, the effects shown in Fig. 12A indicate that in the simple model where the interstitial energy is taken to be constant within a phase [24, 29], an increase of $D_m = |H_m|$, which is caused by the increase of temperature can induce the transformation from L_α to H_{II} lipid phase. Taking into account the interstitial energy for small $|H_m|$ (lower temperature) renders, the L_α phase is energetically the most favorable, while at a certain threshold

$D_m = |H_m|$ (higher temperature), the H_{II} phase becomes energetically the most favorable.

Having eliminated the M_{II} phase due to high packing frustration (Fig. 12), in the following, we compare only the L_α and the H_{II} phases by using an improved model for the void filling energy, where stretching of the lipid tails in the actual hexagonal geometry is taken into account (Fig. 6 and Eq. (52)). Figure 13 shows the free energy per lipid molecule F/n_0A in dependence on the intrinsic mean curvature H_m for the L_α and the H_{II} phase.

We can compare the total free energy per molecule for anisotropic and isotropic phospholipid molecules in dependence on the mean intrinsic curvature H_m. It can be seen in Fig. 13 that there are three curves corresponding to the inverted hexagonal phase with different stiffness constants τ and one curve corresponding to the lamellar phase. For stiff hydrocarbon chains (high values of τ), the lamellar phase has lower energy than the inverted hexagonal phase, while for decreasing τ, the inverted hexagonal phase is energetically more favorable than the lamellar phase for high enough $|H_m|$. Isotropic lipid molecules in the inverted hexagonal phase also exhibit the lowest energy for less stiff hydrocarbon chains.

By comparing Fig. 13A and B, it is important to point out that the anisotropy of phospholipid molecules evokes a steeper increase of the absolute value of the energy difference between the lamellar and the inverted hexagonal phases with temperature and therefore promotes and stabilizes the H_{II} phase profoundly.

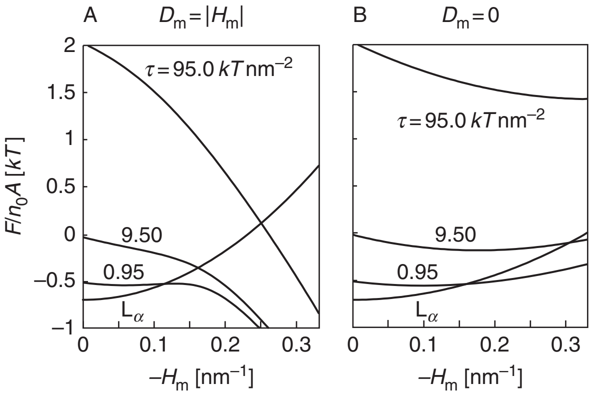

Figure 13 Free energy per lipid molecule F_b/n_0A consisting of the bending and the interstitial contributions in dependence on the intrinsic mean curvature of lipid molecules $|H_m|$ in the L_α and H_{II} phase for various stiffnesses of hydrocarbon chains τ for (A) $|H_m| = D_m$ and (B) $D_m = 0$. See Eq. (58). $\tilde{k}/kT = 1$. Adapted from Ref. [29].

For a more detailed study of the H_{II} phase we have constructed graphs its structural parameters. Figure 14 shows the dependence of the cylinder radius r and of the distance between the centers of the lipid cylinders a, respectively, (Fig. 6), on the intrinsic curvature $|H_m|$ for three values of τ of anisotropic lipid molecules. The H_{II} phase is composed of lipid cylinders with small radius r and small separation a for lipids of large mean intrinsic curvatures. Decreasing the absolute value of the mean intrinsic curvature $|H_m|$ increases both the radius of the H_{II} cylinders and the lattice length. However, cylinders of large radii increase the void space and the corresponding stretching of hydrocarbon chains. Therefore, the maximum radii of the cylinders are limited by the energy of interface region between the cylinders. If the hydrocarbon chains are stiff (large value of τ), the creation of voids is energetically unfavorable. In this case, the small radii of cylinders are preferred as they provide small void spaces (Fig. 14A). On the other hand, if the stretching of hydrocarbon chains does not require much energy (small τ), larger radii of hydrocarbon chains are permitted.

It is instructive to compare the given plots with experimental data [28, 34] (Fig. 14, dashed lines). First, it teaches us that realistic value of the stretching moduli τ most probably lie between 0 and $20kT\ \mathrm{nm}^{-2}$ (for large enough τ, e.g., $\tau = 95kT\ \mathrm{nm}^{-2}$ no realistic dimensions of the H_{II} lattice can be predicted). Second, the range of realistic intrinsic mean curvatures $-H_m$ lies probably in the range of $0.1-0.2\ \mathrm{nm}^{-1}$. Note that this comes close to the value of the mean curvature $-H$ of the POPE/water system (Table 1) and is also in agreement with values of intrinsic curvatures of lipids given by other authors [52]. The effect of contact energy in the

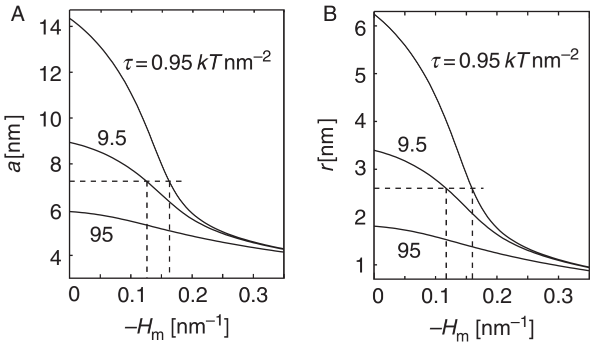

Figure 14 Structural parameters of the H_{II} phase for the case where $D_m = |H_m|$. (A) The optimal unit cell parameter a and (B) the optimal pivotal plane radius r (core center to polar/apolar interface) are plotted versus the absolute value of the mean curvature H_m for different lipid chain rigidities τ. The two horizontal dashed lines mark the realistic values for a and r, respectively (Table 1). For definitions of a and r, see Fig. 6. $\tilde{k}/kT = 1$. Adapted from Ref. [29].

Table 1 Geometrical parameters of the L_α and the H_{II} phases at $T = 74\,°C$

Parameter	$L_\alpha = 74\,°C$	$H_{II} = 74\,°C$
D, a (nm)	4.99	7.24
d_{pol}, r (nm)	2.5	2.67
ζ_0 (ζ_{min}, ζ_{max}) (nm)	1.47	1.13 (0.95, 1.51)
a_0 (nm^2)	0.65	0.65
H (nm^{-1})	0	0.187

The structural parameters are defined in Fig. 6. The experimental values are taken from Ref. [28].

stabilization of the hexagonal phase is obvious if the value of τ is large enough. Large diameter of the lipid cylinder r produces larger voids that are energetically unfavorable.

5.3. Influence of the Direct Interaction Constant $\tilde{k}$

Figure 15 shows the effect of the direct interaction constant $\tilde{k}$ [21] on the calculated free energy per lipid molecule. The energy $\tilde{k}/kT$ was estimated by the van der Waals interactions between the tails of orientationally ordered and orientationally disordered nearest neighbors of a given molecule [21].

It can be seen in Fig. 15 that for low values of $\tilde{k}/kT$ the behavior of the anisotropic lipid molecules in our theoretical model are energetically close to the behavior of isotropic molecules.

6. LAMELLAR TO INVERTED HEXAGONAL PHASE TRANSITION

6.1. Determination of Pivotal Map of Nucleation Contour by Minimization of Monolayer Bending Energy

Following the nucleation model of the L_α–H_{II} transition given in [28, 34], the surface of the monolayer forming a closure is described by the radius vector $\mathbf{r} = (x,\ y,\ z(x))$ (Figs. 7 and 16), wherefrom the mean and the Gaussian curvatures are

$$2H = \frac{-\frac{\partial^2 z}{\partial x^2}}{\left(1 + \left(\frac{\partial z}{\partial x}\right)^2\right)^{3/2}} \tag{59}$$

and

$$C_1 C_2 = 0 \tag{60}$$

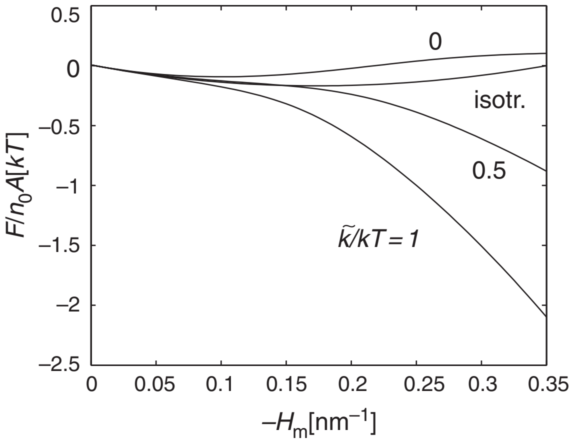

Figure 15 Influence of the direct interaction constant $\tilde{k}$ on the calculated free energy per lipid molecule F/n_0A in the H_{II} phase. Comparison with free energy per isotropic phospholipid molecule is given.

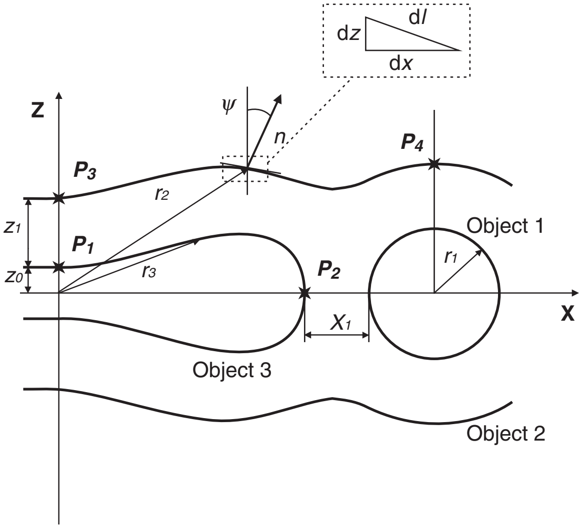

Figure 16 Parametrization of the pivotal surface. Two bulby closures (objects 3) are placed between adjacent bilayers (objects 2) and a cylinder (object 1). The geometry of the system is symmetrical with respect to the *x*-axis.

The surface is given in terms of the arclength l, so that $\sin\psi = \mathrm{d}z/\mathrm{d}l$ and $\cos\psi = \mathrm{d}x/\mathrm{d}l$. Considering the above definitions, the mean curvature is expressed as $2H = 2D = \mathrm{d}\psi/\mathrm{d}l$, while the area element is $\mathrm{d}A = \mathrm{Y}\,\mathrm{d}l$. Due to symmetry, only the part of the contour above the x-axis is considered in determination of the equilibrium shape of the closure.

The coordinates, the area, the area element, and the bending energy are written in dimensionless form. Normalizing the curvatures and distances by an arbitrary unit of length z_0 (in our case we set $z_0 = 1$ nm) gives dimensionless curvatures:

$$h = z_0 H,\ \ d = z_0 D,\ \ h_{\mathrm{m}} = z_0 H_{\mathrm{m}},\ \ d_{\mathrm{m}} = z_0 D_{\mathrm{m}} \tag{61}$$

and a dimensionless arclength:

$$\tilde{l} = \frac{l}{z_0} \tag{62}$$

The area element is normalized to Yz_0. The bending energy is normalized to $n_0 \xi Y/2z_0$:

$$\begin{aligned} f_{\mathrm{b}} = &\int (\zeta - \zeta_{\mathrm{m}})^2\, \mathrm{d}\tilde{l} + \int (d^2 + d_{\mathrm{m}}^2)\, \mathrm{d}\tilde{l} \\ &- \kappa \int \ln[2\cosh[\Big(1 + (\tilde{k}/kT)\Big)\vartheta 2 d_{\mathrm{m}} d]]\, \mathrm{d}\tilde{l} \end{aligned} \tag{63}$$

where

$$\kappa = \frac{1}{\vartheta} = \frac{2kTz_0^2}{\xi} \tag{64}$$

To minimize the bending energy (63), a functional

$$\begin{aligned} L = &\left(\frac{1}{2}\frac{\mathrm{d}\psi}{\mathrm{d}\tilde{l}} - \zeta_{\mathrm{m}}\right)^2 + \frac{1}{4}\left(\frac{\mathrm{d}\psi}{\mathrm{d}\tilde{l}}\right)^2 \\ &- \kappa \ln\Big(2\cosh\Big((1 + \tilde{k}/kT)\vartheta 2 d_{\mathrm{m}} d\Big)\Big) \\ &- \lambda\left(\cos\psi - \frac{\mathrm{d}x}{\mathrm{d}\tilde{l}}\right) - \nu\left(\sin\psi + \frac{\mathrm{d}z}{\mathrm{d}\tilde{l}}\right) \end{aligned} \tag{65}$$

is minimized by solving a system of Euler–Lagrange equations:

$$\frac{\partial L}{\partial \psi} - \frac{\mathrm{d}}{\mathrm{d}\tilde{l}}\left(\frac{\partial L}{\partial \psi_{\tilde{l}}}\right) = 0 \tag{66}$$

$$\frac{\partial L}{\partial x} - \frac{\mathrm{d}}{\mathrm{d}\tilde{l}}\left(\frac{\partial L}{\partial x_{\tilde{l}}}\right) = 0 \tag{67}$$

$$\frac{\partial L}{\partial z} - \frac{\mathrm{d}}{\mathrm{d}\tilde{l}}\left(\frac{\partial L}{\partial z_{\tilde{l}}}\right) = 0 \tag{68}$$

where $\psi_{\tilde{l}} = \mathrm{d}\psi/\mathrm{d}\tilde{l}$, $x_{\tilde{l}} = \mathrm{d}x/\mathrm{d}\tilde{l}$, and $z_{\tilde{l}} = \mathrm{d}z/\mathrm{d}\tilde{l}$. By introducing the variable

$$\Upsilon = x\frac{\mathrm{d}\psi}{\mathrm{d}\tilde{l}} \tag{69}$$

a system of equations (66)–(68) yields

$$\frac{\mathrm{d}\Upsilon}{\mathrm{d}\tilde{l}} = \frac{\Upsilon}{x}\cos\psi + \frac{(\lambda\sin\psi - \nu\cos\psi)x}{1 - \left[(\kappa\tilde{\vartheta}^2 d_{\mathrm{m}}^2)/\left(\cosh^2(\tilde{\vartheta} d_{\mathrm{m}}\Upsilon/x)\right)\right]} \tag{70}$$

$$\lambda = \mathrm{const},\ \ \nu = \mathrm{const},\ \ \tilde{\vartheta} = \vartheta\left(1 + \frac{\tilde{k}}{kT}\right) \tag{71}$$

where λ and ν are local Lagrange multipliers. The system of equations (70)–(71) was solved numerically by using the Merson method to yield the equilibrium contour map of the pivotal plane of the bulby closure as shown in Fig. 16.

6.2. Determination of Equilibrium Configuration of Lamellar to Inverted Hexagonal Phase Transition by Monte Carlo Simulated Annealing Method

The configuration of monolayers adjacent to the central cylinder representing a nucleation line for the L_α–H_{II} phase transition is described by the radius of the central cylinder and a set of N angles, ψ_i, $i = 1, 2, \ldots, N$, describing the bulby closure and the surrounding monolayers (Fig. 16), which were divided into N sufficiently small parts. The boundary conditions were introduced to reflect connections within the different parts of the system. Due to symmetry, this unit includes a quarter of the cylinder, half of the bulby closure and one neighboring monolayer.

The minimization of the free energy of the system was performed by the Monte Carlo simulated annealing sampling strategy [53]. The method was invented by Kirkpatrick *et al.* [53] as an adaptation of the Metropolis–Hastings algorithm, which constitutes the Monte Carlo method [54]. The method is inspired by physical process of annealing in metallurgy, when the heating and subsequent slow cooling of a material is used for the increase of the crystal size in the material and thus reduces defects.

By analogy of this effect, each step of the simulated annealing algorithm moves the current solution to a sufficiently near random solution. The probability of excepting of a new solution depends on the difference in the corresponding function values and a global parameter T (temperature), which is decreasing during the process under a cooling schedule. For high values of temperature the randomness of the choice is considerable, thus the solution can jump out from local minima. With decreasing of temperature the probability for acceptance of a solution corresponding to higher energy is decreased, hence the solution is smoothed in a low temperature mode.

Within this approach, it is assumed that any local minimum is accessible from any other minimum after a finite number of random sampling steps [54]. In contrast to the conventional Metropolis Monte Carlo method, all values of angles ψ together with the radius of the central cylinder r were updated in each step [53]. After each step, the total free energy of the system was evaluated by the Metropolis criterion [54] and compared with the free energy of the previously accepted state. To find the global minimum in the multivariational space, the simulation was started at sufficiently high temperature according to the Metropolis criterion, while according to the cooling schedule the temperature was decreased after each step until it reached the zero value.

The initial configuration of the system composed of the contour shape of the bulby closure was determined by solving the Euler–Lagrange equations, the radius of the central cylinder was determined by the maximal value of z coordinate of this bulby closure, and two adjacent flat monolayers sandwiching the bulby closure and the cylinder were taken as a first approximation in the procedure of the energy minimization by the Monte Carlo simulation annealing method. This choice of the initial configuration considerably increased the speed of the time-consuming Monte Carlo simulated annealing method.

6.3. Results: Equilibrium Configuration of Nucleation of the Lamellar to Inverted Hexagonal Phase Transition

Solving the equilibrium configuration of the system with an inverted cylinder surrounded by two monolayers and two bulby closures yielded results depicted in Figs. 17 and 18.

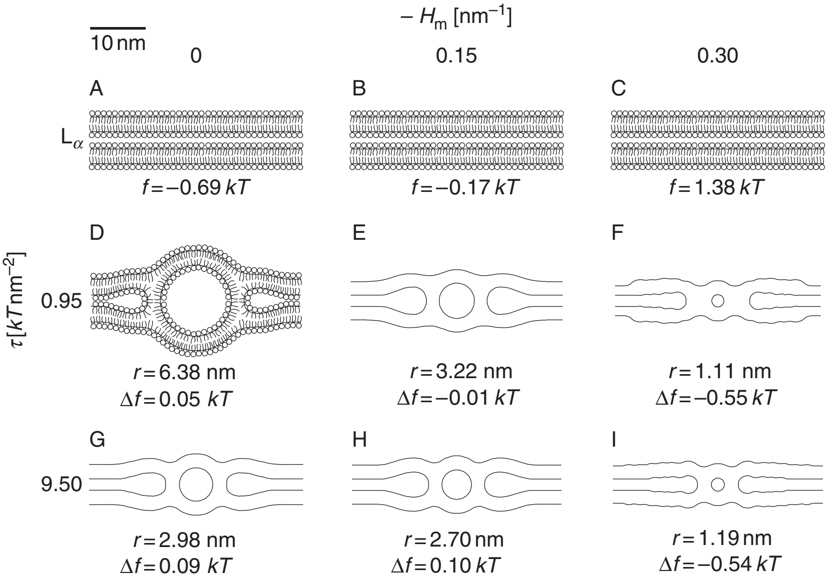

Figure 17 Configuration of the system of two monolayers, a first cylinder of H_{II} phase and two bulby closures representing a nucleation line in the L_α–H_{II} transition for different intrinsic curvature H_m and different stretching moduli of the phospholipid chains τ. We assume that phospholipid molecules are anisotropic corresponding to $D_m = |H_m|$. The free energy per lipid molecule and the radius of the central cylinder are given for each configuration. Adapted from Ref. [29].

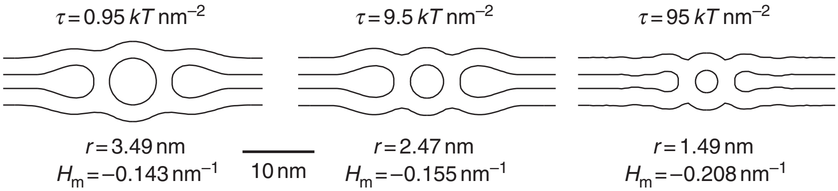

Figure 18 Nucleation configurations for different values of stretching modulus of phospholipid tails (τ) at transition point from L_α to H_{II} phase where $\Delta f = 0$. Anisotropic case ($D_m = |H_m|$). Adapted from Ref. [29].

In Fig. 17, snapshots of the equilibrium configurations for anisotropic phospholipids (setting $D_m = |H_m|$) and different values of model parameters are displayed. The top row presents the L_α phase with values of the free energy per lipid molecule of the pure L_α phase. The next two rows show the equilibrium configuration of the system with the first cylinder of the H_{II} phase embedded between two monolayers. The energy of these structures is described by energy difference $\Delta f = f_{\mathrm{H_{II}}} - f_{\mathrm{L}_\alpha}$, where $f_{\mathrm{H_{II}}}$ is the energy per lipid molecule in the hexagonal phase and f_{L_α} is the energy per lipid molecule in the lamellar phase at given values of model constants. From top to bottom, the stretching modulus of the phospholipids is increased: τ = (0.95 and 9.5) kT nm^{-2}. From left to right the lipid intrinsic mean curvature $|H_\mathrm{m}| = 0$ is increased: $|H_\mathrm{m}| = (0, 0.15, 0.3)$ nm^{-1}.

It can be seen in Fig. 17 that the inverted hexagonal phase ($\mathrm{H_{II}}$) configuration is energetically more favorable than the pure lamellar L_α phase at sufficiently high values of the mean intrinsic curvature $|H_\mathrm{m}|$. In the model increase of the temperature is simulated by increasing of $|H_\mathrm{m}|$. For higher values of the mean intrinsic curvature $|H_\mathrm{m}|$, the energy difference Δf decreases, thereby the configuration with the cylinder is favored. This phenomenon is in accordance with experimental results showing that the formation of the $\mathrm{H_{II}}$ phase is promoted with increasing temperature [28].

It is evident from Fig. 17 that the radius of the cylinder r decreases with increasing stretching modulus of the phospholipid chains τ and increasing $|H_\mathrm{m}|$ which is in agreement with the results presented in Fig. 14. Creation of a cylinder in the lamellar phase becomes less disturbing for adjacent lipid layers when the radius of the cylinder r is decreased enough.

For high enough values of τ there is a negligible effect of H_m on the equilibrium radius of the central cylinder r because the stretching modulus τ plays a considerable role in the energy balance and also because the contact energy is much higher than the bending energy. On the other hand small τ means a low contact energy that cannot compete with the bending energy. Consequently, the radius of the central cylinder r approaches $r_\mathrm{m} = 1/H_\mathrm{m}$.

The transition from the L_α to $\mathrm{H_{II}}$ phase in the nucleation model occurs at the energy difference $\Delta f = 0$, that is, when the energy of $\mathrm{H_{II}}$ phase is equal to energy of L_α phase for $|H_\mathrm{m}| = D_\mathrm{m}$, (Fig. 18). By comparison of three different configurations of $\mathrm{H_{II}}$ phase nucleation corresponding to different phospholipid chain stiffness, one can see that for low τ the L_α–$\mathrm{H_{II}}$ transition takes place for smaller $|H_\mathrm{m}|$ and the predicted radius of initial cylinder does not have a realistic value ($r = 3.49$ nm), that is, it is much larger than the experimental values [28, 34]. However, for larger values of τ the calculated r corresponds to experimental values much better. At $|H_\mathrm{m}| = 0.155$ nm^{-1} the nucleation cylinder radius is 2.47 nm, which agrees well with data obtained from X-ray experiments [28, 49]. As the decrease of the free energy with increasing $|H_\mathrm{m}|$ is more pronounced in the pure hexagonal phase (Fig. 13) than in the nucleation configuration (Fig. 18), the values of τ around $9.5kT$ nm^{-2} would lead to the stabilization of the $\mathrm{H_{II}}$ phase at higher temperatures. For large τ (e.g., $\tau = 95kT$ nm^{-2}), the predicted nucleation transition is again less realistic due to the too small value of $r = 1.49$ nm.

7. DISCUSSION AND CONCLUSIONS

The stability of the inverted hexagonal phase depends on energy balance between different contributions to the system free energy, hence the main problem in theoretical description of the lamellar to inverted hexagonal phase transition and explanation of the stability of the H_{II} lipid phase consists in finding the proper expression for the free energy of the system. Most of contemporary theoretical models of the free energy of the inverted hexagonal phase have shown that in addition to the bending energy term, it is necessary to consider also the energy term, which depends on the dimension of the "voids" in the hexagonal lattice, the so-called interstitial energy [24, 31]. We followed this assumption and took into account the interstitial energy which in our model is expressed by the stretching energy of phospholipid chains.

In our theoretical analysis we did not take into account the dependence of the chain stretching modulus τ on the temperature [55], which is based on the elasticity of lipid chains. We expect that neglecting the temperature dependency of τ predicts that the slope of the energy dependence of $|H_m|$ is less pronounced (Fig. 13). Another simplification introduced in our theoretical model is the assumption of spherical cross sections of lipid tubes in the H_{II} phase. The nonspherical cross section of lipid tubes would probably lower the stretching energy of phospholipid chains, but would also contribute to higher bending of the monolayer. To include the deviations from sphericity in our computations will be one of our future tasks in theoretical description of stability of nonplanar lipid phases.

In conclusion, our results indicate that the deviatoric bending can explain the stability of the H_{II} phase at higher temperatures. However, for the L_α–H_{II} transition, tuning of the deviatoric bending energy by the isotropic bending energy and the interstitial energy is needed. Models based on the isotropic elasticity described the L_α–H_{II} phase transition by showing that at a certain temperature, the free energy of the system is lowered as it converts from the L_α phase to the H_{II} phase [56]. However, the energy difference was found to be lower than $0.1kT$ [24]. Our results pursue the general conclusions of the previous models; however, the obtained energy difference becomes much larger at elevated temperatures if the average orientational ordering of anisotropic lipid molecules on highly curved surfaces of the H_{II} phase is taken into account (i.e., if anisotropic elasticity of lipid monolayer is considered). This energy difference is sufficient for the stability of a single cylinder within the lamellar stack and therefore supports previously suggested nucleation models, which are based on LDs [28, 34, 57, 58].

In spite of many simplifications introduced in our theoretical description, results of our modeling and simulations are in good agreement with experimental results [28, 34, 59, 60]. Among others we have shown that with increasing absolute values of intrinsic curvatures of lipid molecules C_{1m} and C_{2m} (which were assumed to increase with increasing temperature), the L_α–H_{II} phase transition occurs beyond a certain threshold temperature. Further we could also reproduce realistic structures in good agreement with experimental results. Our results thus show that deviatoric bending plays an important role in the stability of the inverted hexagonal phase and in the L_α–H_{II} phase transition. It should be stressed at the end that considering the deviatoric bending of lipid monolayer [15, 21, 29, 45, 46] does not assume lattice-like packing of anisotropic lipids with fixed orientation and fixed position but just takes into account the possibility of decrease of the free energy of lipid monolayer (bilayer) due to average orientations of laterally mobile rotating anisotropic lipids.

ACKNOWLEDGMENTS

This work was supported by the bilateral Slovenian–Austrian and Austrian–Slovenian Grants BI-AT/07-08-022 and WTZ SI22/2007, respectively, bilateral Slovenian–Czech Grant BI-CZ/07-08-006, and the Grants MSM-6840770012, J3-9219-0381-06, and P2-0232-1538.

REFERENCES

[1] J.M. Seddon, R.H. Templer, Polymorphism of lipid–water systems, in: A.J. Hoff, R. Lipowsky, E. Sackmann (Eds.), Handbook of Biological Physics: Structure and Dynamics of Membranes—From Cells to Vesicles, Vol. 1A Elsevier SPC, Amsterdam, Netherlands, 1995.

[2] D. Chandler, Two faces of water, Nature 417 (2002) 491.

[3] D. Chandler, Interfaces and the driving force of hydrophobic assembly, Nature 437 (2005) 640–647.

[4] V. Luzzati, A. Tardieu, T. Gulik-Krzywicki, E. Rivas, F. Reiss-Husson, Structure of the cubic phases of lipid–water systems, Nature 220 (1968) 485–488.

[5] P.R. Cullis, M.J. Hope, C.P.S. Tilcock, Lipid polymorphism and the roles of lipids in membranes, Chem. Phys. Lipids 40 (1986) 127–144.

[6] V. Luzzati, Biological significance of lipid polymorphism: The cubic phases, Curr. Opin. Struct. Biol. 7 (1997) 661–668.

[7] K. Larsson, F. Tiberg, Periodic minimal surface structures in bicontinuous lipid–water phases and nanoparticles, Curr. Opin. Colloid Interface Sci. 9 (2005) 365–369.

[8] A. Yaghmur, P. Laggner, S. Zhang, M. Rappolt, Tuning curvature and stability of monoolein bilayers by short surfactant-like designer peptides, PLoS One 2 (2007) e479.

[9] G.S. Attard, J.C. Glyde, C.G. Goltner, Liquid crystalline phases as templates for the synthesis of mesoporous silica, Nature 378 (1995) 366–368.

[10] O.G. Mouritsen, Life—As a Matter of Fat Springer, Berlin-Heidelberg, 2005.

[11] J. Israelachvili, Intermolecular and Surface Forces Academic Press Limited, London, UK, 1997.

[12] S. Leikin, M.M. Kozlov, N.L. Fuller, R.P. Rand, Measured effects of diacylglycerol on structural and elastic properties of phospholipid membranes, Biophys. J. 71 (1996) 2623–2632.

[13] L. Mathivet, S. Cribier, P.F. Devaux, Shape change and physical properties of giant phospholipid vesicles prepared in the presence of an AC electric field, Biophys. J. 70 (1996) 1112–1121.

[14] V. Kralj-Iglič, G. Gomišček, J. Majhenc, V. Arrigler, S. Svetina, Myelin-like protrusions of giant phospholipid vesicles prepared by electroformation, Colloids Surf. A 181 (2001) 315–318.

[15] V. Kralj-Iglič, A. Iglič, G. Gomišček, F. Sevšek, V. Arrigler, H. Hägerstrand, Microtubes and nanotubes of a phospholipid bilayer membrane, J. Phys. A: Math. Gen. 35 (2002) 1533–1549.

[16] A. Iglič, H. Hägerstrand, M. Bobrowska-Hägerstrand, V. Arrigler, V. Kralj-Iglič, Possible role of phospholipid nanotubes in directed transport of membrane vesicles, Phys. Lett. A 310 (2003) 493–497.

[17] M. Bobrowska-Hägerstand, V. Kralj-Iglič, A. Iglič, K. Bialkowska, B. Isomaa, H. Hägerstrand, Torocyte membrane endovesicles induced by octaethyleneglycol dodecylether in human erythrocytes, Biophys. J. 77 (1999) 3356–3362.

[18] M. Fošnarič, M. Nemec, V. Kralj-Iglič, H. Hägerstrand, M. Schara, A. Iglič, Possible role of anisotropic membrane inclusions in stability of torocyte red blood cell daughter vesicles, Colloids Surf. B 26 (2002) 243–253.

[19] M. Kandušer, M. Fošnarič, M. Šentjurc, V. Kralj-Iglič, H. Hägerstrand, A. Iglič, D. Miklavčič, Effect of surfactant polyoxyethylene glycol (C12E8) on electroporation of cell line DC3F, Colloids Surf. A 214 (2003) 205–217.

[20] M. Fošnarič, V. Kralj-Iglič, K. Bohinc, A. Iglič, S. May, Stabilization of pores in lipid bilayers by anisotropic inclusions, J. Phys. Chem. B 107 (2003) 12519–12526.

[21] V. Kralj-Iglič, B. Babnik, D.R. Gauger, S. May, A. Iglič, Quadrupolar ordering of phospholipid molecules in narrow necks of phospholipid vesicles, J. Stat. Phys. 125 (2006) 727–752.

[22] A. Iglič, V. Kralj-Iglič, Effect of anisotropic properties of membrane constituents on stable shape of membrane bilayer structure, in: H.T. Tien, A. Ottova-Leitmannova (Eds.), Planar Lipid Bilayers (BLMs) and Their Applications Elsevier SPC, Amsterdam, Netherlands, 2003, pp. 143–172.

[23] V. Kralj-Iglič, M. Remškar, A. Iglič, Deviatoric elasticity as a mechanism describing stable shapes of nanotubes, in: A. Riemer (Ed.), Horizons in World Physics, Vol. 244, Nova Science Publishers, Hauppauge, NY, 2004, pp. 111–156.

[24] M.M. Kozlov, S. Leikin, R.P. Rand, Bending, hydration and interstitial energies quantitatively account for the hexagonal–lamellar–hexagonal reentrant phase transition in dioleoylphosphatidylethanolamine, Biophys. J. 67 (1994) 1603–1611.

[25] M. Rappolt, The biologically relevant lipid mesophases as "seen" by X-rays, Adv. Planar Lipid Bilayer and Liposomes 5 (2006) 253–283.

[26] S. Hyde, S. Anderson, K. Larsson, Z. Blum, T. Landth, S. Lidin, B.W. Ninham, The Language of Shape Elsevier, Amsterdam, 1997.

[27] J.M. Corless, M.J. Costello, Paracrystalline inclusions associated with the disk membranes of frog retinal rod outer segments, Exp. Eye Res. 32 (1981) 217–228.

[28] M. Rappolt, A. Hickel, F. Bringezu, K. Lohner, Mechanism of the lamellar/inverse hexagonal phase transition examined by high resolution X-ray diffraction, Biophys. J. 84 (2003) 3111–3122.

[29] T. Mareš, M. Daniel, Š. Perutkova, A. Perne, G. Dolinar, A. Iglič, M. Rappolt, V. Kralj-Iglič, Role of phospholipid asymmetry in the stability of inverted hexagonal mesoscopic phases, J. Phys. Chem. B. 8 (2008) 16575–16584.

[30] D.P. Siegel, Inverted micellar intermediates and the transitions between lamellar, cubic, and inverted hexagonal lipid phases, Biophys. J. 49 (1988) 1155–1170.

[31] V.S. Malinin, B.R. Lentz, On the analysis of elastic deformation in hexagonal phases, Biophys. J. 86 (2004) 3324–3328.

[32] D.P. Siegel, The modified stalk mechanism of lamellar/inverted phase transitions and its implications for membrane fusion, Biophys. J. 76 (1999) 291–313.

[33] D.C. Turner, S.M. Gruner, X-ray diffraction reconstruction of the inverted hexagonal (H_{II}) phase in lipid–water systems, Biophys. J. 31 (1992) 1340–1355.

[34] M. Rappolt, A. Hodzic, B. Sartori, M. Ollivon, P. Laggner, Conformational and hydrational properties during the L_β- to L_α- and L_α- to H_{II}-phase transition in phosphatidylethanolamine, Chem. Phys. Lipids 154 (2008) 46–55.

[35] B. Kachar, T.S. Reese, Evidence for the lipidic nature of tight junction strands, Nature 296 (1982) 464–466.

[36] S.W. Hui, T.P. Stewart, L.T. Boni, The nature of lipidic particles and their roles in polymorphic transitions, Chem. Phys. Lipids 33 (1983) 113–116.

[37] W. Helfrich, Elastic properties of lipid bilayers: Theory and possible experiments, Z. Naturforsch. C 28 (1973) 693–703.

[38] R.P. Rand, N.L. Fuller, S.M. Gruner, V.A. Parsegian, Membrane curvature, lipid segregation, and structural transitions for phospholipids under dual-solvent stress, Biochemistry 29 (1990) 76–87.

[39] D.P. Siegel, Energetics of intermediates in membrane fusion: Comparison of stalk and inverted micellar intermediate mechanisms, Biophys. J. 65 (1993) 2124–2140.

[40] M. Hamm, M.M. Kozlov, Tilt model of inverted amphiphilic mesophases, Eur. Phys. J. B 6 (1998) 519–528.

[41] J.B. Fournier, Nontopological saddle-splay and curvature instabilities from anisotropic membrane inclusions, Phys. Rev. Lett. 76 (1996) 4436–4439.

[42] V. Kralj-Iglič, V. Heinrich, S. Svetina, B. Žekš, Free energy of closed membrane with anisotropic inclusions, Eur. Phys. J. B 10 (1999) 5–8.

[43] L.D. Landau, E.M. Lifshitz, Theory of Elasticity Reed Educational and Professional Publishing Ltd., Oxford, UK, 1986.

[44] P.B. Canham, The minimum energy of bending as a possible explanation of the biconcave shape of the human red blood cell, J. Theor. Biol. 26 (1970) 61–81.

[45] T. Fischer, Bending stiffness of lipid bilayers. 3. Gaussian curvature, J. Phys. II (France) 2 (1992) 337–343.

[46] T. Fischer, Bending stiffness of lipid bilayers. V. Comparison of two formulations, J. Phys. II (France) 3 (1993) 1795–1805.

[47] T.L. Hill, An Introduction to Statistical Thermodynamics General Publishing Company, Toronto, Canada, 1986, pp. 209–211.

[48] S. May, A molecular model for the line tension of lipid membranes, Eur. Phys. J. E 3 (2000) 37–44.

[49] P. Laggner, M. Kriechbaum, G. Rapp, Structural intermediates in phospholipid phase transitions, J. Appl. Crystal. 24 (1991) 836–842.

[50] J.M. Seddon, J. Robins, T. Gulik-Krzywicki, H. Delacroix, Inverse micellar phases of phospholipids and glycolipids, Phys. Chem. Chem. Phys. 2 (2000) 4485–4493.

[51] H. Delacroix, T. Gulik-Krzywicki, M. Seddon, Freeze fracture electron microscopy of lyotropic lipid systems: Quantitative analysis of the inverse micellar cubic phase of space group *Fd*3*m* ($Q^2$27), J. Mol. Biol. 258 (1996) 88–103.

[52] M.A. Churchward, T. Rogasevskaia, D.M. Brandman, H. Khosravani, P. Nava, J.K. Atkinson, J.R. Coorssen, Specific lipids supply critical negative spontaneous curvature—An essential component of native Ca^{2+}-triggered membrane fusion, Biophys. J. 94 (2008) 3976–3986.

[53] S. Kirkpatrick, C.D. Gelatt, M.P. Vecchi, Optimalization by simulated annealing, Science, New Series 220 (1983) 671–680.

[54] N. Metropolis, A.W. Rosenbluth, M.N. Rosenbluth, A.H. Teller, E.J. Teller, Equations of state calculations by fast computing machines, Chem. Phys. 21 (1953) 1087–1092.

[55] D. Boal, Mechanics of the Cell Cambridge University Press, New York, Cambridge, UK, 2002.

[56] G. Kirk, S.M. Gruner, D.L. Stein, A thermodynamic model of the lamellar to inverse hexagonal phase transition of lipid membrane–water systems, Biochemistry 23 (1984) 1093–1102.

[57] D.P. Siegel, Inverted micellar intermediates and the transitions between lamellar, cubic, and inverted hexagonal lipid phases. II. Implications for membrane-membrane interactions and membrane fusion, Biophys. J. 49 (1986) 1171–1183.

[58] S.J. Marrink, A.E. Mark, Molecular view of hexagonal phase formation in phospholipid membranes, Biophys. J. 87 (2004) 3894–3900.

[59] P.E. Harper, D.A. Mannock, R.N.A.H. Lewis, R.N. McElhaney, S.M. Gruner, X-ray diffraction structures of some phosphatidylethanolamine lamellar and inverted hexagonal phases, Biophys. J. 81 (2001) 2693–2706.

[60] G.E.S. Toombes, A.C. Finnefrock, M.W. Tate, S.M. Gruner, Determination of L_α–H_{II} phase transition temperature for 1,2-dioleoyl-*sn*-glycero-3-phosphatidylethanolamine, Biophys. J. 82 (2002) 2504–2510.

CHAPTER TEN

ATTRACTION OF LIKE-CHARGED SURFACES MEDIATED BY SPHEROIDAL NANOPARTICLES WITH SPATIALLY DISTRIBUTED ELECTRIC CHARGE: THEORY AND SIMULATION

Klemen Bohinc,[1,2] Jasna Zelko,[3] P.B. Sunil Kumar,[4]
Aleš Iglič,[2,*] *and* Veronika Kralj-Iglič[3]

Contents

Abstract

The interaction between equal, uniformly charged flat surfaces, separated by a solution of spheroidal nanoparticles was studied theoretically. The nanoparticles were assumed to have spatially distributed electric charge. The nonlocal Poisson–Boltzmann (PB) theory for the spheroidal nanoparticles, which play the role of counterions, was developed. In the model the center of the spheroidal nanoparticle could not approach the charged surfaces closer than the radius of the nanoparticle. It was shown that for large enough diameters of nanoparticles

---

* Corresponding author. Tel.: +386 31 356 953; Fax: +386 1 4768 850;
E-mail address: ales.iglic@fe.uni-lj.si

[1] Laboratory of Physics, Faculty of Electrical Engineering, University of Ljubljana, Slovenia
[2] Faculty of Health Studies, University of Ljubljana, Slovenia
[3] Laboratory of Clinical Biophysics, Faculty of Medicine, University of Ljubljana, Slovenia
[4] Department of Physics, Indian Institute of Technology Madras, Chennai, India

Advances in Planar Lipid Bilayers and Liposomes, Volume 9
ISSN 1554-4516, DOI: 10.1016/S1554-4516(09)09010-3

and large enough surface charge densities of membrane surfaces, the two equally charged surfaces could experience an attractive force due to the spatially distributed charges within the nanoparticles. The results presented in this chapter may add to a better understanding of the coalescence of negatively charged membrane surfaces induced by positively charged nanoparticles (e.g., proteins) which are proposed to play an important role in the complex vital processes such as blood clot formation.

1. INTRODUCTION

The outer surface of biological membranes is usually negatively charged [1]. For example, blood involves negatively charged red blood cells [2, 3]. Also the outer membrane surface of the membrane microvesicles released from red blood cells, platelets, and lymphocytes, as well as from apoptotic cells (with negatively charged cardiolipin and phosphatidylserine in the outer membrane layer) are negatively charged [4–8].

Clinical evidence indicates that microvesicles are prothrombogenic, as they form catalytic surfaces for reactions of blood clot formation. A mechanism which could be relevant in microvesiculation is the coalescence of negatively charged membraneous structures mediated by multivalent ions [9–11]. Possible candidates for such multivalent polyions could be various membrane proteins, including antibodies [9–12] and also artificial nanoparticles (entering the body from the environment). Spheroidal multivalent ions (nanoparticles) may thus play an important role in the formation of blood clots.

The phenomena of ion-mediated attractive interaction between two equally charged surfaces has been observed previously in many other cases as well. The first experimental observation of attraction between two highly negatively charged clays was reported for $CaCl_2$ solution [13, 14]. Attraction between charged lamellae [15], DNA condensation [16–18], network formation in actin solutions [19], complexation of DNA with positively charged colloidal particles [20], and virus aggregation [21] have also been observed. However, origins of these attractive interactions are still not fully understood.

Theory of equally charged surfaces separated by a solution containing dimensionless ions in the mean field approach yields electrostatic repulsion [22–25]. However, it was indicated recently that large multivalent ions in solution between two equally charged surfaces can induce at close distances, also an attractive force between these two surfaces [26, 27]. Monte Carlo simulations showed the existence of attractive interaction between equally charged surfaces immersed in a solution composed of multivalent ions in the limit of high surface charge densities [28–31]. Therefore, different improvements with respect to Poisson–Boltzmann (PB) theory were suggested in order to explain the observed attraction between like-charged surfaces. Among others, direct ion–ion interactions were considered as a possible explanation for attractive interaction within hypernetted chain theory

[32–35], density functional theories [36–39], and by taking into account in-plane Gaussian fluctuations [40–42].

New fields of research interest that were opened in past decade offer new possibilities for the application of modified PB theories, especially in the study of polyelectrolyte solutions [43, 44] and of protein–membrane interactions [45–48]. In such systems, charge distribution along the polyelectrolyte chain or within the protein is essential to explain the attraction between two like-charged membranes. Bridging mechanism, where polyions are oriented in such a way that they electrostatically bind together the neighboring equally charged surfaces, was proposed in the case of polyelectrolyte-induced attraction between two charged surfaces [43, 44, 49]. Electrostatic interactions may also play a crucial role in interaction of proteins with the membrane. It was suggested that charge distribution within a protein influences the orientation of the protein at the membrane surface [50].

The importance of finite ion size [51–54] and charge distribution [55] in polyions for their solvation and double layer effects has been considered previously. If spheroidal multivalent nanoparticles have an internal charge distribution with charges being located at different, well-separated positions [56], the classical PB description of the electric double layer fails to describe the experimentally obtained spatial distribution and orientation of the multivalent nanoparticles [57]. A generalization of the PB theory of the electric double layer for the case of multivalent nanoparticles could be made by taking into account the internal space charge distribution of a single spheroidal multivalent nanoparticle [58]. Theoretical description of such large multivalent spheroidal nanoparticles in between two planar charged surfaces that takes into account the internal charge distribution was proposed recently [56], using a simple three-state model for the orientation of the multivalent ions in the gradient of the electric field and applying the methods of statistical physics. It was assumed that the distance between the electric charges within a single multivalent nanoparticle is small enough to justify the Taylor series expansion [58] in calculation of the electrostatic energy of a single spheroidal multivalent nanoparticle in the electric field gradient [56]. The orientational ordering of the multivalent nanoparticles near the charged membrane surface was predicted [56]. However, within this model the internal space charge distribution was taken into account only in the entropic part of the free energy.

In this work we present a theoretical model with an improved description of the effect of the spatial charge distribution within the spheroidal nanoparticle on the electric field and the free energy of the system. In our case the two charges are placed oppositely on a surface of the spherical nanoparticle; however, the theory presented can be generalized to include any separation between charges within the spherical nanoparticle. The distance of closest approach of the spherical nanoparticles to the charged surface was taken into account [59] while the direct particle–particle hard core interactions were not taken into account.

2. THEORETICAL MODEL

We consider an aqueous solution containing spheroidal (Fig. 1) multivalent nanoparticles, which are positively charged and have a diameter a. In the model the electric charge of each spheroidal nanoparticle is described by two equal charges $e = Ze_0$, separated by an arbitrary distance l, where Z is the valency and e_0 the elementary charge. The solution is sandwiched between two large, planar surfaces of area A (Fig. 2), each carrying a uniform negative surface charge density σ. The distance between the two surfaces is D. For the sake of simplicity we take $l = a$. The volume of the spheroidal nanoparticle is given by $v_0 = (4\pi/3)(a/2)^3$. The electrostatic field between the two charged surfaces varies only in the direction normal to the surfaces (x-direction). We assume that there is no electric field on the other side of each charged plate.

For each spheroidal nanoparticle, the center of the charge distribution (also its geometric center) is located at x. The two point charges are located at geometrically opposite points separated by a distance l. When projected onto the x-axis, their positions are at $x + s$ and $x - s$ respectively, as shown in Fig. 2. We describe the spheroidal nanoparticles by the local concentration of nanoparticles $n(x)$. Furthermore, we refer to one of the charges of the nanoparticle as the reference charge. The location of the reference charge of a given spheroidal nanoparticle is specified by the conditional probability $p(s|x)$, x denoting the location of the center of the nanoparticle. The probability density $p(s|x)$ satisfies the relation

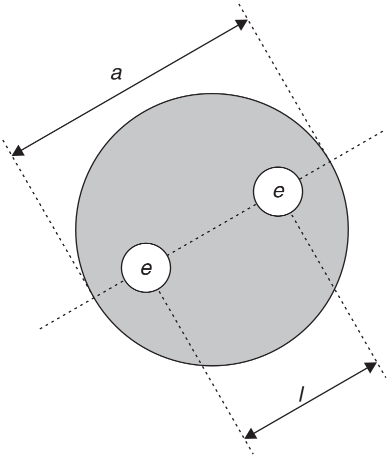

Figure 1 Schematic diagram of a large spheroidal multivalent nanoparticle with net electric charge $2e$ and average diameter a. In the model the space charge distribution of the multivalent nanoparticle is described by two effective polyions of charge e located at different, well-separated positions $l \leq a$. The main axis of the nanoparticle coincides with the line connecting the two polyions.

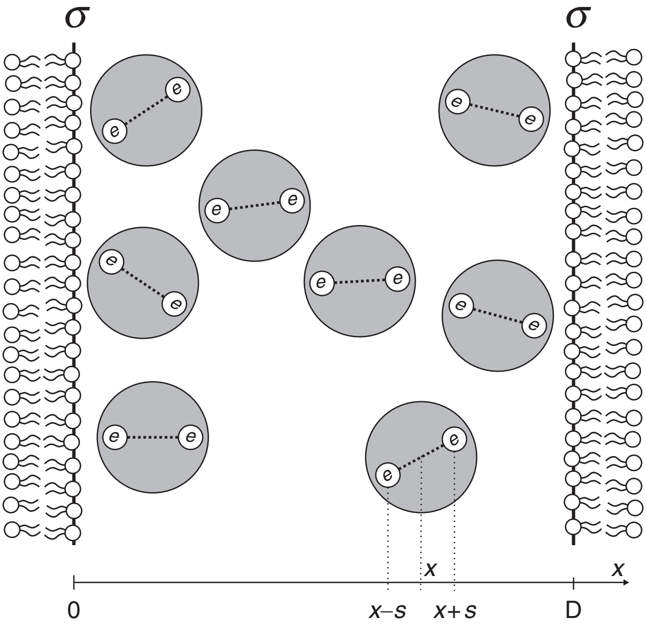

Figure 2 Schematic illustration of two like-charged planar cell surfaces of surface charge density σ, interacting in a solution that contains multivalent spheroidal nanoparticles. The coordinate x specifies the center of the spheroidal nanoparticle while the coordinates $x - s$ and $x + s$ specify the positions of two charges in a spheroidal nanoparticles. The distance between the planar surfaces is D.

$$\frac{1}{l}\int_{-l/2}^{l/2} p(s|x)\mathrm{d}s = 1 \tag{1}$$

and $p(s|x) = 0$ for any x and $|s| > l/2$.

The electrostatic free energy of the system F measured per unit area A and expressed in units of the thermal energy kT (here k is the Boltzmann constant and T is the absolute temperature) can be expressed as

$$\begin{aligned}\frac{F}{AkT} = \int_{-\infty}^{\infty} \mathrm{d}x \Bigg[\frac{\Psi'(x)^2}{8\pi l_\mathrm{B}} + n(x)\ln n(x)\nu_0 + \frac{1}{\nu_0}(1 - n(x)\nu_0). \\ \ln(1 - n(x)\nu_0) + n(x)\langle p(s|x)[\ln p(s|x) + U(x)]\rangle \Bigg]\end{aligned} \tag{2}$$

where the first term is the electrostatic energy, the second and the third terms are contributions to the positional entropy including the excluded volume effect and the fourth term is the orientational entropy. The reduced electrostatic potential is denoted by Ψ where $l_\mathrm{B} = \frac{e_0^2}{4\pi\varepsilon\varepsilon_0 kT}$ is the Bjerrum length, ε is the dielectric constant of the solution and ε_0 is the permittivity of the vacuum. The average of an arbitrary function $g(s)$ is defined as

$$\langle g(s)\rangle = \frac{1}{l}\int_{-l/2}^{l/2} g(s)\mathrm{d}s \tag{3}$$

while the function

$$U(x) = \begin{cases} 0, & \frac{l}{2} \leq x \leq D - \frac{l}{2} \\ \infty, & \text{elsewhere} \end{cases} \tag{4}$$

is introduced in order to ensure that the spheroidal nanoparticles are confined within the region specified by the charged walls.

Equation (2) can be written in the following form:

$$\begin{aligned} \frac{F}{AkT} = \int_{-\infty}^{\infty} \mathrm{d}x \Bigg[& \frac{\Psi'(x)^2}{8\pi l_\mathrm{B}} + n(x)\ln n(x)v_0 - n(x) \\ & + \gamma\left[\frac{1}{v_0}(1 - n(x)v_0)\ln(1 - n(x)v_0) + n(x)\right] \\ & + n(x)\langle p(s|x)[\ln p(s|x) + U(x)]\rangle \Bigg] \end{aligned} \tag{5}$$

where we introduce parameter γ as

$$\gamma = \begin{cases} 0, & \text{excluded volume not taken into acount} \\ 1, & \text{excluded volume taken into acount} \end{cases} \tag{6}$$

The equilibrium state of the system is determined by the minimum of the total free energy F, subject to the constraints that (1) the orientational probability of the spheroidal nanoparticles, integrated over all possible projections (Eq. (1)), is equal to 1 and that (2) the system is electroneutral $\left(2Z\int_{-\infty}^{\infty} n(x)\mathrm{d}x = 2\sigma/e_0\right)$. To solve this variational problem, a functional $\int_{-\infty}^{\infty}\mathcal{F}\mathrm{d}x$ is constructed:

$$\begin{aligned} \textstyle\int_{-\infty}^{\infty}\mathcal{F}\mathrm{d}x = \frac{F}{AkT} + \int_{-\infty}^{\infty} \lambda(x)n(x)\left(\frac{1}{l}\int_{-l/2}^{l/2} p(s|x)\mathrm{d}s - 1\right)\mathrm{d}x \\ + \mu\textstyle\int_{-\infty}^{\infty}\left[2Zn(x) - \frac{2\sigma}{e_0 D}\right]\mathrm{d}x \end{aligned} \tag{7}$$

where $\lambda(x)$ and μ are the local and global Lagrange multipliers, respectively. By taking into account Eq. (5), we can rewrite Eq. (7) in the form

$$\begin{aligned}\int_{-\infty}^{\infty}\mathcal{F}\,\mathrm{d}x = \int_{-\infty}^{\infty}\mathrm{d}x\Bigg[&\frac{\Psi'(x)^2}{8\pi l_\mathrm{B}} + n(x)\ln(n(x)v_0)\\ &- n(x) + \gamma\left[\frac{1}{v_0}(1-n(x)v_0)\ln(1-n(x)v_0) + n(x)\right]\\ &+ n(x)\langle p(s|x)[\ln p(s|x) + U(x)]\rangle\Bigg]\\ &+ \int_{-\infty}^{\infty}\mathrm{d}x\; n(x)\lambda(x)[\langle p(s|x)\rangle - 1]\\ &+ \mu\int_{-\infty}^{\infty}\left[2Zn(x) - \frac{2\sigma}{e_0 D}\right]\mathrm{d}x\end{aligned} \tag{8}$$

In equilibrium,

$$\delta\int_{-\infty}^{\infty}\mathcal{F}\,\mathrm{d}x = 0 \tag{9}$$

Using expression (8) we can perform the first variation of F as follows:

$$\begin{aligned}\delta\mathcal{F} = \delta&\left(\frac{1}{8\pi l_\mathrm{B}}\int_{-\infty}^{\infty}\Psi'^2\mathrm{d}x\right)\\ &+ \textstyle\int_{-\infty}^{\infty}\mathrm{d}x\;\delta n(x)[\ln(n(x)v_0) - \gamma\,\ln(1-n(x)v_0)]\\ &+ \textstyle\int_{-\infty}^{\infty}\mathrm{d}x\;\delta n(x)\langle p(s|x)[\ln p(s|x) + U(x)]\rangle\\ &+ \textstyle\int_{-\infty}^{\infty}\mathrm{d}x\;\delta n(x)\{\lambda(x)(\langle p(s|x)\rangle - 1) + 2Z\mu\}\\ &+ \textstyle\int_{-\infty}^{\infty}\mathrm{d}x\;\langle\delta p(s|x)n(x)[\ln p(s|x) + 1 + U(x) + \lambda(x)]\rangle\end{aligned} \tag{10}$$

We shall first perform the variation of the electrostatic energy (see the first term in Eq. (10)):

$$\delta\left(\frac{1}{8\pi l_\mathrm{B}}\int_{-\infty}^{\infty}\Psi'^2\mathrm{d}x\right) = \frac{1}{4\pi l_\mathrm{B}}\int_{-\infty}^{\infty}\Psi'\delta\Psi'\mathrm{d}x \tag{11}$$

Using per-partes integration the last term can be transformed into

$$\int_{-\infty}^{\infty} \Psi' \delta\Psi' \mathrm{d}x = \int_{-\infty}^{\infty} (\Psi\delta\Psi')' \mathrm{d}x - \int_{-\infty}^{\infty} \Psi\delta\Psi'' \mathrm{d}x \tag{12}$$

The first integral on the right side of Eq. (12) can be rewritten as

$$\int_{-\infty}^{\infty} (\Psi\delta\Psi')' \mathrm{d}x = \int_{-\infty}^{\infty} \mathrm{d}(\Psi\delta\Psi') = \Psi\delta\Psi'|_0^D \tag{13}$$

The surfaces at $x = 0$ and $x = D$ are uniformly charged, the variation of the first derivative of the potential at both charged surfaces is zero ($\delta\Psi'|_{x=0} = 0$ and $\delta\Psi'|_{x=D} = 0$) and the first integral on the right hand side of Eq. (12) is zero. Thus, Eq. (12) becomes

$$\int_{-\infty}^{\infty} \Psi' \delta\Psi' \mathrm{d}x = -\int_{-\infty}^{\infty} \Psi\delta\Psi'' \mathrm{d}x \tag{14}$$

We insert the Poisson equation

$$\Psi''(x) = -\varrho(x)\frac{4\pi l_\mathrm{B}}{e_0} \tag{15}$$

into Eq. (12) and get

$$\delta\left(\frac{1}{8\pi l_\mathrm{B}} \int_{-\infty}^{\infty} \Psi'^2 \mathrm{d}x\right) = \int_{-\infty}^{\infty} \Psi(x)\delta\left(\frac{\varrho(x)}{e_0}\right)\mathrm{d}x \tag{16}$$

where $\varrho(x)$ is the volume charge density.

Using the above derived relation (16) we can rewrite Eq. (10) as

$$\begin{aligned}
\delta\mathcal{F} = &\textstyle\int_{-\infty}^{\infty} \Psi(x)\delta\left(\frac{\varrho(x)}{e_0}\right)\mathrm{d}x \\
&+ \textstyle\int_{-\infty}^{\infty} \mathrm{d}x\ \delta n(x)[\ln(n(x)v_0) - \gamma\ln(1 - n(x)v_0)] \\
&+ \textstyle\int_{-\infty}^{\infty} \mathrm{d}x\ \delta n(x)\langle p(s|x)[\ln p(s|x) + U(x)]\rangle \\
&+ \textstyle\int_{-\infty}^{\infty} \mathrm{d}x\ \delta n(x)\{\lambda(x)(\langle p(s|x)\rangle - 1) + 2Z\mu\} \\
&+ \textstyle\int_{-\infty}^{\infty} \mathrm{d}x\langle \delta p(s|x) n(x)[\ln p(s|x) + 1 + U(x) + \lambda(x)]\rangle
\end{aligned} \tag{17}$$

The volume charge density is determined by both charges of spheroidal nanoparticle:

$$\frac{\rho(x)}{Ze_0} = \langle n(x-s)p(s|x-s) + n(x+s)p(s|x+s)\rangle \tag{18}$$

The first variation of the volume charge density $\delta\varrho(x)$ is

$$\begin{aligned}\frac{\delta\rho(x)}{Ze_0} &= \langle \delta n(x-s)p(s|x-s) + n(x-s)\delta p(s|x-s)\rangle \\ &\quad + \langle \delta n(x+s)p(s|x+s) + n(x+s)\delta p(s|x+s)\rangle\end{aligned} \tag{19}$$

Inserting Eq. (19) into the first term of variation $\int_{-\infty}^{\infty}\Psi(x)\delta(\varrho(x)/e_0)\mathrm{d}x$ we get

$$\begin{aligned}&\int_{-\infty}^{\infty}\Psi(x)\delta\left(\frac{\varrho(x)}{e_0}\right)\mathrm{d}x \\ &= \int_{-\infty}^{\infty}\langle\Psi(x)Z[\delta n(x-s)p(s|x-s)+\delta n(x+s)p(s|x+s)]\rangle\mathrm{d}x \\ &\quad + \int_{-\infty}^{\infty}\langle\Psi(x)Z[n(x-s)\delta p(s|x-s)+n(x+s)\delta p(s|x+s)\mathrm{d}]\rangle x\end{aligned} \tag{20}$$

By introducing the new variables $\bar{x} = x + s$ and $\tilde{x} = x - s$, Eq. (20) can be rewritten as

$$\begin{aligned}&\int_{-\infty}^{\infty}\Psi(x)\delta\left(\frac{\varrho(x)}{e_0}\right)\mathrm{d}x \\ &= \int_{-\infty}^{\infty}\langle\delta n(x)p(s|x)[Z\Psi(x+s) + Z\Psi(x-s)]\rangle\mathrm{d}x \\ &\quad + \int_{-\infty}^{\infty}\langle n(x)\delta p(s|x)[Z\Psi(x+s) + Z\Psi(x-s)]\rangle\mathrm{d}x\end{aligned} \tag{21}$$

If we insert Eq. (21) into Eq. (17) we get

$$\begin{aligned}\delta F = &\int_{-\infty}^{\infty}\langle\delta n(x)p(s|x)[Z\Psi(x+s) + Z\Psi(x-s)]\rangle\mathrm{d}x \\ &+ \int_{-\infty}^{\infty}\langle n(x)\delta p(s|x)[Z\Psi(x+s) + Z\Psi(x-s)]\rangle\mathrm{d}x \\ &+ \int_{-\infty}^{\infty}\mathrm{d}x\delta n(x)[\ln n(x)v_0 - \gamma\ln(1 - n(x)v_0)] \\ &+ \int_{-\infty}^{\infty}\mathrm{d}x\delta n(x)\langle p(s|x)[\ln p(s|x) + U(x)]\rangle \\ &+ \int_{-\infty}^{\infty}\mathrm{d}x\delta n(x)\{\lambda(x)(\langle p(s|x)\rangle - 1) + 2Z\mu\} \\ &+ \int_{-\infty}^{\infty}\mathrm{d}x\langle\delta p(s|x)n(x)[\ln p(s|x) + 1 + U(x) + \lambda(x)]\rangle\end{aligned} \tag{22}$$

Equation (9) has to be fulfilled for variations $\delta p(s|x)$ and $\delta n(x)$. This means that the expressions multiplied by $\delta p(s|x)$ and $\delta n(x)$ in Eq. (22) have to be zero. First, we consider the term multiplied by $\delta p(s|x)$:

$$\ln p(s|x) + 1 + U(x) + \lambda(x) + Z\Psi(x+s) + Z\Psi(x-s) = 0 \quad (23)$$

from which the conditional probability density can be calculated

$$p(s|x) = \exp[-Z\Psi(x+s) - Z\Psi(x-s) - 1 - U(x) - \lambda(x)] \quad (24)$$

The normalization condition (1) determines the local Lagrange parameter, and Eq. (24) becomes

$$p(s|x) = \frac{\mathrm{e}^{-Z\Psi(x\,+\,s) - Z\Psi(x\,-\,s)}}{\langle \mathrm{e}^{-Z\Psi(x\,+\,s) - Z\Psi(x\,-\,s)} \rangle} \quad (25)$$

We also consider the terms multiplied by $\delta n(x)$:

$$\begin{aligned} &\ln n(x)v_0 - \gamma \ln(1 - n(x)v_0) \\ &\quad + \langle p(s|x)[Z\Psi(x+s) + Z\Psi(x-s)] \rangle \\ &\quad + \langle p(s|x)[\ln p(s|x) + U(x)] \rangle + 2Z\mu = 0 \end{aligned} \quad (26)$$

2.1. Including the Excluded Volume Effect

In the following we consider the situation in which the excluded volume of the spheroidal nanoparticles is taken into account. Therefore, $\gamma = 1$.

By inserting Eq. (25) into Eq. (26) and setting $\gamma = 1$, we obtain the equation for the concentration:

$$n(x) = \frac{q(x)\mathrm{e}^{-U(x) - 2Z\mu}}{v_0[1 + q(x)\mathrm{e}^{-U(x) - 2Z\mu}]} \quad (27)$$

where we defined

$$q(x) = \langle \mathrm{e}^{-Z\Psi(x\,+\,s) - Z\Psi(x\,-\,s)} \rangle \quad (28)$$

The ionic distribution function can be obtained by inserting Eqs. (27) and (25) into equation $n(x,s) = n(x)p(s|x)$:

$$n(x,s) = \frac{\mathrm{e}^{-Z\Psi(x\,+\,s) - Z\Psi(x\,-\,s) - U(x) - 2Z\mu}}{v_0[1 + q(x)\mathrm{e}^{-U(x) - 2Z\mu}]} \quad (29)$$

The volume charge density (18) can then be rewritten in the form

$$\frac{\rho(x)}{Ze_0} = \langle n(x-s,s) + n(x+s,s) \rangle \tag{30}$$

where we took into account the definition of the ion distribution function.

By inserting Eq. (29) into Eq. (30) we get

$$\rho(x) = \frac{Ze_0}{v_0} \left\langle \frac{\mathrm{e}^{-Z\Psi(x)-Z\Psi(x-2s)-U(x-s)-2Z\mu}}{1+q(x-s)\mathrm{e}^{-U(x-s)-2Z\mu}} + \frac{\mathrm{e}^{-Z\Psi(x)-Z\Psi(x+2s)-U(x+s)-2Z\mu}}{1+q(x+s)\mathrm{e}^{-U(x+s)-2Z\mu}} \right\rangle \tag{31}$$

In the first term of Eq. (31) we replace $-s$ with s and add both terms

$$\rho(x) = \frac{2Ze_0}{v_0} \left\langle \frac{\mathrm{e}^{-Z\Psi(x)-Z\Psi(x+2s)-U(x+s)-2Z\mu}}{1+q(x+s)\mathrm{e}^{-U(x+s)-2Z\mu}} \right\rangle \tag{32}$$

By taking into account Eq. (28), Eq. (32) can be rewritten as

$$\rho(x) = \frac{2Ze_0}{v_0} \left\langle \frac{\mathrm{e}^{-Z\Psi(x)-Z\Psi(x+2s)-U(x+s)-2Z\mu}}{1+\langle \mathrm{e}^{-Z\Psi(x+\bar{s}+s)-Z\Psi(x-\bar{s}+s)} \rangle \mathrm{e}^{-U(x+s)-2Z\mu}} \right\rangle \tag{33}$$

The outer averaging is performed over s while the inner averaging is performed over $\bar{s}$.

Using the expression (33) for volume charge density $\varrho(x)$ in the Poisson Eq. (15) yields the integro-differential equation for the reduced electrostatic potential in the form

$$\Psi''(x) = -\frac{8\pi l_{\mathrm{B}} Z}{v_0} \left\langle \frac{\mathrm{e}^{-Z\Psi(x)-Z\Psi(x+2s)-U(x+s)-2Z\mu}}{1+\langle \mathrm{e}^{-Z\Psi(x+\bar{s}+s)-Z\Psi(x-\bar{s}+s)} \rangle \mathrm{e}^{-U(x+s)-2Z\mu}} \right\rangle \tag{34}$$

The boundary conditions for this integro-differential equation are given at the charged surfaces:

$$\Psi'(x=0) = -\frac{4\pi\sigma l_{\mathrm{B}}}{e_0}, \qquad \Psi'(x=D) = \frac{4\pi\sigma l_{\mathrm{B}}}{e_0} \tag{35}$$

2.2. Excluding the Excluded Volume Effect

Here we consider the situation in which the excluded volume effect of spheroidal nanoparticles is not taken into account. Therefore, $\gamma = 0$.

By inserting Eq. (25) into Eq. (26) and setting $\gamma = 0$, we obtain the equation for the concentration:

$$n(x) = \frac{q(x)}{v_0} \mathrm{e}^{-U(x) - 2Z\mu} \tag{36}$$

where $q(x)$ is given by Eq. (28). The ion distribution function can be obtained by inserting Eqs. (36) and (25) into equation $n(x, s) = n(x)p(s|x)$:

$$n(x, s) = \frac{1}{v_0} e^{-Z\Psi(x+s) - Z\Psi(x-s) - U(x) - 2Z\mu} \tag{37}$$

Again, the volume charge density (18) can then be rewritten in the form

$$\frac{\rho(x)}{Ze_0} = \langle n(x - s, s) + n(x + s, s) \rangle \tag{38}$$

where we took into account the definition of the ion distribution function.

Inserting Eq. (37) into Eq. (38) we get

$$\begin{aligned} \rho(x) = \frac{Ze_0}{v_0} \langle &\mathrm{e}^{-Z\Psi(x) - Z\Psi(x-2s) - U(x-s) - 2Z\mu} \\ &+ \mathrm{e}^{-Z\Psi(x) - Z\Psi(x+2s) - U(x+s) - 2Z\mu} \rangle \end{aligned} \tag{39}$$

In the first term of Eq. (39) we replace $-s$ with s and add both terms:

$$\rho(x) = \frac{2Ze_0}{v_0} \langle \mathrm{e}^{-Z\Psi(x) - Z\Psi(x+2s) - U(x+s) - 2Z\mu} \rangle \tag{40}$$

The averaging is performed over s.

Using the expression (40) for volume charge density $\varrho(x)$ in Poisson Eq. (15) yields the integro-differential equation for the reduced electrostatic potential in the form

$$\Psi''(x) = -\frac{8\pi l_{\mathrm{B}} Z}{v_0} \langle \mathrm{e}^{-Z\Psi(x) - Z\Psi(x+2s) - U(x+s) - 2Z\mu} \rangle \tag{41}$$

The boundary conditions for this integro-differential equation are given at the charged surfaces by Eq. (35).

2.3. Numerical Methods

The integro-differential Eq. (41) was solved numerically. The boundary value problem was restated as a fixed-point equation $\Psi = \mathcal{G}(\Psi)$, where $\mathcal{G}(\Psi)$ is the solution Ξ of the ordinary differential boundary value problem:

$$\begin{aligned}\Xi''(x) &= -8\pi l_{\mathrm{B}} \frac{1}{v_0} Z \mathrm{e}^{-Z\Xi(x)-2Z\mu} \\ &\quad\times \frac{1}{2l} \int_{\max[-l,\, l-x]}^{\min[l,\, D-x]} \mathrm{d}s \, \exp(-Z\Psi(x+s))\end{aligned} \tag{42}$$

with boundary conditions

$$\Xi'(x=0) = -\frac{\sigma e}{\varepsilon k T} \tag{43}$$

$$\Xi'(x=D) = \frac{\sigma e}{\varepsilon k T} \tag{44}$$

The domain $[0, D]$ was represented by a mesh of N Chebyshev nodes, the function Ψ by an N-dimensional vector Ψ_N of values of Ψ at the mesh nodes, and the fixed-point equation was discretized into a finite dimensional algebraic equation $\Psi_N = \pi_N\left[\mathcal{G}\left({}_{p N}(\Psi_N)\right)\right]$, where $p_N(\Psi_N)$ is the interpolating polynom through the values of Ψ_N at the mesh nodes and $\pi_N(\Xi)$ is the N-dimensional vector representing the values of the function Ξ at the mesh nodes. The discretized fixed-point equation was rewritten as $G[\Psi_N] = \Psi_N - \pi_N\left[\mathcal{G}\left({}_{p N}(\Psi_N)\right)\right] = 0$ and then solved by "fsolve" MATLAB function (available in the optimization toolbox), which finds solutions of nonlinear algebraic equations by a least-squares method. The function "fsolve" requires the solution of the above-defined second-order ordinary boundary value problem which was restated as a system of first-order equations and solved by the "bvp4c" MATLAB function by collocation. The integral in the second-order ordinary boundary value problem was computed by the "quad" MATLAB function.

2.4. Monte Carlo Simulation

In the simulation, the standard Monte Carlo Metropolis algorithm [60] with Lekner periodic boundary conditions [61] in the directions parallel to the charged walls was used. A system of 100–200 spheres confined between two impenetrable charged surfaces was considered. Translational and rotational moves were taken into account. To make contact with the theory, the hard core interaction between particles and the walls was taken into account by means of the distance of the closest approach. The influence of the direct hard core interaction between spheres on the charge density distribution was also calculated for two cases (Figs. 4 and 5).

3. RESULTS

Electrostatic potential Ψ, volume charge density ρ, orientational order parameter S, and free energy F of the system are calculated for different values of model parameters: surface charge density σ, size of the spherical particles which corresponds to the distance between both charges l and distance between the charged surfaces D. The minimal distance D we can achieve is equal to the size of the particles l [when density of the particles (surface charge density) is not too high]. We keep constant valency of the charges $Z = 1$, which are positioned on the surface of the sphere ($l = a$).

Electrostatic potential between the charged surfaces is obtained for three different particle sizes at a distance between the surfaces $D = 20$ nm, which is much larger than the diameter of the particles l (Fig. 3A). We observe that the electrostatic potential monotonously decreases with increasing distance from the left charged surfaces and reaches its minimal value in the midplane. The slope of the electrostatic potential changes essentially at the distance

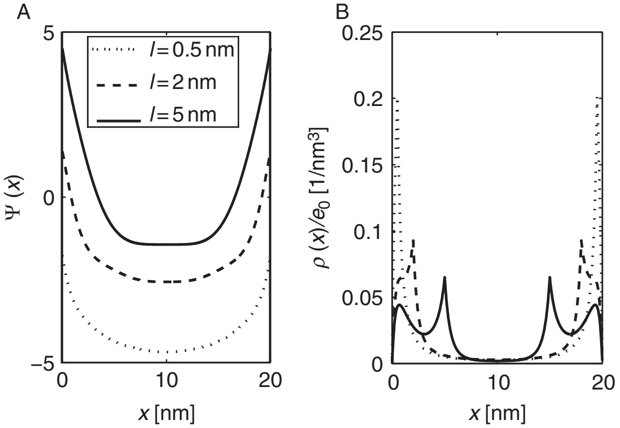

Figure 3 (A) Electrostatic potential Ψ and (B) volume charge density ρ as functions of the distance from the left charged surface x for three different diameters of the spheroidal nanoparticles. The model parameter is $|\sigma| = 0.033$ As/m^2.

$x \cong l$ from the charged surface for all values of l. In Fig. 3B we present the volume charge density distribution between both surfaces.

We can see one peak in the volume charge density near each surface for small particles ($l = 0.5$ nm). If we increase l, an additional minimum appears at $x \approx l/2$ (see full line in Fig. 3B). The reason for the existence of the additional minimum is that the probability to find nanoparticles with the center at $x = l/2$ which are oriented parallel to the surfaces decreases with increasing dimension of the nanoparticles.

It can be seen in Fig. 3 that for small particles in the limit of vanishing l, the electrostatic potential $\psi(x)$ as well as charge density distribution $\rho(x)$ converge towards the corresponding potential and concentration obtained by standard PB theory for point-like particles.

Although in the theory direct particle–particle interactions are not explicitly taken into account (since the theory is essentially the mean field approach), comparison of calculated volume charge density distribution with corresponding Monte Carlo simulations shows satisfactory agreement (Figs. 4 and 5). By using Monte Carlo simulations, we also checked the influence of the particle–particle hard core interactions which are not taken into account in the theoretical model. It can be seen in Fig. 4 that for distance $D = 2.5$ nm there is practically no difference in volume charge density profile between the predictions of theoretical model and Monte Carlo simulations. This ceases to be true when the distance between the surfaces is increased to $D = 4$ nm at the same surface charge density $|\sigma| = 0.033$ As/m^2 and the same size of the particles $l = 2$ nm (Fig. 5). Taking into account the particle–particle hard core interactions in MC

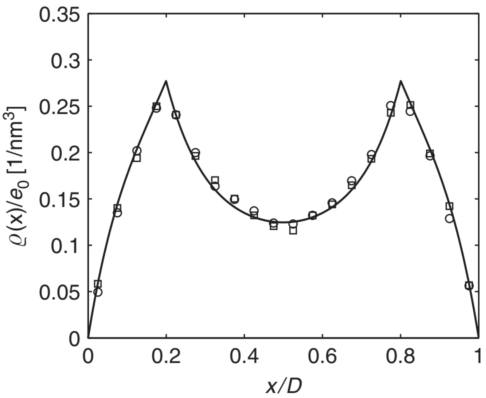

Figure 4 Influence of the hard core interaction between the spherical particles on the volume charge density $\rho(x)$ calculated for surface charge density $|\sigma| = 0.033$ As/m^2 and distance between the charged surfaces: $D = 2.5$ nm (squares: MC simulation with hard core interaction; circles: MC simulation without hard core interaction; solid line: theoretical prediction).

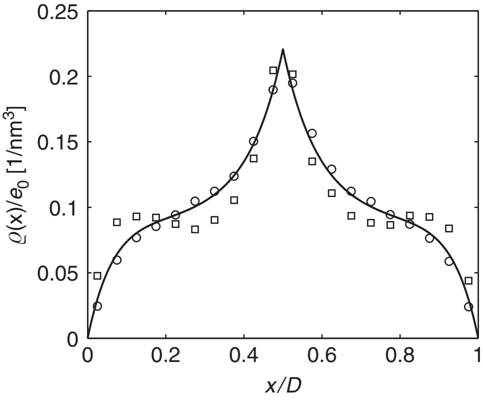

Figure 5 **Influence of the hard core interaction between the spherical particles on the volume charge density $\rho(x)$ calculated for surface charge density $|\sigma| = 0.033$ As/m^2 and distance between the charged surfaces: $D = 4$ nm (squares: MC simulation with hard core interaction; circles: MC simulation without hard core interaction; solid line: theoretical prediction).**

simulations, two peaks in $\rho(x)$ appear for $D = 4$ nm (Fig. 5), which means that the orientation of the particles is slightly stronger if the hard core interactions are taken into account. Therefore, the effects predicted by the theory are expected to be even more expressed because of the hard core interactions.

Figure 6 shows the average order parameter $S = \langle(3cos^2\vartheta - 1)/2\rangle$ as a function of the distance between the charged surfaces D. The angle ϑ describes the angle between the line connecting both charges of the nanoparticle (Fig. 1) and the x-axis. The dependence of S on the distance D exhibits a maximum at D slightly larger than the size of the particles l, then it falls down with increasing D to nearly fixed value and practically remains the same for any larger distance D. Monte Carlo results agree well with theoretical predictions, especially at smaller distances. For larger values of the surface charge density σ, the dependency $S(D)$ is shifted up, while it is decreased for smaller values of σ [26]. Figure 7 shows the order parameter S in dependence on the distance of the center of the spherical nanoparticles from the charged surface (x_c) for different values of surface charge density σ and the distance between the surfaces $D = 2.5$ nm. The order parameter S increases with increasing surface charge density $|\sigma|$ and exhibits two maxima near the charged surfaces (especially for higher surface charge densities), which means that the ordering near the charged surfaces is stronger than far from the surfaces.

The orientational ordering effect which we already observed in the volume charge density distribution and in the spatial dependency of the order parameter is also reflected in the free energy calculations. We consider

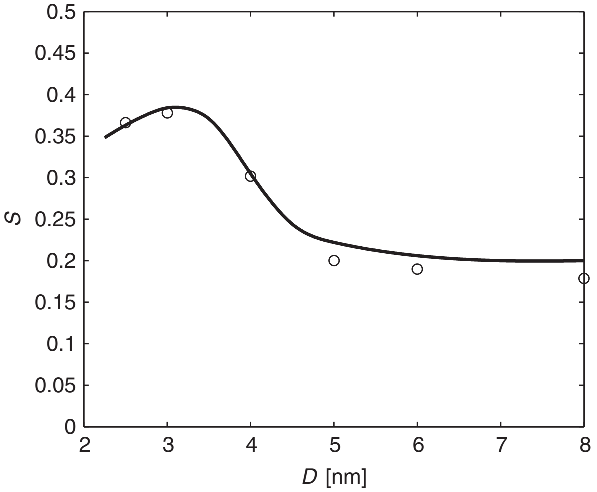

Figure 6 The average order parameter $S = \langle (3cos^2\vartheta - 1)/2 \rangle$, where ϑ is the angle between the main axis of nanoparticles and the x-axis. In dependence on the distance between the charged surfaces D for $l = 2$ nm, $|\sigma| = 0.07$ As/m^2.

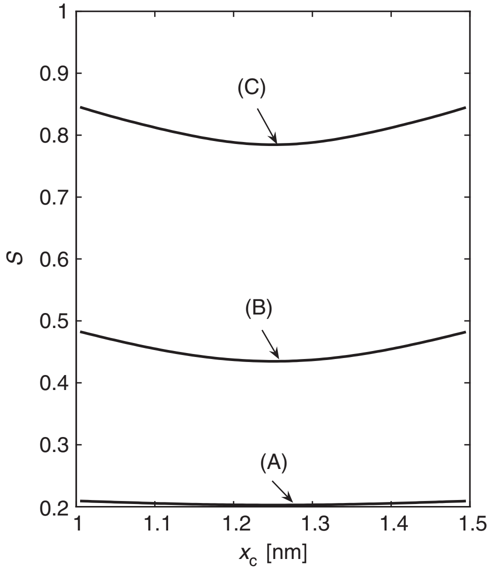

Figure 7 The order parameter S of spherical counterions as a function of the average position of their centers x_c for the distance between the charged walls $D = 2.5$ nm and diameter of ions 2 nm. The surface charge densities are (A) $|\sigma| = 0.033$ As/m^2, (B) $|\sigma| = 0.1$ As/m^2, and (C) $|\sigma| = 0.4$ As/m^2.

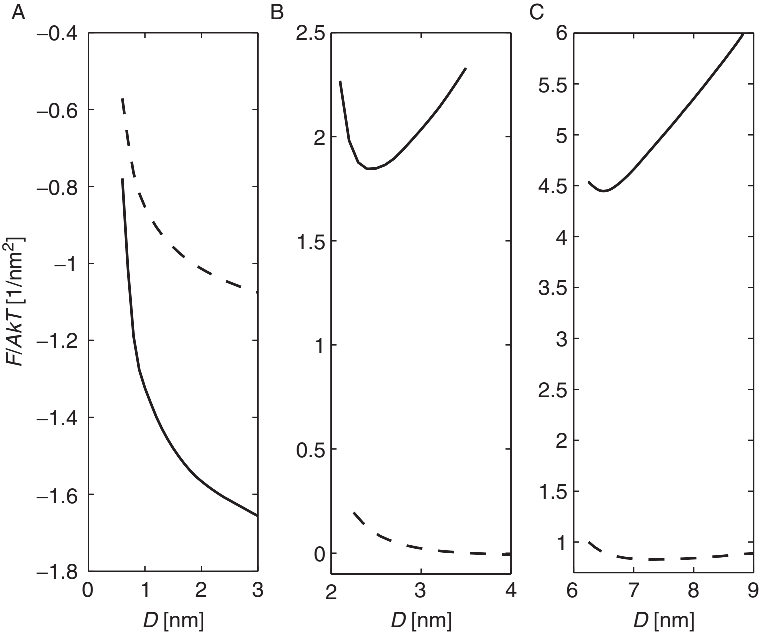

Figure 8 Electrostatic free energy F, measured per unit area of the charged surface A and per thermal energy kT as a function of the distance between two equally charged plates D for two different surface charge densities (solid lines: $|\sigma| = 0.1$ As/m^2, dashed lines: $|\sigma| = 0.033$ As/m^2). The diameters of the spheres are (A) $l = 0.5$ nm, (B) and $l = 2$ nm, and (C) $l = 6$ nm.

the interaction between two like-charged planar surfaces as a function of the distance D between them. The electrostatic free energy as a function of D is shown in Fig. 8 for two surface charge densities and for three sizes of the particles: $l = 6$ nm, $l = 2$ nm and $l = 0.5$ nm. It can be seen in Fig. 8A and B that for small surface charge density $|\sigma| = 0.033$ As/m^2, for the size of the particles $l = 0.5$ nm and $l = 2$ nm, the interaction between charged surfaces is repulsive, meanwhile for very large particles ($l = 6$ nm), the interaction also becomes attractive for small surface charge density σ with the minimum of the free energy at the value of D slightly larger than the size of the particles. On the other hand, the interaction between the like-charged surfaces is attractive for large surface charge densities (e.g., $|\sigma| = 0.1$ As/m^2) and large enough diameter of the nanoparticle ($l = 6$ nm or $l =$ 2 nm). In this case the repulsive behavior is observed only when the size of particles decreases below a certain value and approaches to the limit of point particles (see Fig. 8A). When the attraction between like-charged surfaces is predicted, the minima in the free energy occur at distances D close to the size of the particles l. Based on presented results it can be therefore concluded that the particle size plays a decisive role in the free energy dependency on the distance D and can revert the system from repulsive to attractive regime. As we have shown before, the orientational order parameter of the particles increases with decreasing distance between the surfaces D and with increasing surface charge density $|\sigma|$, indicating that orientational ordering of the particles near the surfaces mediates attractive interaction between the two like-charged surfaces.

4. CONCLUDING REMARKS

We studied the interactions between equally charged planar surfaces in a solution containing large multivalent spheroidal nanoparticles, that is, counterions with two charges placed diametrically on the surface of the nanoparticle. The distance of closest approach of the center of spherical nanoparticles to the charged surfaces was taken into account as the boundary condition for distribution of nanoparticles. Particle–particle hard core interactions were not taken into account in presented theoretical predictions, which according to our opinion leads to underestimation of the predicted attractive force. Although ion–ion interactions are not taken into account within the mean field approach, the comparison of the predicted volume charge density distribution with the corresponding results of the Monte Carlo simulations shows a good agreement, meaning that direct interactions do not play a major role in this case. The internal charge distribution with spatially separated charges within a single nanoparticle is reflected in intraionic correlations. Within the presented theoretical model, the expression for the free energy of the system contains in addition to usual electrostatic and entropic contribution to the free energy also the term due to orientational ordering of nanoparticles which is in our system the main reason for the predicted attractive interaction between the like-charged surfaces [27].

For large enough diameters of the multivalent spheroidal nanoparticles, the attraction between the equally charged surfaces takes place even at small surface charge densities. Attraction occurs at smaller sizes of the particles if the surface charge density of charged surfaces is large enough, which means that either the surface charge density or the size of the particles has to be large to yield attraction between like-charged surfaces. In the limit of the point-like particles, the presented theory reduces to PB theory where attraction between equally charged surfaces cannot be obtained.

The fact that the distance between the charged surfaces with minimal free energy is close to the diameter of the nanoparticles (Fig. 8), indicates that the bridging mechanism plays an important role in the predicted attractive force between like-charged surfaces [49, 62]. The calculated orientational order parameter (Fig. 6) shows that the most probable orientation of spheroidal nanoparticles coincides with the orientation of the particle's main axis (connecting the two charges) in perpendicular direction to the charged planar surfaces. The two point charges of the nanoparticle (Fig. 1) energetically prefer to be in close vicinity of both charged surfaces, so they connect them as a bridge which is most efficient when the distance between the charged surfaces becomes comparable to the distance between the two charges of the nanoparticle.

Our results could be used to explain the behavior of more complicated systems such as large spherical membrane surfaces immersed in a solution composed of complex nanoparticles with spatially distributed charges.

In biological systems, a relevant system is composed of negatively charged membranes in the solution containing large multivalent ions, such as in blood where blood cells and derived membranous vesicular structures are immersed in plasma. According to our results, proteins with dimeric distribution of localized positive charge (such as some antibodies) can mediate attractive interaction between negatively charged membranous structures. Indeed, it has been observed that anticardiolipin antibodies induce the coalescence of negatively charged phospholipid vesicles.

Mediated interaction between like-charged membranes may have an important impact on the process of microvesiculation of the cell membrane. Microvesicles are formed in the final stage of the process of membrane budding, that is, when the bud is pinched off the mother membrane to become a free microvesicle. While narrowing of the neck connecting the bud and the mother membrane, the membranes of the bud and of the mother membrane are in close proximity and are subject to the short-ranged interaction mediated by the plasma proteins. Proteins with appropriate distribution of charge act as mediators of the attractive interaction and cause adhesion of the bud to the mother membrane, thereby preventing the bud to become free microvesicle. Since microvesicles are prothrombogenic, the mediating effect of certain plasma proteins can be interpreted as an anticoagulant effect of plasma proteins. The results presented in this work may therefore add to a better understanding of the mechanisms that are important for the formation of blood clots.

REFERENCES

[1] S. McLaughlin, The electrostatic properties of membranes, Annu. Rev. Biophys. Biophys. Chem. 18 (1989) 113–136.

[2] G. Cevc, Membrane electrostatics, Biochim. Biophys. Acta 1031 (1990) 311–382.

[3] A. Iglič, M. Brumen, S. Svetina, Determination of the inner surface potential of the erythrocyte membrane, Bioelectrochem. Bioenerg. 43 (1997) 97–103.

[4] H. Hägerstrand, B. Isomaa, Lipid and protein composition of exovesicles released from human erythrocytes following treatment with amphiphiles, Biochim. Biophys. Acta 1190 (1994) 409–415.

[5] H. Hägerstrand, V. Kralj-Iglič, M. Bobrowska-Hägerstrand, A. Iglič, Membrane skeleton detachment in spherical and cylindrical microexovesicles, Bull. Math. Biol. 61 (1999) 1019–1030.

[6] M. Sorice, A. Circella, R. Misasi, V. Pittoni, T. Garofalo, A. Cirelli, A. Pavan, G.M. Pontieri, G. Valesini, Cardiolipin on the surface of apoptotic cells as a possible trigger for antiphospholipid antibodies, Clin. Exp. Immunol. 122 (2000) 277–284.

[7] M.C. Martinez, A. Tesse, F. Zobairi, R. Andriantsitohaina, Shed membrane microparticles from circulating and vascular cells in regulating vascular function, Am. J. Physiol. Heart Circ. Physiol. 288 (2005) H1004–H1009.

[8] T.J. Greenwalt, The how and why of exocytic vesicles, Transfusion 46 (2006) 143–152.

[9] K. Balasubramanian, J. Chandra, A.J. Schroit, Immune clearance of phosphatidylserine-expressingcells by phagocytes, J. Biol. Chem. 272 (1997) 31113–31117.

[10] S.K. Moestrup, I. Schousboe, C. Jacobsen, J.R. Leheste, E.I. Christensen, T.E. Willnow, Beta2-glycoprotein-I (apolipoprotein H) and beta2-glycoprotein-I-phospholipid complex harbor a recognition site for the endocytic receptor megalin, J. Clin. Invest. 102 (1998) 902–909.

[11] P. Thiagarajan, A. Le, C.R. Benedict, β2-Glycoprotein I promotes the binding of anionic phospholipid vesicles by macrophages, Arterioscler. Thromb. Vasc. Biol. 19 (1999) 2807–2811.

[12] B. Bouma, P.G. de Groot, J.M.H. van den Elsen, R.B.G. Ravelli, A. Schouten, M.J.A. Simmelink, Adhesion mechanism of human β_2-glycoprotein I to phospholipids based on its crystal structure, EMBO J. 18 (1999) 5166–5174.

[13] J. Marra, Direct measurement of the interaction between phosphatidylglycerol bilayers in aqueous electrolyte solutions, Biophys. J. 50 (1986) 815–825.

[14] R. Kjelander, S. Marčelja, R.M. Pashley, J.P. Quirk, Double-layer ion correlation forces restrict calcium-clay swelling, J. Phys. Chem. 92 (1988) 6489–6492.

[15] M. Dubois, T. Zemb, N. Fuller, R.P. Rand, V.A. Parsegian, Equation of state of a charged bilayer system: Measure of the entropy of the lamellar–lamellar transition in DDABr, J. Chem. Phys. 108 (1998) 7855–7869.

[16] V.A. Bloomfield, DNA condensation, Curr. Opin. Struct. Biol. 6 (1996) 334–341.

[17] V. Teif, Ligand-induced DNA condensation: Choosing the model, Biophys. J. 89 (2005) 2574–2587.

[18] I. Rouzina, V. Bloomfield, Macroion attraction due to electrostatic correlation between screening counterions. 1. Mobile surface-adsorbed ions and diffuse ion cloud, J. Phys. Chem. 100 (1996) 9977–9989.

[19] T.E. Angelini, H. Liang, W. Wriggers, G.C.L. Wong, Like-charge attraction between polyelectrolytes induced by counterion charge density waves, Proc. Natl. Acad. Sci. USA 100 (2003) 8634–8637.

[20] W.M. Gelbart, R. Bruinsma, P.A. Pincus, V.A. Parsegian, DNA-inspired electrostatics, Phys. Today 53 (2000) 38–44.

[21] J.C. Butler, T. Angelini, J.X. Tang, G.C.L. Wong, Ion multivalence and like-charge polyelectrolyte attraction, Phys. Rev. Lett. 91 (2003) 028301.

[22] D.F.H. Evans Wennerström, The Colloidal Domain: Where Physics, Chemistry, Biology, and Technology Meet. (1994) VCH Publishers, New York.

[23] J.N. Israelachvili, Intermolecular and Surface Forces. (1997) Academic Press, London.

[24] E. Verwey, J. Overbeek, Theory of the Stability of Lyophobic Colloids. (1948) Elsevier Publishing Company Inc.

[25] J. Sadar, D. Chan, Long-range electrostatic attractions between identically charged particles in confined geometries and the Poisson–Boltzmann theory, Langmuir 16 (2000) 324–331.

[26] J. Urbanija, K. Bohinc, A. Bellen, S. Maset, A. Iglič, V. Kralj-Iglič, P.B. Sunil Kumar, Attraction between negatively charged surfaces mediated by spherical counterions with quadrupolar charge distribution, J. Chem. Phys. 129 (2008) 105101.

[27] K. Bohinc, A. Iglič, S. May, Interaction between macroions mediated by divalent rodlike ions, Europhys. Lett. 68 (2004) 494–500.

[28] A.G. Moreira, R. Netz, Simulations of counterions at charged plates, Eur. Phys. J. E 8 (2002) 33–58.

[29] L. Guldbrand, B. Jönsson, H. Wennerström, P. Linse, Electrical double layer forces. A Monte Carlo study, J. Chem. Phys. 80 (1984) 2221–2228.

[30] B. Svensson, B. Jönsson, Chem. Phys. Lett. 108 (1984) 580.

[31] D. Bratko, V. Vlachy, Distribution of counterions in the double layer around a cylindrical polyion, Chem. Phys. Lett. 90 (1982) 434–438.

[32] R. Kjellander, S. Marčelja, Chem. Phys. Lett. 112 (1984) 49.

[33] H. Greberg, R. Kjellander, Charge inversion in electric double layers and effects of different sizes for counterions and coions, J. Chem. Phys. 108 (1998) 2940–2953.

[34] R. Kjellander, Ion–ion correlations and effective charges in electrolyte and macroion systems, Berichte der Bunsen-Gesellschaft 100(6) (1996) 894–904.

[35] V. Vlachy, Ionic effects beyond Poisson–Boltzmann theory, Annu. Rev. Phys. Chem. 50 (1999) 145–165.

[36] M. Stevens, M. Robbins, Density functional theory of ionic screening: When do like charges attract? Europhys. Lett. 12 (1990) 81.

[37] Z. Tang, L. Scriven, H. Davis, Interactions between primitive electrical double layers, J. Chem. Phys. 97 (1992) 9258–9266.

[38] A. Diehl, M. Tamashiro, M. Barbosa, Y. Levin, Density-functional theory for attraction between like-charged plates, Physica A 274 (1999) 433.

[39] J. Forsman, A simple correlation-corrected Poisson–Boltzmann theory, J. Phys. Chem. B 108(26) (2004) 9236–9245.

[40] P.A. Pincus, S.A. Safran, Charge fluctuations and membrane attractions, Europhys. Lett. 42 (1998) 103–108.

[41] D.B. Lukatsky, S.A. Safran, Pressure of correlated layer-charge and counterion fluctuations in charged thin films, Phys. Rev. E 60 (1999) 5848–5857.

[42] A.W.C. Lau, D.B. Lukatsky, P. Pincus, S.A. Safran, Charge fluctuations and counterion condensation, Phys. Rev. E 65 (2002) 051502.

[43] T. Akesson, C. Woodward, B. Jonsson, Electric double layer forces in the presence of polyelectrolytes, J. Chem. Phys. 91 (1989) 2461–2469.

[44] I. Borukhov, D. Andelman, H. Orland, Effect of polyelectrolyte adsorption on intercolloidal forces, J. Phys. Chem. B 103 (1999) 5042–5057.

[45] A. Watts (Ed.), Protein–Lipid Interactions (1993) Elsevier.

[46] N. Ben-Tal, B. Honig, C. Miller, S. McLaughlin, Electrostatic binding of proteins to membranes. Theoretical predictons and experimental results with charybdotoxin and phospholipid vesicles, Biophys. J. 73 (1997) 1717–1727.

[47] D. Murray, A. Arbuzova, G. Hangyas-Mihalyne, A. Gambhir, N. Ben-Tal, B. Honig, S. McLaughlin, Electrostatic properties of membranes containing acidic lipids and adsorbed basic peptides: Theory and experiment, Biophy. J. 77 (1999) 3176–3188.

[48] D. Murray, S. McLaughlin, B. Honig, The role of electrostatic interactions in the regulation of the membrane association of G protein $\beta\gamma$ heterodimers, J. Biol. Chem. 276 (2001) 45153–45159.

[49] R. Podgornik, Polyelectrolyte-mediated bridging interactions, J. Polym. Sci.: Part B: Polym. Phys. 42 (2004) 3539–3556.

[50] B. Yoon, A. Lenhoff, Computation of the electrostatic interaction energy between a protein and a charged surface, J. Phys. Chem. 96 (1992) 3130–3134.

[51] V. Kralj-Iglič, A. Iglič, A simple statistical mechanical approach to the free energy of the electric double layer including the excluded volume effect, J. Phys. II (France) 6 (1996) 477–491.

[52] E. Trizac, J. Raimbault, Long-range electrostatic interactions between like-charged colloids: steric and confinement effects, Phys. Rev. E 60 (1999) 6530–6533.

[53] P.M. Biesheuvel, M. van Soestbergen, Counterion volume effects in mixed electrical double layers, J. Colloid Interface Sci. 316(2) (2007) 490–499.

[54] M.V. Fedorov, A.A. Kornyshev, Ionic liquid near a charged wall: Structure and capacitance of electrical double layer, J. Phys. Chem. B 112(38) (2008) 11868–11872.

[55] W. Fawcett, Charge distribution effects in the solution chemistry of polyatomic ions, Condens. Matter Phys. 8 (2005) 413–424.

[56] A. Razinger, A. Iglič, V. Kralj-Iglič, Orientation of multivalent ions near charged planar surfaces, J. Phys. A: Math. Gen. 39 (2006) 3275–3282.

[57] N. Cuvillier, F. Rondelez, Breakdown of the Poisson–Boltzmann description for electrical double layers involving large multivalent ions, Thin Solid Films 327–329 (1998) 19–23.

[58] J.C. Jackson, Classical Electrodynamics. (1999) John Wiley and Sons. Inc., New York.

[59] K. Bohinc, V. Kralj-Iglič, A. Iglič, Thickness of electrical double layer. Effect of ion size, Electrochim. Acta 46 (2001) 3033–3040.

[60] D. Frenkel, B. Smit, Understanding Molecular Simulations Academic. (1996) New York.

[61] J. Lekner, Summation of coulomb fields in computer-simulated disordered systems, Physica A 176 (1991) 485.

[62] A.Yu. Grosberg, T.T. Nguyen, B.I. Shklovskii, Colloquium: The physics of charge inversion in chemical and biological systems, Rev. Mod. Phys. 74 (2002) 329.

SUBJECT INDEX